

The Chemistry of Reticular Framework Nanoparticles: MOF, ZIF, and COF Materials

Evelyn Ploetz,* Hanna Engelke,* Ulrich Lächelt,* and Stefan Wuttke*

Nanoparticles have become a vital part of a vast number of established processes and products; they are used as catalysts, in cosmetics, and even by the pharmaceutical industry. Despite this, however, the reliable and reproducible production of functional nanoparticles for specific applications remains a great challenge. In this respect, reticular chemistry provides methods for connecting molecular building blocks to nanoparticles whose chemical composition, structure, porosity, and functionality can be controlled and tuned with atomic precision. Thus, reticular chemistry allows for the translation of the green chemistry principle of atom economy to functional nanomaterials, giving rise to the multifunctional efficiency concept. This principle encourages the design of highly active nanomaterials by maximizing the number of integrated functional units while minimizing the number of inactive components. State-of-the-art research on reticular nanoparticles—metal-organic frameworks, zeolitic imidazolate frameworks, and covalent organic frameworks—is critically assessed and the beneficial features and particular challenges that set reticular chemistry apart from other nanoparticle material classes are highlighted. Reviewing the power of reticular chemistry, it is suggested that the unique possibility to efficiently and straightforwardly synthesize multifunctional nanoparticles should guide the synthesis of customized nanoparticles in the future.

1. Introduction

Reducing the size of a material down to the nanoscale sounds trivial at first thought, but in reality, it entails more than just synthesizing small particles: it opens the doors into a world of materials with fundamentally different properties. Nanoparticles have uniquely high surface-to-volume ratios, particular size- and surface-dependent properties that ensure accessibility of the outer surface, and distinct size-dependent quantum effects.^[1] Nanoparticles also form colloiddally stable emulsions, which allows them to not only offer sites for chemical reactions, but also to participate in reactions as reactants. This allows for combination of established chemistry with the new physical and chemical properties of nanoparticles. With these features, nanoparticles can revolutionize a plethora of applications, such as solar cells and optoelectronics, nanophotonics and nanoplasmonics, catalysis, drug delivery and biomedical imaging.^[2]

Based on this wide range of applications,

nanotechnology has developed into a key technology. It continually makes major contributions in healthcare, agriculture,^[3] energy,^[4] resource efficiency,^[5] environmental programs,^[6] climate protection,^[7] mobility,^[8] and civil security.^[9] The huge variety of applications in all these different fields has turned nanotechnology into a very interdisciplinary science combining chemistry, physics, engineering, material science, theory, biology, pharmacy, medicine, and many others.

All of these applications require specific chemical and physical properties that are dependent on the size and chemical composition of the material. Ultimately, high-quality nanoparticles are needed with size and composition tuned to meet the specific purpose of the applications. Thus, not only the size is desired to be tunable, but also the composition of the material. In recent years, this has been enabled by the invention of reticular chemistry, where molecular building blocks are connected by strong bonds into extended structures such as metal-organic frameworks (MOFs),^[10] zeolitic imidazolate frameworks (ZIFs),^[11] and covalent organic frameworks (COFs).^[12] This allows for the synthesis of crystalline materials whose chemical composition, structure, porosity, and functionality can be controlled with atomic precision. Organic building units (OBUs) can either create frameworks on their own (resulting in COF materials) or assemble with inorganic building units (IBUs)

Dr. E. Ploetz, Dr. H. Engelke
Department of Chemistry and Center for NanoScience (CeNS)
LMU Munich
81377 Munich, Germany
E-mail: evelyn.ploetz@cup.uni-muenchen.de;
hanna.engelke@cup.uni-muenchen.de

Dr. U. Lächelt
Department of Pharmacy and Center for NanoScience (CeNS)
LMU Munich
81377 Munich, Germany
E-mail: ulrich.laechelt@cup.uni-muenchen.de

Prof. S. Wuttke
BCMaterials
Basque Center for Materials
UPV/EHU Science Park, 48940 Leioa, Spain
E-mail: stefan.wuttke@bcmaterials.net

Prof. S. Wuttke
Ikerbasque
Basque Foundation for Science
48013 Bilbao, Spain

 The ORCID identification number(s) for the author(s) of this article can be found under <https://doi.org/10.1002/adfm.201909062>.

© 2020 The Authors. Published by WILEY-VCH Verlag GmbH & Co. KGaA, Weinheim. This is an open access article under the terms of the Creative Commons Attribution License, which permits use, distribution and reproduction in any medium, provided the original work is properly cited.

DOI: 10.1002/adfm.201909062

to form 3D extended hybrid materials (resulting in MOF or ZIF materials). To date, reticular synthesis has produced thousands of new materials—over 68 000 structures are reported in the Cambridge Structural Database (CAS)—each with unique topologies, geometries, structural backbone, and appended functional groups.^[13] The distinct ability of reticular chemistry to produce tailor-made materials makes this field a prime candidate for solving problems associated with gas storage,^[14] separation,^[14c,e,15] water harvesting,^[16] catalysis,^[17] energy,^[18] sensing,^[19] diagnosis,^[19a,20] and therapy.^[21]

By combining the modular design of reticular materials with the unique properties of nanoparticles, we can conceivably synthesize materials that can be tuned exactly to the needs of their respective applications. Exploring this space has led (and will continue to lead) to materials with entirely new, unforeseen properties that push the limits of materials in current applications and pave the way for even more novel applications.

To this end, reticular nanoparticles that consist of active building blocks are particularly interesting.^[5a] In contrast to the traditional approach (in which the nanoparticle serves only as passive scaffolding or carriers), nanoparticles themselves will consist of functional building blocks that actively participate in the respective function of the nanoparticle. In biomedical applications, nanoparticles often serve as carrier systems that are loaded with a drug or are surface-functionalized with a drug, but the nanoparticle itself does not contribute to the therapeutic effect. After the drug has been released, the now useless nanoparticles and their metabolites have the potential to cause a variety of side effects in the body before they are excreted. This problem can be alleviated if a nanoparticle could incorporate the drug into its own structure, using it as a molecular building block and therefore actively participating in the therapeutic function of the treatment.^[5a] This would reduce the risk of adverse effects, since the nanoparticle is the drug—it just dissolves during treatment and disappears.

It is likewise desirable to maximize the functional efficiency of nanoparticles in any other applications. To reach the maximum multifunctional efficiency, the integrated functional building units need to be tuned as precisely as possible and the number of inactive components has to be minimized. The ideal nanoparticle does not contain any components that do not directly contribute to its function; instead all components actively participate in as many functions as possible, creating a highly efficient multitool.^[5a]

The aim of this review is to provide a comprehensive overview of MOF, ZIF, and COF nanoparticle functionalization chemistry and the implementation of these strategies in key applications. The key idea is to give a fresh perspective to the reader that would stimulate the field to build on the past and shape the future.

We divide the review into nine sections with the first section being the introduction and the last section the conclusion. The seven sections in between elucidate different aspects of reticular framework nanoparticles (see **Figure 1**). We start with an explanation of different synthesis methods (Section 2) including solvothermal, microwave-assisted, ultrasound radiation synthesis, the use of modulating agents, electrochemical synthesis, grinding, and microfluidic synthesis. Next, we



Evelyn Ploetz received a PhD in physics at the LMU Munich. Her research focuses on the development and application of advanced imaging approaches to study transport processes and interactions of porous materials with living systems. She employs label-free nonlinear, multimodal imaging as an analytical tool to study dynamics in porous materials.

Hanna Engelke is a group leader at the Department of Chemistry at LMU Munich. Her main research interests are nanoparticle-cell interactions as well as mechanobiology employing optogenetics and bioengineering. The goal of her work with nanoparticles is to employ biophysical methods to develop and characterize nanoparticles for biomedical applications.

Ulrich Lächelt is a research group leader at the LMU Munich working on new routes and materials for drug delivery. His research focuses on the intracellular delivery of biomacromolecules such as nucleic acids, peptides, and proteins and the development of nanopharmaceuticals based on inorganic-organic hybrid materials.

Stefan Wuttke is an Ikerbasque Professor at the BCMaterials, Spain. His research is focused on developing methodologies to write and read chemical information onto and from the backbone of hybrid framework materials. In addition, his research interests also include the acquisition of a fundamental understanding of the chemical and physical processes involved in their synthesis and functionalization.

describe different characterization techniques (Section 3), which are essential for any application. We address techniques for characterization of shape and morphology, particle size and heterogeneity, crystal size, crystallinity and phase, porosity, and surface charge and characteristics followed by a brief summary. In Section 4, we provide an overview of methods for inner surface functionalization and introduce the idea of multifunctional efficiency. Section 5 summarizes host-guest interactions from theory and experimental point of view covering interactions in various states of matter. We then describe different functionalization strategies of the outer surface with polymers and with lipids based on noncovalent and covalent conjugation as well

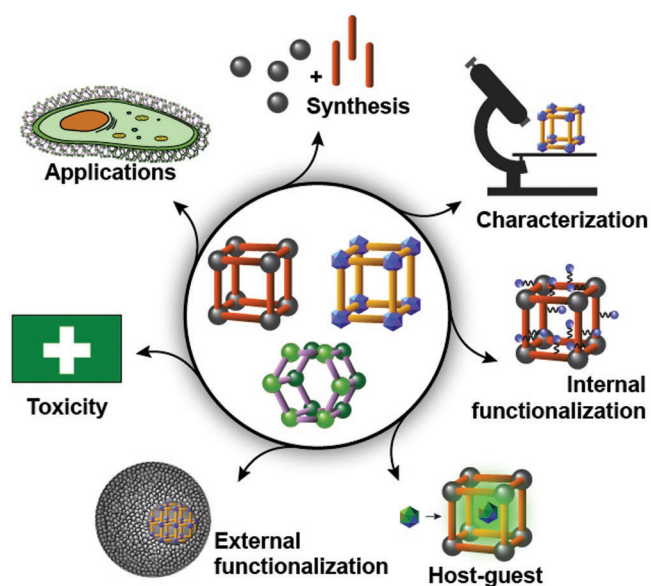


Figure 1. Schematic overview of the key topics of this review: chapter 2 (synthesis of reticular nanoparticles), 3 (characterization of reticular nanoparticles), 4 (inner surface functionalization), 5 (host-guest interactions), 6 (external surface functionalization) 7 (toxicity of reticular nanoparticles), and 8 (applications).

as self-assembly. Toxicity of reticular framework nanoparticles, another key parameter that needs to be assessed for applications, is the topic of Section 7. Finally, in Section 8 we review a variety of applications of reticular framework nanoparticles. The selected applications are in therapy, diagnostics, biotechnology, and heterogeneous catalysis.

2. Synthesis of Reticular Nanoparticles

The synthesis of reticular materials in bulk is challenging enough, but the synthesis of reticular nanoparticles is even more demanding, requiring the products to have uniform size and shape at a scale that is nearly impossible to monitor. Successful reticular nanoparticle synthesis will produce particles with high crystallinity, homogenous morphology, colloidal stability, and a uniform size distribution. All of these can be achieved through controlled nucleation/crystal growth and effective suppression of agglomeration processes.^[1a] Agglomeration is an intrinsic property of reticular nanoparticles with coordinatively unsaturated metal and linker sites at the external surface, resulting in high surface energy that favors agglomeration. Agglomeration is particularly prevalent in the synthesis of colloidal stable COF nanoparticles which tend to form insoluble microcrystalline powders.^[22] Fortunately, COF nanoparticle chemistry is in its nascency, so we are confident that the creativity of reticular researcher will address this challenge in the near future.

In general, reticular nanoparticles are synthesized with wet chemical approaches. Under these conditions, the formation of the nanoparticles can be described by the three-step LaMer mechanism:^[23] 1) the dissolution of precursors leading

to supersaturation of the reaction solution and the formation of reactive monomers; 2) reactive monomer concentration increases until it reaches the critical nucleation concentration; and 3) steady crystal growth until the precursors and crystals reach equilibrium. This process can be influenced by a variety of different factors, such as temperature, solvent, precursor, concentrations, and/or the presence of modulating agents. Other factors that contribute to the final size and shape of reticular nanoparticles include the equilibria of the substeps and side reactions, such as linker deprotonation, solvent degradation, and Ostwald ripening or digestive ripening.^[21b,24]

2.1. Solvothermal Synthesis

The most convenient approach to reticular nanoparticle synthesis is simply mixing metal-salt and linker precursor solutions at room temperature to precipitate nanoparticles (Figure 2). Size can be controlled by setting a particular stirring speed, carefully selecting solution concentrations or quenching the reaction at a certain time, as shown in the synthesis of HKUST-1 and ZIF-8.^[25] In some cases, nanoparticle formation has to be triggered by adding initiation solvents to the precursor solutions poorly soluble nanoparticle species will precipitate.^[26] In other cases, spontaneous precipitation has to be slowed down by using cooled reaction mixtures or stopping crystal growth instantaneously by using freeze-drying.^[27]

Solvothermal synthesis is commonly used in bulk synthetic methods and can be applied to initiate spontaneous precipitation by introducing additional heating steps. Reaction times usually range from a few hours to a week.^[26b,28] Solvothermal nanoparticle usually requires the use of diluted bulk-reaction conditions to slow down the reaction kinetics and enable homogenous nanoparticle growth.^[29] Choosing a suitable solvent or a solvent mixture is another important aspect in solvothermal reticular nanoparticle synthesis. A prominent example is the synthesis of NH₂-MIL-53(Fe) where particle morphology can be controlled by changing the ratio of water to DMF.^[30]

2.2. Microwave-Assisted Synthesis

Microwave-assisted synthesis is another common technique in nanoscience because it ensures homogenous internal heating by direct coupling of microwave radiation to molecular dipoles and ions present in the reaction mixture (Figure 2). The conversion of electromagnetic energy into heat is very efficient, and results in particles with homogenous morphology and narrow size distributions.^[31] As shown in a quantitative theoretical and experimental study on many MOFs and ZIFs, microwave heating can accelerate nucleation and crystal growth up to 30 times more than conventional heating.^[32] Microwave synthesis is therefore a fast and efficient technique for the generation of monodisperse reticular nanoparticles. Famous studies include MOF MIL-88A and MIL-101(Cr) nanoparticles,^[33] in which particle size and crystallinity were altered by varying the reaction temperatures, irradiation times, precursor concentrations, and pressure.

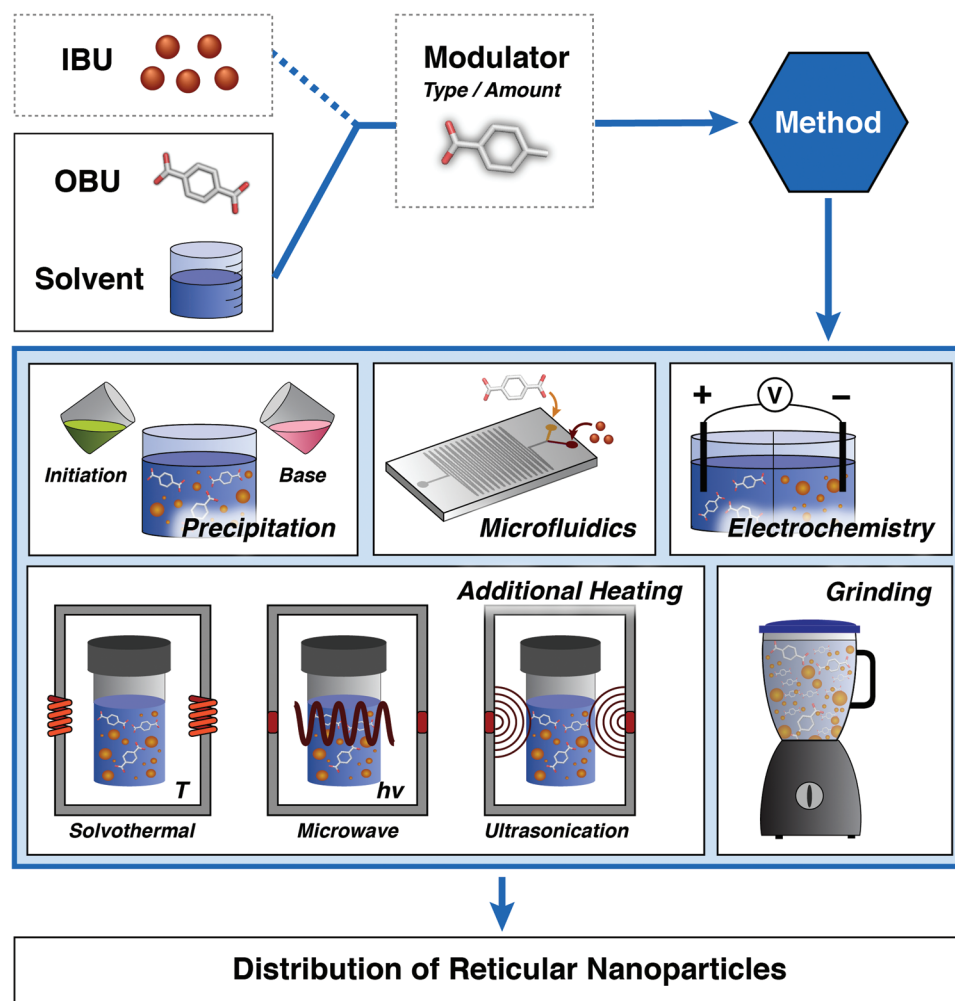


Figure 2. The synthesis of reticular nanoparticles by wet chemical approaches starts with the dissolution of precursors, followed by nucleation and crystal growth. Experimental techniques to control the crystallization process include spontaneous and solvothermal precipitation, heating by microwave radiation and ultrasonication, mechanical grinding, as well as approaches based on microfluidics and electrochemistry.

2.3. Ultrasound Radiation Synthesis

Ultrasound irradiation (Figure 2) is another heating technique for the generation of nanoparticles. Hotspots that are caused by collapsing microbubbles generated by sonication provide locally high temperatures (5000 K) and pressures (1000 bar) and initiate rapid crystal growth.^[34] As shown in an extensive study on MIL-53 that compared conventional heating, microwave heating, and ultrasound synthesis, ultrasound methods were the fastest to produce a crystalline product.^[35] In this study, ultrasound synthesis exhibited reaction rates that were up to a 100 times higher than those of conventional heating at comparable temperatures. Additionally, the method yielded the smallest nanoparticles. Another study on MIL-88A showed that the resulting nanoparticles depend on the type of ultrasound radiation delivered.^[36] In these experiments, the use of an ultrasonic bath led to the formation of microparticles that became smaller as sonication time increased. Pulsed versus continuous ultrasonic probes create nanoparticles with new size and width aspect

ratios, but the particles also grew smaller overall with longer exposure times. Perhaps most importantly, sonication can also be used to break up agglomerated nanoparticles, as shown for HKUST-1.^[37]

2.4. Modulating Agents

One of the most common approaches to control the size and morphology of reticular nanoparticles is the addition of modulating agents (Figure 2) to the reaction mixture.^[28,38] The influence of modulator concentration during solvothermal nanoparticle synthesis has two effects: in small amounts, the modulating agent increases the concentration of deprotonated ligands causing nucleation centers and decreases the particle size. Second, modulator molecules compete with the organic linkers for the coordination sites of the metal-centers, slowing the reaction kinetics which in turn regulates the size and shape of the nanoparticles. High modulator concentrations increase the tendency of particles

to agglomerate into large particles due to the increased probability of crystal collision. Using the modulator approach, it is possible to promote anisotropic crystal growth as shown in $\text{Cu}_2(\text{ndc})_2(\text{dabco})$ ($\text{ndc} = 1,4\text{-naphthalene dicarboxylate}$; $\text{dabco} = 1,4\text{-diazabicyclo-[2,2,2]-octane}$) using acetic acid in DMF.^[38b]

Systematic variation of the acidity of monocarboxylic modulators is another way to control nanoparticle growth, as shown for MIL-101(Cr).^[39] A plethora of studies have been conducted on this zirconium based MOF, especially for UiO-66. In this system, weak bases such as triethylamine can be used to precisely tune the nanoparticle size by deprotonating linker molecules. However most common, modulating agents are short-monocarboxylic acids that compete with organic ligands for coordination to metal-centers.^[40] For UiO-66 and many other MOFs, this coordination-modulation can be realized with many molecules, such as acetic acid, benzoic acid, trifluoroacetic acid, and dichloroacetic acid.^[21b,41] Side effects of modulating agents include the accumulation of the modulators on the particle's surface, changing its functionality and introducing defects into the framework.^[5a,42]

Surfactants are a special class of modulating molecules added during MOF, ZIF, or COF synthesis.^[43] They are long, nonpolar alkyl chains terminated with a polar group. In solution, surfactants form colloids called micelles, which minimize the interaction of their nonpolar groups within the polar medium (or vice versa). Surfactants can be used to stabilize nanosized droplets by forming a layer at the interface of two immiscible phases. Depending on the ratio of the individual components and nature of the surfactants, the shape of the nanodroplets can be adjusted. In reticular nanoparticle synthesis, microemulsion droplets can be used as nanoreactors. Water/oil based microemulsion, for example, has been used to generate rare-earth MOF nanoparticles, in which the shape and size of the resulting nanoparticles is controlled by surfactant/solvent ratio.^[44] The size and morphology control of La-BTC MOFs in an ionic liquid/water/surfactant system was explained by the interfacial reaction of La^{3+} ions dissolved in the water with linker molecules dissolved in the ionic liquid droplets.^[45] The shape of the droplets dictated the final shape of the MOF nano- and micromorphologies. There are many variations of microemulsion-based MOF nanoparticle synthesis, including liquid–solid-solution (LSS) growth that has been used for the size-controlled synthesis of HKUST-1 nanoparticles. In this approach, copper-ions and BTC linkers were added in two successive steps to an oleic acid/oil-phase/aqueous-phase microemulsion. This led first to the formation of Cu-oleic acid clusters which then reacted at the water/oil interface with BTC ligands forming HKUST-1 nanoparticles through hydrophobic coating.^[46] Surfactants additionally open up the possibility of using templates to induce certain structures during reticular nanoparticle synthesis. For MIL-101(Cr), adding CTAB to the aqueous synthesis mixture resulted in mesoporous nanoparticles as the framework crystallizes around the micelles.^[47]

In addition to these common synthesis methods, there are many synthesis procedures that are less common but still

worth mentioning. In some cases, special solvents such as ionic liquids are used as structural directing agents or to improve reaction times during nanoparticle synthesis. For example, the synthesis of Zn-BDC MOF nanoparticles in a supercritical CO_2 /ionic liquid/surfactant system resulted in hexagonally porous Zn-BDC MOF nanoparticles.^[48]

Similarly, UiO-66 nanoparticles have been synthesized by assaying the influence of ionic-liquid reaction conditions on the properties of the resulting particles.^[49] Compared to solvothermal reactions, the UiO-66 particles formed with higher speed. This phenomenon was explained by hydrogen bonding between ionic liquids and acetic acid (the modulating agent). The hydrogen bonding enabled rapid exchange of modulator for linker molecules in the initial metal-clusters that were formed in the reaction, and therefore increased the nucleation speed.

2.5. Electrochemical Synthesis

Electrochemical synthesis (Figure 2) of MOF nanoparticles has been shown for IRMOF-3 in a DMF/ethanol/TATB electrolyte.^[50] In this setup, linker molecules are deprotonated at the copper cathode and move to the anode for MOF assembly. At the anode, the Zn^{2+} ions required for the MOF are generated by anodic oxidation of the electrode. The size of the resulting nanoparticles is modulated either by increasing voltage or changing solvent ratios.

A recent study demonstrated that MIL-100(Fe) nanoparticles could be produced by heterogeneous nucleation on polystyrene nanospheres.^[51] In the first step of this synthesis, nanocolloids are functionalized with linker molecules by immersion in an aqueous solution. Subsequent addition of iron(III) precursors and solvothermal treatment lead to the growth of MIL-100(Fe) nanoparticles on the bead surface. Removal of the polystyrene beads via DMF washing results in nanoparticles that are smaller than conventionally synthesized particles and can be tuned by varying the amount and size of the polymer colloids in the reaction mixture.

Many reticular nanoparticles have also been synthesized with dry-chemical approaches. Especially noteworthy is the synthesis of MIL-101(Cr), which was produced by solvent-free grinding and dry heating.^[52] The resulting phase-pure nanoparticles were smaller than solvothermally produced particles, but the nanoparticles were also strongly aggregated and lost their homogeneous morphology.

2.6. Grinding

Liquid assisted grinding relies on the mechanochemical reaction of precursor materials in the presence of catalytic amounts of solvents (Figure 2). Using this method, phase-pure $\text{NH}_2\text{-UiO-66}$ nanoparticles have been synthesized in less than 2 h.^[53] In the same study, nanoparticles of the same MOF were also synthesized by exposing the precursors to methanol vapors for 3 days at elevated temperatures. Another study has demonstrated the synthesis of Pd-loaded ZIF-8 nanoparticles via room temperature ball milling.^[54] The synthesis was based on sacrificial ZnO

nanoparticle templates that were completely converted to ZIF-8 nanoparticles using catalytic amounts of solvent.

2.7. Microfluidic Synthesis

Microfluidic flow reactors have gained popularity in the last few years as they possess the highest degree of reaction time and temperature control, which can be required to ensure precise crystallization conditions.^[55] In a microfluidic reactor, the reaction solutions are pressed through narrow channels, either in tubing or on a chip, with a diameter of a few hundredths of micrometers (Figure 2). While traversing the reactor-channel, a reaction mixture passes through heated segments. The small channel diameters provide fast heat transfer resulting in a high control over nucleation and crystal growth. For MOFs, this results in smaller particle and reaction speeds up to 400 times faster than conventional solvothermal heating.^[56] The heating time is controlled by the speed at which the reaction solution passes through the heated sections, which can be controlled to fractions of seconds. This allows for the fine-tuning of nanoparticle sizes, as shown for UiO-66 and other MOFs and ZIFs, as well as for COFs.^[56,57] Microfluidic setups are easily customizable: pressure regulators and heat resistant equipment allow for solvothermal MOF synthesis under pressurized conditions (as shown for cerium(III) terephthalate MOF nanoparticles).^[58] Surfactants and nonmiscible solvents are the basis for droplet-microfluidic setups that function similar to microemulsions and feature highly controlled droplet-sizes.^[59] Using this setup, nanoparticles of the MOFs Ru₃BTC₂ and UiO-66 have been synthesized, and size modulation can be carefully controlled (as demonstrated for MIL-88B).^[60]

Taken as a whole, controlled reticular nanoparticle synthesis is the key for the precise formulation and subsequent application of nanoparticles. While reviewing this topic, however, we recognized that only little attention is given to qualitative studies approaching this topic. This is certainly due to the fact that synthesis of high-quality reticular nanoparticles is very challenging due to the intrinsic rich chemistry of those materials, which is often a blessing and a curse at the same time. Nevertheless, the realization of monodisperse, colloiddally stable reticular nanoparticles is a fundamental prerequisite for their application. Thereby, future studies should be dealing with the systematic screening of different synthesis conditions as well as using all available synthesis approaches. Such studies should be accompanied by a comparatively and comprehensive characterized as it was recently demonstrated and will be discussed in the next section.^[61]

3. Characterization of Reticular Nanoparticles

The outcome of nanoparticle synthesis is invariably a polydispersion and as a consequence very susceptible to small variations in the reaction mixture. Many parameters, such as temperature and solvent (or even the form of the magnetic stirrer!), influence the outcome and hence the physicochemical properties of reticular nanoparticles. In the following section, we will give an overview on current state-of-the-art methods

to characterize those properties, namely, shape, size, surface charge, and porosity. Our key intention is that we provide the reader with guidelines how to characterize specific properties of nanoparticles and discuss experimental pitfalls and limitations. The characterization of the chemical composition and the chemical stability of the materials is not scope of this review. Further in-depth reading of nanoparticle characterization and specific techniques can be hence found in further reviews.^[10a,42a,61a,62]

Given the incredible diversity of MOF, COFs, and ZIF nanoparticles in terms of composition and functionalization, the number of chemical combinations and structural possibilities are nearly endless. These particles feature a completely different chemistry with a varying set of physicochemical properties. In addition, these nanoparticles display—as every nanoparticle—often properties that are governed by their nanometer dimensions (e.g., size-determined properties). The statistic characterization of their full set of different physicochemical parameters is limited fundamentally by the fact that each of the available characterization methods itself is based on different physical process. Only a combination of complementary methods will provide a full overview on all subsets of properties. In order to gain a comprehensive understanding of the properties of specific nanoparticles, the characterization of morphology, shape, size, porosity, and surface charge is indispensable (Figure 3), to predict their behavior on nanometer scale. Beside chemical composition these properties majorly affect the application of nanoparticles. Size and morphology influence, e.g., the functionalization capacity of nanoparticles, determine their motional behavior in solution, decide upon their optical properties^[63] or the uptake into cells,^[64] to name a few. The accessible outer and inner surface-area are the key for specific surface functionalization in host–guest interactions (Section 5)^[65] or loading of molecules to nanoparticle drug delivery systems (Section 8.2).^[66] In particular in aqueous solution, the surface charge of nanoparticles dominates the interactions between the particle and its surrounding and determine its trend toward aggregation. In the following section, we therefore describe the physical mean of the above-mentioned properties, their implication and experiments methods, to describe them.

3.1. Morphology and Shape

Reticular nanoparticles like MOF particles are composed of at least two types of primary building blocks, e.g., organic linkers and single metal atoms or polyatomic clusters with several metal atoms. These assemble into secondary building units (SBUs) with predetermined, commonly polyhedral structure. The SBUs are again connected by strong coordination bonds and form a net with higher topology. Depending on the presence of modulating agents during synthesis, SBUs can have various coordination numbers. Zirconium-based MOFs, e.g., have been reported^[67] with a coordination number of 12, 10, 8, and 6. The morphology of the SBUs hence predetermines the network topology^[68] such as cubic and hexagonal skeletons and the resulting pore sizes. Even more complicated structures can be achieved by combining heterogeneous SBUs.^[69] In addition to the framework structure, modulating ligands also affect the

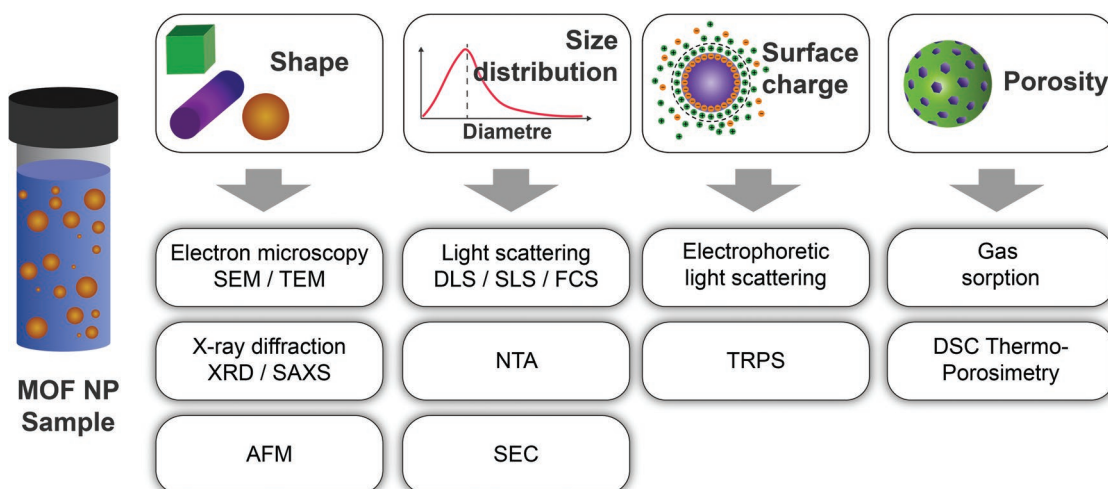


Figure 3. Characterization methods of reticular nanoparticles.

overall crystal size, morphology and shape of the assembled nanoparticle.^[70]

The term morphology describes the structural, respectively geometrical appearance of nanoparticles. It takes into account the physical size, flatness, roundness, sphericity, and aspect ratio of the particles. By selecting the appropriate precursors and control strategies diverse morphologies have been synthesized:^[71] 0D polyhedra like hexa-, octa-, and decahedral nanoparticles (**Figure 4A**), but also extended nanoparticles like 1D full and hollow rods, tubes and flat polyhedra with finite thickness.

The term shape is the other aspect that describes the appearance of a particle without considering its dimensions. It characterizes the deviation from an isometric particle, i.e., a spherical nanoparticle. While spherical particles have the same length in all three dimensions (so does its projection), anisometric particles have different extensions for different dimensions (**Figure 4B**). Polyhedral particles like decahedra can appear in various shapes including pentagons when imaged as 2D projection by high-resolution scanning technique. Since nanoparticles feature a wide range of morphologies, complementary techniques for 2D and 3D analysis should be employed to determine the “size” of them.

Shape and morphology of nanoparticles are usually characterized in dry state by high-resolution microscopy techniques in particular electron microscopy, which analyses nanoparticles

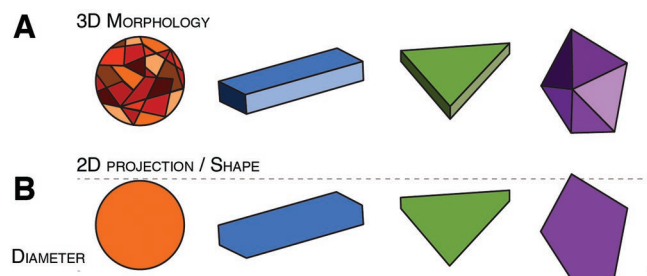


Figure 4. Shape and morphology of nanoparticles.

at the single-particle level with sub-nanometer resolution in 2D. The combination of electron microscopy and electron diffraction provides additional information about the relationship between the inner crystal structure and the overall morphology of the nanoparticle. However, the above-mentioned techniques are carried out under vacuum and require oxide-free, electrically conductive surfaces. To determine the particles’ true 3D geometry in solution, Atomic force microscopy (AFM) in tapping mode can be an option. Further techniques including small-angle X-ray scattering (SAXS) and analytical ultracentrifugation (AUC) can also be employed to describe the shape of nanoparticles in solution. Since they serve more to determine the physical and crystal size, we describe them in detail in the following sections.

3.1.1. Scanning Electron Microscopy (SEM)

In electron microscopy, nanoparticles in dry state are exposed to an electron beam. Incident electrons cause various radiations including the emission of i) elastically scattered electrons, ii) inelastic scattered low-energy secondary electrons, and iii) X-ray radiation from atoms within the sample. The detection of secondary electrons is commonly employed in SEM.^[72,73] The electron beam is scanned over the sample where secondary electrons are taken as readout for the topology and atomic composition of nanoparticles. SEM allows to determine the size, shape and surface morphology of nanoparticles with a reduced resolution of about 1 nm compared to transmission electron microscopy (TEM) (0.05–0.1 nm). This is due to the fact that lower beam energies with an acceleration voltage below 30 kV are employed. SEM is hence limited in penetration depth, and only reports about the sample’s surface, however at the benefit of less beam-induced sample damage as in TEM. SEM requires conductive substrates. Most reticular nanoparticles, however, are insulating, which results in image artefacts due to charging effects. To decrease the charge build-up from the electron source, the sample is commonly coated with a thin

film (5–10 nm) made of gold or carbon, which modifies the physical size and surface structure. The accelerating voltage of the electron beam further on alters the appearance of the investigated particles. While image resolution benefits from higher voltages, less surface details like defects are visible. To obtain quantitative information on the elemental composition regarding metal dispersion and incorporation, e.g., in MOF nanoparticles, SEM is often coupled with complementary techniques like energy-dispersive X-Ray spectroscopy and inductively coupled plasma optical emission spectroscopy (ICP-OES) for element determination.

3.1.2. Transmission Electron Microscopy

TEM^[72a,e,74,75] is an established imaging technique of sub-micrometer sized objects based on the scattering of an electron beam with an acceleration voltage around several 100 kV. The transmitted electron beam is commonly detected on a phosphorescent screen as a function of position on the ultrathin sample. The transmission of unscattered electrons depends on the thickness and elemental composition of the nanoparticles. Areas of heavy elements are intrinsically characterized by a higher density of electrons and therefore appear darker since they prevent the transmission of the incident electrons. Based on this imaging contrast, TEM reports on the morphology, the physical size, shape, phase and orientation of nanoparticles on a particle-to-particle basis. In order to provide statistics on the particle dimensions, automated imaging^[76] is employed, which can be quite time consuming. TEM provides images of 3D nanostructures with sub nanometer precision, however as 2D projection on the imaging plane: while spherical particles are simple to describe, irregularly shaped particles suffer from the projection in 2D. The derived size parameters do not necessarily reflect the real sample geometry as the projections strongly depends on the particle orientation. Moreover, if particles are deposited to densely or aggregate, their structures can be obscured. TEM relies on a high energy electron beam that can damage the sample and might alter the physical dimensions of the particles and requires high vacuum environment. It is hence not suited for fragile nanoparticles that have to be kept in a solvent. Conventional TEM does not require any coating as in SEM, but it directly interacts with the fixed sample that is commonly stained by vacuum-deposited platinum for increased imaging contrast. To prevent fixation, cryo-TEM^[77] is an alternative based on shock freezing the sample. Further realizations comprise correlative TEM,^[78] freeze fracture TEM,^[79] and scanning transmission electron microscopy (STEM).^[72b]

3.1.3. Atomic Force Microscopy

AFM^[80,81] is a scanning probe microscopy technique with atomic resolution that mechanically probes the sample surface of nanoparticles using a cantilever. The sharp tip at the end of the cantilever is scanned over the surface. The interaction between the tip and the sample induces a force on the cantilever mainly due

to electrostatic and van der Waals repulsion. The induced tilt of the cantilever is readout by reflecting of a laser beam from the tip onto a photodiode. Spatial changes in reflection can be related to spatial information about the sample's surface topology. The displacement on the detector can be either a vertical or lateral deflection depending on the measurement mode. As a major benefit, AFM provides 3D images down to 0.1 nm resolution under ambient condition without sample preparation by filtration or coating as it is required for SEM. Samples can be measured under dry condition but also in solution using AFM in tapping mode. Similar to SEM and TEM methodologies, AFM is a tool for characterizing the shape, structure and size of nanoparticles. The main strength of AFM, however, is its capability to image biomaterials and their interactions, like sorption and aggregation in aqueous fluids.^[80b] The main drawback is its intrinsic overestimation of lateral size due to the discrepancy between the size of the cantilever tip and the dimensions of the nanostructures. AFM images have a size of a few hundred micrometers. Since data acquisition can take several minutes depending on the imaging mode, AFM is hence not dedicated for high throughput characterization of nanoparticles.^[80a]

3.2. Particle Size and Heterogeneity

Given their small size (1–100 nm) and large surface-area-to-volume ratio, nanoparticles have unique properties. Size is therefore one of the key parameters that—in its basic definition—refers to the spatial extent of a particle. On the nanometer length scale, however, size refers to three different properties: i) the physical diameter, i.e., its dimension given by the atomic structure of the particle; ii) the effective crystal size; and iii) the radius of gyration or hydrodynamic radius that describes the effective size of the particle in a viscous environment due to its diffusion behavior and motion. This last parameter strongly takes into account the interaction between the nanoparticle's surface and surrounding matrix and/or other particles. All three “sizes” can be measured by a wide range of analytical techniques that characterize different aspects.

Nanoparticles are neither necessarily spherical nor homogeneous. Complementary techniques are required that characterize the size of particles at the single-particle level, as well as their size distribution in bulk. A further important property that needs to be taken into account is the stability: since nanoparticles can show varying dimensions depending on environment, particles need to be characterized in dry state but also in liquid environment.^[61a] The most common techniques in dry state or even vacuum include SEM, TEM, and AFM for size determination. Soft-angle X-ray scattering and X-ray diffraction are employed to characterize crystal size of nanoparticles at sub-nanometer resolution. For particle suspensions with similar dimensions, diffusion-based methods such as (static/dynamic) light scattering (LS, SLS, and DLS), fluorescence correlation spectroscopy (FCS), and differential centrifugal sedimentation (DCS) along with size-exclusion chromatography (SEC) can be employed.^[82] For nanoparticle above 30 nm, nanoparticle tracking analysis (NTA; 30–1000 nm) and fluorescence-activated nanoparticle sorting (FANS; >100 nm) have become complementary approaches.^[83]

3.2.1. Physical Size and Size Distribution

Nanoparticles are classified according to their dimensions, i.e., they are materials of which at least 50% have one or more external dimensions between 1 and 100 nm.^[84] The physical size, i.e., its physical dimension, is commonly characterized with sub-nanometer resolution using EM and AFM. As discussed in the last section, these methods provide images of the 2D projection of 3D particles. Given the fact that every monodisperse sample will show a certain degree of variability in size and morphology, the derived size values represent average values of a particle preparation. As these techniques are hampered in throughput it is cumbersome to derive a representative size distribution by high-resolution scanning microscopy.

3.2.2. Radius of Gyration and Hydrodynamic Radius

Light scattering, diffusion, and sedimentation are further tools to investigate particles suspensions. Aside of the intrinsic variability in size and morphology, the majority of particles is nonspherical. Hence, aside of the averaged size value of the distribution, the actually derived diameter does not reflect the physical dimensions, but rather refers to a hypothetical spherical particle with identical physical properties. The determined size will vary between different techniques. While there is a sufficiently good agreement for monodisperse colloidal suspensions, irregularly shaped particles result in deviating size values. Ensemble techniques based on light scattering are biased toward larger size values within heterogeneous samples. Methods with single-particle resolution like nanoparticle tracking analysis and analytical ultracentrifugation provide an average size value that is based by the equally weighted number of counted particles. Distributions are hence not only characterized by their arithmetic mean but also width given by its standard deviation and standardized procedures have been introduced.^[85]

Light Scattering: LS techniques play a central role in the characterization of nanoparticles. In a typical LS experiment,^[86] colloidal suspensions are exposed to a monochromatic beam of light, such as a laser source, and scattered light is monitored on a sensitive detector. Particles in solution are subjected to random forces due to constant collisions with the surrounding solvent molecules. This leads to a random walk of particles, also referred to Brownian motion. Their movement causes translation friction, which is temperature dependent and linked to the particle's size, i.e., the hydrodynamic radius R_H and viscosity η of the surrounding medium. Translational friction and diffusion are inversely related and can be described via the Stokes–Einstein equation for uncharged nanoparticles as

$$D = \frac{1}{f} k_B T = \frac{k_B T}{6\pi\eta R_H} \quad (1)$$

with k_B being the Boltzmann's constant, D the diffusion coefficient, and f the friction coefficient. The diffusion coefficient is not only size- and shape-dependent, but also dependent on surface properties, like surface charge (see electrophoretic light

scattering (ELS)) and surface coating. Molecules like polymers or lipids, which adsorbed to the MOF particle or were added to the particles for surface functionalization, will alter the surface and hence diffusion properties. All methods dealing with the size of particles fail to properly describe nonspherical particles. They all are more/less sensitive to the scattering intensity (e.g., NTA) or projected 2D area (EM) and will result in mean distribution of sizes for any given sample. If the shape is changing, the hydrodynamic radius will be directly affected. For a needle-shaped particle, changes concerning its length will immediately affect the diffusion, whereas changes in the diameter of the particle will hardly be detected.

Static Light Scattering: In SLS,^[87,88] the intensity of scattered light is analyzed as time-averaged intensity and serves as readout for the molecular weight of nanoparticles and their radius of gyration. Complementary results can be obtained using SAXS. The radius of gyration R_g is defined as an average root mean squared distance from the center of the mass of all constituent within the MOF nanoparticle, which can be written as

$$\langle R_g^2 \rangle = \frac{\sum_i m_i r_i^2}{m_i} \quad (2)$$

with m_i and r_i being the mass and distance to the center for every element within the nanoparticle. SLS allows to determine the size of particle suspensions from 100 to 1000 nm, if the particle shape is known. SLS is therefore often applied only to obtain the average molecular weight M of macromolecular particles such as polymers. SLS is an ensemble-based technique that returns information about the size distribution of particles. Since its scattering amplitude is strongly size dependent, it is biased toward larger particles and should only be applied to nearly monodisperse samples. Nevertheless, SLS and DLS are largely complementary and often used in conjunction since they circumvent each other's limitation with respect to viscosity, temperature, weight concentration and refractive index.

Dynamic Light Scattering: DLS^[87–89] represents the most common method to characterize reticular nanoparticles with respect to size, shape and dispersity in suspensions. In DLS, the temporal fluctuations of scattered light are analyzed via photon correlation. DLS characterizes particle ensembles and determines the mean hydrodynamic diameter of MOF nanoparticles down to 1 nm within only short acquisition times. The concentration^[83a] employed for DLS measurements ranges between 10^8 and 10^{12} particles mL^{-1} . Technical implementations have been described in large details.^[90] Shortly, a coherent light source is imposed onto a nanoparticle suspension, where light is scattered on the particles. Scattering is detected perpendicular or under $\approx 180^\circ$. Brownian motion of the particles causes time-dependent fluctuations of the detected signal. The normalized autocorrelation function $G_2(\tau)$ of equally sized particles in suspension that describes the motion, is approximated^[91] to

$$G_2(\tau) = \frac{\langle I(0)I(t+\tau) \rangle}{\langle I(t) \rangle^2} = A \cdot \left[1 + B \cdot e^{(-2Dq^2\tau)} \right] \quad (3)$$

where τ is the time delay between compared time points t and $t + \tau$. A and B refer to baseline and intercept of the correlation

function. D is the diffusion coefficient and $q = (4\pi n/\lambda \cdot \sin(\theta/2))$ resembles the scattering vector linked to the refractive index n of the suspension, wavelength λ of light and scattering angle θ . For monodisperse samples, the determined diffusion coefficient D can be linked to the sphere-equivalent hydrodynamic diameter d_H via the Stokes–Einstein equation (Equation (1)). For nonspherical particles, the hydrodynamic diameter can differ substantially from the physical diameter derived from electron microscopy. For polydisperse sample systems, the autocorrelation function becomes a sum of exponential decays associated with each additional population in size. Different algorithms have been developed to analyze multidisperse populations.^[92] The interpretation becomes, however, exceedingly difficult for heterogeneous particle distributions, for which NTA is the technique of choice. The scattered light is proportional to the sixth power of the particle diameter, which makes DLS very sensitive to detect small amounts of large particles. DLS hence often overestimates the actual particle size. It is biased toward large particles that can even shield small sized nanoparticles. A further well-known pitfall of DLS is its low peak resolution. Particle populations have to differ at least by a factor^[83a] of 3 in size. DLS is very sensitive to temperature and solvent viscosity. For diffusion-based approaches we hence advice to calibrate and verify the accuracy via calibrated, mono-disperse standard samples with diameters at 50, 200, and 600 nm in the same solvent as employed for the MOF suspension. By this, the temperature dependent viscosity of the employed solvent can be determined. The accurate temperature for DLS experiments must be determined separately.

Fluorescence Correlation Spectroscopy: FCS analysis and fluorescence cross correlation (XCS) analysis are commonly used to study the interaction and binding of, e.g., proteins to the nanoparticle corona.^[93,94] When labeling both binding partners, FCS and XCS allow to monitor the binding, even when the diffusion properties of the particle are not altered significantly. The concentration employed for FCS measurements should not exceed 10^{12} particles mL^{-1} . FCS characterizes particle ensembles and determines the mean hydrodynamic diameter of nanoparticles down to 1 nm within acquisition times of minutes (cf. section 3.2.2.).

Nanoparticle Tracking Analysis: NTA^[83a] provides direct and real-time visualization of reticular nanoparticles on a particle-by-particle basis. It offers a simultaneous, multiparameter analysis of nanoparticles in the range^[83a] of 0.03–1 μm in liquid suspensions with respect to size distribution and concentration. Similar to DLS, it is based on free diffusion of particles in solution and hence relates the degree of movement due to Brownian motion to the hydrodynamic diameter of the particle. NTA measures the diffusion by parallel tracking the random position of particles and is suitable for characterizing mixed particle size distributions at high resolution. The experimental principle and instrumentation have been reviewed in details.^[61a,83a,95] Briefly, NTA combines laser light scattering microscopy^[96] with a charge-coupled device (CCD) camera. A monochromatic light source is directed on the sample cuvette and gets scattered by individual particles. The Mie scattered signal of nanoparticles within the field of view gets recorded by the CCD camera over time. Next, the NTA software identifies individual particles during data analysis and tracks their movement between consecutive frames of the movie. Brownian

motion occurs in three dimensions, while NTA extracts the 2D displacement $(x, y)^2$ of each particle. This is linked to the particle diffusion coefficient D , from which the hydrodynamic diameter can be determined via the Stokes–Einstein equation (Equation (1))

$$\overline{(x, y)^2} = 4Dt \quad (4)$$

NTA shows several advantages compared to other more frequently used methods, such as DLS or size-exclusion chromatography.^[97] It is slightly more accurate for sizing monodisperse populations^[83a] and allows to simultaneously count the detected particles.^[95a] Additionally, particle properties like the refractive index or surface coating influence the scattering amplitude. This makes NTA a preferred tool for polydisperse samples.^[83a] On the other hand, NTA is restricted to working concentration around 10^7 and 10^9 particles mL^{-1} and requires several optimization steps with respect to identifying suitable settings for the video capture and analysis. This fact in combination with the requirement of high level of scattering in solution has limited the wide application of NTA as routine method compared to DLS.

Differential Centrifugation Sedimentation: DCS^[98,99] determines the size distribution and density of nanoparticles by its sedimentation time in fluids during differential centrifugation. DCS works for particles with sizes ranging^[98d] between 10 nm and 50 μm and has the ability to distinguish polydisperse particle distributions with size difference of less^[97a] than 3% even in strongly agglomerated samples when nanoparticles are exposed to biological media.^[98c] The sedimentation of particles is based on Stokes law

$$F = f\dot{v} = 6\pi\eta R_H \dot{v} \quad (5)$$

which links the frictional force F that acts between the MOF nanoparticle and the solvent and the flow velocity \dot{v} relative to the particle. The friction coefficient f depends on the temperature dependent viscosity η of the solvent and the hydrodynamic radius R_H of a hypothetical spherical particle that has the same translational diffusion as the particle under investigation. Technically, DCS is realized using a rotating transparent disc,^[98d] which is filled by a fluid density gradient, often made of water sucrose.^[98a] This liquid gradient ring is created by a series of injections of mixtures with decreasing density. Once it is established, the particle suspension is injected in the center of the disc. During the constant rotational motion, particles sediment from the center toward the outside edge of the disc. Their speed only depends on particle size and density. Heavier particles arrive first. A laser source is guided through the liquid near the edge and the light extinction caused by traversing nanoparticles is recorded on a photodetector. The determined sedimentation time t between injection and detection can be related to the radius of the nanoparticle that is subjected to Stokes force, centrifugal force and flotation force. It can be expressed as^[98c,100]

$$R_H = \sqrt{\frac{\alpha}{4t(\rho - \rho_0)}} \quad (6)$$

with

$$\alpha = \frac{18\eta \ln(r_d/r_0)}{\omega^2} \quad (7)$$

The hydrodynamic radius R_H of the particle depends on its density ρ and density of the medium ρ_0 as well as the systems constant α that summarizes the influence of the solvent's viscosity η , the angular frequency of rotation ω , and the radial position of the detector r_d and beginning of the gradient r_0 , respectively. The setup parameter α has to be calibrated via standardized particles samples^[98c] of known size $R_{H,cal}$ and density ρ_{cal} under identical experimental conditions before each experiment. This procedure is necessary, since viscosity and density of the gradient will change due to dilutions between consecutive measurements as well as frictional heating of the disc over time. DCS results show good agreement with size distributions obtained from electron microscopy,^[98c] however, its accuracy strongly depends on the user. Referencing with particles of known size introduce a systematic bias into the measurement procedure. Nevertheless, DCS has proven to a technique that is less invasive than SAXS and able to determine both, size and density of reticular nanoparticles.

Analytical Ultracentrifugation: AUC^[101] reports on size, size distribution and particle number of nanoparticle suspensions based on the sedimentation properties during ultracentrifugation. Due to high rotor speed on the order of 50 000 rpm it can separate even very small nanoparticles down to 1 nm and less with Ångström resolution.^[102] Large particles (>600 nm) sediment too quickly for AUC.^[83c] DCS on the contrary is able to detect nanoparticles up to 10 μm due to slower centrifugation making it complementary. In AUC, the sample is left to sediment in an optically clear quartz cell, which is fixed onto the rotor of an ultracentrifuge. The centrifugal force pushes nanoparticles outward and generates a time-dependent concentration gradient $C(r, t)$ as a function of radial distance r to the rotor center. During the measurement, this concentration gradient is followed over time via absorbance spectroscopy and recorded on detectors in radial direction. It has to be considered that particles of different size and molecular weight separate and sediment at different rates. The time dependent distribution is analyzed afterward to determine the sedimentation coefficient $C(s)$ that is linked to the particle size distribution. AUC can analyze nanoparticles with broad size distribution by using a rotational ramp composed of many speed steps.^[101b] The main limitation of AUC lies in the fact that the density of particles needs to be known prior calculating the particle size distribution from the sedimentation coefficient. This makes it challenging to study nanoparticles suspensions were aggregation might play a role. The introduction of multiwavelength detection for AUC, however, largely expanded its applicability even to nanoparticle–protein interactions and might turn AUC into a widespread technique.

Size-Exclusion Chromatography: SEC^[103] is frequently employed to analyze and separate macromolecules, such as proteins or polymers, but also nanoparticles according to their hydrodynamic radius in some cases also molecular weight.^[104] It is a liquid gel-filtration chromatographic technique and employs columns filled with specific resins for particles separation. These resins are commonly made of polyacrylamide, agarose or dextran and prepared as porous

spheres with size ranges from 3 to 20 μm and pore sizes in the higher nanometer range depending on the dimension of the sample that shall be fractionated. The underlying concept of SEC is the dependence of the hydrodynamic radius on the particle size. Here, larger molecules in size and weight elute faster than small ones. This can be explained by less frequent entry and exclusion from pores and hence shorter retention times. Its interaction with the resin is primarily controlled by entropy (see (8)) since ideally there is no adsorption to the resin particles and no enthalpic contribution, hence $\Delta H = 0$. With this, the retention factor in SEC,^[105] i.e., the fraction of resin pore volume that is accessible for the nanoparticles is only dependent on entropy and can be described by the retention volumes of the loaded nanoparticle V_{NP} , the void volume V_0 and the resin V_R

$$K_D = \exp\left(\frac{\Delta G^0}{RT}\right) = \exp\left(\frac{\Delta S^0}{R}\right) = \frac{V_{NP} - V_0}{V_R} \quad (8)$$

For an SEC measurement, the sample suspension is inserted onto the column and pressure is applied, to force the molecules or nanoparticles through the resin by low flow of buffer. The filtered solution, i.e., the eluate is collected in constant volumes and examined by spectroscopic techniques, most commonly by UV/Vis absorption, refractive index measurements, light scattering, but also fluorescence detection. SEC is employed to produce highly monodisperse samples and facilitates the purification of nanoparticles. Its main strength is its capability to fractionate particles according to their size and hence retention time. SEC, however, does not serve to determine the actual physical diameter of particles quantitatively. Based on the hydrodynamic radius, identically sized particles with different surface charge will interact differently with the resin and will elute at different times. SEC in combination with AUC however will precisely successfully determine the size distribution of even heterogeneous particle suspension.

3.2.3. Crystal Size, Crystallinity, and Phase

Reticular nanoparticles are built up hierarchically from preformed secondary building blocks that are arranged in periodically structured network.^[68] An increasing number of MOF nanoparticles, e.g., is made of two or even more metal-containing SBUs and/or mixed linkers leading to diverse networks.^[106] Their occurring nets are classified using RCSR notation^[107] and their overall structures are documented at the Cambridge structural database.^[13] Porous, crystalline solids, such as COF and MOF nanoparticles, possess frameworks of variable stability and highly variable crystallographic densities^[106] down to 1 g cm^{-3} .

Crystal structures are traditionally determined by X-ray diffraction techniques, even though they are only partially suited for organic framework nanoparticles due to their small size and density. Low-density particles are additionally challenging: they are prone to crystal twinning due to high symmetry^[106] and often “contaminated” with small guest molecules inside pores that distort the underlying

framework. Electron and neutron diffraction can overcome this hurdle and characterize nanosized crystals since they provide better resolution due to differing scattering cross-sections. Selected area electron diffraction in combination with TEM is frequently used to study the crystallinity in a spatially resolved manner. Another complementary technique represents solid-state NMR^[62e] that can precisely locate hydrogen atoms correctly which are often involved in adsorption and guest binding. Nevertheless, X-ray-based techniques are more commonly employed to reticular nanoparticles and regarded as most reliable methods for newly synthesis framework particles.^[106]

Single-Crystal X-Ray Diffraction: Single-crystal X-ray diffraction^[108] can be used to solve the tertiary structure of a well-ordered framework nanoparticle at the atomic level. SC-XRD determines the lattice dimension, phase composition, orientation and crystallinity. X-ray scattering on nanomaterial is challenging, since the detected signal is weaker than for bulk material and less coherent. To improve the data quality, either longer measurement times are required or X-ray sources with higher brilliance, i.e., with higher flux per focused X-ray beam. Standard laboratory X-ray sources operate by bombarding an anode material, e.g., copper with electrons from a hot filament and have typically brilliances^[109] on the order of 10^8 photons $s^{-1} \text{ mm}^{-2} \text{ mrad}^{-2}$. Current synchrotron X-ray sources provide tremendously higher brilliances even beyond $10^{28} s^{-1} \text{ mm}^{-2} \text{ mrad}^{-2}$ as reported for XFELs^[110] and can provide better data quality however potentially at the cost of radiation damage.

SC-XRD is based on scattering experiments based on X-ray radiation. Since the wavelength λ is on the order of 1 \AA and comparable to the distances d between atomic layers within the crystalline material, X-ray scattering leads to diffraction that arises through constructive interference from the crystal layers according to Bragg's law

$$2d \sin \theta = n\lambda \quad (9)$$

with θ being half of the diffraction angle. The position of diffracted pattern, also termed Bragg peaks are given by the unit cell dimension and angles of the crystal. Their intensities are influenced by the underlying sort of atoms and their relative orientation. For a defined orientation and crystallographic direction, the average value in crystallize size can be extracted from the broadening of diffraction peaks observed via SC-XRD. Assuming a monodisperse and cubic framework, the Scherrer equation

$$D_{hkl} = \frac{K\lambda}{B_{hkl} \cdot \cos \theta} \quad (10)$$

links the crystallite size D_{hkl} perpendicular to the lattice plane with the FWHM B_{hkl} of the diffraction peak and Bragg angle θ . The lattice plane responsible for evaluated Bragg reflection is indicated by its Miller indices hkl . The numerical fit parameter K related to the shape of the peak.

The data quality of SC-XRD is mainly limited by the size and quality of the grown crystal. To obtain high quality structures independent of the size of nanoparticles, crystals have to be greater than $5 \mu\text{m}$ in size. In order to grow reticular nanoparticles to such large dimensions, parameters such as

temperature, reagent concentration and time need to be varied during synthesis, which might alter the crystal structure. Hence, it is indispensable to characterize the single-crystal and bulk crystal properties. As mentioned above, crystallography of reticular nanoparticles is additionally challenging due adsorbed "guest" molecules like disordered solvent that affect the overall structure. A common method to eliminate these contributions computationally is solvent masking by SQUEEZE^[111] or OLEX2.^[112] Similarly challenging are symmetry mismatches between the lattice of the SBUs and organic linkers. Frameworks with high-symmetry subunits are overall easier to determine.

Powder X-Ray Diffraction (PXRD): In case single-crystal growth is impossible due to small particle size, PXRD can determine the structure of reticular nanoparticles^[70] from powdered sample to derive its bulk crystallinity. The PXRD pattern still give answers on the phase purity and crystallinity^[62b] including information on unit cell size. The phase purity can be evaluated in comparison to computational modeling.^[113] PXRD is normally run on powdered samples on a flat sample holder. Powdering the MOF nanoparticles ensures randomly oriented crystallites. For samples with preferred orientations, such as particles with needle morphology, the nanoparticle preparation needs to be rotated during data collection,^[114] to ensure a nearly random orientation of crystallites with respect to the detector. PXRD comes to its limits for particles size smaller than 30 nm . In this case, diffraction peaks suffer from strong Scherrer broadening that is associated with undersized crystallites. While data quality can be improved for synchrotron radiation instead of X ray radiation, the overall performance of PXRD can be greatly improved by applying the charge-flipping method.^[115]

Soft-Angle X-Ray Diffraction (SAXS): SAXS^[116] is complementary to XRD and provides structural information not only about crystalline but also amorphous and soft framework materials, which are not perfectly crystallized. SAXS serves to obtain low-resolution structures of particles, i.e., essentially information on shape, size (distribution), crystallinity, and orientation. It is preferably used for mesoscale nanoparticles between 2 and 50 nm . Similar to LS for solution-based experiments in terms of experimental settings, SAXS is based on elastic scattering of light with an ultrashort wavelength, i.e., it employs X-ray radiation. The elastically scattered radiation is detected perpendicular to the incident beam under a small scattering angle $2\theta < 0.1^\circ - 3^\circ$. The diffraction pattern is then monitored on a 2D X-ray detector. The small angle scattering makes SAXS a nondestructive method that strongly profits from the simplified sample preparation that works for powders, mediocre-grown crystals as well as colloidal suspensions. Similar to PXRD, SAXS strongly benefits from synchrotron radiation.

3.3. Porosity

Porosity in hybrid framework nanoparticles describes the property of crystalline materials, which provide open spaces termed pores in at least one crystal phase.^[10b] These pores are structurally arranged in a repeating fashion and need to be accessible to external guest molecules. Hybrid framework nanoparticles

can be classified accordingly to this key parameter in three categories:^[10b] i) first-generation nanoparticles possess a fragile porosity. Their network is instable and collapses irreversibly dependent on guest molecules. ii) Second-generation nanoparticles stay crystalline and maintain a robust framework independent of any guest molecules. iii) Third-generation nanoparticles possess flexible networks and pores that adapt their size and shape in a reversible fashion by external stimuli—such as guest molecules, solvent, heat, or electric fields.^[10b] The internal surface area, i.e., the pore volume is therefore an important parameter that determines the capacity of adsorption and permeability to guest molecules and hence applicability, e.g., for catalysis, gas storage, and drug delivery. Pore sizes are hence adapted between a few Ångström up to several nanometers in MOF nanoparticles.^[10a,71]

The inner volume of reticular nanoparticles can be derived from crystal structures by calculations^[62d] including density functional theory^[117] and Barrett–Joyner–Halenda theory.^[118] Adsorption isotherms for nonreactive gases at cryogenic temperatures can report experimentally on the apparent surface area and pore volume of reticular nanoparticles with size between 1 and 50 nm.^[119] Gas adsorption however can only provide insights to dry nanoparticles and is little suited for third-generation materials with variable pore volumes. Nitrogen is commonly employed as small and inert gas at a temperature close to its boiling point of 77 K. The shape of the adsorption and desorption isotherms provide information about the material's porosity. In case the sorption isotherm shows a distinct plateau, the pore volume can be determined from the maximum gas load at a partial pressure p/p_0 of 0.9 with p_0 being the saturation pressure. Following the Gurvich assumption^[120] that the density of saturated nitrogen in the pores is equal to its liquid density the pore volume v_{pore} and fraction ϕ of unoccupied space within the crystal can be

$$v_{\text{pore}} = \frac{n_{N_2}^{\text{ads}}}{\rho_{N_2}} \quad \text{and} \quad \phi = v_{\text{pore}} \cdot \rho_{\text{NP}} \quad (11)$$

ρ describes the density of the liquid nitrogen and nanoparticle, respectively and $n_{N_2}^{\text{ads}}$ is the amount of adsorbed nitrogen (weight of nitrogen/weight of nanoparticle). Brunauer–Emmett–Teller (BET) theory evaluates sorption isotherms more elaborately and allows to categorize materials according to their porosity being microporous (pore size < 2 nm), mesoporous and macroporous (>50 nm).^[121] The BET method links the relative pressure, monolayer capacity n_m of the nanoparticle and amount of adsorbed nitrogen $n_{N_2}^{\text{ads}}$

$$\frac{p/p_0}{n_{N_2}^{\text{ads}}(1-p/p_0)} = \frac{1}{n_m C} + \frac{C-1}{n_m C} (p/p_0) \quad (12)$$

It derives the apparent surface area, which is the sum of the internal and external surface, by plotting the left term of (12) as a function of partial pressure. Following Rouquerol's criteria,^[121,122] a linear regime of the data is selected. From the slope and intercept the apparent surface area, monolayer capacity and BET constant can be extracted. If a second linear regime is present at high partial pressures $\left(\frac{p}{p_0} > 0.6\right)$ the slope

can be related to the external surface of the nanoparticle. The total surface area S_{Total} and specific surface area S_{BET} are given by

$$S_{\text{Total}} = \frac{n_m N_A \sigma}{V} \quad \text{and} \quad S_{\text{BET}} = \frac{S_{\text{Total}}}{m} \quad (13)$$

with the Avogadro's constant N_A the adsorption cross-section σ and molar volume V nitrogen. The specific surface area is normalized to the mass m of the adsorbent and have values higher than 6000 m² g⁻¹ for certain MOF nanoparticles.^[123] Hysteresis between adsorption and desorption reports on host-guest-induced distortion of the framework. Incorrect choice of the BET region can easily lead to over- and underestimation of surface areas.^[124] A comparison between theoretical expected values from crystal structures with those of BET analysis is advisable. A mismatch between both can also hint toward a partial collapse of the framework.

3.4. Surface Charge and Characterization

Charged nanoparticles interact with their surrounding medium. An electric double layer (EDL) is formed around the surface of a charged nanoparticle once it is dispersed in a medium.^[125] The inner layer termed Stern layer is mainly formed of ions and molecules of opposite charge to the surface charge of the particle.^[126] The outer layer is made of diffusing positively and negatively charged ions and molecules. The thickness of this layer is given by Debye's law and is described by the Debye length,^[127] i.e., the distance to the particle's surface at which the electrostatic effects of the surface charge have decreased by a factor of $1/e$. The diffusive outer layer depends on the medium's composition. Within an external electric field E , charged ions and molecules of the outer layer will move accordingly. The slipping plane, also termed plane of shear describes the interface between the mobile species and the dispersant.^[128] A common parameter, to characterize the net surface charge of particles is the zeta potential ζ . It represents the value of the electrostatic potential at the plane of shear^[129] and provides a measure for electrophoretic mobility of particles in suspension.^[128] The zeta potential is directly proportional to the electrophoretic mobility μ following the Henry equation

$$\mu = \frac{2\epsilon\epsilon_0 f(KA)}{3\eta} \zeta \quad (14)$$

that links the particles velocity v linearly to the applied external electric field E . Here, η denotes the viscosity, $f(KA)$ the Henry function and ϵ the permittivity of the medium. $\epsilon_0 = 8.854 \times 10^{-12} \text{ C}^2 \text{ N}^{-1} \text{ m}^{-2}$ represents the vacuum permittivity. While the electric potential describes the amount of work that is necessary to bring a unit positive charge from infinity to the particles surface, the zeta potential describes the potential difference between the EDL surrounding the particle and the layer of dispersant medium at the slipping plane. In case the thickness of the EDL is much smaller than the particle radius the Henry function becomes 3/2; if it is much larger, $f(KA)$ equals 1 and Henry's law rewrites to Hückel's law.^[126]

3.4.1. Electrophoretic Light Scattering

ELS^[130] is an ensemble technique that derives the average zeta potential via electrophoresis, i.e., the velocity of charged dispersed particles within fluid environment under the force of an external electric field. Equal to DLS, a laser is scattered on a particle suspension, however in presence of an external electric field. ELS is hence often employed in combination with DLS due to similar experimental settings.^[131] The mobile particles will move according to the electric field. When traversing through the sample, the impinging light is scattered at the charged particles. Their electrophoretic movement is seen by a shift in frequency of the detected scattered light compared to the excitation light source (Doppler shift) and can be translated to the particles velocity, and hence zeta potential (see (14)). Given its definition, the zeta potential strongly depends on the pH, ionic strength and particle concentration of the suspending medium. It is further altered by the interaction with molecules, in particular proteins within the medium that might adhere at the particle's surface. Unwanted aggregation can easily obscure the measurement. We hence strongly advise to carry out the experiment in the desired buffer that describes best the final application of the nanoparticles and to repeat it with gauged particle standards, i.e., nanoparticles of known charge and size.

3.4.2. Tunable Resistive Pulse Sensing (TRPS)

TRPS^[129,130b,131,132] is based on the Coulter principle and characterizes the size, zeta potential and particle concentration of a suspension. TRPS provides single-particle resolution^[130b,132b,133] and measures the reduction in ionic current across a membrane pore that occurs once the nanoparticle traverses and hence temporarily blocks the ion current. Induced variations in current are on the order of 0.1 nA. The precise diameter of the pore can be tuned based on a stretchable polyurethane membrane. TRPS is hence suited for particles with sizes between 50 nm and 10 μm and allows to extract the size distribution on a particle-by-particle basis. Since the precise pore diameter varies for each experiment, calibration particles have to be measured in comparison, i.e., the voltage (and pressure) is recorded as a function of time until the current recovers after blockage of the pore.^[129] TRPS measures the current, which requires a conductive solvent during the experiment. This makes TRPS a perfect technique for biotechnological and nanomedical application since it has the capability to characterize the behavior of particles in physiological buffers including nanoparticles, colloids, but also liposome, cells and viruses.^[134] The overall flux of particles through the pore within a thin membrane is driven by three contributions: i) electrophoresis J_E due to an applied electric field E , ii) electroosmosis J_{EO} due to concentration gradient between the both sides of the membrane, and iii) convection through an applied pressure J_P . It can be approximated^[126] to

$$J \approx J_E + J_{EO} + J_P = \frac{C\epsilon\epsilon_0}{\eta} (\zeta_{\text{particle}} - \zeta_{\text{pore}}) E + \frac{C}{A} Q \quad (15)$$

with C being the particle concentration, A the opening area of the pore, and Q the volume flow rate. ζ denotes the respective zeta potential. The concentration C can be derived in case of large convection: when electrophoretic and electroosmotic contribution are negligible, the particle concentration can be determined by calculating the rate of recorded blocking events after calibrating pressure-driven flow with standards of known concentration. Typical particle concentrations are around 10^5 – 10^{12} mL⁻¹. The physical size of particles is linked to the amplitude in current variation and is proportional to the ratio in cross sections of particle and pore. The net charge, i.e., zeta potential of single particles, can be either determined in the absence of convection or in case of calibrated volume flow rates. Following (14), the zeta potential is derived in this case from the particle's velocity that scales with the width of the induced drop in current.^[132a]

TRPS simultaneously determines size and zeta potential on a particle-to-particle basis. Hence, it has best prerequisites for heterogeneous particle mixtures. TRPS size distributions have been demonstrated to be consistent with those obtained with TEM.^[97a] The biggest measurement uncertainties however rise from altered, nonspherical particle and/or pore geometries and binding interactions, respectively. Slow-moving particles or particles having the same size as the pore itself lead to altered trajectories that obscure the physical size. Current efforts are strongly focused to extend the semianalytical model for nanoparticles with demanding surface chemistry and shape in biological fluids.^[129]

3.5. Further Reading

Nanoparticles are characterized by a plethora of different properties. The last section described state-of-the-art methods that address the most important properties of newly synthesized particles. Depending on the desired application, however, further physiochemical properties of the particles might be of interest. We hence provide a short summary and overview on common methods, the parameters of nanoparticles they address, their benefits and shortcomings including a short list with literature for further reading in **Table 1**.

Overall, we give the following guidelines to characterize nanoparticles:

- 1) Start with a structural characterization based on EM microscopy to measure the size, shape, and heterogeneity of the particles. In case your sample cannot be handled in vacuum, a combination of AFM, DLS, and NTA is an alternative.
- 2) In combination with PXRD the crystal size, phase purity, and overall crystallinity should be approached and compared to theoretical data.
- 3) Gas sorption measurements are the method of choice to characterize the porosity and apparent surface area of the synthesized particle.
- 4) The colloidal stability and aggregation formation in aqueous solution should be characterized when targeting applications in liquids (e.g., drug delivery) as a function of pH, e.g., via DLS or NTA.

Table 1. Summary of methods to characterize size, shape, morphology, porosity, and surface charge.

Method	State	Resolution	Parameter	Excess advantage	Limitations	Further reading
TEM	Vacuum	Particle	Size/morphology	Atomic resolution physical size in 2D	Limited throughput higher beam energy	[72a,e,74,75]
SEM	Vacuum	Particle	Size/morphology	Sub-nanometer resolution Physical size in 2D	Limited throughput; lower resolution than TEM; only for conductive samples	[72,73]
AFM	Dry/liquid	Particle	Size/morphology	Nanometer resolution Physical size in 3D	Limited throughput	[80,81]
XRD	Dry	Ensemble	Crystallite size		Complex data interpretation	[108]
SAXS	Dry/liquid	Ensemble	Size/morphology	Large dynamic range radius of gyration	Complex data interpretation	[116]
SLS	Liquid	Ensemble	Size/morphology	Mass-weighted size	Bias toward large particles	[87,88]
DLS	Liquid	Ensemble	Size/morphology	Hydrodynamic radius	Bias toward large particles	[86–89]
FCS	Liquid	Ensemble	Size/morphology	Hydrodynamic radius	Need of fluorescent labels	[93,94]
DCS	Liquid	Particle	Size/morphology	Hydrodynamic radius	Requires calibration	[98,99]
AUC	Liquid	Particle	Size/morphology	Hydrodynamic radius	High-cost equipment	[101]
NTA	Liquid	Particle	Size/morphology	Hydrodynamic radius	Scattering/fluorescent NP only	[83a]
SEC	Liquid	Ensemble	Size/morphology	Sample fractionation Hydrodynamic radius	No absolute size quantification	[103,105]
Gas sorption	Dry	Ensemble	Porosity	Pore size and volume surface area	No differentiation between inner and outer surface	[119]
(ICP-)MS	Dry		Element distribution	High mass sensitivity	No morphology information	[135]
NMR	Dry/liquid	Ensemble	Element/Linker ratio	High molecular sensitivity	No morphology information	[42a,62e,136,242,255]
ICP-OES	Dry	Ensemble	Element distribution	Fast screening	No morphology information	[62b]
ELS	Liquid	Ensemble	Surface charge/size/morphology	Combined with LS: hydrodynamic radius	Indirect estimation of ζ -potential	[126,130,131]
TRPS	Liquid	Particle	Size/surface charge	Large dynamic range Physical size in 2D	Only for conductive samples	[129,130b,131,132]

5) Last but not least, in case that building blocks of the nanoparticles were modified, e.g., by exchange of metal centers, organic linkers, surface coating or adsorption of guest molecules, a combination of MS,^[135] ICP-OES, and NMR^[136] can characterize the purity of sample, as well as the ratio of elements and linkers.

4. Inner Surface Functionalization and Multifunctional Efficiency

Advances in solid state and materials chemistry rely on our ability to functionalize the molecular backbone of porous materials with atomic level precision. There are two ways to enrich the backbone of MOF, ZIF, and COF materials with functionalities. The first approach—the presynthetic method—requires functionalization of the building blocks, which can be carried out with atomic precision (Figure 5), and the second—postsynthetic method—adds functionalities to the structure after the molecular backbone has been formed (Figure 6).

The molecular building blocks that comprise reticular materials have unique, complementary geometries that determine the chemical composition, structure, topology, porosity, and

functionality of the final material. Importantly, all these material characteristics can be controlled and tuned with atomic precision. The key challenge for presynthetic functionalization methods is the introduction of the functional group(s) such that they do not interfere with the formation of the scaffold. Reticular materials are made from two different kinds of build blocks: inorganic building unit (IBU) and organic building unit (OBU); MOFs and ZIFs are made from a combination of inorganic and organic units, and COFs are made from organic units only.

The chemistry of the metal ions used to form the inorganic building units (e.g., metal-oxo clusters, also known as secondary building blocks or SBUs) is well understood, and numerous cations (di-, tri-, or tetravalent) can be incorporated in the backbone. Different IBUs can be made using a variety of synthetic conditions, and 20 years of research has produced a wealth of methodologies to form almost any IBU. Where the literature falls short, high-throughput methods can be applied to systematically investigate the IBU formation.^[137] The only reasonable way to functionalize an IBU is by adding a functionality to the metal ion itself. One prominent example for reticular nanoparticles is the use of magnetic resonance imaging (MRI) active IBUs.^[20a]

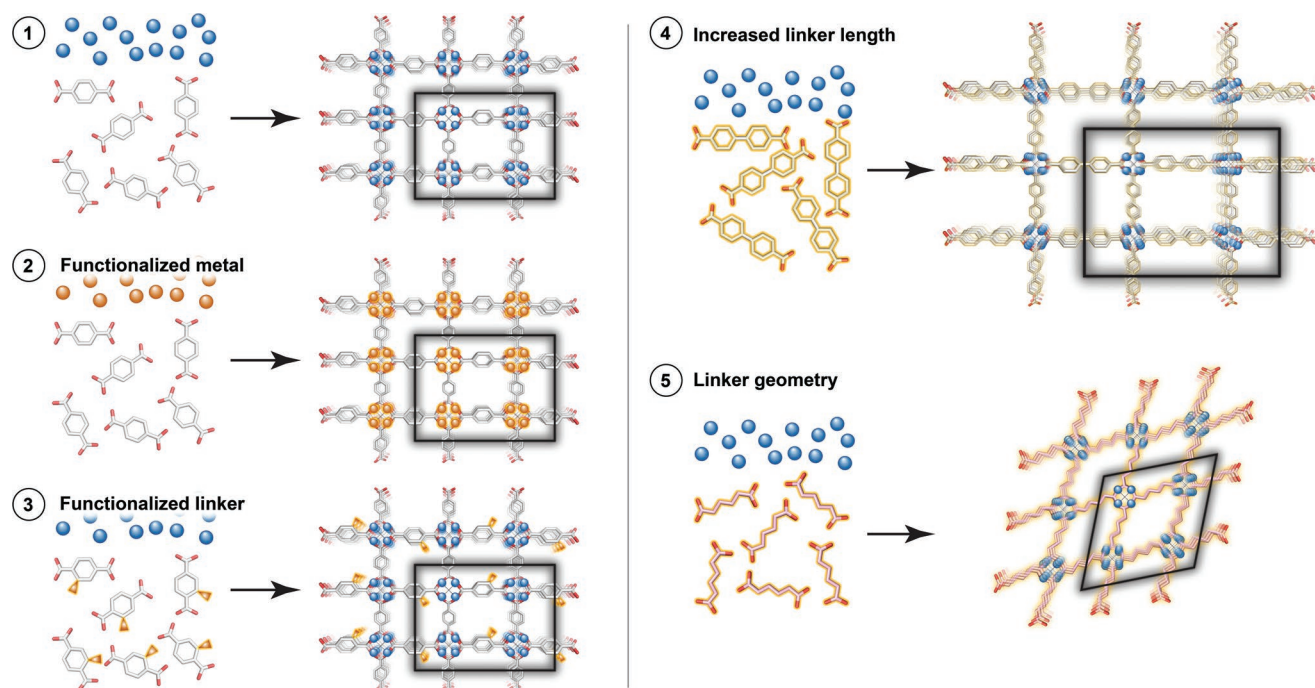


Figure 5. Presynthetic functionalization.

Uniting porous nanoscale characteristics and porosity with functionalization will define the future of nano and materials science. Materials researchers have realized that they need to optimize simplicity- and functional-driven approaches to address the global problems of our time.^[138] For this reason (and to encourage a fundamental rethinking of the synthesis of functional nanomaterials) the multifunctional efficiency concept was established (see **Box 1**).^[139] This concept enables universal evaluation of functional nanomaterials no matter if they are organic, inorganic, or hybrid materials) from the perspective or angle of simplicity (process efficiency (PE)) joined with functionality (functionality ratio (FR)) to foster functional material solutions that are reliable, highly performing and easily modifiable. The key

aspect thereby is that only solutions with high multifunctional efficiency have the chance to leave the lab bench and impact society.

Due to the straightforward crystal engineering, reticular nanomaterials can incorporate different functionalities—in the IBU as well as in the OBU—in addition to the intrinsic functionalities, namely porosity and the size-dependent properties of nano materials. In this way, reticular chemistry offers the unique possibility for the efficient, straightforward synthesis of multifunctional nanoparticles.^[139]

Unlike IBUs, OBUs remain unaltered during framework synthesis and can therefore be precisely designed and tuned through organic transformations a priori. In this way, the geometry and connectivity of OBUs dictate the final structure

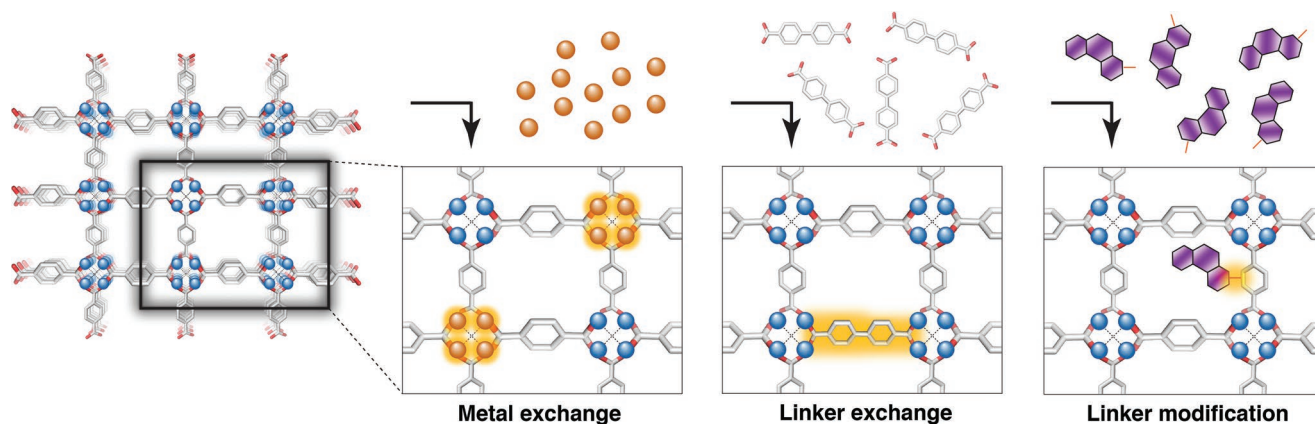


Figure 6. Postsynthetic functionalization.

of reticular materials. OBUs can be categorized by their chemical nature, coordination number and orientation of the Lewis base side.^[12a,c,18a,140] OBUs need not be strictly linear (ditopic) molecules, but instead range from tri- to octatopic complexes, or even be completely asymmetric.^[140a]

Box 1. Definition of multifunctional efficiency

The functionality ratio (FR) describes the degree of functionality of the nanomaterial

$$FR = n_{FU}/m_{BU}$$

where n_{FU} is the number of functional units and m_{BU} is the total number of building units of the nanomaterial.

The process efficiency (PE) reflects how simply the nanomaterial can be synthesized

$$PE = n_{FU}/r_{PRS}$$

where n_{FU} is the number of functional units and r_{PRS} is the number of process steps.

The multifunctional efficiency (MFE) is the product of both parameters and is expressed as

$$MFE = n_{FU}^2/m_{BU} \cdot r_{PRS}$$

MFE provides a quantitative parameter for comparing economic and synthetic efficiency of nanomaterials. Nanomaterials with a high multifunctional efficiency (e.g., materials that are highly functionalized and easily prepared) can be easily reproduced, optimized, and applied and are impactful solutions as they are intrinsically reliable, robust, and have high performance to cost ratios.

Reticular materials offer the distinct possibility to tune pore and aperture size by increasing the length of the OBUs (Figure 6) without changing the topology and in this way increasing systematically the pore and aperture size.^[12a,141] However, increasing the length of the OBU can lead to interpenetration structures, which result in smaller pores.^[142] Furthermore, the solubility of the OBU may be compromised since increasing linker length is generally associated with decreasing solubility.^[143] Nevertheless, the possibilities to implement functionalities are huge: metallo-OBUs with catalytic activity,^[144] fluorescence^[42c,145] or chemiluminescent OBUs,^[146] over biologic activity,^[21b,147] conductivity,^[148] all the way up to molecular rotors^[149] addressing the challenge to interlock dynamic functionality into a rigid backbone^[150] and multivariate functionality.^[69,151] Multiple functionalities can be aperiodically incorporated into the periodic organic backbone of reticular materials which opens the door to synergistic properties.^[152]

All in all, the large diversity of both the IBUs and the OBUs has allowed for the synthesis of a huge number of different reticular materials; currently over 70 000 unique structures have been reported.^[13] Besides crystal engineering of reticular materials at the molecular level, functionalization can also be performed after the framework is complete. The large pore

volume allows molecules to diffuse deeply into the scaffold and react with either the IBUs (e.g., unsaturated metal sites) or the moieties on the OBUs, resulting in postsynthetic modifications (PSMs) of the material.^[153] This method can be used to generate an infinite number of topologically identical but functionally diverse reticular materials (Figure 6). All PSM strategies can be grouped into two main classes: framework functionalization and linker/cation exchange. It is important to note that PSM strategies can rarely control the location and extent of functionalization of the framework's pores, so functionalities are randomly distributed over the framework backbone.^[42c]

Framework functionalization uses the framework backbone (OBUs and/or IBUs) as a pin board onto which organic moieties (e.g., functionalities) are attached. The resulting chemically modified frameworks inherit the properties from discrete molecules bearing the same functional groups.^[140c] This strategy bridges the gap between homogenous and heterogeneous systems by loading molecules with high fidelity, serving, e.g., as catalysts^[17a,154] and dyes.^[42c,155] One advantage of pinning functional groups onto frameworks is that small molecules that tend to cluster in solution and thus lose their functionality can be fixed to a backbone, resulting in permanent spatial separation and accessibility.^[21g,156]

All PSM strategies require the scaffold to resist the chemical functionalization conditions, e.g., strong acids or bases. Therefore, the development of mild PSM methods is desirable so that the crystallinity and porosity of the scaffold can be preserved, and also to avoid disruption of thermally and/or chemically sensitive molecules (e.g., biomolecules). A good example is the first comparative study of the efficiency of different peptide coupling reagents for PSM of MOFs to identify the best candidate. This knowledge could be used to carry out seven PSM reactions within a MOF crystal leading to enzyme-like complexity.^[157]

The mechanism of postsynthetic exchange of metal centers (transmetalation)^[153b,158] or linkers (stepwise ligand exchange, also known as solvent-assisted linker exchange, bridging linker replacement, or stepwise ligand exchange; Figure 7)^[158e,159] in MOFs,^[160] ZIFs,^[161] or COFs^[162] without any alteration of its arrangement has been up for debated for a long time. Advanced fluorescence spectroscopy using a fluorescent dye as the functionality is the only way to monitor single crystal-to-crystal transformation and observe whether or not these exchanges actually dissolve and reform the crystal.^[42c] Obviously, for metal and linker exchange the coordination geometry of the substituting OBU or IBU should be compatible with the original. The interesting aspect of transmetalation and PS linker exchange is the realization of a functional framework that could not be synthesized with other functionalization strategies discussed before.

5. Host–Guest Interactions

5.1. Big Picture

Porous host–guest systems play an important role in a variety of applications. The nature and structure of the host, the dynamics of guests inside the host, and the interaction of the guests with the host are of great importance and define the scope of applications of the porous system. Therefore, a

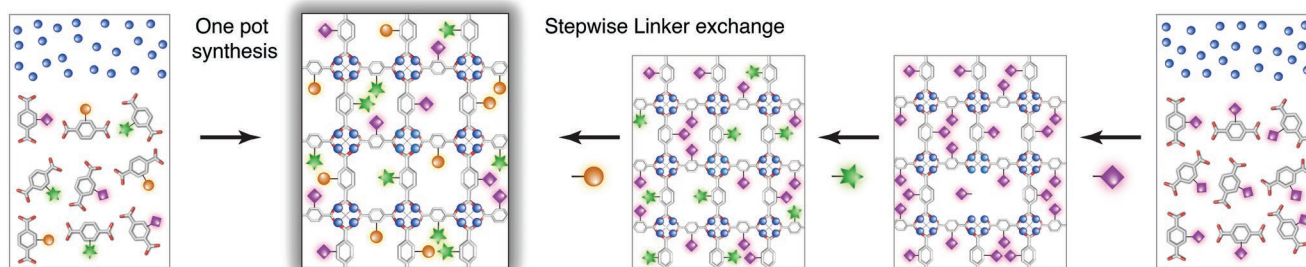


Figure 7. Multivariate reticular materials.

precise control of the host structure is the key to enable any kind of application. Host–guest chemistry in reticular nanoparticles is based on molecular recognition: both partners will react at the inner surface of the porous host in case the physicochemical and structural properties of the guest molecule match the one of the reticular frameworks. This recognition occurs in a defined and controllable fashion and is mediated through noncovalent bonding. It arises from five major contributions including hydrogen bonding, metal coordination, electrostatic and van der Waals forces, such as π – π stacking, and the precise matching in size and shape between the guest molecule and the internal cavity of the pore. Hence, strategies to control their interaction are often based on tuning the host's architecture, i.e., the dimension^[163] and shape^[164] of the pores and chirality^[165] of the framework. While the aperture of pores allows for sorting guest molecules according to the geometry and physicochemical properties, the inner surface of pores provides space for hosting them. Aside of passive adsorption of molecules, specific, localized binding within the pore can be additionally achieved by incorporation of molecular recognition sites into linker molecules.^[166] Here, the selective attachment of guest molecules is controlled by stereochemistry and electronic interaction.

5.2. MOFs, COFs, and ZIFs—Designer Materials

In principle, reticular chemistry enables the incorporation of almost any function (see Section 4) in the framework by combining atomic level control over structure and porosity with postsynthetic modification of the framework. Therefore, this structure–property design in combination with ultrahigh porosity of those materials makes them ideal to specifically control the host–guest interaction. Given the fact that the manipulation of any element of reticular frameworks will most likely result in a new structure, guest molecules are mainly considered as targets of an application, rather than constituents of the structure.^[167] The presence of guest molecules within the framework can alter the host in two ways: it can change the framework's original physicochemical properties like its geometrical structure or conductivity. However, it can also add additional functionalities to the nanoparticle like magnetic sensitivity or luminescence due to properties of the guest molecule itself without affecting the synthesized particle at all. The addition of guest molecules is a design element beyond the extendable nature of reticular chemistry of nanoparticles. While the

highly ordered structure of the host allows for precise positioning of guest molecules, the host–guest interaction is tunable in strength and affinity. The attachment of guest molecules and hence addition of new properties can be reversed and is tunable as well. Host–guest interaction is hence not only the key for various applications, like drug-delivery or sensing in biology, but also a new concept to tune the electronic and optical properties of nanoparticles. Here, we give a brief overview how to theoretically model and design reticular nanoparticles, as well as how to measure the interaction of host and guest molecules. We finish the section with recent examples from literature with respect to difference in host–guest interactions, their external control and the physical state in which the interaction occurs.

5.3. MOFs, COFs, and ZIFs—Host–Guest Interaction: Theoretical Studies

Theoretical studies^[168] on host–guest interactions are invaluable for understanding the physical and chemical mechanism of adsorption and release of guest molecules from reticular material. Different models describe experimental data from different perspectives. On the one hand, we learn about the potential entry, diffusion through the pores and interaction with the material, and on the other hand we can use modeling to predict properties of the material that might affect the specific application.^[169] In addition, theoretical studies allow for sequential screening of available networks for appropriate materials, which would be tedious experimentally.

Frequent starting points of simulations are guest-free framework structures obtained from X-ray diffraction data. They serve as starting configuration, since finding the most stable cluster configuration for a given composition by simulations is a tedious and time-consuming endeavor. Molecules like oxygen atoms or water ligands tend to remain within crystals during diffraction even under vacuum. Their contributions need to be removed from the structure before studying the interaction with other molecules. Next, the force field for distinct frameworks^[170] need to be chosen and adopted to the guest molecule of interest, such as CO₂. Lastly, the atomic partial charges of the reticular particles are derived by density functional theory (DFT) prior to simulating the host–guest interaction between, e.g., the gas molecule and the particle's framework.^[171]

Different theoretical methods and models have been implemented to describe reticular frameworks. This task is quite demanding due to the many-body nature of reticular

nanoparticles. The potential energy surface E of a Cluster $A_k B_l C_m$ such as the reticular framework, which might consist of metal centers A , linkers B , and other components C , becomes highly complex with increasing total number of atoms $N = k + l + m$. Main goal of computational chemistry is therefore, to model the macroscopic behavior of a porous material by a simplified model that still connects the properties of condensed matter with its atomic components.^[168b] The tool of choice for modeling processes in reticular systems is statistical thermodynamics (mostly applied in equilibrium), which describes the system, i.e., the nanoparticle, by an ensemble of thermodynamical variables, such as the number of atoms N , volume V , or temperature T within the canonical ensemble (N, V, T) . The current state and the macroscopic properties of the system is completely determined by the statistical distribution of the available microstates. It is represented by its partition function Z that depends on the energy of available discrete microstates within the system.

Computational methods differ at the level of approaching the energy of states. Quantum chemical simulations,^[168c] in particular density functional theory treat reticular frameworks at the electronic level for fixed framework structures (<nm; **Figure 8**). They allow for localized investigations of structural properties, like Coulomb interactions between guest molecules and the framework or changes in chemical bonding on the picosecond time regime. Numerical simulations based on force fields that use classical potentials following Newton's law of motion aim to explain processes at the atomic level (nanometer regime) such as the dynamics within the structure during breathing of the MOF frameworks. Here, the static potential energy of the framework is represented by a global minimum in the free energy landscape. Each atom is exposed to forces from all other neighboring atoms (or guest molecules). The static potential hence evolves with time. The transition state—represented as transient local energy minimum—is reevaluated

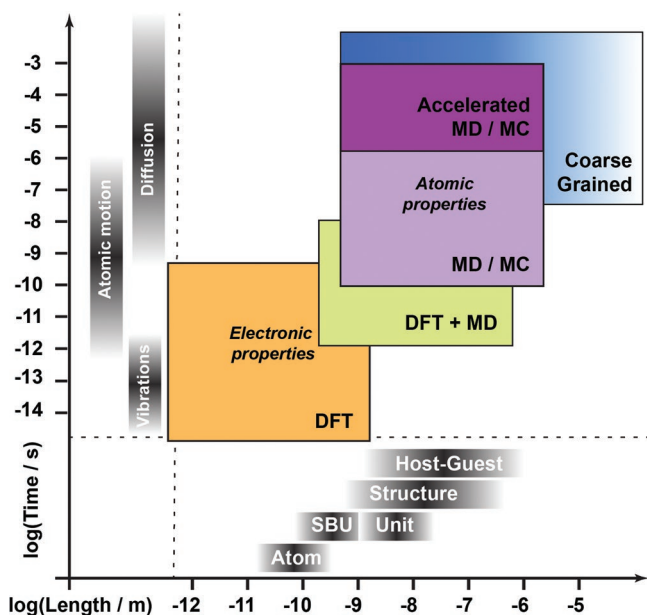


Figure 8. Computation methods to simulate host–guest interactions in reticular nanoparticles. Figure is based on ref. [168a].

iteratively, providing a trajectory for each atom within the framework. Monte Carlo simulations can incorporate stochastic processes, e.g., due to the thermally driven movement of gas and its adsorption within the nanoparticle by calculating the transient states for stochastic displacement of the guest molecule. Coarse Graining methods come into play for the prediction of dynamics on the μ s time scale and longer. All simulations describe simplified sets of parameters to decrease the computational time to a feasible duration. The appropriate method of choice hence depends on the underlying scientific question.

Methods based on density functional theory (DFT)^[168c,e,172] can describe multi atom systems up to a few hundred atoms arranged within symmetric structures.^[173] DFT has been employed to MOF,^[174] ZIF,^[175] and COF^[17a,176] nanostructures to study their structure and properties in the electronic ground state. It derives the electronic wavefunction ψ , which solves the Schrödinger equation related to the total energy of the system. The Hamiltonian \hat{H} includes terms on the kinetic energy of electrons, the interaction between nuclei and electrons as well as the Coulomb interaction between all electrons. In particular the interaction terms turn the Hamiltonian functional and subsequently the electronic wavefunction into a highly complex expression that cannot be solved analytically. Following the formalism of Hohnberg–Kohn^[172b] and Kohn–Sham,^[177] the $3N$ dimensions due to N electrons can be reduced to N dimensions, by introducing the ground state electron density. The correct density function minimizes the overall energy function and subsequently solves the Schrödinger equation. Although the many-body problem can be greatly reduced, DFT calculations are highly time-consuming as they calculate the electron density of the full framework, to describe the nanoparticles' physical properties. DFT is hence not suited for a structural optimization of complete particles, but can rather address localized questions such as host–guest interaction,^[178] charge transfer reactions on the 10–100 ps time scale,^[179] catalytic reactions,^[180] or the comparison of known framework structures.^[181] DFT can investigate cell parameters and elastic properties^[182] of the periodic structure of reticular framework. To extend the theoretical description to more atoms, DFT calculations are often combined with approximate models for the preselection of structures.^[173] Semiempirical potential approaches^[183] allow to model frameworks on a larger scale including complete nanoparticles (Figure 8, green area). Here, DFT is only employed in the second step to locally re-optimize the chosen models. Semiempirical, hybrid functionals include, e.g., GGA,^[168a] B3-LYP,^[184] and PBESOL.^[185]

DFT calculations, particularly mean field theories neglect thermal fluctuations. Molecular mechanics (MM) simulations, i.e., molecular dynamics (MD) in combination with Monte Carlo (MC) simulations can overcome this limitation. They can incorporate barrier crossing including relaxation between different local minima within the free energy landscape, i.e., they can describe thermally or externally driven transitions between different framework structures. The fundamental idea behind MD simulations is based on forces: every atom within the framework experiences a force introduced by all neighboring atoms. This force is linked to motion by Newton's law, and hence atoms within the framework will move in space over

time. MD simulation predicts the position of each atom stepwise in time and recalculates the force present on each atom. By iteration, MD simulations determine the trajectory of each atom in time and space. MD simulations are applicable for systems up to 10^4 – 10^5 atoms and time scales on the order of 1–100 ns. For dynamics, faster than 1 ns, like the movement of nuclei, MD simulations are combined with DFT (Figure 8, green/orange area).

The responsible force fields $F = -\nabla V(r)$ are derived from an empirical potential energy function $V(r)$ that comprises all energetic contributions within the framework as well as interacting guest molecules. These contributions include covalent bonding and angles, molecular torsions, solvation, van der Waals interactions described by the Lennard–Jones potential as well as electrostatic interactions described by the Coulomb potential. In this sense, MD simulations are static, as they deal with a fixed set of atoms and charges. They cannot deal with chemical reaction, i.e., the formation or deletion of bonds. Another limitation arises from localized charges: MD simulations cannot describe particles in which electronic polarization or conduction of charges plays a role. Both aspects can only be approached by full quantum mechanical simulations. Simulations of MOF and ZIF nanoparticles require additionally modified potentials due to the fundamentally strong bonding. For these systems, empirical many body potentials have been developed,^[186] such as the Finnis–Sinclair potential.^[187] Popular force field extensions for MOF nanoparticles include the extension for universal force field (UFF),^[188] DREINDING,^[189] Quick-FF,^[190] and ab initio force fields like MOF-FF.^[170e]

MD simulations are a powerful tool that can handle large multiatom systems. The application of (quantum) statistical mechanics allows for calculating ensemble properties such as the entropy, inner energy or pressure. Originally, MD simulations are carried in various thermodynamical ensembles, including the canonical ensemble (N, V, T) for chemically static processes and the grand-canonical ensemble (μ, P, T) in case of chemical reactions, like complexation or adsorption of (increasing number of) guest molecules. For each ensemble, a corresponding partition function Z can be formulated that determines the macroscopic behavior of a system from a thermodynamical point that links macroscopic and microscopic properties. Moreover, in combination with Monte Carlo (MC) simulations, thermal fluctuations in the system can be modeled, by computing random movements of the atoms and corresponding minimization of the potential energy of the resulting structure—instead of calculating the forces on each atom to solve its temporal development in 3D.

Coarse Graining methods come into play for systems with more than 10^5 atoms or dynamics on a μs time scale and longer. Simplified coarse graining models of various complexity have been introduced.^[191] These models do not calculate the coordinates of every atom, but reduce the number of atoms by center of mass approximations over two and more atoms that are connected by springs of different stiffness.^[191] This stiffness, respectively the interaction of these new “atoms,” is summarized in the CG force field. Frequently, CG force fields like the MARTINI force field^[192] are employed to describe physical properties, like the mechanical deformations of the material. For more complex applications, additional input is required.

This can be achieved by reversed Monte Carlo simulations^[193] on experimentally available data or atomistic simulations, like DFT.

Reticular nanoparticles are unique materials at the interface of chemistry and solid-state physics. Modeling their properties as complete particle is still challenging, as already its single unit cell easily consists of a few hundred atoms.^[194] In order to describe the relevant properties, simulations have to include structures of several unit cells in size. Quantum mechanical simulations are therefore often coupled with MD simulations and other field approaches when studying framework particles and their interactions.

Simulations have been employed to reticular nanoparticles under various aspects ranging from crystal structure prediction and optimization over large-scale screening, the influence of geometrical properties like pore size and linker length, to physical properties like the mechanical elasticity or adsorption of guest molecules.

5.3.1. Structure

In most cases, crystal structures are determined experimentally. Taken the nature of reticular frameworks, different methods, like the automated assembly of secondary building units have been developed, to simulate the assembly processes *in silico*.^[195] This computational tool has been trained on existing structures, e.g., via the zeolite or RCBS database,^[107] to successfully “predict” known structures, such as HKUST-1,^[196] and is used to support experimentalist during synthesis. A further approach, also termed decoration strategy, constructs frameworks by filling topological nets with known SBUs. “Feasible” structures are derived via energy minimization based on force field or QM simulations that evaluate the formation enthalpy. This approach has been applied to all three types of reticular networks, i.e., MOF,^[197] ZIF,^[198] and COF^[199] frameworks. Recent developments for the prediction of new frameworks, and structures in presence of host molecules comprise even machine-learning algorithms.^[200] The described approaches are not only employed for structural optimization and search for isoreticularity,^[201] they are used as large-scale computational screening for porous materials for specific applications^[202] such as separation and storage of environmental gases^[203,218] like carbon dioxide,^[204] hydrogen,^[200b,205] or methane.^[204a,206] Besides gas capture and storage applications, this approach is employed to investigate potentially new technological materials for various other applications as part of the materials project.^[207] These comprise photovoltaics,^[208] piezoelectrics,^[209] catalysis,^[210] topological insulators,^[211] batteries,^[212] and drug-delivery systems.^[213]

5.3.2. Geometry: Inner Surface Area and Pore Size

Based on structural considerations, computational methods are employed to evaluate the geometrical properties, i.e., internal surface area and pore volume. In these calculations, each atom within the framework is approximated by a sphere with the diameter of twice the van der Waals radius of the atom. The

accessible surface is the tangential surface area along the van der Waals radii that faces guest molecules. The minimal distance between the guest molecule and an atom in the crystal structure is given by the particle radius r_p of the guest molecule plus the van der Waals radius of the crystal atom. The accessible surface area—which serves as comparison to BET surfaces from experimental nitrogen isotherms—is conventionally calculated for nitrogen with a particle radius r_p of 3.68 Å.

Due to the strong application in gas storage and separation, many theoretical studies have looked into the diffusion and adsorption behavior of gases such as hydrogen, CO₂, CH₄, and gas mixtures.^[169,171,189,214] These processes are mainly modeled by Monte Carlo simulations, which take into account the randomness of diffusion and adsorption. Within the grand-canonical ensemble the number of guest molecules can fluctuate in time, i.e., molecules can simply be added and removed stochastically, which allows to determine thermodynamic properties of the reactions. Combined MD and GC-MC simulations have investigated the adsorption and diffusion properties of CO₂ for various different reticular frameworks including MOF-5, MOF-177, and HKUST-1.^[171,215] The adsorption of CO₂ increases with decreasing pore sizes, which should be of the order of 1–2 nm. An identical behavior was found for H₂.^[216] The strength of adsorption dominates the interaction between gases and nanoparticles at low pressure. The number of adsorbed particles is mainly determined by the accessible surface area, free volume, and electrostatic interactions at low pressures. MD in combination with GC-MC simulations allow to derive adsorption isotherms and thermodynamical properties like the enthalpy.^[189,217] They reveal, e.g., that IRMOF-1,6,8,14 as well as MOF-2,3 cannot store significant amounts of H₂ at room temperature.^[189] Recently, a high-throughput computational study based on MD and GC-MC simulations^[218] investigated 3806 structures of metal-organic frameworks to assess their adsorption and diffusion properties concerning CO₂ and N₂ in gas separation applications. For the ten most promising materials the adsorption affinity of CO₂ dominates the diffusion selectivity of N₂. This property is strongly influenced by the presence of water, which decreases the selectivity and permeability for CO₂.

Adhesion of guest molecules can lead to changes in topology of the particles. For this type of interactions additional quantum mechanical simulations are necessary together with MM computations. Ab initio calculations^[214g] on CAU-1 (= [Al₄(OH)₂(OCH₃)₄(O₂C-C₆H₃NH₂-CO₂)₃]) revealed why hydrogen can bind to the framework with storage capacities up to 4 wt% although all metal sites are fully coordinated. Here, the hydrogen sorption is based on cooperative guest-guest interaction and host-guest interaction to the organic linker molecules. These lead to a contraction of the framework structure and change of electronic potential inside the pores and subsequently enhanced binding. Periodic DFT simulations in combination with GC-MC^[214h] studied the structural changes occurring in ZIF-8 upon adsorption of O₂, N₂, Ar, and CH₄ and investigated the adsorption mechanism. The computational study revealed six symmetry-independent adsorption sites and could elucidate the phase transition between the two framework conformations. DFT in combination with GC-MC has proven to be a great tool for simulations on the influence of linker length

and type, pore size, and pore topology on the adsorption and diffusion.^[168e] All-Atom MD simulations on IRMOFs^[219] with varying linker lengths revealed that host-guest interaction between benzene and the framework cannot be described by diffusion and adsorption alone, but rather by inter- and intra-compartment transitions. Benzene follows a hopping-type of “diffusion” mechanism in which primarily adsorption dominates. This behavior explains why increasing the linker length, hence pore size, does not decrease the free energy barrier for the diffusion. The interaction between benzene and MOF-5 was additionally investigated using MD simulations and extended MM3 forcefield.^[220] Benzene molecules do not only hop, but gather together in pockets. Here, the accumulation is increased by the correlated lattice motion which strongly impacts the diffusion of benzene.

5.3.3. Physical Properties: Elastic, Optical, Electronic, and Conductive Properties

Aside of geometrical properties, physical properties are equally important. The elasticity of nanoparticles plays an important role, e.g., in drug-delivery applications^[221] where the elasticity of nanoparticles directs tumor accumulation. Using DFT calculations, the individual elastic properties including Young and shear modulus can be approached. By this method, different frameworks like MOF-5^[222] and ZIF-8^[223] have been investigated. Force fields in combination with DFT are employed to simulate the elastic properties, e.g., for MOF,^[170d] ZIF,^[224] and COF frameworks. The anisotropy of the elastic modulus is a signature of soft porous materials^[10b] and finds application in the classification of porous materials. Many frameworks, such as MIL-88-based nanoparticles are prone to breathing, i.e., they change their structural shape reversibly as reaction to an external stimulus such as heat or binding of guest molecules (the solvent).

MD simulations take the interaction of water with the MOF-5 framework correctly into account and explain its instability after solvation in water.^[225] For MOF-53 they successfully capture the two-step structural switching behavior upon CO₂ adsorption.^[226] MD simulations using a universal force field have evaluated the pore opening of MIL-88B-based particles as a function of linkers and presence of different solvents and revealed that the breathing amplitude is largely dependent on the functionalization and number of incorporated groups per linker molecule.^[227] The adsorption of molecules in liquid phase is driven by the minimal accessible pore size and the energy of the host-guest interaction within the framework. The interaction between MIL-88B(Fe) based particles and molecules in solid phase for drug delivery applications, like caffeine, has been investigated by means of force field and QSAR modeling.^[228] Grafting the organic linker with polar and H-donor groups strongly increased the drug uptake capabilities, which suggests that the functional groups serve as anchoring points for the drug molecule.

Coupling of adsorption and deformation, e.g., during breathing of the guest framework is challenging for MD simulations due to the stochastic nature of the interaction.^[168e] Depending on the application, Monte Carlo stimulations are hence employed within the grand-canonical or osmotic^[229]

ensemble, which take the temperature, number of unit cells, the mechanical pressure and the chemical potential of the guest molecules into account.^[230] Using Grand Canonical Monte Carlo simulations in combination with experimental data,^[231] the adsorption and release of ibuprofen was investigated for the soft-porous frameworks MIL-53, MIL-100, and MIL-101. The computational model was then employed for screening biocompatible metal-organic framework nanoparticles for potential drug carrier applications, in particular CDMOF-1, MOF-74-(Mg), and BioMOF-100. GC-MC served for the prediction of macroscopic performances and analysis of the adsorption and delivery of ibuprofen. Using MC in combination within the osmotic ensemble, the interaction between methanol and NH₂-MIL-53(Al) was investigated and revealed an anomalous type of translational diffusion.^[232] The diffusion of methanol comprises two types of motion: localized diffusion and translational jumps in a zigzag scheme between hydroxide groups of the host material. Host–guest interactions in combination with reversible pore opening of this soft-porous material are responsible for violating the Stokes–Einstein relation.

Host–guest interactions do not only influence the structural properties of reticular nanoparticles, but also their optical, electronic and conductive properties. Optical properties comprise (among others) the absorption and luminescence of UV/Vis radiation. Electronic and conductive properties are mainly determined by the material's band gap. To describe and model host–guest interactions for optical and electronic and optoelectronic application, a full quantum chemical description of the material is required. Electronic band structures, dipole moment or charge transfer reactions can only be approached via time-dependent DFT calculations.^[233]

Conductivity in reticular nanoparticles can be evaluated by probing their electronic bandgap by DFT calculations. These can model and predict electronic and optical properties, e.g., of COF frameworks X₄Y(Z)₃, with Z being boronic acid functioning as linker.^[234] For stable frameworks based on nodes X₄Y made of X being C and Si, and Y being C, Si, Ge, Sn, and Pb various parameters including bulk modulus, formation enthalpy, chemical bonding as well as band gap and optical properties can be simulated. All COFs of these two series are found to be semiconductors with band gaps between 2.7 and 3.8 eV that have an absorption wavelength between 300 and 500 nm. DFT simulations on MOF-5 revealed a bandgap of 2.5 eV,^[235] which is at the border between isolating to semiconducting material. MD simulations on its thermal conductivity could classify MOF-5 as insulator. Reticular nanoparticles without optical activity in the UV/Vis can be turned into emitting particles by inclusion of fluorescent molecules, such as the 1,4-bis-*p*-cyanostyrylbenzene (bpcb) and 1,4-bis(5-phenyloxazol-2-yl)benzene (bpob) into MOF-5.^[236] The resulting particles emit around 400 nm. The blueshifted fluorescence of the incorporated guest molecules, is due to a modified electronic structure of the guest and host material as revealed by DFT calculations.^[236]

5.4. Experimental Approaches to Monitor Host–Guest Interactions

In order to experimentally evaluate the interaction between guest molecules and reticular nanoparticles, we need to consider the

phase of guest molecules involved as well as the environment in which the interaction is taking place. While reticular nanoparticles are porous solid-state compounds, their guest molecules can have any phase ranging from solid state in drug delivery applications, to gas phase in catalysis. To track the uptake and release of guest molecules within the porous framework, the applied method needs to be capable to detect a change in the host's physicochemical properties in a quantitative manner. These properties can be, e.g., the morphology, crystallinity, surface charge, porosity, or conductivity. Various methods have been introduced to measure these properties (see Section 3). In the following section, we describe how to measure the interaction of guest molecules with the framework in dry, wet, and gaseous states. We consider solid hosts and guest molecules in different phases.

5.4.1. Gaseous State

Gas Sorption: Gas adsorption experiments are used to determine the porosity, in particular the apparent surface area and pore volume of reticular frameworks (see Section 3). Sorption experiments are also frequently employed to study the interaction of guest molecules in the gas phase with modified groups within the porous framework. One example is the characterization of binding preferences and sorption properties of urea pyridyl (URPy) groups.^[214f] Adsorption experiments on H₂O@MIL-101(Al;Cr)-X (with X equal to amino and URPy groups) show nearly identical uptake of H₂O and hence interaction with both moieties.^[214f] Some desorption branches however also show a hysteresis, which indicates the weaker interaction of H₂O to the organic linkers and a stronger interaction to the coordinatively unsaturated metal sites.

IR Spectroscopy: Gases, such as CO₂, feature strong absorption cross-sections of light in the infrared (IR) region.^[237] Here, the absorption leads to a direct vibrational excitation of the material at specific frequencies. These molecular transitions can be employed to identify molecular species and quantify their amount via IR spectroscopy. The IR spectrum $S(\lambda)$ of a sample follows the Lambert–Beer law (Equation (1))

$$S(\lambda) = \log_{10} \left(\frac{I_0(\lambda)}{I(\lambda)} \right) = \varepsilon(\lambda) \cdot c \cdot d \quad (16)$$

that connects the wavelength dependent absorption coefficient $\varepsilon(\lambda)$, the concentration c and thickness d of the sample. The spectrum can be determined by recording the wavelength dependent intensity of the incident radiation $I_0(\lambda)$ in comparison with light that is transmitted by the sample $I(\lambda)$. The spectrum acts as molecular fingerprint of the molecule under investigation. As long as the IR radiation does not lead to saturating absorption within the material, the amplitude of the recorded IR signature scales linear with the concentration c and allows quantifying chemical species. This can be used to qualitatively and quantitatively identify the nature of the host–guest interaction in porous materials, where the probes molecular interaction with the host alter the spectral features of the IR spectra. This approach is also applicable to study the interaction of adherent molecules in liquid and solid state. IR absorption

can serve as imaging contrast in IR microscopy; however, IR microscopy possesses only reduced spatial resolution in the micrometer range, which is not very suitable for spatial characterization of nanoparticles.

In a recent example, small precursor molecules were immobilized in porous MOF frameworks by adsorption before assembly into functional catalysts (see Section 5.5; PEGS strategy).^[238] IR spectroscopy served to characterize the created catalyst by evaluating the weak interaction between CO molecules and RuO₂ synthesized within the framework. Temperature-dependent desorption of CO molecules adsorbed on coordinatively unsaturated Ru at the surface of RuO₂@MOF-808-P was monitored. CO molecules detach from the surface above room temperature, as seen by the disappearance of the main peak at 2061 cm⁻¹. No desorption was observed for RuO₂/SiO₂ surfaces.

In another application, IR spectroscopy was employed to characterize the designed Co-MOF-74-TTF,^[239] which was formed by host-guest interaction and infiltration of tetrathiafulvalene (TTF) into the Co-MOF-74 framework. IR spectroscopy could prove the incorporation of TTF into the pore causing reduced water adsorption site at the open Co metal sites.

Raman Spectroscopy and Imaging: A complementary technique is based on Raman scattering.^[240] Here, monochromatic light is inelastically scattered at the sample. The interaction leads to a transfer of energy between the incident light field and the molecule that matches vibrational transitions. Its spectral signature equally serves as molecular fingerprint. Raman transitions depend on the polarizability of the molecule while IR transitions are due to changes in the dipole moment. IR spectroscopy is therefore only sensitive to vibrations in heteronuclear molecular bonds, while Raman spectroscopy can also monitor homo-nuclear vibrations, such as single, double, and triple carbon-carbon bonds. Additionally, Raman scattering can serve as imaging contrast. Here, Raman imaging benefits from wavelengths in the UV/Vis which provides enhanced spatial resolution down to ≈200 nm, which allows for single particle characterization of nanoparticles.

Raman scattering can measure host-guest interactions between reticular frameworks and guest molecules in any physical state. Combined Raman and IR spectroscopy was employed to intensively study the interaction between small gas molecules, including H₂, CO₂, N₂, NO, and MOF frameworks such as MOF-74, MIL-53, MOF-5, and HKUST-1.^[241]

In the above-mentioned example, Co-MOF-74-TTF was formed by host-guest interaction between the MOF and TTF.^[239] Raman imaging revealed a heterogeneous distribution of different phases on the micrometer scale. Similar to IR spectroscopy, Raman scattering could prove the presence of TTF however in a spatially resolved manner. This allowed to assign different phases: one phase to the empty Co-MOF-74 and a second phase to Co-MOF-74 with adsorbed TTF molecules. In further investigation of the Co-MOF-74(-TTF) under vacuum, CO₂ and N₂ atmospheres via Raman spectroscopy showed attenuated adsorption of gas molecules to the modified framework, which is in line with less accessible surface areas within the porous material.

Solid-State NMR Spectroscopy: Solid-state NMR (SS-NMR) spectroscopy has evolved into an important tool for the

characterization of host-guest interactions with adsorbed species,^[242] such as CO₂, xenon and other molecules, that are involved in catalytic reactions.^[243] It is an excellent method to study reticular nanoparticles and their host-guest interaction. A wide variety of parameters, such as the chemical shifts, widths, anisotropy, and longitudinal relaxation, are influenced by both, the host and guest molecules. Aside of structural characterization of the host framework, adsorption processes as well as induced structural rearrangements within the framework can be monitored. Solid-state NMR is frequently used to investigate the interaction between xenon and MOF framework^[242] since it is not vibrationally active, i.e., its interaction cannot be directly monitored via IR or Raman spectroscopy. The ¹²⁹Xe chemical shift of adsorbed gas is influenced by four contributions^[244]

$$\delta = \delta_0 + \delta_{\text{Xe-MOF}} + \delta_{\text{Xe-Xe}} + \delta_{\text{M}} \quad (17)$$

including the chemical shift δ_0 of Xe alone, an additional shift due to interaction between Xe and the framework $\delta_{\text{Xe-MOF}}$, a contribution due to intermolecular interactions $\delta_{\text{Xe-Xe}}$ as well as a contribution caused by paramagnetic sites δ_{M} . SS-NMR can monitor the adsorption of xenon itself, the interaction between partners as well as the applied gas pressure within the system. Applied pressure leads to an increase in Xe-Xe interactions and is seen as shift within the NMR spectrum which increases nearly linearly with pressure.

Similarly, SS-NMR has been employed to study the interaction between CO₂ or H₂ and MOF frameworks in a plethora of different applications.^[242,243] NMR spectroscopy provides high sensitivity against subtle structural changes, e.g., during the adsorption^[245] of H₂ on MOF-5 and has been proven to be a valuable tool for systems with amorphous phases, e.g., within COF particles.

5.4.2. Liquids

Mobility based methods enable to determine the size and zeta potential of reticular nanoparticles in liquids. It is important to keep in mind that these methods do not monitor the inner solvent-framework interaction. As described in Section 3, porosity, accessible surface area or pore volume are generally investigated in gas phase and do not report on the interaction of liquids with reticular nanoparticles. Particles with flexible framework, however, adopt their shape and pore sizes depending on the solvent they are suspended in, such as MIL-88A.^[246] This alteration affects the actual pore size, which in turn can hinder the entry of liquid into the pores and hence interaction with the particle itself. Moreover, while porous transport of gasses is uncontrolled and little hindered – fluids possess a high surface tension and will form a meniscus above the pore opening and might not enter into small pores at all.

Recently a new methodology, termed nanomechanical mass correlation spectroscopy, has been introduced to measure the interaction between liquids and nanoparticles, in particular MOF nanoparticles.^[247] In this technique a micromechanical resonator^[248] with embedded fluidic channels is employed to directly measure the buoyant mass of nanoparticles in solution.^[249] The resonator acts as mass/frequency transducer.

Table 2. Density estimations for the functionalized and unfunctionalized MIL-101 (Cr) MOF nanoparticles in different solvent mixtures. Reprinted with permission from Modena et al.^[247] Published 2018 by Wiley-VCH under the Creative Commons Attribution Non-Commercial (CC BY-NC) License.

MIL-101 (Cr)	Dry ^{a)}	EtOH/HFE [g cm ⁻³]	EtOH/H ₂ O [g cm ⁻³]	Fully permeable ^{b)} [g cm ⁻³]
No function	0.66	1.25 ± 0.02	1.77 ± 0.12	3.1
Pyrazine-functionalized	–	1.31 ± 0.03	1.42 ± 0.06	–
Pyridine-functionalized	–	1.30 ± 0.05	1.12 ± 0.02	–

EtOH: ethanol; HFE: methoxyperfluorobutane. ^{a)}No solvent within pores (Case I).; ^{b)}Fully permeable to solvents (Case II).

A shift in resonance frequency of the device reports on traversing particles and can be related to their mass. The shift is linear proportional to the ratio of masses between the particle and the resonator and can report on particle weights down to >10⁻¹⁸ g.^[250] The detection limit can be further reduced by four orders of magnitude by correlation analysis of the recorded signal.^[251] The interaction between the solvent and reticular nanoparticles is described by the apparent density of the nanoparticle under investigation. To determine this density, an equal number of nanoparticles is dispersed in a mix of solvents at varying ratios. The mass, respectively resonance frequency fluctuations are recorded over time within a fixed volume of 10 pL, and an autocorrelation analysis is carried out. The autocorrelation amplitude $C(0)$ as a function of varying solution densities can be employed to extract the particle's density.^[247]

To establish the technique for porous nanoparticles, colloiddally stable MIL-101(Cr) nanoparticles in comparison to MIL-101(Cr) nanoparticles functionalized with pyridine or pyrazine at coordinatively unsaturated metal sites were investigated.^[247] Particles with a diameter of roughly 40 ± 10 nm in dry state as determined by SEM and 105 ± 31 nm in ethanol as determined by DLS were synthesized. Already first experiments of nonmodified particles reveal strongly varying densities between 0.66 and 1.77 g cm⁻³ depending on the solvent. While all three nanoparticles preparations show similar results in an apolar solvent mix made of ethanol and methoxyperfluorobutane (EtOH/HFE) (Table 2, lane 2), their densities strongly vary in a polar solvent mix made of ethanol and water (Table 2, lane 3).

The observed dependence of mass density is the result of different types of interactions between the solvent and the inner pores of the MOF nanoparticles. The apparent density of porous particle does not only depend on its dry mass and volume but also on the accessibility of the pore to solvent molecules. Looking at the reaction volume, two areas are differentiated (see Figure 9, left): the outer solvent and the nanoparticle (its volume is shown by a dashed line). To explain the different interactions, one can again distinguish two, potentially different compartments within the particle volume (see Figure 9, left). The first compartment (light blue) represents a volume with identical composition of the liquid to the surrounding solvent. The second compartment (blue/yellow) represents the volume with fixed, but different composition, i.e., with different ratios of solvent constituents.

Their ratio depends on the polar nature of the solvent components, and hence their specific interaction with the pores. For a solvent mix between two constituents A and B with densities ρ_A and ρ_B , the apparent mass density ρ_{app} of a particle can be determined to

$$\rho_{app} = \frac{1 + \alpha + \beta}{\frac{1}{\rho_F} + \frac{\alpha}{\rho_A} + \frac{\beta}{\rho_B}} \quad (18)$$

where the adsorption coefficients α and β denote the mass fraction of the solvent components that are bound to the particle. ρ_F describes the density of the framework, which depends on the accessibility of the pore to the solvent.^[247] We can distinguish three cases (see Figure 9, right). i) The particle is fully accessible to all solvent components (i.e., both adsorption coefficients are 0). Then, the apparent density $\rho_{app} = \rho_F = \frac{M_F}{V_F}$ is directly related to the dry mass M_F and volume V_F of the framework. ii) The particle is impermeable to any solvent: the apparent density $\rho_{app} = \rho_{NP} = \frac{M_F}{V_{NP}}$ is related to the hard-sphere

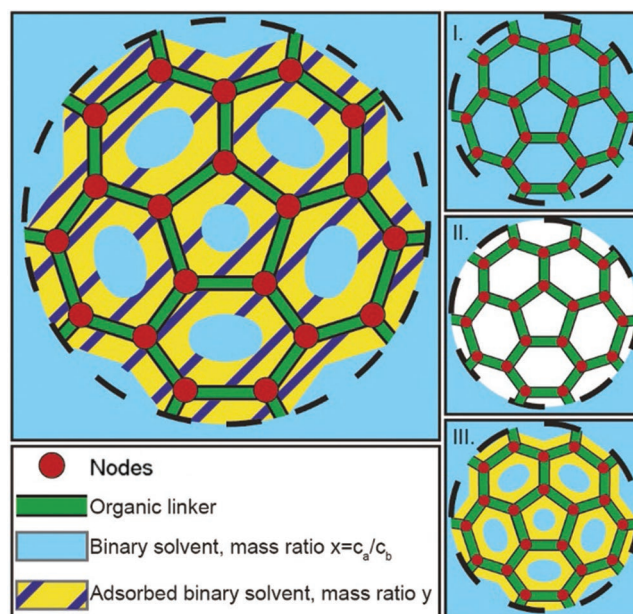


Figure 9. Schematic representation of the selective sorption of mixed solvents to porous nanoparticles. The dashed line symbolizes the size of the nanoparticle. Solvent components can access the pore volume differently. In the first half of the volume (shown in light blue), the mass ratio x of solvent components matches that of the surrounding fluid. In the second half (yellow/blue hatched region), the composition is altered by specific interactions between the solvent components and the framework. The mass ratio of solvent components in this region can differ significantly from the surrounding fluid. We distinguish three special cases of this model. I) All solvent components can freely access the entire pore volume. II) No solvent molecules can access the internal volume. III) One of the solvent components (light yellow) can access a larger portion of the internal volume than the other. Reproduced with permission.^[247] Copyright 2018, Wiley-VCH.

volume of the nanoparticle. iii) One solvent component preferably binds to the framework (i.e., $\alpha > 0$ and $\beta = 0$). MIL-101(Cr) clearly belongs to group III.^[247] Depending on the hydrophobicity of the inner surface, varying numbers of ethanol molecules will adhere to the framework which explains the density's dependence (see Section 5.5). The novel density method gives direct access to classify the interaction between solvent and porous nanoparticles experimentally.

5.4.3. Solid Compounds

Several methodologies, e.g., X-ray-based crystallography (see Section 3), have been introduced to investigate the interaction between solid-state guest molecules and porous nanomaterials. In addition, vibrational techniques based on IR absorption, Raman scattering are applicable to guest molecules in any physical state. To study host–guest interactions between solid-state partners, solid-state NMR (SS-NMR) is frequently employed. Recent applications are shortly summarized in the following section.

SS-NMR spectroscopy is often employed to characterize the interaction and nature of incorporated drugs in reticular nanoparticles for drug delivery studies, as it studies both frameworks and guest molecule.^[252] Frequently, ^1H and ^{13}C spectra are taken of the pure compound, the nanoparticle and the loaded nanoparticles. Changes in chemical shifts within the separate NMR signatures give insights, which residues of the drug molecule interacts with the framework and vice versa. Frequently studied compounds are chemotherapeutics and analgesics, such as doxorubicin and ibuprofen.^[253] The model drug ibuprofen has been investigated by NMR in various frameworks including MIL-53, MIL-100, MIL-101, and MOF-74,^[178,254] to monitor and understand its loading behavior to the framework. ^1H in combination with ^{13}C SS-NMR revealed that ibuprofen is interacting as anion with MIL-101 nanoparticle.^[178,254] Incorporation of ibuprofen into the framework leads to deprotonation of the carboxylic acid group.

SS-NMR allows studying dynamical processes, such as the vibration of the porous framework. It is frequently employed to follow artificial molecular machines, such as molecular motors, rotors and switches in reticular framework.^[255] A specific type of such systems are mechanically interlocked molecules (MIMs).^[255a,b] In particular “molecular shuttles” are special cases of MIM and represent molecular superstructures, where a macrocyclic ring is allowed to move forward and backward between two turning points. SS-NMR was, e.g., employed to characterize the movement of a rotaxane within the metal-organic framework designated UWDM-1 ($\text{Cu}_2(\text{MIM})(\text{H}_2\text{O})_2 \cdot 3\text{H}_2\text{O}$).^[256] The MIM linker is built from four axes connected by a linking strut around which a molecular wheel can move between the two anchor points of the strut.^[256] Two 3,5 benzene-dicarboxylic acid groups served as linking struts, a benzyl-aniline recognition site as crossbar and [24]crown-6 macrocycle as the moving wheel.^[256]

To monitor the dynamic movement of the ring, the rotaxane molecule was deuterated and ^2H SSNMR spectra of active UWDM-1 were carried out over a wide temperature range between 292 and 477 K (Figure 10). In combination with

theoretical simulations, four different type of motions could be identified, which comprise the rotation of the macrocycle, the rocking of the CD groups and combinations of both motions.

5.5. MOFs, COFs, and ZIFs—Host–Guest Interaction Practical Examples

Targeted recognition of guest molecules in reticular nanoparticles is a key property for any application and strongly influenced by hydrogen bonding, metal coordination, Coulomb and van der Waals forces and the geometric match of guest molecules and the host's framework.

Hydrogen bonding can mediate selective host–guest interaction in reticular frameworks, e.g., via donor–acceptor recognition sites in MOFs such MIL-101 nanoparticles.^[214f] MIL-101-NH₂ nanoparticles were postmodified by incorporation of 2-pyridyl urea, which acts as hydrogen bond donor. 2- and 3-Aminopyridine were successfully adsorbed to the mesoporous material by double- and single-hydrogen bond formation, respectively. This approach follows the key-lock-principle of supramolecular chemistry and can easily applied into other reticular frameworks. COF particles have only recently started to be employed as 3D solid-state carrier of guest molecules.^[257] 2D COF-1 were shown to incorporate 1,2,4-trichlorobenzene guest molecules in to the framework's pores with stabilization through hydrogen bonds.^[258] The interaction with water molecules modulates the 3D structure of the diamond-net based COF-300 (Figure 11).^[259] While 1,4-dioxane, cyclohexane and THF trigger the crystal to expand, water vapor results in a contracted framework due to hydrogen bonds.^[259]

ZIF nanoparticles employ hydrogen bonds to incorporated molecules in all states, e.g., ethane,^[260] glycol,^[261] and doxorubicin,^[262] or acidic drugs^[263] such as ketoprofen or aspirin. ZIF-8 serve as host matrix for the incorporation of metalloporphyrines into pores via hydrogen bonding for catalysis.^[264] The formed Mn-Por@ZIF-8 nanoparticle show enhanced catalytic efficiency mimicking the functionality of hemoglobin. A complementary development in the field is so called hydrogen-bonded organic frameworks (HOFs). They are based on the inverted approach that employs hydrogen bonds to form permanent porous networks.^[265] These porous hosts possess highly flexible frameworks that can be stabilized by guest molecules but also adopted to guests of varying size, shapes, and amounts^[266] and provide specificity^[267] and responds to external triggers.^[268] HOFs are an excellent example for the strength of reticular chemistry to assemble building blocks into supramolecular structures. Their rational design, however, is challenging due to the missing ability to regulate self-assembly and hence to control their size. A further limitation is given by the insufficient stabilization of particles in the absence of solvent guest molecules.

Metal coordination strongly determines the loading and release capacities of reticular nanoparticles. Unsaturated metal sites decide upon the sorption affinity and selectivity and mediate the coordination between the host molecule and the metal ion based on its Lewis acidity. Hard Lewis metals like aluminum facilitate the absorption of hard Lewis bases.^[214f]

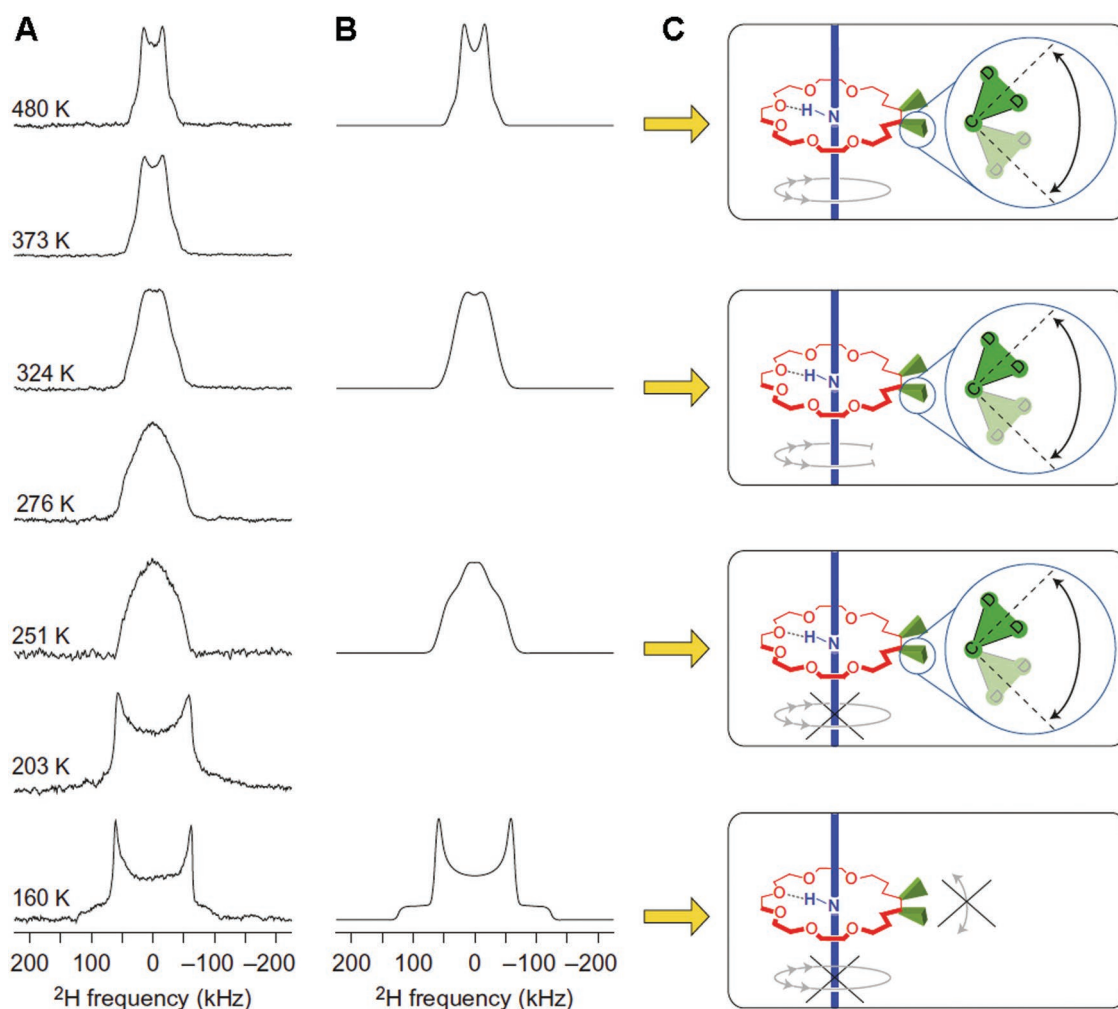


Figure 10. A,B) Variable-temperature ^2H NMR lineshape, both experimental A) and simulated B). C) Schematic representation of the motion of the rotaxane macrocycle inside the MOF UWDM-1. Reproduced with permission.^[256] Copyright 2012, Springer Nature.

MIL-100 (Al, Fe, Cr, and V) adsorbs N/S heterocyclic aromatic compounds by enthalpic, coordinative interaction with the unsaturated metal sites in a reversible fashion.^[269] The binding strength is correlated with increasing Lewis acidity. Similarly, MIL-101(Cr) adsorbs nitrogen-containing compounds like pyridine by coordination at the chromium site with increasing basicity^[269b,270] of the guest molecule. This observation is also valid for CPO-27-(Ni, Co) and HKUST-(Cu).^[269b,271] The bond formation for Lewis acid/base pairs is reversible.

Coulomb interactions depend on the local electrostatic field strength of the reticular framework and the dipole moment of the guest molecule, meaning the stronger the dipole moment of the guest molecule for a given host material the stronger the adsorption of the guest molecule to the framework. While electrostatic forces play a major role in the solid state, Coulomb interactions play an underpart for guest molecules like gases that have no permanent dipole moment. In this case, their interaction is mainly dominated by the induced dipole given by polarizability, which is much weaker. Permanent storage of, e.g., CO_2 gas due to Coulomb interaction is barely possible and mainly facilitated by van

der Waals interactions.^[272] Based on Coulomb interactions, the Pourbaix-enabled guest synthesis (PEGS) approach was successfully introduced that predicts guest confinement and synthesis inside MOF cavities for low temperature catalysis.^[238] Often, reagents, such as catalysts are too large for direct incorporation within the host framework. The author therefore extended the ship in a bottle approach, using the ability of small precursor molecules to intrude the framework via impregnation^[238] and immobilization within the framework via electrostatic interactions. The guest molecules are directly synthesized in a follow-up step (e.g., by redox reactions) within the framework. Based on Pourbaix diagrams (redox potential vs pH diagrams), precursor solutions and synthetic conditions are predicted for the design the desired catalysts.^[238] Different MOFs including MOF-808-P ($\text{Zr}_6\text{O}_5(\text{OH})_3(\text{BTC})_2(\text{HCOO})_5(\text{H}_2\text{O})_2$; BTC = 1,3,5-benzene-tricarboxylate) and zeolite Y served as model framework for the successful synthesis of RuO_2 and MnOx and resulted in an improved CO oxidation performance.

van der Waals forces are rather weak forces and are based on noncovalent host-guest interactions. Although van der

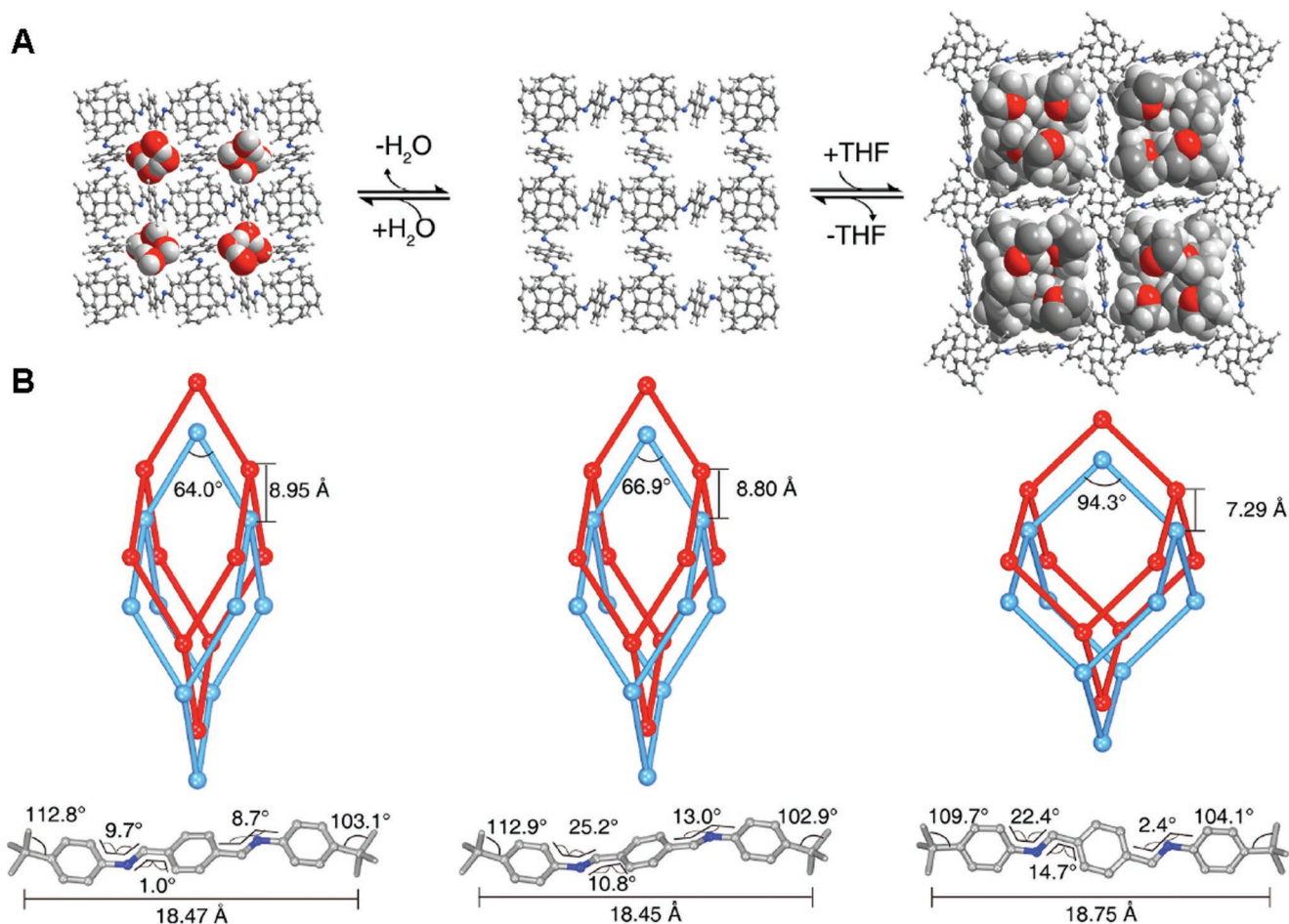


Figure 11. Structural determination of guest-dependent dynamics in COF-300 determined by PXRD. A) Molecular geometries and configurations. B) Hydrated (left), activated (middle) and THF-solvated (right) COF-300. Reproduced with permission.^[259] Copyright 2019, American Chemical Society.

Waal interactions intrinsically lack the strength and directionality of hydrogen bonds, when used in combination with an appropriate surface and molecular design strategy, they are extremely effective in directing surface self-assembly.^[273] DFT and dispersion-corrected DFT calculations revealed that van der Waals forces play a role for the structural features of the MOF pore.^[274] Using such calculations to describe van der Waals forces between the small guest molecules and the walls of reticular materials in comparison with IR adsorption and Raman spectroscopy data, let to remarkable results.^[275] In the same way, the importance of van der Waals forces for the adsorption of small gases can be predicted and used for practical application.^[276]

The dimension of guest and host pore is often a neglected topic. Theoretically, the minimum and maximum projection diameter of a guest can be easily calculated and compared to channel, cage and window size of reticular materials but a huge number of practical examples show that reticular materials are more flexible.^[276] It could be demonstrated that even a protein (cytochrome *c*) can enter in the interior of an MOF despite the larger dimension compared to the pore size.^[277] On the other hand the pore dimension can be used to selectively sieve different guest molecules.^[278] Due to the designability of reticular

materials the pore and the dynamic framework can be optimized for trapping specific guest molecules.^[279]

5.5.1. Host–Guest Interaction between “Solids”

The host–guest interactions are not only the key in adsorption-based applications, they also represent a tool to modularly extend reticular nanoparticles with additional properties that are not inherent to the host framework itself. In the following section, we discuss recent advances of modular host–guest interactions in the solid state. Example for drug-delivery systems and catalysis are discussed in following sections.

Conductivity: Reticular materials normally do not show electronic conductivity.^[148a,280] Metals centers in MOF nanoparticles are mainly in reduced states and coordinated to linkers of low electron density. Most frameworks feature highly localized electronic structures, which makes charge-transfer reactions between different metals centers or linker and metal centers very inefficient. Selective host–guest interactions play therefore an important role in tuning the ion conductivity of framework particles. For the majority of reticular materials, water as adsorbed guest molecule acts as the major conductor.

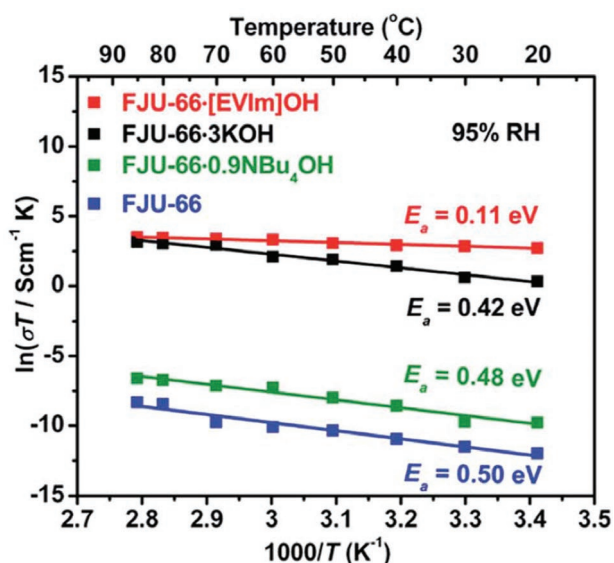


Figure 12. Arrhenius plots for FJU-66 (blue), FJU-66-[EVI]mOH (red), FJU-66-3KOH (black), and FJU-66-0.9NBu₄OH (green). Reproduced with permission.^[281] Copyright 2017, The Royal Society of Chemistry.

Recently, conductive solid state MOF material has been created based on postmodification of FJU-66 with various rationally tuned bases (Figure 12).^[281] Naphthalene di-imide residues of the parental material interact with 1-ethyl-3-vinylimidazolium (EVI^m). Free hydroxide ions were observed in the synthesized FJU-66-[EVI]mOH (FO-MOF) with strong host-guest interaction between the guest cations and the FO-MOF material. FO-MOF exhibit a conductivity between 10⁻² and 10⁻⁷ S cm⁻¹ depending on the incorporated number of guest molecules. The high conductivity on the order of 10⁻² S cm⁻¹ at simultaneously low activation energy of 0.11 eV, suggests

that ionic conduction is based on proton back transfer.^[282] The electron accepting molecule 7,7,8,8-tetracyanoquinodimethane (TCNQ) is another excellent example how to introduce conductivity into an insulating host material.^[283] TCNQ bridges the copper dimers in the pores of HKUST-1 (i.e., Cu₃BTC₂; BTC = 1,3,5-benzenetricarboxylate) and leads to an increase in electrical conductivity of more than seven orders of magnitude.^[284] A recent density functional theory study on HKUST-1 confirms the correct geometry and orientation of the copper paddlewheel for TCNQ in order to bridge two copper dimers.^[285] Electrically conductive nanoparticles are still at the beginning,^[286] however they hold great promises for future applications like fuel cells or printed, flexible electronics.^[287]

Reticular Particles as Tool for Crystallography: The development of reticular nanoparticles strongly benefits from the secondary building unit (SBU) approach. The polynuclear nature of SBUs allows not only do develop new materials, but also to design new, rigid, and directional 3D structures for nanotechnology. The pore confinement of MOF nanocrystals does not only serve as seed for core-shell nanoparticles^[288] or crystal growth,^[289] but also for innovative single-crystal X-ray diffraction analysis of small, flexible molecules and molecular complexes.^[165b,290]

The key advantage of this approach, also termed “sponge method,” is that crystallization of the target molecule itself is not required. The pore environment of the MOF nanocrystals serves as host framework and anchoring point for the selective crystallization of guest molecules (Figure 13). Their adsorption crystallization is mediated via covalent bonds formation to unoccupied metal sites or modified linker molecules. Coordinating the guest molecules within the MOF framework restricts their free movement and helps to align and orient them within the crystalline framework. An additional benefit lies in the chirality of the caging 3D MOF material and hydrophobic/hydrophilic interaction between the guest molecule and pore volumes. It serves as an additional ruler system for chiral guest molecules

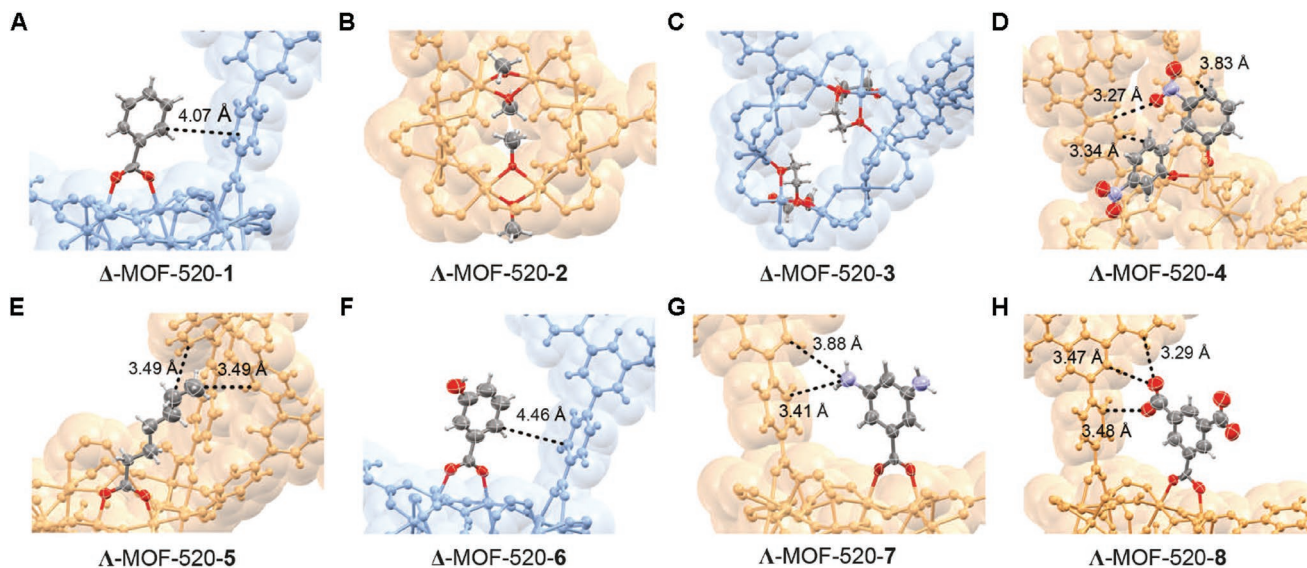


Figure 13. Refined structures of various small molecules crystallized within MOF-520 obtained from SCRD data. The interaction between the molecule and the host-framework aligns the guest species in one orientation. Left-handed and right-handed chirality of the MOF framework are depicted in orange and blue, respectively. Reproduced with permission.^[165b] Copyright 2016, The American Association for the Advancement of Science.

during X-ray diffraction. Single-crystal X-ray diffraction on loaded MOF nanoparticles has been demonstrated for several materials including MOF-520 [Al₈(μ-OH)₈(HCOO)₄(BTB)₄; BTB = 1,3,5-benzene-tribenzoate], [(ZnI₂)₃(TPT)₂·x(solvent)]_n and [(Co(NCS)₂)₃(TPT)₄·x(solvent)]_n, (TPT = tris(4-pyridyl)-1,3,5-triazine). It works best for molecules with molecular weights below 500 g mol⁻¹, such as diclofenac [2-(2,6-dichloranilino)-phenylacetic acid].^[165b,290] The uptake of guest molecules is most efficient for saturated solutions pushing the guest molecule into the porous material due to diffusion. Removal of the solvent can be achieved by evaporation or solvent exchange; however, care should be taken to slowly remove the solvent from the pores to ensure correctly bound guest molecules. Sample volumes as small as 80 ng have been demonstrated.

Imaging Probes: Guest molecules can turn nanoparticles into probes for tracking applications in live cell imaging as well as theranostics applications when combined with drug delivery systems.^[21e,f,253,291] Different types of reticular nanoparticles have been developed for clinical diagnostics including computed tomography (CT)^[292] and magnetic resonance imaging (MRI).^[20a,293,296] Magnetic response of active moieties or molecules can be incorporated into a porous framework, either as metal center, building block^[20a,294] or guest-molecule occupying the host's pores.^[295] MRI-MOFs are synthesized following the first strategy (see Section 8.2). They are often made of paramagnetic gadolinium ions Gd³⁺ such as the (Gd-bis(methylammonium)-benzene-1,4-dicarboxylate)_{1.5}(H₂O)₂ framework.^[44b,296] It features large longitudinal and transversal relaxivities on the order of 10²–10⁷ mM⁻¹ s⁻¹.^[20a,44] To increase the biocompatibility of the designed particles MRI-MOF manganese instead of gadolinium has also successfully been implemented.^[294] Luminescent derivatives have been synthesized by replacing Gd³⁺ with additional 5 mol% of Eu³⁺ or Tb³⁺.^[297] Following the second strategy, nanoparticles for CT-imaging have been designed based on iodinated linker-molecules.^[298] These are equally potent as the conventional contrast agents, but provide higher loading of ions and surface functionalization for biocompatibility and targeting.^[298]

Host–guest interaction for the design of magnetic imaging probes with therapeutic function is mainly employed in superparamagnetic iron-oxide-based MOF and ZIF nanoparticles.^[20a,299] These particles hold great promises for biomedicine,^[253,295] since they are biocompatible in contrast to particles containing toxic metal chelates like gadolinium. The most employed systems are MIL-88, MIL-100, and MIL-101(Fe) nanoparticles for combined multimodal imaging. The studied particles with diameters between 100 and 200 nm show relaxivities between 2 and 70 mM⁻¹ s⁻¹.^[210,300] for MRI imaging. They have been demonstrated as multimodal probes with fluorescence imaging,^[301] positron emission tomography,^[302] CT,^[303] and photoacoustical imaging^[304] (see Section 8.2).

Reticular nanoparticles, i.e., MOF, COF, and ZIF nanoparticles, as imaging sensors for live-cell imaging have been developed in various types based on fluorescence and luminescence. Here, care during synthesis needs to be taken to avoid contact induced quenching and photobleaching of the chromophores within the frameworks. Coronene (a polycyclic aromatic hydrocarbon of seven fused benzene rings) shows luminescence originating from the triplet state, which results

in a stable phosphorescence as optical readout as guest molecule in ZIF-8 material.^[305] Fluorescent 3D pyrene-based COF particles^[306] were designed based on 1,3,6,8-tetrakis(4-formylphenyl)pyrene (=TFFPy) and tetra(*p*-amino-phenyl)methane (=TAPM). The pts-framework features a large surface area with small pore sizes. In a recent work, boron dipyrromethene (BODIPY) derived fluorophores were incorporated in a solvent-free manner into ZIF-8 frameworks leading to emissive solids that show an tenfold enhancement in photostability compared to single emitter.^[307] The electronic properties of the chromophores could be preserved yielding in solid frameworks with fluorescent emission between 500 and 800 nm. Imaging contrast via near-infrared excited upconversion radiation originated from the rare-earth metal ytterbium and erbium that were used for doping the core of MIL-101 nanoparticles.^[301]

The host–guest interaction defines, whether a fluorophore stays permanently bound within the framework. To prevent fluorophores from “leaking” from the structure, one strategy could be reticular framework-based nanoshells. Fluorescein was demonstrated, to get enclosed within ZIF-8 by forming the MOF framework around the dye.^[308] The interaction with MIL-100 and MIL-101 particles is mainly transient. The loading and release of fluorescein to MIL-100(Fe) and MIL-101(Cr) nanoparticles studied using fluorescence spectroscopy. Already at room temperature, the available surface area is maximally occupied by dye molecules.^[309] This results in more than 1000 fluorophores per nanoparticle. Fluorophores comprise long π-conjugated electron systems. Nonsurprisingly, loading and release of fluorescein from MOF particles is strongly dominated by electrostatic interactions between the fluorophore and the MOF nanoparticle.^[309] This results in a tunable pH dependency and controlled release between 3% and 40%, a property that is vital for clinical applications and drug delivery.

Despite its great developments over the last years, the design of efficient, fluorescent MOF-based nanoparticles for sensing remains challenging due to photostability and reduced penetration depth of light in cells and tissue. Recently, two-photon MOF nanoparticles (TP-MOF) based on PCN-58^[310] have been introduced as intracellular sensing platform for H₂S and ions Zn²⁺.^[311] This zirconium derived MOF employed azide-appendant organic linkers (TPDC-2CH₂N₃; 2',5'-bis(azidomethyl)-[1,1':4',1''-terphenyl]-4,4''-dicarboxylic acid). Based on azide-alkyne cycloaddition three different two-photon probes were attached to the MOF framework and benchmarked. The designed probes feature excellent biocompatibility and sensitivity to monitor H₂S (>30 × 10⁻⁶ M) and Zn²⁺ (400 × 10⁻⁹ M) over hours. The NIR excitation source facilitates a penetration depth of 130 μm.

5.5.2. Liquids

Host–guest interaction between liquid molecules and reticular nanoparticles are the most common interaction, as most nanoparticles are synthesized in solution and prone to aggregation depending on the solvent. To understand the structure–activity relationships at the microscopic world (e.g., the nano/biointerface) it is imperative that researchers deeply characterize NPs and their properties by choosing and employing the appropriate

characterization techniques. This holds in particular true for applications in the field of sensing, liquid separation and water harvesting

Sensing: Ideal chemical sensors need to be sensitive to their analytes, to provide a stable readout signal and long-lasting chemical stability, i.e., they should be reusable. Chemically ultrastable MOF, ZIF and COF frameworks have been synthesized.^[312] The reticular nature of these porous host materials allows to simultaneously incorporate guest molecules or postmodifications for sensing and readout. Due to the selectivity of the pores, reticular material can preconcentrate analytes to achieve (enhanced) sensitivity. While *n*-hexane, e.g., can adsorb to ZIF-8, cyclohexane is not taken up due to small pore sizes.^[313] Moreover, a comparison study on the absorption behavior of alkane, alkene, and aromatics by ZIF-8, HKUST-1 and CPO-27 and others shows that ZIF behave like apolar adsorbents that adsorb in the order alkanes > alkene > aromatic.^[314] MOFs with coordinatively unsaturated sites behave like polar adsorbents and preferentially adsorb alkenes over aromatics.^[314] The selectivity of MOF as sensor for specific guest molecules depends on the specific coordination and/or hydrogen bonding between the guest molecules with the framework, as it is the case in frameworks with uncoordinated metal sites. The Cu²⁺ centers in HKUST-1, e.g., have an axial coordination site open that points into the pore, acting as Lewis acidic site.^[315] When applied for the separation of ethane and ethylene, HKUST-1 primarily interacts with ethylene.^[316] Computational studies^[317] revealed that the strong interaction between ethylene and the MOF originates from two contributions: hydrogen bond formation between the -CH₂ side group and the oxygen atoms in the

copper paddlewheel units and π -backbonding from the copper centers and the ethylene.^[278a]

Liquid Separation: Over the last two decades, porous materials have been introduced as tools for liquid separation.^[15c,318] Reticular nanoparticles are of particular interest due to their uniquely high surface to volume ratio, which allows them to interact with the solvent more than any other material available to date. Therefore, MOF nanoparticles could be of great use for liquid filtration and separation,^[15c] perhaps even in the desalination of water. Using the MOF nanoparticles embedded in a polymer matrix,^[319] liquid could be pressed through the membrane and separated via size exclusion (**Figure 14**). Molecules larger than the pores of the MOF and even ions that may adsorb through MOF nanoparticles are blocked by the membrane (several types of reticular materials for ion sensing and capture have been developed; see previous section).

This approach has already been employed for organic solvent nanofiltration, using various frameworks including ZIF-8, MIL-53, and MIL-101(Cr) as MOF filter embedded in a polyamide thin film. The nanoparticles had an average size between 50 and 100 nm and were equally dispersed within the polymer matrix. The performance and permeability of the thin film nanocomposite membranes (TFN) was evaluated by methanol/polystyrene and THF/polystyrene nanofiltration experiments. Best results were observed for mesoporous MIL-101(Cr)@TFN, where the flux for the passing solvent increased with increasing amounts of nanoparticles. The increase in flow performance can be explained by the liquid's preference to flow through MOF nanoparticles instead of the polymeric host matrix. Tunable membranes hold

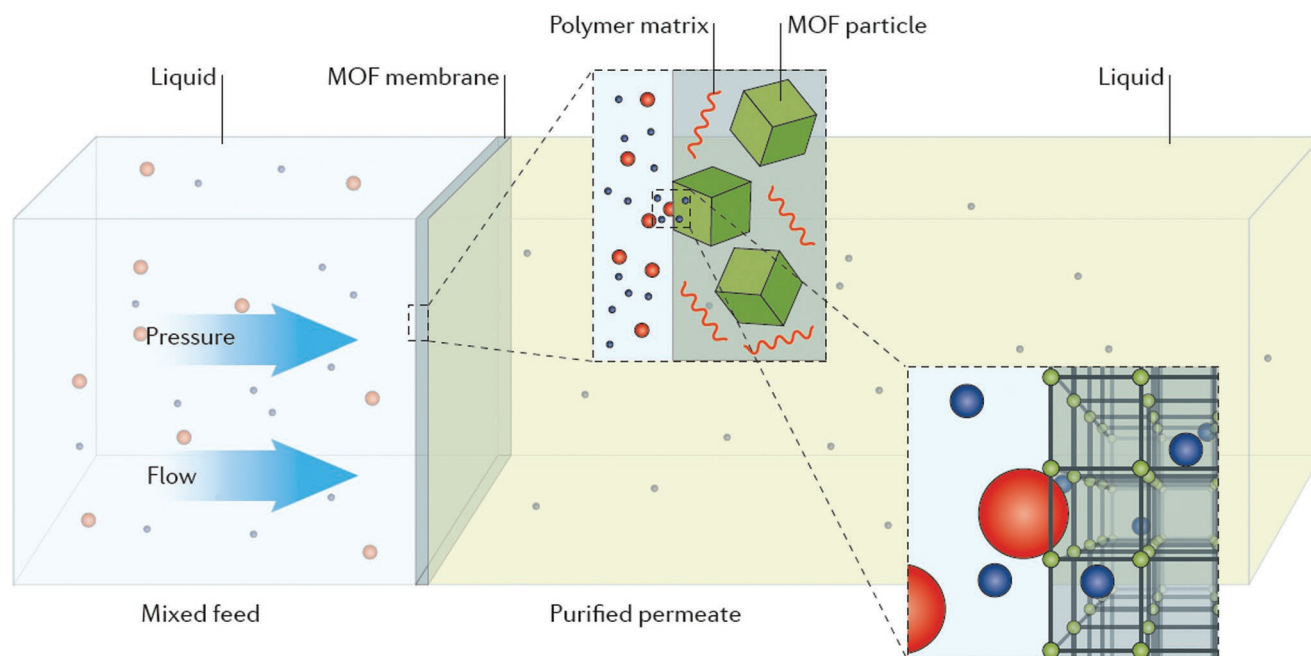


Figure 14. Schematic illustration of a potential solvent filtration and desalination. Solvent passes through a membrane made of MOF particles embedded within a polymer matrix. The membrane has two functions: only species that are smaller than the membrane pores can pass through the layer. Large molecules and species like ions that adsorb through the MOF nanoparticles are blocked by the membrane. Reproduced with permission.^[15c] Copyright 2016, Springer Nature.

great promise for size-dependent separation and filtration of liquids and the incorporation of ion-capturing frameworks can further pave the way for desalination and ion exchange.

Water Harvesting: Water harvesting from air represents an attractive and innovative way to address the global water problem. Current estimations assume that atmospheric water is a resource equivalent to $\approx 10\%$ of all fresh water in lakes on earth, which is equivalent to 13 thousand trillion liters.^[16b,c] Nevertheless, energy-efficient technology solutions for “harvesting” this water have not been developed, yet. A proof-of-concept device for harvesting water at low relative humidity using only natural sunlight was reported very recently.^[16c] An MOF-based water harvesting system could be developed (**Figure 15**) and practically tested in the desert.^[16c] These breakthrough approach could revolutionize this field, which was featured as one of the top 10 emerging technologies by the World Economic Forum in 2017.^[320] Further studies could optimize the sorption dynamics to reach production scale matching human consumption, capable of generating $1.3 \text{ L kg}_{\text{MOF}}^{-1}$ per day in an indoor arid environment (32% relative humidity, 27 °C) and $0.7 \text{ L kg}_{\text{MOF}}^{-1}$ per day in the Mojave Desert (in conditions as

extreme as 10% RH, 27 °C).^[321] This technology is currently pushed by designing new concepts for next-generation MOFs for passive adsorption-based water-harvesting. The approach could even further benefit from the introduction of MOF nanoparticle to the field, by employing their uniquely high surface to volume ratio and hence potentially increased surface areas for water adsorption and harvesting.

5.5.3. Gas Delivery

Reticular frameworks are studied for long time as materials in gas separation, catalysis and storage applications. Strong efforts are currently made to employ them as material for long-term CO_2 storage and reversible H_2 storage and delivery to reduce environmental pollution.^[7a-e] The application of reticular nanoparticles to (reversible) gas storage, however, is strongly related to the bioactivity of the gas. Bioactive gases, also termed gas-transmitters,^[322] act as signaling molecules in cells and are produced enzymatically by the cell itself, in particular NO , H_2S , and CO .

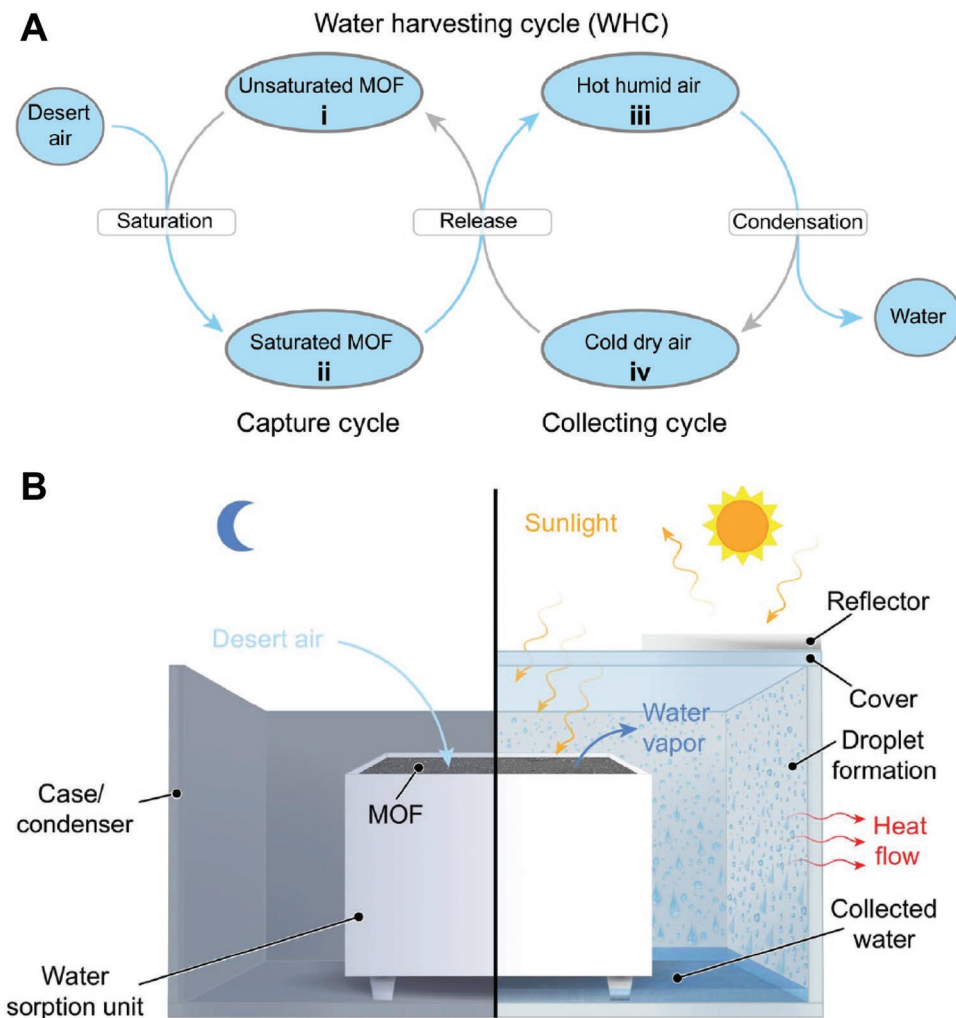


Figure 15. A) Water harvesting cycle (WHC) for water production under natural cooling and day sunlight. B) Schematic illustration of MOF-based water harvesting system. Reproduced with permission.^[16c] Copyright 2018, The American Association for the Advancement of Science.

NO is a biomedically key player involved in nervous,^[323] immune^[324] and cardiovascular^[325] processes. NO is produced in cells, e.g., by the NO synthase at varied concentrations in the nano- to micromolar range and acts as neurotransmitter in the peripheral and central nervous system,^[323] anticoagulant agent,^[326] and stimulus for tissue growth and wound healing.^[327] Moreover, NO possesses antibacterial^[328] properties and regulates inflammatory processes^[329] and tumor progression^[330] depending on concentration^[331] and site in the body. Due to its strong biomedical importance, great effort has gone into the design of reticular nanoparticles that release NO in a controllable fashion. The design of MOF,^[332] COF,^[333] zeolites,^[326a,334] and polymer^[332f,335] nanoparticle has been reported for targeted delivery^[12] of exogenous NO at different amounts and rates.

Storage of NO can be achieved by reversible adsorption to coordinatively unsaturated metal sites. Several biocompatible MOF materials with open metal sites have been synthesized.^[332b,c,f,g] NO-loaded HKUST-1 nanoparticles^[332g] made of copper benzene tricarboxylate were introduced first. They adsorb and release NO in presence of water with an increased sorption capacity of $\approx 3 \text{ mmol g}^{-1}$ at room temperature due to their rigid framework but a surprisingly low release of $1 \mu\text{mol g}^{-1}$. This property, however, nicely meets the requirements of NO in the pico- to nanomolar range for antiplatelet action in blood. NO-loaded HKUST-1 nanoparticles can successfully prevent the aggregation of platelets.^[336] Applications like antimicrobial tackling in wound-healing, however require sources with high NO release. Biocompatible MIL-88(Fe) nanoparticles^[332d] feature a low sorption capacity of $1\text{--}2 \text{ mmol g}^{-1}$ due to low accessibility of the pores and framework flexibility and release about 10%. Nanoparticles derived from MIL-100(Cr), MIL-100(Fe), and MIL-127(Fe) that feature less flexibility and larger pore sizes show an increased average adsorption capacity^[332c] of $\approx 2.8 \text{ mmol g}^{-1}$, with an $\approx 20\%$ release rate. CPO-27-(Ni/Co), dihydroxyterephthalate nanoparticles^[332f] are exceptionally reversible materials that adsorb $\approx 7\text{--}8 \text{ mmol g}^{-1}$ with fully reversible release of NO in presence of water vapor. Although secondary metals (Ni, Co) are not ideal in terms of toxicity, the extraordinary performance in storage and delivery of pure NO opens up exciting possibilities for biomedical. Zinc analogs^[332a], might be very interesting candidates to improve on biocompatibility.

An additional strategy to improve the performance of reticular nanoparticles in NO delivery, is based on NO donor molecules,^[337] most notably nitrates, S-nitrosothiols and diazeniumdiolates^[338] that are incorporated into the framework. NONOates that carry a diazeniumdiolate ion ($\text{N}(\text{O})=\text{NO}^-$) are among the most employed NO donors for biomedical application due to the high release capacities that can be temporarily tuned.^[339] They are used as permanent linker molecules in framework particles and contain a nucleophile adduct, usually a secondary amine. Reaction with exogenous NO results in a bound diazeniumdiolate ion ($\text{N}(\text{O})=\text{NO}^-$) in the absence of H_2O .^[326b] Stable^[326b,340] diazeniumdiolated MOF nanoparticles have been successfully realized and introduced as potential antithrombosis material^[326b] that can tissue growth and adhesion of blood constituents in particular RBCs.

In order to act as NO-donating nanoparticle, stored NO needs to be release in a reversible and controlled fashion.^[341] Its release can be triggered externally in various ways including pH, moisture, ions, and light. Zeolite^[326a,342] and MOF^[332g] nanoparticles have been synthesized that release NO based on NONOate hydrolysis. They showed antibacterial properties^[343] and acted as anticoagulant agent^[332g] which highlights their potential biomedical application. Postmodified MOF nanoparticles^[340] that contain functional amine groups for NO storage have been described. IRMOF-3 and UMCM-NH₂ strongly bind NO and release NO with 8% and 6%, respectively.

Photoactive release of NO from organic molecules^[341b,c] is an elegant way to employ light as external, noninvasive trigger. To introduce NO photodons to nanoparticle, these can either be immobilized on the surface^[344] of nanoparticles or can serve as building blocks.^[341c,345] Photoactive ZIF particles^[334a] based on zinc (and cobalt) complexed with 2-nitroimidazole and 5-methyl-4-nitroimidazole have been realized. They release NO by nitro to nitrite transition upon external photoactivation and allow for rapid release of $\approx 3 \mu\text{mol g}^{-1}$ of NO, which corresponds to $\approx 50\%$ of the conversion yield. Light-triggered NO delivery was demonstrated in cells in a spatiotemporal manner via two-photon excitation microscopy and induced intracellular Ca^{2+} influx.

Besides NO, further biologically active gases are hydrogen sulfide and carbon monoxide that strongly affect (patho-) physiological functions within the body, including the regulation of vasodilation, neurotransmission and inflammation.^[346] The adsorption of H_2S and CO to reticular framework nanoparticles are addressed^[347] including MIL-53,^[348] MIL101,^[349] and CPO-27.^[350] Biomedical applications,^[333,336,351] however, are only shown for H_2S nanoparticles. Porous CO-releasing nanoparticles have not been reported yet. CPO-27(Ni) only was shown to adsorb CO in dry form due to coordination with Ni^{2+} .

6. External Surface Functionalization

The modification of the nanoparticles' external surface is crucial for any kind of future applications,^[352] since its properties determine the interactions of the nanoparticles with each other as well as with their surroundings. As a result, the development of material chemistry, which precisely functionalizes the external surface of COF, MOF, and ZIF nanoparticles was a very active focus of the field in the last 5 years. A key challenge was to create a highly functionalized shell, which has to fulfill different tasks such as recognition of specific receptors, triggered drug release or avoidance of agglomeration within the bloodstream, without effecting (e.g., blocking and/or altering) the internal porous scaffold.

Two functionalization strategies have been developed so far: i) the functionalization during the nanoparticle synthesis, known as coordination modulation approach and ii) postsynthetic modification (PSM).^[42a] In the following, the different strategies for the external surface functionalization of COF, MOF, and ZIF nanoparticles with polymers and lipids are discussed.

6.1. External Polymer Functionalization

Due to their flexible design, polymers are excessively used for the functionalization of nanomaterials.^[352,353] The knowledge of specific characteristics of different polymers and their effects on nanomaterials can also be translated to MOF, ZIF, or COF nanoparticles. Several approaches for the generation of MOF–polymer hybrid materials have been reported. In many cases the materials are based on polymer matrices or scaffolds which embed MOFs into monolithic hybrid composites.^[354] In contrast, here the focus lies on the functionalization strategies for the generation of colloidal polymer-functionalized framework nanoparticles. For the functionalization of any nanomaterial, its individual chemical properties and structural composition have to be taken into consideration for the selection of suitable strategies (Box 2).

Box 2. Selection of suitable polymer-functionalization strategy, which depends on the framework nanomaterial, the polymer, and the intended purpose

MOF, ZIF:

- 1) unsaturated metal sites available
→ coordinative polymer impregnation,
- 2) unsaturated linker sites (e.g., carboxylic acid) available
→ covalent polymer conjugation,
- 3) integration of linker with grafting site during synthesis
→ covalent polymer conjugation, and
- 4) shell polymerization.

COF:

- 1) integration of linker with grafting site during synthesis
→ covalent polymer conjugation,
- 2) framework dispersible by polymer surfactants
→ nanoemulsion, and
- 3) shell polymerization.

In the case of MOFs and ZIFs, the inorganic and organic building units, external surface or inner pore volumes can be utilized for polymer association. For COF materials, the chemically different organic building units (most of the time two or more) can be considered for functionalization. In general, external polymer functionalization can be classified into three groups (Figure 16):

1. Noncovalent polymer impregnation
2. Covalent polymer conjugation
3. Supported shell polymerization

6.1.1. Noncovalent Polymer Impregnation

Straightforward approaches for the external polymer functionalization are based on noncovalent interaction and passive polymer impregnation which generally do not require sophisticated synthetic procedures or specific coupling reagents. A first example of polymer functionalized MOF nanoparticles was realized by in situ integration during MOF formation.^[295]

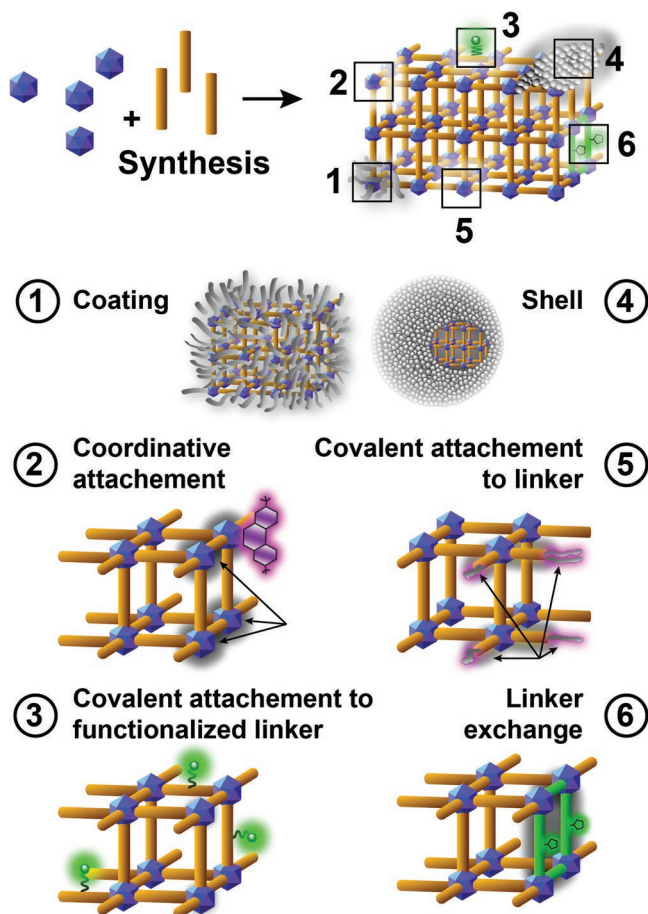


Figure 16. Strategies for external functionalization of nanoparticles.

Mono-amino-PEG has been integrated noncovalently into MIL-88A and MIL-100(Fe) in situ during the particle synthesis. By this means, MOF nanoparticles with PEG contents of up to 17 wt% were obtained. The steric shielding shifted the zeta-potential values of MOF nanoparticles upon PEG functionalization toward neutrality and reduced aggregation.

Subsequently, alternative strategies for the postfunctionalization of preformed MOF nanoparticles have been developed. The modification of MIL-100(Fe) at the external surface by impregnation with different saccharides in facile one-pot procedures was demonstrated in several cases.^[355] Surface coating with well tolerated cyclodextrin (CD) was developed as a green strategy for the noncovalent functionalization of MIL-100(Fe) nanoparticles (Figure 16; coating).^[355a] The surface-modification of the MOF nanoparticles was carried out by impregnation with phosphorylated β -CD in aqueous solution. The phosphate groups strongly bind to coordinatively unsaturated metal sites at the surface, which is stable in aqueous solution and leads to up to 17 wt% CD phosphate association. This functionalization strategy did not show any reduction of the crystallinity and surface area of the MOF nanoparticles. Beside the effect of CD on colloidal stabilization, the CD impregnation is also suggested to be applicable for subsequent additional surface functionalization by the formation of inclusion complexes with adamantyl end group functionalized polymers or other functional units.

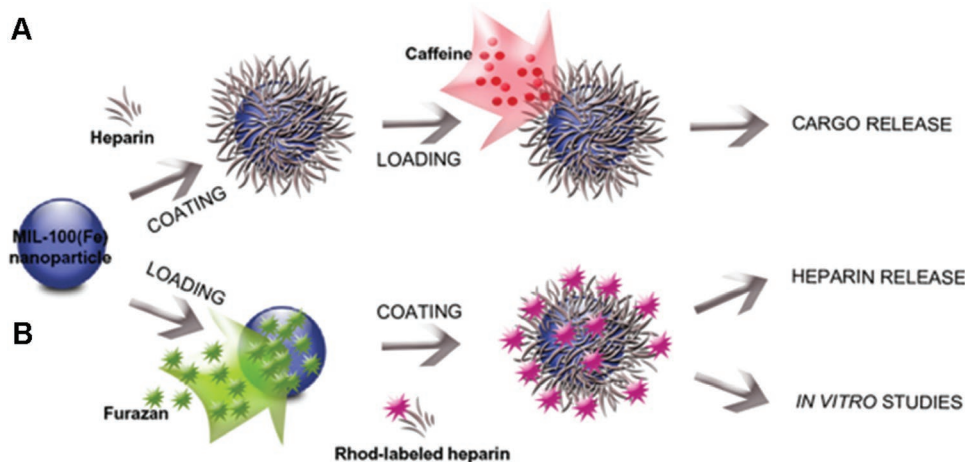


Figure 17. Heparin coating and loading of MIL-100(Fe) nanoparticles with different procedures. A) External heparin coating followed by postloading with caffeine. B) Preloading with furazan followed by external coating with rhodamine-labeled heparin. Reproduced with permission.^[355b] Copyright 2015, Wiley-VCH.

The naturally occurring anticoagulant saccharide heparin can also be used for surface functionalization of MOF nanoparticles; impregnation of MIL-100(Fe) nanoparticles with heparin was reported.^[355b] Heparin-coated MIL-100(Fe) were generated (Figure 17) via a biocompatible one-pot method by simple impregnation of nanoparticles using a heparin solution in water:ethanol (30:70). The grafting method provided efficient attachment of around 88% of the offered heparin and a final heparin content of $\approx 12.5\%$ (w/w). The resulting heparin coated MIL-100(Fe) nanoparticles exhibited a hydrodynamic diameter of around 170 nm and a zeta potential below -20 mV. The crystalline structure and BET surface of MIL-100(Fe) remained unaffected by the coating process. The preserved accessibility of nanopores for small molecules was confirmed by caffeine loading which led to equal extent in case of uncoated and coated MIL-100(Fe) nanoparticles. Theoretical calculations determined a number of ≈ 6500 heparin chains attached to a single nanoparticle at a density of 0.1 molecules nm^{-2} and a thickness of around 10 nm. These parameters suggest a PEG grafting in “brush regime” which provided an increased colloidal stability of the MIL-100(Fe) nanoparticles and decreased the uptake into macrophages in experimental settings. A selective external surface modification of MIL-100(Fe) with bioadhesive chitosan can be achieved with a similar impregnation method as described for the heparine coating.^[355c] Main interaction is suggested to occur between chitosane hydroxyl groups and terminal coordinatively unsaturated iron metal sites. It was confirmed that porosity and crystallinity is maintained which is a basic requirement for the utilization as drug carrier. In addition, an increased cellular uptake and intestinal permeability was demonstrated in vitro due to the positive charge and mucoadhesive properties of chitosan. Therefore, utilization for oral administration of drugs and active agents seems to be feasible for this particular MOF polymer hybrid.

Other strategies used diverse polymers or functional units with a discrete Lewis base motif for coordinative postfunctionalization of MOF nanoparticles. A versatile functionalization strategy uses coordinative binding of RAFT-polymers containing a terminal thiol-group.^[356] By attachment of different

polymers to $\text{Gd}^{3+}/1,4\text{-BDC}$ MOF nanoparticles a tuning of their magnetic resonance imaging (MRI) properties was demonstrated. The versatile approach enabled production and attachment of a heterogenous set of hydrophilic and hydrophobic polymers, such as poly[*N*-(2-hydroxypropyl)methacrylamide] (PHPMA), poly(*N*-isopropylacrylamide) (PNIPA), polystyrene (PS), poly(2-(dimethylamino)ethyl acrylate) (PDMAEA), poly(((poly)ethyleneglycol) methyl etheracrylate) (poly(mPEG-acrylat)), and poly(acrylic acid) (PAA). First, the polymers were produced by polymerization using a trithiocarbonate RAFT agent. The trithiocarbonate was then converted into a free thiol for coordination with Gd^{3+} ions at the MOF surface. The characterization of MRI properties revealed that in case of hydrophilic polymers an increase in molecular weight mediated an increase in the longitudinal relaxivity. In contrast, hydrophobic polymer coatings mediated minimal changes in the longitudinal relaxivity but strong increase in the transverse relaxivity properties. The strategy for the grafting of RAFT-derived homopolymers to Gd-MOF NPs was extended to the assembly of multifunctional NPs containing fluorescent tags, peptidic receptor targeting ligands and methotrexate as therapeutic cargo for cancer treatment.^[356b]

A similar coordinative binding approach for the functionalization of MOF nanoparticles uses oligohistidine tags (His-tags) as discrete Lewis bases compatible with peptide and protein chemistry (Figure 18).^[357] His-tags are peptide motifs with high affinity toward metal-ions, which are frequently used for the purification of recombinant proteins via immobilized metal affinity chromatography (IMAC). Here, coordinative binding of His-tags to unsaturated metal-sites at the external MOF surface was demonstrated with MIL-88A, HKUST-1 and Zr-*fum* nanoparticles. Simple mixing of His-tag containing functional units in aqueous environment resulted in rapid association with the MOF nanoparticles. The pH-dependent dissociation at acidic pH showed the reversible nature and the suitability for biomedical applications. In this regard, Zr-*fum* nanoparticles were used as a vehicle for the intracellular transport of fluorescent and proapoptotic peptides or proteins which are generally cell-impermeable under other conditions.

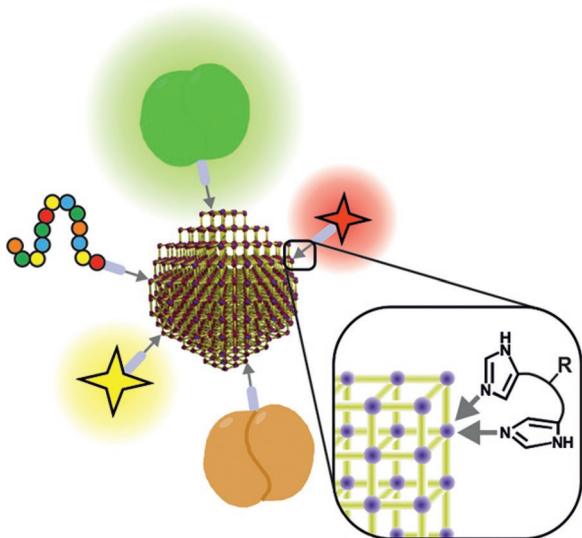


Figure 18. Schematic illustration of postfunctionalized MOF nanoparticles generated by coordinative interaction with oligohistidine-containing functional units. Reproduced with permission.^[357] Copyright 2017, American Chemical Society.

Entire polymer blocks can also be used as discrete binding motifs in block copolymers with other nonbinding polymer segments. As a logic consequence of an observed differential polymer binding, a copolymer composed of a discrete binding and a shielding (nonbinding) block was recently used to control the interactions of Zr-*fum* nanoparticles at the biointerface.^[5a] The MOF nanoparticles were postmodified by simple mixing with aqueous/ethanolic polymer solutions at room temperature. A systematic assessment of different polymers for their ability to bind to MOF nanoparticles identified carboxylic acid (polyacrylate, polyglutamate) and amine-containing polymers (PEI, PAMAM dendrimer) to effectively bind to Zr-*fum* nanoparticles in a coordinative modulator replacement reaction (Figure 19). Neutral polymers (PEG, Tween) did not bind to Zr-*fum* nanoparticles. As a consequence of the strong binding of polycarboxylates, efficient surface shielding was achieved with a polyglutamate-polysarcosine block copolymer. The resulting Zr-*fum*@PGLu-PSar nanoparticles exhibited a remarkable colloidal stability over a broad pH range and in biological

media and strongly reduced protein binding as determined by fluorescence correlation spectroscopy.

6.1.2. Covalent Polymer Conjugation

Depending on the molecular composition of the framework material, covalent conjugation can be an alternative generic strategy for flexible and robust polymer attachment. In many cases amine-, hydroxy-, or carboxyl functions in the framework have been used for well-established coupling reactions, but in principle any conjugation strategy could be adapted if the framework provides the chemical anchor points. Although not exhaustively used for polymer functionalization, a convenient covalent postmodification strategy has been demonstrated in several cases with MOF nanoparticles containing amino-functionalized linkers in the MOF scaffold. Analogs of MIL-101(Fe) with incorporated 2-aminoterephthalic acid (NH₂-BDC) linkers have been reported first for MOF NP postmodification by using peptide coupling reagents.^[358] The successful functionalization by amidation of amino-containing linkers was demonstrated with a fluorescent dye (Br-BODIPY) and ethoxysuccinato cisplatin as prodrug for cancer treatment. Another work systematically compared different peptide coupling reagents for postmodification of related amino-tagged MIL-101(Al)-NH₂ nanoparticles.^[359] Diisopropylcarbodiimide was identified as a potent reagent for postmodification and the feasibility of the approach was shown by conjugation of different molecules: Boc-Glycine, acetylsalicylic acid, and chlorambucil. An alternative strategy has been established for the covalent polymer postmodification of carboxylic acid based MOF nanoparticles without requirement of chemically modified linkers in the MOF structure (Figure 20).^[360] Free unsaturated carboxylic acid groups at the external surface of MIL-100(Fe) nanoparticles were activated with ethyl(dimethylaminopropyl) carbodiimide (EDC) and *N*-hydroxysulfosuccinimide (Sulfo-NHS) and amidated with amine-containing polymers (PEG and a cationic oligoethanamine amide C-Stp₁₀). Based on geometry and mass density parameters of the nanoparticles, a content of $\approx 10\text{--}20$ nmol C-Stp₁₀ per milligram MIL-100(Fe) were estimated. This corresponds to $\approx 460\text{--}920$ single polymer molecules per nanoparticle and a graft density of around $9\text{--}17$ pmol cm⁻². The covalent derivatization under mild reaction conditions preserved the

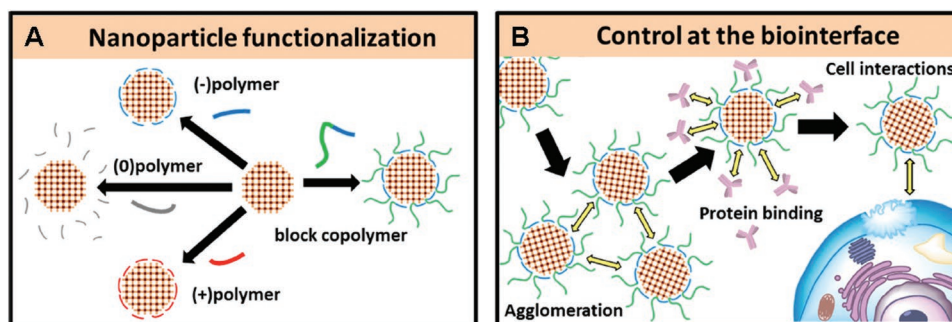


Figure 19. Schematic illustrations of A) a systematic study comparing the binding of acidic (-), neutral (0), or basic (+) polymers to MOF nanoparticles and B) the effect of a copolymer containing a discrete binding (polyglutamate) and shielding (polysarcosine) block on the interactions at the MOF biointerface. Reproduced with permission.^[5a] Copyright 2019, American Chemical Society.

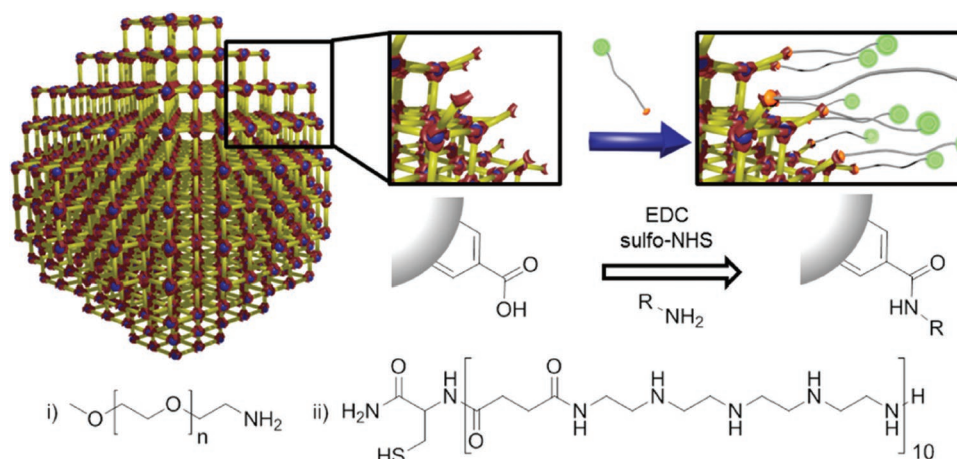


Figure 20. Strategy for the covalent postmodification of carboxylic acid-based MOF nanoparticles by amidation reaction at free carboxylic functions at the nanoparticle surface. Reproduced with permission.^[360] Copyright 2016, American Chemical Society.

crystallinity but strongly increased colloidal stability in aqueous and serum containing media. The MIL-100(Fe)@Polymer core-shell nanoparticles were well tolerated by Neuro2A cells without adverse effects on metabolic activity up to a rather high concentration of $300 \mu\text{g mL}^{-1}$.

In the COF field, a sequential postsynthetic modification of covalent organic nanosheets (CONs) with several different functional units have been reported.^[22c] The work reports the first example of targeted drug delivery using postsynthetically modified CONs (**Figure 21**). Folate was conjugated for specific cellular uptake into folic acid receptor positive cells, 5-fluorouracil (5-FU) as a therapeutic anticancer cargo and rhodamine-B for fluorescence-based cellular uptake studies. The COF scaffold (TpASH) was synthesized by salt-mediated Schiff base condensation between 1,3,5-triformylphloroglucinol (Tp) and 4-aminosalicylhydrazide (ASH). In the sequential modification approach, the phenolic hydroxyl groups of ASH were first converted into alkyl hydroxyl groups by conjugation of glycidol. In

the next step, the hydroxyl groups were modified with 3-aminopropyltriethoxysilane (APTES) resulting in amines on the CON surface. In the last step, the introduced amines were used as attachment sites for EDC/NHS coupling of the targeting receptor folic acid or labeling with rhodamine-B-isothiocyanate (RITC). Soaking of the folate modified TpASH in an aqueous 5-FU solution resulted in a targeted drug carrier with $\approx 12\%$ loading, increased uptake into folate-receptor overexpressing cancer cells and a sustained release at acidic pH 5.

6.1.3. Supported Shell Polymerization

A completely different approach for the association of MOF, ZIF, or COF nanoparticles with polymerized materials is the shell polymerization around the framework nanoparticle core. In contrast to the discussed noncovalent and covalent polymer functionalization strategies above, the approach does not use

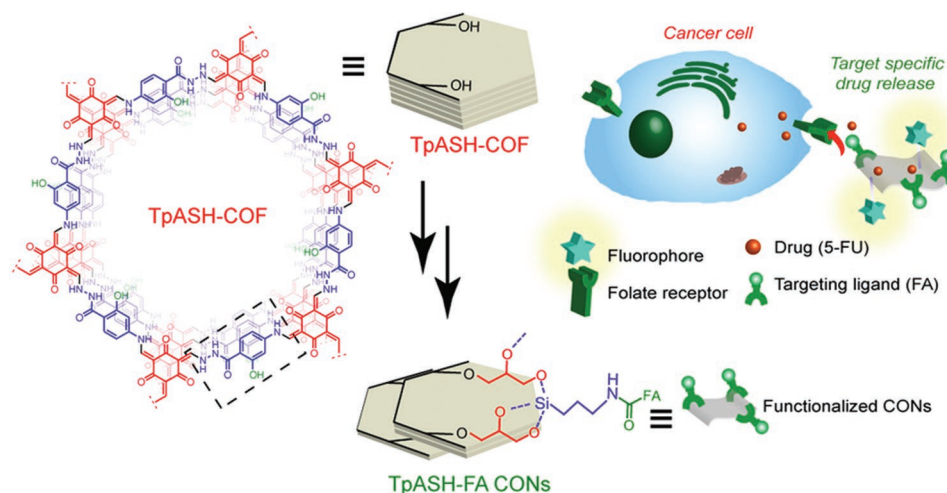


Figure 21. Targeted COF anticancer drug carrier generated by sequential postsynthetic modification. Phenolic hydroxyl groups in the COF scaffold (TpASH) are converted into alkyl hydroxyl groups, modified with 3-aminopropyltriethoxysilane (APTES) and conjugated with folic acid as receptor targeting ligand. The final TPASH-FA is used for folate receptor targeted delivery of 5-fluorouracil. Reproduced with permission.^[22c] Copyright 2017, American Chemical Society.

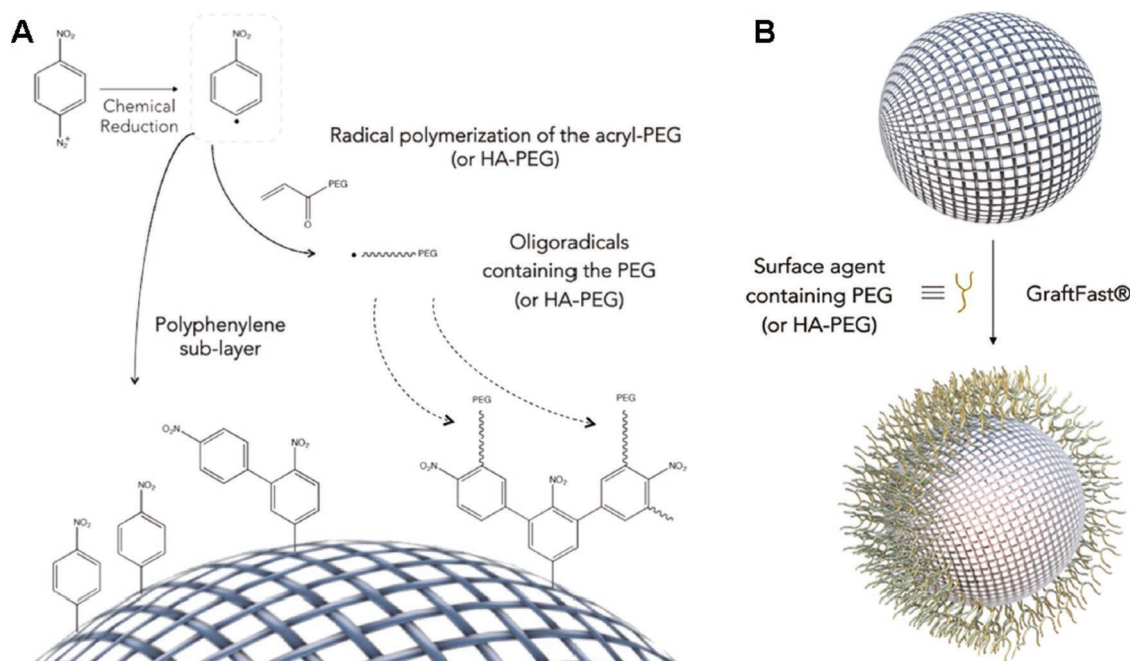


Figure 22. GraftFast functionalization. The shell polymerization is based on radical polymerization of vinyl- or acryl-derivatives and enables postfunctionalization with different polymers. Reproduced with permission.^[361] Copyright 2018, Wiley-VCH.

existing polymers for association with the nanoparticles; the polymerized material is generated in situ at the external surface support.

This strategy is particularly useful for the stabilization of a labile nanoparticle core, as it has been demonstrated with a nanoscale coordination polymer (NCP-1) from Tb^{3+} ions and disuccinatocisplatin for cancer therapy.^[26a] The amorphous NCP was stable and dispersible in most organic solvents, but disassembled in aqueous environment. To address this issue, the drug containing cores were stabilized by a shell of polymerized amorphous silica. The NCP were first coated with polyvinylpyrrolidone (PVP), and then treated with tetraethyl orthosilicate (TEOS) in a 4% (v/v) aqueous ammonia/ethanol mixture. The thickness of the polymerized silica shell can be tuned by the reaction time and TEOS concentration which has influence on the drug release under physiological conditions. A TEOS derivative conjugated to the cyclic peptide c(RGDfK) was used for additional surface functionalization with an integrin targeting ligand resulting in a targeted drug delivery vehicle.

The “GraftFast” technology is a green, versatile and simple functionalization strategy based on shell polymerization (Figure 22).^[361] Here, aryl radicals are generated from aryl diazonium salts by iron powder and on the one hand serve as initiator for radicalic polymerization of vinyl- or acryl-derivatives and on the other hand forms a polyphenylene shell on the nanoparticle surface. Postfunctionalization of MIL-100(Fe), MIL-100(Al), and MCM-41 silica with several polymers, such as PEGs of different lengths (480 Da, 2 kDa, and 5 kDa) and poly(ethylene glycol) hyaluronic acid acrylate (acryl-HA-PEG) moieties were demonstrated. The GraftFast methodology provides a homogenous coating with enhanced colloidal and chemical stability under physiological conditions. PEG-coated MIL-100(Fe) nanoparticles

exhibited maintained drug loading and release properties, reduced macrophage uptake and lowered cytokine excretion from peripheral blood mononuclear cells.

In order to synthesize nanomaterials with the characteristics desired for their application, different postfunctionalization approaches can also be combined. An example is doxorubicin loaded ZIF-8 nanoparticles, which were postfunctionalized by combination of an initial shell polymerization followed by external coordinative polymer binding.^[362] The ZIF-8 nanoparticles were loaded with doxorubicin by co-encapsulation during nanoparticle synthesis in a one-pot process. A polydopamine shell surrounding the DOX@ZIF-8 core was then generated via a “mussel-inspired polymerization.” This extremely versatile strategy (Figure 23), was inspired by the composition of adhesive proteins in mussels which are rich in DOPA and lysine amino acids.^[363] Dopamine combines the catechol and amine functions and undergoes self-polymerization at a pH similar to a marine environment. By this means, polydopamine films can be generated and deposited on a diverse range of inorganic and organic materials. DOX@ZIF-8 nanoparticles were dispersed in an aqueous dopamine solution at pH 8.5 and incubated for 4 h. An additional external modification with hyaluronic acid was achieved by a Fe^{3+} -mediated coordination reaction. DOX@ZIF-PDA was supplemented with a $FeCl_3$ solution and stirred for 1 h. Subsequently, hyaluronic acid was coordinatively bound to DOX@ZIF-PDA NPs during a 3 h reaction. The hyaluronic acid coating mediated a zeta potential shift from 27.1 to -30.2 mV and increased colloidal stability in water, PBS, cell culture medium and FBS. A doxorubicin content of 9% with pH-dependent release at pH 5 was determined.

Presynthesized polymers, which on the one hand can self-assemble at the nanoparticle surface and on the other hand contain initiator groups for polymerization reactions, enable

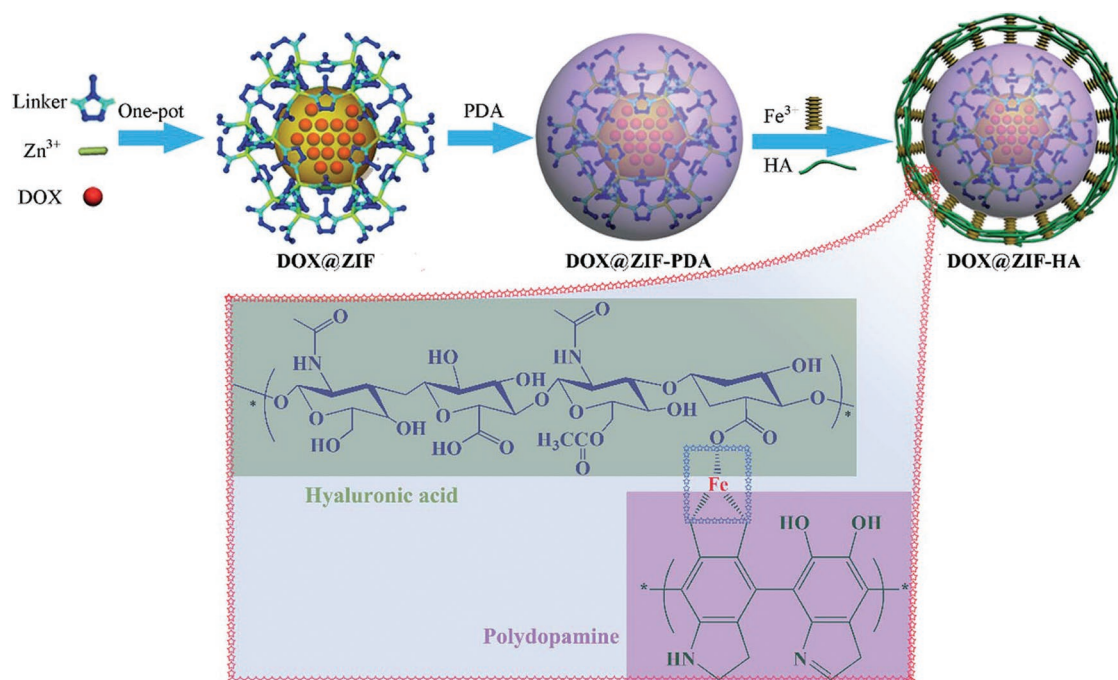


Figure 23. “Mussel-inspired” shell polymerization. Dopamine combining catechol and amine functions in a single molecule mimics the composition of adhesive proteins in mussels and undergoes self-polymerization at pH 8.5. Coordinative binding of Fe^{3+} to catechol hydroxy and carboxy functions in polymers enables external attachment of hyaluronic acid. Reproduced with permission.^[362] Copyright 2018, The Royal Society of Chemistry.

generation of stable, functionalized nanocomposites based on supported shell polymerization. Such a generic strategy was demonstrated to be feasible with UiO-66, ZIF-8, ZIF-67, MIL-96, and MIL-101(Cr).^[364] Here, a random copolymer containing carboxylic acid groups and bromoisobutyrate groups as initiator for atom transfer radical polymerization (ATRP) reactions where initially assembled on the MOF surface by inter-chain hydrogen bonds and weak MOF/polymer interactions

(Figure 24). Then, ATRP with monomers and cross-linkers generated a stably crosslinked shell with exposed polymer chains. Different parameters of the polymer coating such as thickness, functionality and layer sequence can be controlled and the MOF porosity is maintained. It was demonstrated that a 7 nm polystyrene layer generated by this method, protected crystallinity, morphology and porosity of UiO-66 in 1 M sulfuric acid and 1 M sodium hydroxide solution at 50 °C up to 1 day. Due

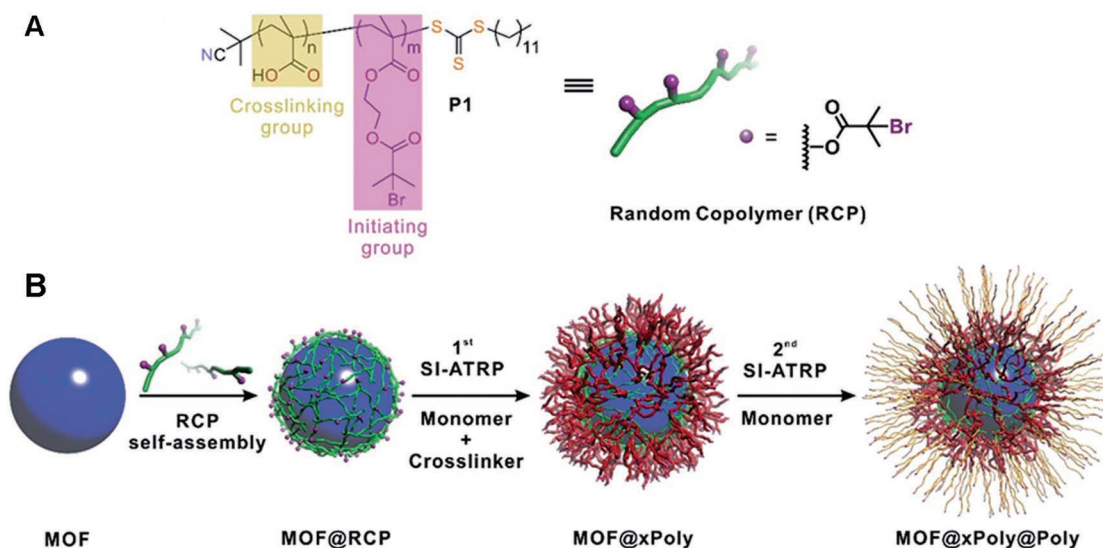


Figure 24. Schematic illustration of MOF functionalization by surface-initiated ATRP. A) Chemical structure of the random copolymer (RCP) initiator. B) Schematic illustration of the approach for supported shell polymerization on MOF particles by ATRP. Reproduced with permission.^[364] Copyright 2019, The Royal Society of Chemistry.

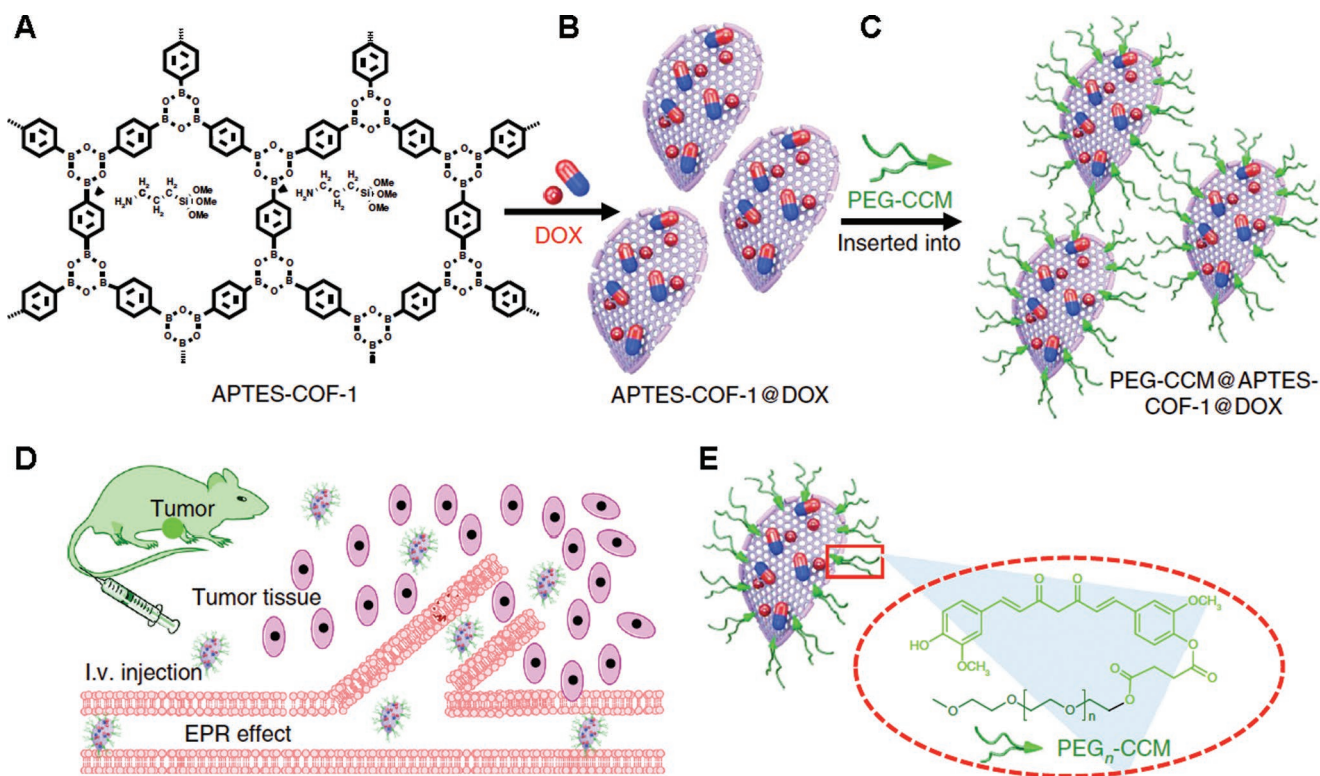


Figure 25. Self-assembled polymer-COF nanocomposite for anticancer drug delivery. Doxorubicin (DOX) loaded amine-functionalized COF-1 (APTES-COF-1) assemble with a PEG-curcumin derivative (PEG-CCM) into water-dispersible nanomicelles. Reproduced under the terms of the Creative Commons CC-BY License 4.0.^[365] Copyright 2018, The Authors. Published by Springer Nature.

to the hydrogen-bond driven self-stabilization of the initially assembled polymer layer, the strategy is suggested to be very flexible and adaptable to different materials.

It has to be mentioned that other strategies for the generation of polymer-functionalized framework nanoparticles exist, which cannot be classified into the categories above. An example is a reported polymer-functionalized COF-based drug carrier which was assembled in an extraordinary nanomicellation process.^[365] Here, the noncovalent integration of PEG-chains was not based on impregnation or absorption onto a preformed nanoparticle scaffold but rather is an essential part of the particle assembly itself. The polymer-COF nanocomposite (PEG-CCM@APTES-COF-1) was generated by self-assembly of a PEG-modified curcumin derivative (PEG-CCM) and amine-functionalized COF-1 (APTES-COF-1). The resulting water-dispersible nanomicelles are built of APTES-COF-1 as the hydrophobic oil-phase and PEG-CCM as surfactant with externally exposed PEG chains (Figure 25). As nanocarriers the nanocomposites exhibited a high DOX loading capacity, strong fluorescence, efficient tumor accumulation and enhanced antitumoral effects compared to free DOX. In vivo imaging and biodistribution studies after injection into mice even demonstrated accumulation in the brain (Figure 26).

The examples illustrate the manifold opportunities of using polymer-modification of reticular framework nanoparticles to tune their properties at the external surface. The changed interaction with a surrounding environment impacts colloidal stability, MRI characteristics, interactions with proteins and

cells or even enable the formation of nanocolloids and strongly influence the in vivo biodistribution.

6.2. Lipid Coating of MOF, ZIF, and COF Nanoparticles

Next to polymer coating, an important strategy for outer surface functionalization of nanoparticles is lipid coating. Specifically, for biomedical applications, it represents a promising technique. To this end, it offers a biocompatible, sometimes even biogenic, surface that impedes premature release of cargo stored in the porous nanoparticle and allows for easy modification for further addition of targeting peptides or other functional groups.^[366] Moreover, it prevents nanoparticles from aggregation and degradation and stabilizes them as colloidal solution.^[367] At the same time, it does not interfere with porosity or structure of the nanoparticle.^[33c] Therefore, a hybrid core that can be functionalized in many different ways (Section 6.1), consisting of MOF, ZIF, or COF nanoparticles combined with the richness of lipids, which may serve for diverse functions (capping system, cargo-release trigger, incorporation of shielding and/or targeting ligands), leads to nanosystems that can fulfil all current requirements in the field of nanomedicine.

In general, two main strategies have been employed for lipid coating of nanoparticles. One relies on direct chemical interaction of lipids and the nanoparticle. The other method is based on lipid self-assembly on the surface of the nanoparticle. In the case of direct chemical interaction of lipids and MOF or ZIF

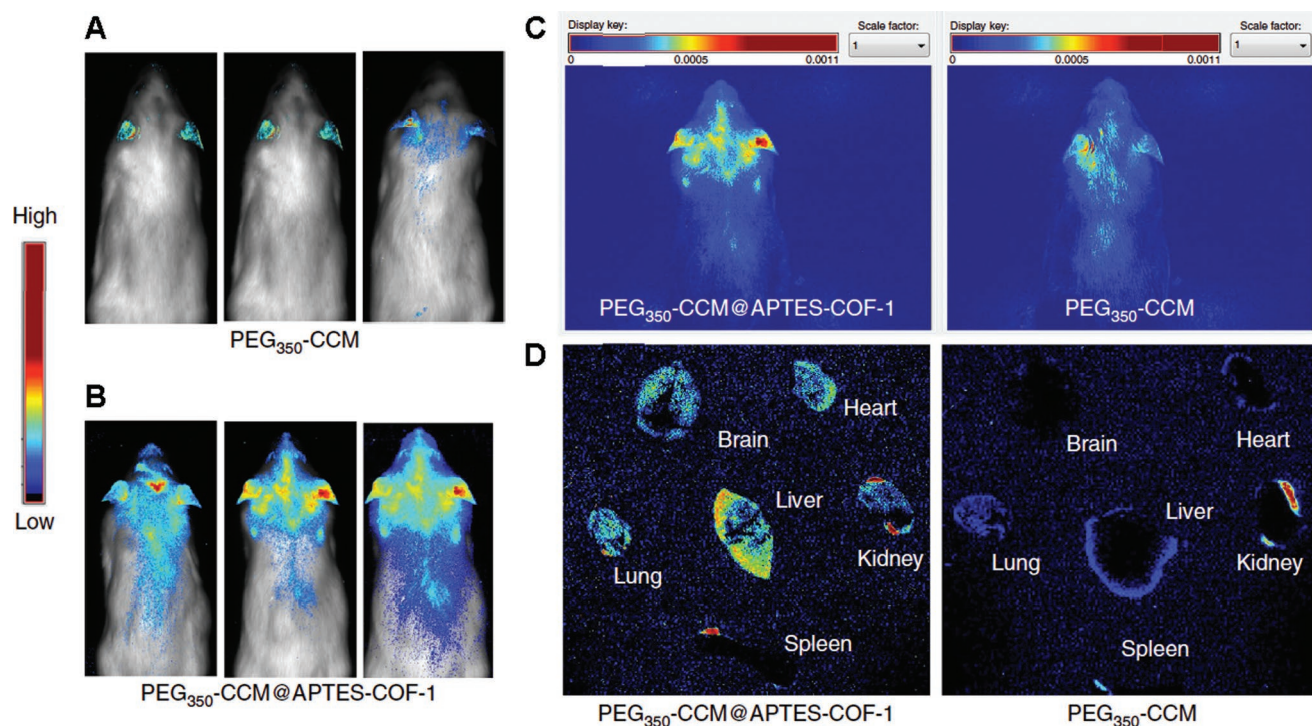


Figure 26. In vivo imaging after injection of PEG-CCM@APTES-COF-1 into mice shows distribution into the brain. Reproduced under the terms of the Creative Commons CC-BY License 4.0.^[365] Copyright 2018, The Authors. Published by Springer Nature.

nanoparticles, the metal sites on the external surface of the nanoparticles can act as reactive group. Ideally, the coordination between lipid and metal is weaker than that of organic building block and metal, which ensures that only the under-coordinated metal sites react with the lipid leaving the nanoparticle's structure intact. If the lipid-metal interaction is stronger than the coordination of the nanoparticle, the nanoparticle may be destroyed, which of course is not desirable. With this method, the lipid 1,2-dioleoyl-*sn*-glycero-3-phosphate (DOPA) has been conjugated to various MOF nanoparticles (UiO-66, UiO-67, and BUT-30) to stabilize them as colloidal material.^[367] Here, the DOPA coordinates to the Zr metal centers in a way that it binds to them, but does not destroy the crystalline network of the MOF. Similarly, a wide range of MOF nanoparticles with different metal building blocks has been coated with 1,2-dipalmitoyl-*sn*-glycero-3-galloyl (DPGG) based on coordination of the galloyl head group to the respective metal.^[368] This complexation is pH-dependent and the described lipid coating can thus be controlled and reversed via the pH.

While direct interaction of lipid and nanoparticle allows for fairly strong binding and control of the lipid density, it is restricted to lipids with functional groups that can interact with the nanoparticle without destroying it, i.e., the interaction has to be weaker than that of organic building block and metal, but strong enough to ensure a stable coating. More flexibility in terms of lipids and metals used is offered by coating techniques based on lipid self-assembly. To this end, two procedures, namely solvent-exchange and lipid fusion, have been adapted from lipid coating of silica nanoparticles to MOF and ZIF nanoparticles.^[369] Solvent exchange is based on a change of solvent from an ethanol/water mixture, which yields lipids as

single molecules or micelles, to pure water, which drives lipid bilayer formation on the surface of nanoparticles.^[370] This has been employed to successfully coat MIL-100(Fe) MOF nanoparticles and later also ZIF nanoparticles (ZIF-4).^[33c,371] For lipid fusion, liposomes are added to nanoparticles and will form around them to yield a substrate-supported bilayer. MIL-88A nanoparticles and Zn- as well as Zr-based coordination polymers^[372] were successfully coated with this approach^[373] and drug loading and release experiments showed that both coating strategies based on self-assembly yield coatings with minimal premature leakage. The fusion method even allows for lipid coating with exosomes (see **Figure 27**).^[366a] These are biogenic liposomes that may facilitate personalized medicine with autologous coatings of nanoparticles. They are present

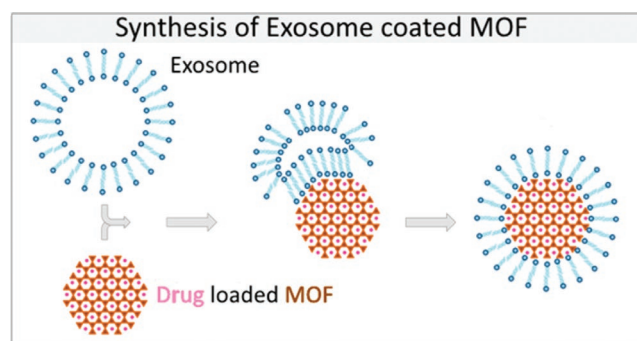


Figure 27. Synthesis scheme for exosome-coating of MOF nanoparticles employing fusion. Exosomes and nanoparticles are incubated together and form an exosome-coated MOF nanoparticle. Reproduced with permission.^[366a] Copyright 2017, American Chemical Society.

in the blood and other body fluids, elude the immune system and are used by cells for communication purposes. In order to facilitate communication between cells, they are able to deliver RNA and proteins from one cell to another. Thus, they represent an autologous delivery system with ideal properties for a biogenic coating of nanoparticles for biomedical applications. When employing the fusion method for exosomes, the membrane is not destroyed and membrane proteins as well as composition stay intact during the process rendering fusion the ideal coating strategy for exosome coating. Another promising approach for biomedical applications, which has been realized with a lipid coating using the fusion method, is combinatorial drug delivery.^[373] This kind of chemotherapy overcomes resistances by application of two (or more) different drugs that yield synergistic effects. In this case, synergistic effects of the delivery of irinotecan and floxuridine could be observed upon concerted delivery in lipid coated MIL-88A nanoparticles.

Recently, combinations of direct chemical reaction and self-assembly have been reported. The first monolayer was deposited onto the nanoparticle via coordination and the second monolayer self-assembled on top of the first layer. With this combination, calcium-zoledronate MOF nanoparticles were coated first with DOPA and in a second step with various lipids, among them a folate-functionalized lipid to yield nanoparticles coated with a lipid bilayer and functionalized with folate as targeting ligand for drug delivery.^[366b] Similarly, Zr-based MOF nanoparticles were first coated with a monolayer of 1,2-dioleoyl-*sn*-glycero-3-phospho-choline (DOPC) based on a Zr-phosphonate interaction followed by self-assembly of a second layer of DOPC yielding a supported lipid bilayer around the nanoparticles for enhanced biostability and cell uptake in biological applications.^[374]

Finally, metal-organic cuboctahedra have also been integrated into lipid bilayers after functionalization with alkoxy-chains for the design of synthetic ion channels.^[375]

All in all, lipid coating of reticular framework nanoparticles yields very promising nanosystems, specifically for biomedical applications. While the currently existing studies show their great potential mainly *in vitro*, their promise for applications has to be investigated *in vivo* and there are many future directions that need to be explored, such as the effect of different types of lipids, the immune-eluding effects of exosome coatings and many more.

7. Toxicity of Reticular Nanoparticles

Similar to any synthetic material, the safety of nanoscale reticular frameworks has to be assessed carefully. Especially in case of intended biomedical applications, knowledge of potential threat to life and physical conditions are indispensable to enable safe usage. Due to the complex interplay of different processes contributing to toxicity and adverse effects, a definite rating of nanosafety and the comparison of literature data is difficult. One key challenge for the identification of structure-toxicity relationships and the reproducible production of safe nanomaterials is the complete understanding of a generally very complex system. The fundamental basis is the thorough material characterization;^[61a] otherwise, the obtained results cannot be

attributed to a certain property of the nanomaterial.^[376] It is essential to characterize the physicochemical properties of a nanoparticle suspension, such as chemical composition, size, shape, surface, charge, coating, dispersion, agglomeration, aggregation, concentration, and matrix.^[61a] However, these properties can change in biological environment; interactions at the biointerface, protein adsorption and degradation, are additional parameters which impact the behavior in biological systems. In this respect, a focus should lay on the characterization of the “protein corona” as it critically impacts the properties of nanoparticles and nanosafety.^[377] We suggest a classification of the properties of reticular framework nanoparticles on different levels, which all have to be addressed during the material characterization:

- 1) *Physical identity*: the basic physical/chemical core of the nanoparticle
- 2) *Synthetic identity*: engineered surfaces and coatings
- 3) *Biological identity*: biological corona

Likewise, adverse effects and toxicity of reticular framework nanoparticles have to be considered on different levels. Due to the modular assembly of reticular nanomaterials, degradation into the building units and their individual biological tolerabilities have to be investigated. In the case of MOF nanoparticles, the metal toxicity is an obvious concern and led to the predominant utilization of better tolerated metal species, such as iron, zinc and zirconium, for biomedical applications. In the *in vivo* situation, characteristics of nanoparticles, which are beneficial for specific therapeutic or diagnostic strategies, such as the ability to cross biological barriers, can also be the reason for severe adverse reactions.^[378] Knowledge about the pharmacokinetics of administered nanoparticles, their circulation, biodistribution and elimination, are essential for the safety assessment. Moreover, interactions at the biointerface such as protein adsorption and aggregation change the properties of nanoparticles and can result in unanticipated effects.^[377a] **Box 3** gives an overview over essential parameters for a safety assessment of reticular framework nanoparticles.

Box 3. Key parameters affecting biosafety of reticular framework nanoparticles

- 1) Cyto- and genotoxicity of framework nanoparticles on different cell types.
- 2) Degradability of the frameworks and toxicity of individual building units.
- 3) Interactions at the biointerface, protein adsorption and aggregation in biological fluids.
- 4) Pharmacokinetics of nanoparticles and framework components (circulation, crossing of biological barriers, tissue/organ accumulation, and elimination).

In vitro studies represent a first step to understand the biological effects on the cellular level.^[379] Since, the identification of toxic effects can vary in different cell lines, an evaluation in different models and their selection with respect to the intended application is required.^[380] Systematic evaluations of

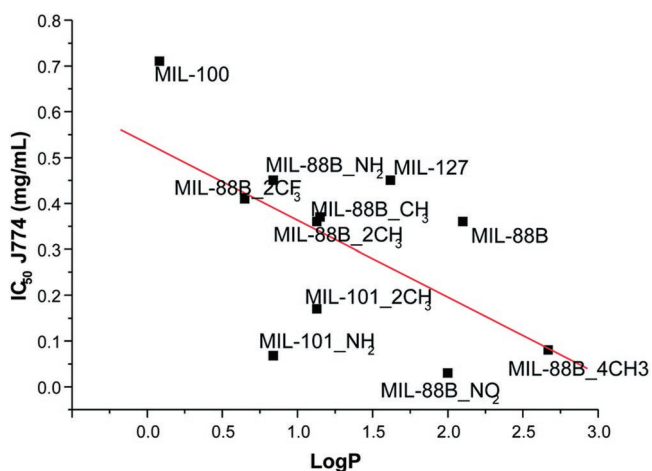


Figure 28. IC₅₀ values of MOF nanoparticles in J774 cells and log P values of contained organic linkers. Reproduced with permission.^[381] Copyright 2014, The Royal Society of Chemistry.

MIL-100(Fe, Al, Cr) nanoparticles in lung (A549 and Calu-3) and hepatic (HepG2 and Hep3B) cell lines revealed a generally good cellular tolerability. Only MIL-100(Fe) mediated observable cytotoxic effects to the hepatocarcinoma cell line Hep3B at high concentrations, presumably due to low expression of the “guardian of the genome“ protein p53.^[380a] A detailed systematic cytotoxicity evaluation of fourteen porous MOFs based on different metal species (Fe, Zn, and Zr) and carboxylates or imidazolates (MIL-100(Fe), MIL-101_NH₂, MIL-101_2CH₃, MIL-88A, MIL-88B_4CH₃, ZIF-8, MIL-88B_CH₃, MIL-88B_2CH₃, MIL-88B_2CF₃, MIL-127, UiO-66, MIL-88B, MIL-88B_NH₂, and MIL-88B_NO₂) has been carried out.^[381] The effect of the MOF nanoparticles on human cervix carcinoma HeLa and murine macrophage J774 cells were assessed by MTT assay and indicated a rather low toxicity in general. Differential cytotoxicity values were mainly attributed to 1) the metal species, with Fe-based MOFs being less toxic than Zr- or Zn-MOFs; 2) the hydrophobic–hydrophilic balance of the organic linker, with a tendency of increasing toxicity with increasing log P (Figure 28); and 3) the faster internalization of MOF nanoparticles into J774 macrophages, which favors toxic effects.

In a combined in vitro (human hepatoma HepG2 and human breast cancer MCF7 cells) and in vivo (zebrafish embryos) evaluation, the toxicity of 16 archetypal nanoscale MOFs was assessed: MIL-100 [Fe₃O(H₂O)₂Cl(btc)₂] (btc: 1,3,5-benzenetricarboxylic acid), MIL-101 [Fe₃Cl(H₂O)₂O(NH₂-bdc)₃] (NH₂-bdc: 2-aminobenzene-1,4-dicarboxylic acid), MOF-5 [Zn₄O(bdc)₃] (bdc: 1,4-benzenedicarboxylic acid), and MOF-74 [M₂(dhbdc)] (M: Zn(II), Cu(II), Ni(II), Co(II), Mn(II), and Mg(II); dhbdc: 2,5-dihydroxy-1,4-benzenedicarboxylic acid), ZIF-7 [Zn(Ph-im)₂] (Ph-im: benzylimidazole), ZIF-8 [Zn(Me-im)₂] (Me-im: 2-methylimidazole), UiO-66 [Zr₆O₄(OH)₄(bdc)₆], UiO-66-NH₂ [Zr₆O₄(OH)₄(NH₂-bdc)₆], UiO-67 [Zr₆O₄(OH)₄(bpdcc)₆] (bpdcc: biphenyl-4,4'-dicarboxylic acid), HKUST-1 [Cu₃(btc)₂], NOTT-100 [Cu₂(bptc)] (bptc: 3,3',5,5'-biphenyl-tetracarboxylic acid).^[382] Zebrafish embryos represent useful first in vivo models and have been used for the evaluation of several nanomaterials since their biology is comparable to mammalian systems and the process steps can be integrated into high-throughput

screenings.^[383] The study also investigated the stability of all nanoscale MOFs in culture medium containing 10% fetal bovine serum at 37 °C for 24 h. Change of the crystal structure was assessed by PXRD and the amount of released metal ions in the supernatant estimated by inductively coupled plasma-optical emission spectrometry (ICP-OES). Table 3 summarizes the effects of serum containing medium on the MOF nanoparticles.

In these toxicity studies, a strong correlation between the cellular in vitro experiments and zebrafish embryo in vivo results were found (Table 4). Mg-MOF-74 exhibited lowest toxicity in both test systems, the highest toxicity was found with Cu(II)-based HKUST-1 nanoparticles. It is suggested that the released metal ions from degraded MOF nanoparticles strongly determine the toxicity of these nanomaterials.

Acute systemic in vivo toxicity of iron(III) carboxylate MOF nanoparticles (MIL-88A with hydrophilic fumarate linker, MIL-100 with hydrophilic aromatic trimesate linker, MIL-88B_4CH₃ with hydrophobic aromatic tetramethylterephthalate linker) was assessed in Wistar female rats.^[26b] Doses of 220 mg kg⁻¹ (MIL-88A, MIL-100) and 110 mg kg⁻¹ (MIL-88B_4CH₃) were injected and animal behavior, body and organ weights and serum parameters were evaluated up to three months after administration. No significant differences to control groups were observable, except a slight increase in the spleen and liver weights, which normalized one to three months after injection and correlates with a temporary accumulation of the unshielded nanoparticles in these major organs of the mononuclear phagocyte system. No signs of immune or inflammatory reactions were detected. In addition, in vivo subacute toxicity was evaluated by repeated injection of MIL-88A at doses of up to 150 mg kg⁻¹ per day at four consecutive days. Here, no significant toxic effects could be observed up to ten days after the administration indicating good biological tolerability. In a detailed biosafety study, the biodistribution, metabolism and excretion of iron(III)-based MIL-100, MIL-88A and MIL-88B_4CH₃ was assessed after injection of high doses up to 220 mg kg⁻¹ into Wistar rats.^[384] The long-term biodistribution was investigated between 1 and 30 days postinjection by determining the concentration of iron in liver, spleen, lung, bone marrow, heart kidney, brain, serum, urine, and feces as well as the organic linkers in liver and spleen. Iron was quantified by atomic absorption spectroscopy (AAS), and the linker concentrations were determined by a specifically developed tissue extraction and high performance liquid chromatography (HPLC) protocol.^[385] Interestingly, all iron carboxylate MOFs mediated lower serum iron concentration compared to the control group one day following intravenous administration. This presumably is the result of an endogenous hyperferitinemia compensation mechanism which persists for some time after remission of the transient iron overload. At the same time iron levels remarkably increased in several organs, such as liver spleen, lung and bone marrow. One day after injection, 26% (MIL-88A), 27% (MIL-100), and 43% (MIL-88B_4CH₃) of injected iron content accumulated in the liver. The highest hepatic iron concentration of 1750 mg g⁻¹ resulted from injections with MIL-88B_4CH₃ nanoparticles. In all cases, hepatic iron levels decreased progressively below 4% of the injected dose between one to seven days. Due to the nanoparticle degradation, iron can be eliminated and 40–47% of the injected dose

Table 3. Degradation of NanoMOFs in culture medium containing 10% fetal bovine serum (FBS). Reprinted with permission from Ruyra et al.^[382] Published 2014 by Wiley-VCH.

nanoMOF	$[M_s] [\times 10^{-6} \text{ M}]^a$	Deg _{min} [%] ^b	XRPD analysis
UiO-67	215.6 ± 6.3	0.3 ± 0.0	Amorphous
MIL-100	316.2 ± 46.1	1.1 ± 0.2	Stable
MIL-101	310.4 ± 90.1	1.1 ± 0.3	Amorphous
UiO-66	1099.8 ± 105.3	1.8 ± 0.2	Stable
UiO-66-NH ₂	1567.5 ± 183.1	2.6 ± 0.3	Stable
ZIF-7	448.5 ± 23.4	4.5 ± 0.2	Stable
MOF-5	3108.6 ± 634.1	7.8 ± 1.6	New crystalline species
Mn-MOF-74	2651.4 ± 73.6	13.3 ± 0.4	Loss of crystallinity; new Crystalline species (MnCO ₃)
Co-MOF-74	3258.1 ± 58.8	16.2 ± 0.3	Loss of crystallinity
ZIF-8	1916.2 ± 75.4	19.1 ± 0.8	Stable
Zn-MOF-74	5442.6 ± 130.6	27.2 ± 0.5	Stable
HKUST-1	9168.6 ± 137.5	30.3 ± 0.5	Loss of crystallinity
Ni-MOF-74	7014.3 ± 174.9	35.1 ± 0.9	Stable
NOTT-100	7967.5 ± 152.8	39.4 ± 0.8	Loss of crystallinity
Cu-MOF-74	9556.8 ± 689.9	47.9 ± 3.4	Loss of crystallinity
Mg-MOF-74	12573.7 ± 273.9	62.9 ± 1.4	Loss of crystallinity

^a)The concentration of the corresponding metal ions solubilized after the incubation of each nanoMOF at 37 °C for 24 h was determined by ICP-OES; ^b)The minimum percentage of degradation (deg_{min} (%)) was calculated as follows: deg_{min} (%) = $([M_s] \cdot V \cdot S) / n_{\text{MOF}}$, where V is the volume of DMEM, S is the stoichiometric ratio of nanoMOF to metal ion, and n_{MOF} is the number of moles of initial nanoMOF.

was accordingly detected in urine and feces. Between 7 and 15 days, iron excretion was very low which might indicate return to iron homeostasis already within 2 weeks. The quantification of organic linkers in liver and spleen one day after administration correlated with the determined iron levels, which confirms the accumulation of framework nanoparticles. Notably, the clearance of the organic linkers turned out to be totally different: 90% of injected trimesate was rapidly removed by urine one day after the injection, whereas excretion of tetramethylterephthalate required more than 4 days. Presumably, the more hydrophobic tetramethylterephthalate linker is excreted more slowly due to its lower solubility compared to trimesate. Only traces of fumaric acid were detected in the urine, since the linker is an endogenous molecule and essential component of the Krebs cycle. Importantly, the quantification of organic linkers

Table 4. Qualitative comparison of in vitro cellular and in vivo zebrafish embryo toxicity of nanoscale MOFs. Reprinted with permission from Ruyra et al.^[382] Published 2014 by Wiley-VCH.

Grade of toxicity	In vitro	In vivo
–	nanoMg-MOF-74, nanoCoMOF-74, nanoUiO-66 and nanoUiO-67	(0) nanoMg-MOF-74
+		1) nanoCoMOF-74, nanoUiO-66 and nanoUiO-67
++	nanoMIL-100, nanoZIF-7 and nanoMIL-101	2) nanoMIL-100 and nanoZIF-7
+++	nanoZIF-8	3) nanoZIF-8 and nanoMIL-101
++++	nanoHKUST-1	4) nanoHKUST-1

in biological specimen did not reveal any metabolites which suggests direct elimination without metabolic transformation. The detailed study illustrates the advantages of reticular framework nanoparticles which can degrade into their separate components and be cleared from the human body.

Finally, it has to be pointed out that with the myriads of bio-nano publications and steadily increasing number of nanomaterials (reticular frameworks and others), an objective comparison of biological data and estimation of safe medical utilization is complicated and the fundamental key challenge for the future success of nanoscience. Frequently, studies are difficult to compare due to lack of sufficient nanomaterial characterization and arbitrary experimental conditions. Guidelines of “Minimum information reporting in bio-nano experimental literature” (MIRIBEL) were suggested and it is strongly encouraged to adhere to the minimal set of obligatory standardized information, which have to be provided in publications, in order to ensure transparency and reproducibility in nanobiomedicine.^[376b,386]

8. Applications

Reticular nanoparticles are employed in various areas, including gas storage and separation, catalysis, energy conversion/storage, (opto-)electronics as well as drug delivery and theranostics. In the following section, we give a brief introduction and overview on the most recent developments in the chosen fields of heterogeneous catalysis, the application of reticular nanoparticles as tool in biotechnology, as well as their application in the field of biomedicine, i.e., sensing, diagnosis and therapy.

8.1. Therapy

Nanoparticles, small enough to circulate in the blood stream and able to cross biological barriers, are attractive devices for innovative therapeutic approaches. Here, both the unique pharmacokinetic and pharmacodynamic characteristics of nanomaterials can conduct specific tasks in the human body. Nanoparticles without intrinsic pharmacological activity but the ability to bind or encapsulate therapeutic molecules can serve for the purpose of drug delivery (drug carriers). Nanoparticles can also exhibit intrinsic biointeraction or activity to be used in a therapeutic fashion independent of encapsulated drugs (therapeutic nanoparticles). Reticular framework nanoparticles, MOFs, ZIFs, and COFs, have demonstrated high potential for the application as nanopharmaceuticals—both including drug carriers and therapeutic nanoparticles. **Box 4** gives explanations of the differential definitions.

Box 4. Definitions of Nanopharmaceuticals

Pharmacokinetics (PK) describes the collective processes which affect the spatiotemporal distribution, transformation and persistence of a pharmacological agent in an organism. These processes include the absorption, distribution, metabolism and excretion (ADME) of the drug. Pharmacokinetic characteristics of drugs depend on the individual molecular structures and cannot be changed without derivatization.

Drug carriers are nanosized objects which can be loaded with pharmacologically active agents. By changing the physicochemical properties (size, shape, charge, hydrophilicity) and specific biointeractions, the PK of drug carriers can be tuned. This enables control over the biodistribution of incorporated drugs without need for derivatization and without effects on the pharmacological activity.

Therapeutic nanoparticles are considered as materials with specific therapeutic activity independent of incorporated drug molecules. Similar to drug carriers, the PK of therapeutic nanoparticles can be tuned.

8.1.1. Reticular Framework Nanoparticles as Drug Carriers

Reticular framework nanoparticles are top candidates for the utilization as drug carriers. Key advantages for this purpose are summarized in **Box 5**.

Box 5. Advantages of reticular framework nanoparticles as drug carriers:

- 1) high porosity and surface area providing high drug loading capacities,
- 2) possibility to tune the inner surface enabling control over host–guest interactions and a triggered drug release,
- 3) possibility to functionalize the external surface enabling control over the interactions at the biointerface and pharmacokinetics, and
- 4) ability to disassemble and degrade into the molecular building units.

The selection of suitable carrier material strongly depends on the therapeutic cargo to provide adequate drug loading and release and the target tissue to achieve adequate pharmacokinetics. In context of therapeutic nanoparticles, reticular frameworks benefit from their modular structure and assembly. Therapeutic entities which are able to assemble (alone or in combination with other building units) into MOFs, ZIFs, or COFs can be the basis for therapeutic reticular framework nanoparticles. In the following, the key parameters of reticular frameworks for utilization as nanopharmaceuticals are discussed.

8.1.2. Drug Loading

MIL-100(Fe) and MIL-101_{NH₂}(Fe) MOFs have been extensively studied as drug carriers due to their very high surface area (3100–5900 m² g⁻¹) and giant pores (25–34 Å) which can be loaded by soaking in saturated drug solutions.^[295] MIL-100(Fe) nanoparticles can load up to 25% of the anticancer drug busulfan, 21% of the antiretroviral therapeutic azidothymidine triphosphate, 16% of the antiviral drug cidofovir, 33% of the analgetic ibuprofen, 24% caffeine, 69% urea and over 60% of the aminoglycoside antibiotic gentamycin.^[295,387] MIL-101 reaches efficiencies of 42% loading of the antiviral drugs azidothymidine triphosphate and cidofovir.^[295] Depending on the individual drug molecules, the liberation follows individual kinetics with sustained release up to several days (**Figure 29**).

The differential release can be explained by different interactions between individual drugs and the MOF surface. The kinetic analysis of uptake and release of fluorescein, as a model compound, into MIL-100(Fe) and MIL-101(Cr) nanoparticles revealed that the loading and release is not only driven by diffusion through an inert porous matrix.^[309] The mass transport can be dissected into three processes (**Figure 30**): external diffusion, retarded intracrystalline diffusion and adsorption/desorption to/from the internal MOF surface. Due to the impact of the adsorption rates the loading and release of MOF nanoparticles is dominated by their surface properties. For this reason,

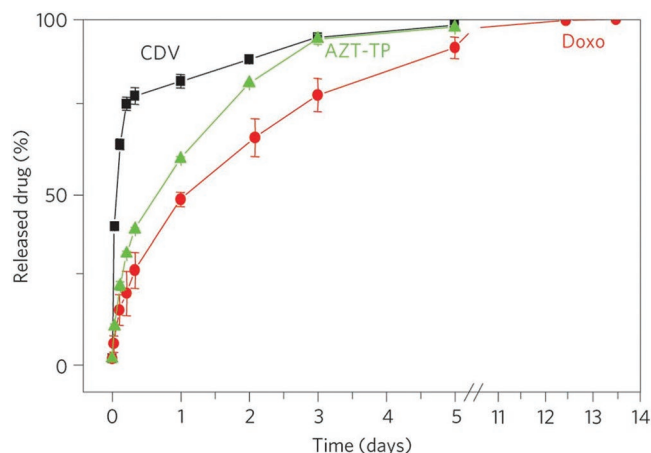


Figure 29. Drug release kinetics from MIL-100 nanoparticles at 37 °C in PBS. CDV, cidofovir (black); AZT-TP, azidothymidine triphosphate (green); Doxo, doxorubicin (red). Reproduced with permission.^[295] Copyright 2009, Springer Nature.

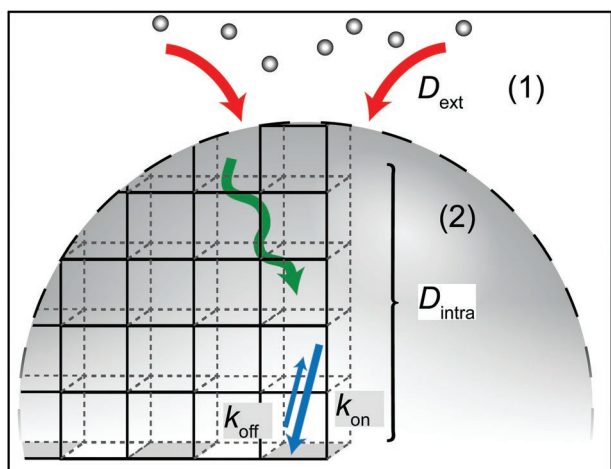


Figure 30. Mass transport during loading of MOF nanoparticles: 1) external diffusion toward the nanoparticles, and 2) concurrent intracrystalline diffusion and adsorption/desorption to/from the internal surface. Reproduced under the terms of the Creative Commons CC-BY 4.0 License.^[309] Copyright 2017, The Authors. Published by MDPI.

the time-resolved fluorescence studies revealed fundamentally different release characteristics of fluorescein from the two MOF species: MIL-100(Fe) showed a strongly pH dependent release with significantly increasing liberation with rising pH,

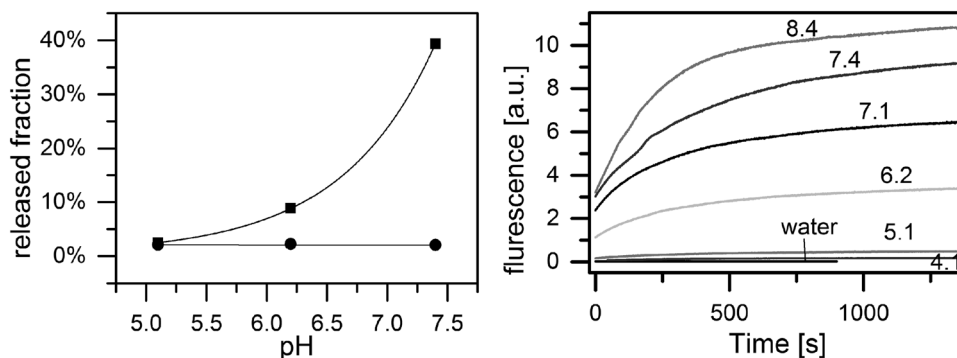


Figure 31. Left: Fraction of fluorescein released from MIL-100(Fe) (squares) and MIL-101(Cr) (circles) nanoparticles after 90 min at different pH values. Right: Time-dependent fluorescein release from MIL-100(Fe) nanoparticles at different pH values. Reproduced under the terms of the Creative Commons CC-BY 4.0 License.^[309] Copyright 2017, Preiß et al. Published by MDPI.

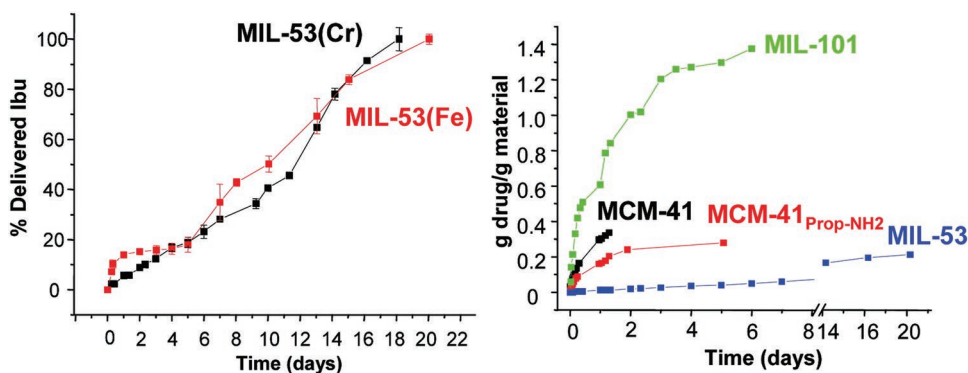


Figure 32. Ibuprofen release profiles from different MOF species. The linear drug release from the flexible MIL-53(Cr, Fe) over time represent a zero-order kinetic in contrast to higher orders and faster release in case of MIL-101 or MCM-41. Reproduced with permission.^[178] Copyright 2008, American Chemical Society.

whereas MIL-101(Cr) did not release fluorescein (<3%) at any pH between pH 5 and 7.4 (Figure 31).

Moreover, it was shown that repeated soaking of MIL-100(Fe) in diluted solutions of the anticancer drug topotecan leads to an entrapment in the porous matrix by a “ship-in-bottle-mechanism.”^[388] Topotecan is initially soaked from the diluted drug solutions and penetrates into the MOF nanoparticles. The repeated procedure increases the payload which triggers association processes. Around 12 drug molecules are hosted within the same large cages of MIL-100(Fe) as aggregates. A loading efficiency of almost 12% can be achieved and the internal aggregates even stabilize the carrier against degradation and burst release in PBS.

Flexible MOF architectures that change their pore size upon adsorption of guest molecules can mediate particularly interesting release profiles due to “breathing” or “swelling” effects.^[178] The two flexible MOFs MIL-53(Fe) and MIL-53(Cr) can load ibuprofen up to 20% which strongly interacts with the framework via its -COOH and -OH groups and causes an adaption of the pore size. The ibuprofen loaded MOFs demonstrated an extraordinary zero-order release kinetic over three weeks in simulated body fluid (SBF) at 37 °C (Figure 32, left). In contrast, the high drug capacity MOF MIL-101 releases its payload within 3 to 6 days under the same conditions (Figure 32, right).

The careful selection of a suitable reticular framework nanomaterial and the knowledge about specific drug-carrier interactions

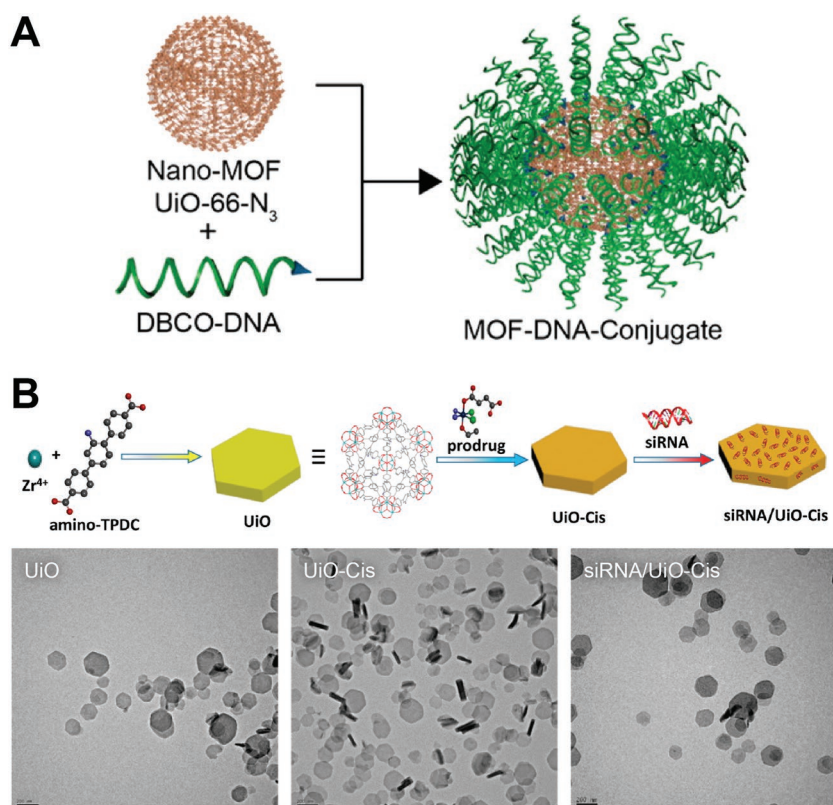


Figure 33. Examples of biomolecules attached to the external surface of MOF nanoparticles. A) Covalent conjugation of DNA strands to azide-containing UiO-66 via strain-promoted azide-alkyne cycloaddition. Reproduced with permission.^[389b] Copyright 2014, American Chemical Society. B) siRNA binding to the surface of amine-containing UiO-68. Reproduced with permission.^[389a] Copyright 2014, American Chemical Society.

are crucial to optimize the loading and release characteristics for an intended therapeutic application.

A trivial prerequisite for postloading of therapeutic molecules into the internal porous matrix of reticular frameworks is an adequate pore size. It has been impressively shown that MOFs with large pore-apertures (>32 Å) can be generated by expansion of the organic linkers.^[143] By this strategy pore apertures are reached that even proteins can enter. Alternative strategies for the loading of large biomolecules, such as nucleic acids or proteins, onto reticular framework nanoparticles with smaller pores are attachment to the external surface^[357,389] (Figure 33) or internal embedding during framework synthesis^[390] (Figure 34).

8.1.3. Biodistribution

As discussed before, the possibility to tune the biodistribution of nanoparticles is a key motivation for their utilization as drug carriers. A generally supposed characteristic of colloidal stable and well-shielded nanoparticles is an accumulation in tumors due to leaky vasculature and the enhanced permeability and retention (EPR) effect.^[391] In recent time, a critical reassessment of the EPR effect regarding its universality has taken place.^[392] At least in specific types of leaky tumors an

accumulation of nanoparticles seems to be evident and can be relevant for drug carriers based on reticular framework nanoparticles. Biodistribution studies in rats revealed that MIL-100(Fe) nanoparticles exhibit a predominant accumulation in the liver and to some extent in the spleen within 24 h after intravenous injection, which is a common behavior of nanoparticles.^[393] It seems that the MOF nanoparticles form a depot in the blood stream during the first hours before being cleared predominantly via the kidney and urine. A specific organ accumulation was reported for MIL-100(Fe) nanoparticles based on a pH-induced aggregation at physiological pH.^[394] MIL-100(Fe) nanoparticles are colloidally stable at pH < 6.5 but begin to aggregate after injection into the blood stream (Figure 35). The agglomerated nanoparticles are retained in small capillaries and accumulate in the lung. Disaggregation and release of loaded gemcitabine monophosphate (GMP) within 24 h caused a significantly reduced number of lung metastasis.

A remarkable example of active targeting to the bone has been achieved with gelatin nanocapsules generated with ZIF-8 as nanotemplates and functionalized with the Ca²⁺ binding bisphosphonate alendronate.^[395] Simvastatin (SIM) was loaded into ZIF-8 during the particle formation in methanol (Figure 36, left). In order to increase the hydrophilicity and dispersibility in aqueous solution, the surface of SIM@ZIF-8 nanoparticles

was modified with a shell of tannic acid (TA) by coordinative interaction with exposed zinc ions. The SIM@ZIF-8 nanoparticles were then coated with dopamine- (catechol-) modified gelatin (GelC). After removal of the ZIF-8 template with EDTA, SIM@GelC nanocapsules were obtained which were further modified with alendronate via Michael addition and Schiff base reactions between the amine and catechol groups. Biodistribution studies in rats demonstrated that nanocapsules without alendronate accumulated mainly in liver and lungs after intravenous injection (Figure 36, right). In contrast, alendronate targeted nanocapsules showed decreased retention in liver and lung and ≈2.5-fold increased accumulation in the bone.

8.1.4. Dynamic Drug Release

Consistent with Paul Ehrlich's envisioned "magic bullet" concept, drug concentrations are desired to be high at the target site and low at off-target sites. This can be achieved by the controlled biodistribution and target-specific accumulation of the drug carriers. In addition, the controlled release of the therapeutic cargo in the right place at the right time can result in increased effective drug levels at the target site. This requires a dynamic release mechanism which can be triggered by external stimuli.^[396] Commonly used triggers for a responsive drug

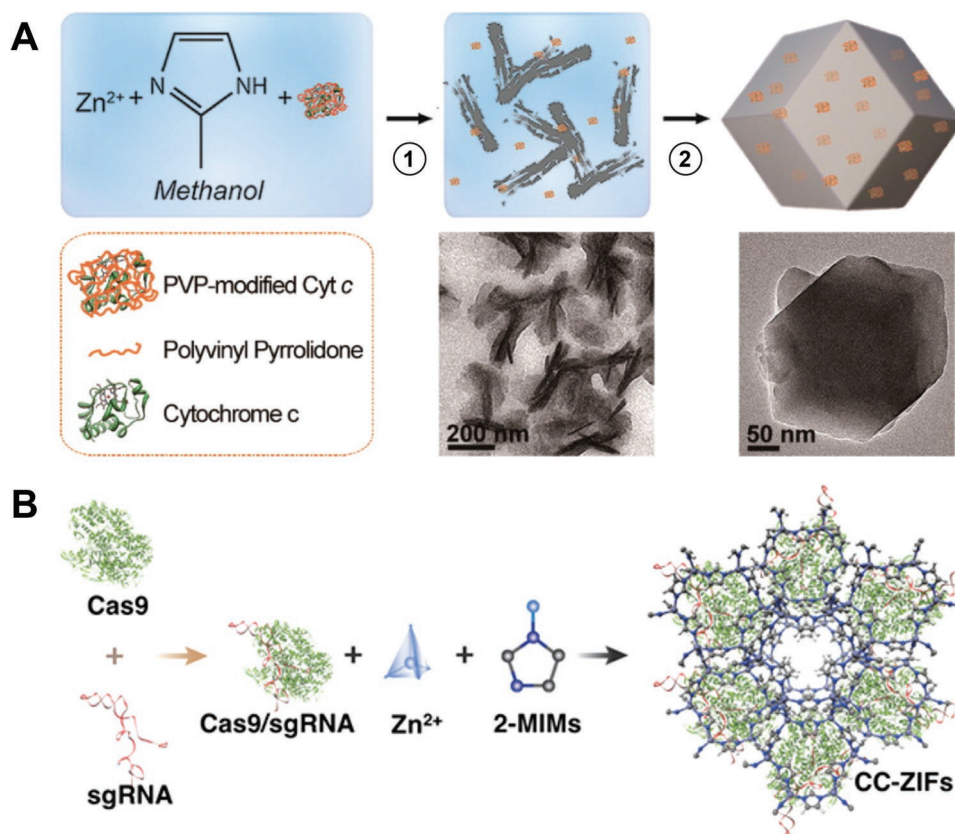


Figure 34. In situ embedding of proteins into ZIF-8 during particle formation. A) Embedment of cytochrome c (Cyt c) is achieved by addition of a Cyt c and polyvinylpyrrolidone (PVP) solution to a methanolic zinc nitrate hexahydrate and 2-methylimidazole solution. Zn^{2+} and 2-methylimidazole first assemble into rods (1) and then form rhombic dodecahedron crystals after 24 h (2). Reproduced with permission.^[390c] Copyright 2014, American Chemical Society. B) Negatively charged Cas9/sgrRNA ribonucleoproteins are embedded into positively charged ZIF-8 by addition of 2-methylimidazole followed by zinc nitrate. After 20 min, cubic ZIF-8 crystals with an average size of 100 nm (TEM) are formed which are suitable for intracellular delivery of the genome editing complex. Reproduced with permission.^[390a] Copyright 2018, American Chemical Society.

release are pH, redox potential, temperature and light. Here temperature and light generally represent externally controlled stimuli, while pH and redox potential can depend on the bioenvironment. Examples for pH-dependent drug-MOF interactions

and loading/release characteristics have been discussed above. Beyond that, pH-triggered drug release can be realized by pH-dependent carrier disassembly. ZIF-8 is one of the most frequently used MOF and ZIF architectures with pH-sensitive

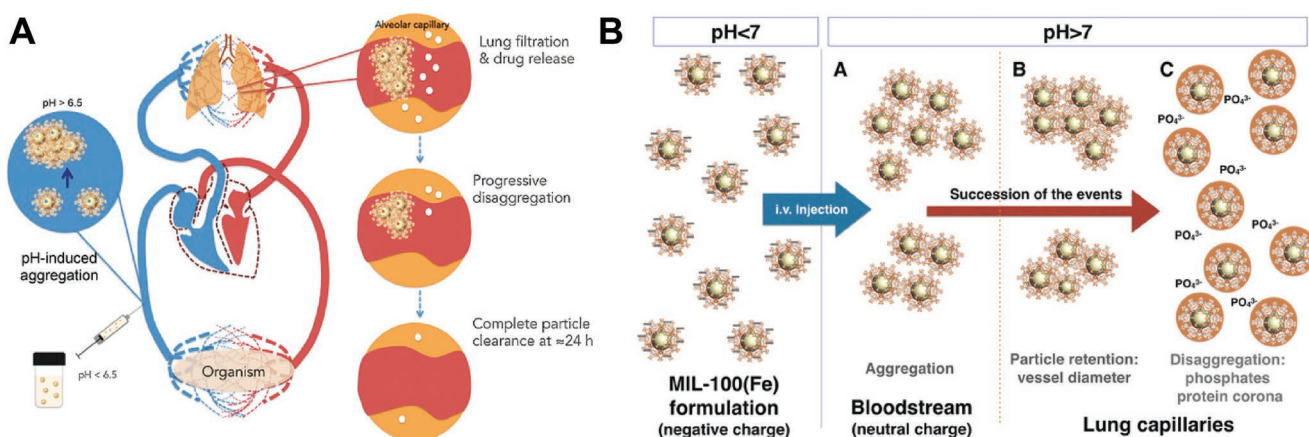


Figure 35. Passive targeting of MIL-100(Fe) to the lung by pH-dependent aggregation. A) A MIL-100(Fe) suspension colloiddally stable below pH 6.5 is administered systemically into the blood stream. The physiological pH causes aggregation and lung accumulation. The particles disaggregate and release their payload within 24 h. B) Detailed illustration of the pH dependent aggregation and lung accumulation in vivo. Phosphate coordination and protein adsorption mediate the progressive disaggregation & drug release. Reproduced with permission.^[394] Copyright 2017, Wiley-VCH.

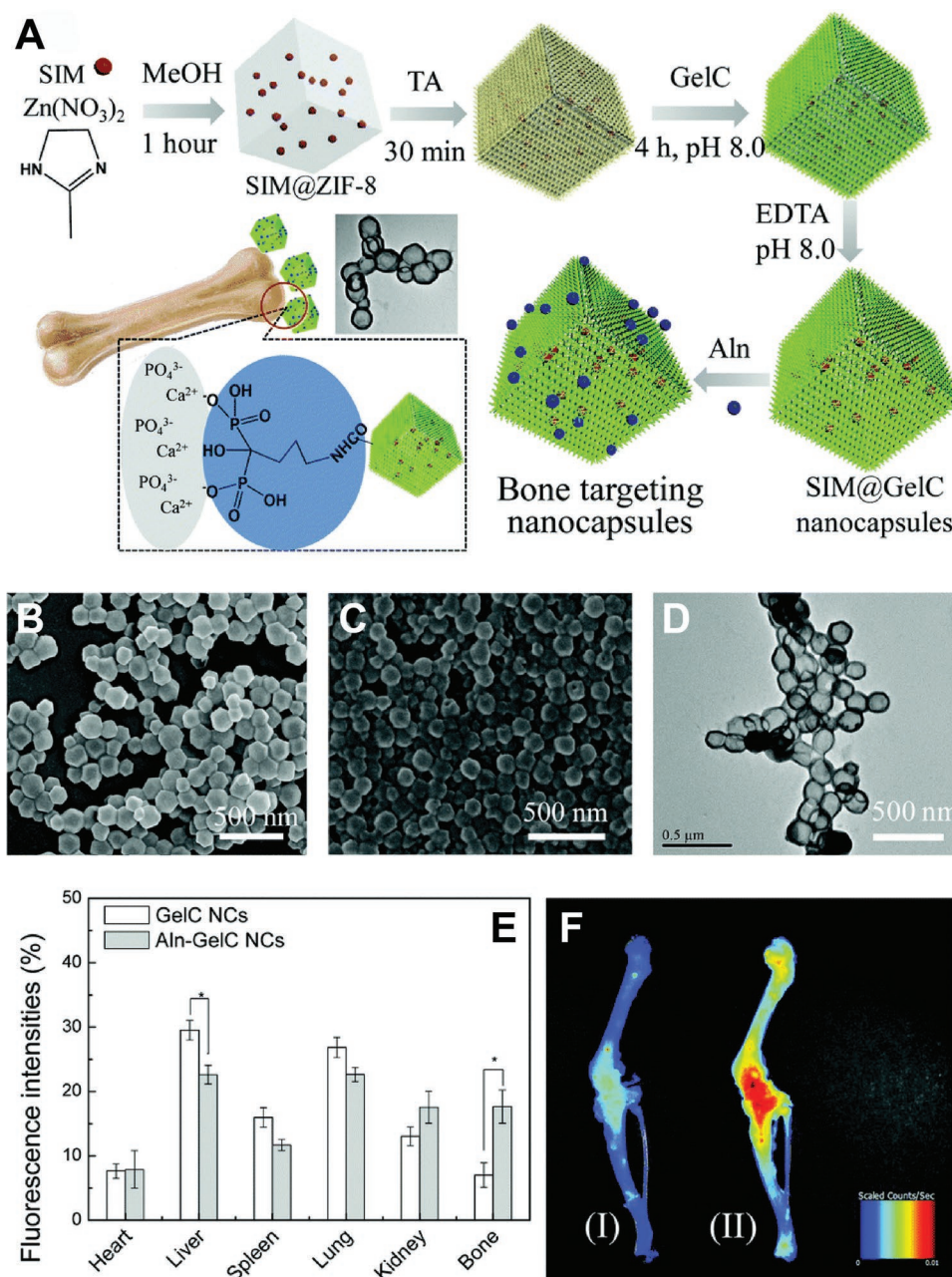


Figure 36. Bone-targeted gelatin nanocapsules generated with ZIF-8 nanotemplates. A–D) Illustration of the nanocapsule synthesis process. Simvastatin is encapsulated into ZIF-8 during synthesis in methanol; SIM@ZIF-8 particles are coated with tannic acid (TA) for improved dispersibility in aqueous medium; a layer with catechol-modified gelatin (GelC) is formed around SIM@ZIF-8; ZIF-8 template is removed with EDTA to obtain SIM@GelC nanocapsules; bone-targeting alendronate (Aln) is attached by Michael addition and Schiff base reaction. E, F) Biodistribution of untargeted (GelC) and alendronate-targeted (Aln-GelC) nanocapsules determined by near-infrared imaging. Reproduced with permission.^[395] Copyright 2017, The Royal Society of Chemistry.

degradation and drug release.^[390a,397] ZIF-8 has a high capacity for the anticancer drug 5-fluorouracil (5-FU) of ≈ 660 mg 5-FU/g ZIF-8. Since the pH in tumors is generally more acidic than in normal tissue, the pH-triggered disassembly of ZIF-8 is an attractive approach to achieve high concentrations of the anticancer drug at the target site. Differential redox potential mediated by elevated levels of glutathione (GSH) is generally used as a trigger for the site-specific drug release in the tumor

tissue or in the intracellular environment.^[398] Redox-sensitive drug release can be achieved by using disulfide-containing organic linkers, which are cleaved in a reducing environment. For this purpose, dithiodiglycolic acid or 4,4'-dithiobisbenzoic acid (DTBA) were used as dicarboxylic acid linkers in MOF nanoparticles (Figure 37).^[399] In the reducing environment containing elevated glutathione levels, the disulfide-linkers are cleaved and the MOF scaffold degraded.

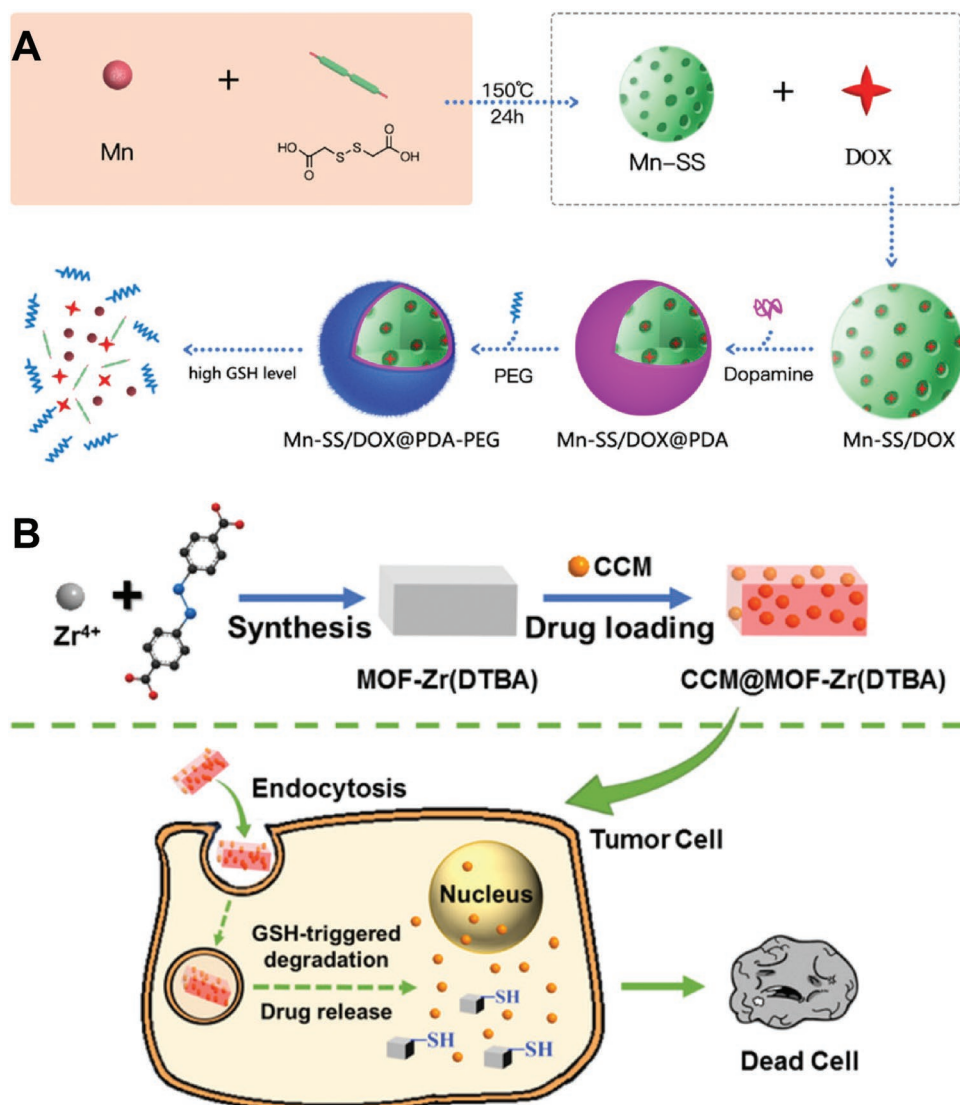


Figure 37. Examples of redox-sensitive MOF carriers based on A) dithiodiglycolic acid (Reproduced with permission.^[399a] Copyright 2017, American Chemical Society) or B) 4,4'-dithiobisbenzoic acid (DTBA) (Reproduced with permission.^[399b] Copyright 2018, American Chemical Society) as redox-cleavable organic linkers. The drug loaded MOF scaffolds are degraded in reducing environment with elevated glutathione levels (GSH).

Zr-based MOFs with photoisomerizable 4,4'-azobenzene dicarboxylate (AZB) as organic linker (UiO-AZB) have been reported as nanocarrier with photoinduced degradation and drug release (Figure 38).^[400] Irradiation with UV light causes photoisomerization of *trans*-AZB to *cis*-AZB which accelerates degradation of UiO-AZB in simulated cerebrospinal fluid.

An alternative smart light-triggered drug delivery system was realized with a nanoscale coordination polymer containing a photosensitizer and reactive oxygen species responsive framework linker.^[401] The coordination polymer consists of hafnium ions and the singlet-oxygen responsive linker bis(alkylthio) alkene (BATA). The nanoparticles are sequentially loaded with the photosensitizer chlorin e6 and doxorubicin. A lipid coating and PEG modification provides high colloidal stability of the resulting NCP-Ce6-DOX-PEG nanocomposite. Under light exposure, singlet-oxygen is generated which

enables photodynamic therapy as well as drug release by cleavage of the BATA linker (Figure 39). Due to a passive accumulation of the nanoparticles in 4T1 tumors ($\approx 5.9\% \text{ ID g}^{-1}$) after intravenous injection into mice a strong inhibition of tumor growth was achieved by the combined chemo- photodynamic therapy with NCP-Ce6-DOX-PEG and light irradiation (660 nm).

Temperature-triggered release in vivo generally requires an external source of heat. Since elevated temperatures used in hyperthermia (thermotherapy) can kill cancer cells without damaging healthy tissues,^[402] the application of thermosensitive drug delivery systems during hyperthermia treatments generally is an attractive approach. MOF architectures with thermosensitive release characteristics have been reported and demonstrate the opportunities for future optimizations of release characteristics triggered by external heat.^[403]

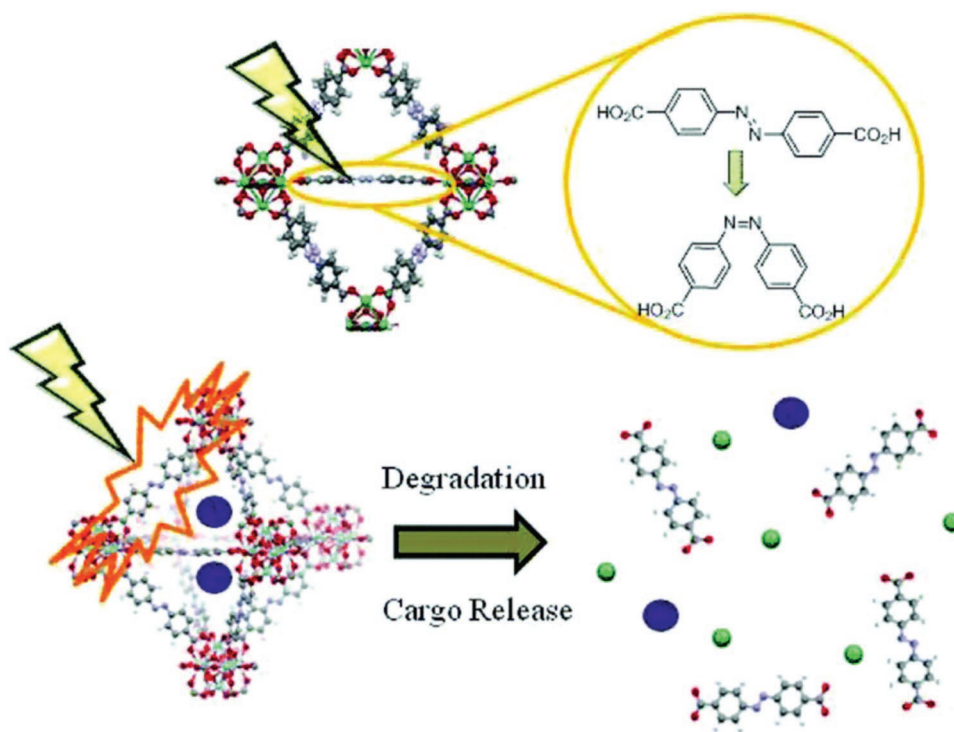


Figure 38. Schematic illustration of light-triggered degradation of UiO-AZB and drug release by photoinduced isomerization of the AZB linker. Reproduced with permission.^[400] Copyright 2017, The Royal Society of Chemistry.

8.1.5. Therapeutic Nanoparticles

Besides the use of reticular framework nanoparticles as carriers for the transport of separate therapeutic cargos, the nanomaterial itself can be the basis for a therapeutic effect. Reticular framework nanoparticles with intrinsic therapeutic activity include frameworks built from one or more pharmacologically active building units (drug containing frameworks) and frameworks containing elements which can convert external energy, such as light. The latter is realized in photodynamic and photothermal therapy approaches.

Drug Containing Framework Nanoparticles: Drug molecules or derivatives containing Lewis base functions can serve as linkers in reticular frameworks or coordination polymers with metal ions. An early example of highly functional therapeutic nanoparticles was realized with a nanoscale coordination polymer of a metal binding derivative of the anticancer drug cisplatin, *c,c,t*-(diamminedichlorodisuccinato)Pt(IV), and Tb³⁺ ions (Figure 40).^[26a] The nanoparticles were precipitated from aqueous solution by addition of a poor solvent and subsequently stabilized with a shell of polymerized amorphous silica. The silica shell prevents rapid dissolution and enables control over drug release. The dissolution half-life of the nanoscale coordination polymer particles was increased from approximately 1 h to 5.5 and 9 h, due to silica shells with 2 or 7 nm thickness. With additional grafting of a c(RGDfK)-silyl derivative onto the surface as targeting ligand to $\alpha_v\beta_3$ -integrins the disuccinatoplatin containing nanoparticles mediated killing of human colon carcinoma HT-29 cells. The general concept has been refined with other drug derivatives and metal-ion combinations. A

Zn(II) bisphosphonate nanoscale coordination polymer was produced containing phosphonate derivatives of platin drugs, a lipid shell and PEGylation.^[404] The therapeutic nanoparticles exhibit drug loadings of over 45% and achieve a remarkable systemic circulation half-life of over 12 h with minimal uptake by the mononuclear phagocyte system. In tumor xenograft models of CT26 colon cancer, H460 lung cancer, and AsPC-1 pancreatic cancer, the platin drug containing coordination polymers mediated significantly higher inhibition of tumor growth compared with the free drugs.

The antifolate drugs methotrexate (MTX) and pemetrexed (PMX), each containing two carboxylic acid functions able to coordinate to metal ions, can be assembled into nanoscale coordination polymers (NCP) with Zn²⁺, Gd³⁺, and Zr⁴⁺ ions without derivatization (Figure 41).^[147b,372] Since the drug molecules represent a major part of the nanomaterial, it exhibits an extraordinary high drug loading content of up to 80% (w/w).

It has been shown that such kind of nanoscale coordination polymers can be formed with a variety of different drug molecules and exhibit a pH-dependent nanoparticle stability which can be utilized for a pH-responsive drug release (Figure 42).^[405] The anticancer drugs daunorubicin, doxorubicin and mitoxantrone were converted into pH-sensitive metal-drug nanoparticles with Cu²⁺, Fe³⁺, Co²⁺, and Zn²⁺ with or without additional “host” additives, such as polyethylene glycol (PEG), oligochitosan (CTS), and Pluronic F127. A generic approach for the assembly of coordination polymers is based on phosphate or phosphonate derivatives of cargo molecules (Figure 43).^[406] Nanoparticles are formed with equimolar amounts of [ZrO]²⁺ or [Mg₂O]²⁺ and phosphorylated drugs (anti-inflammatory

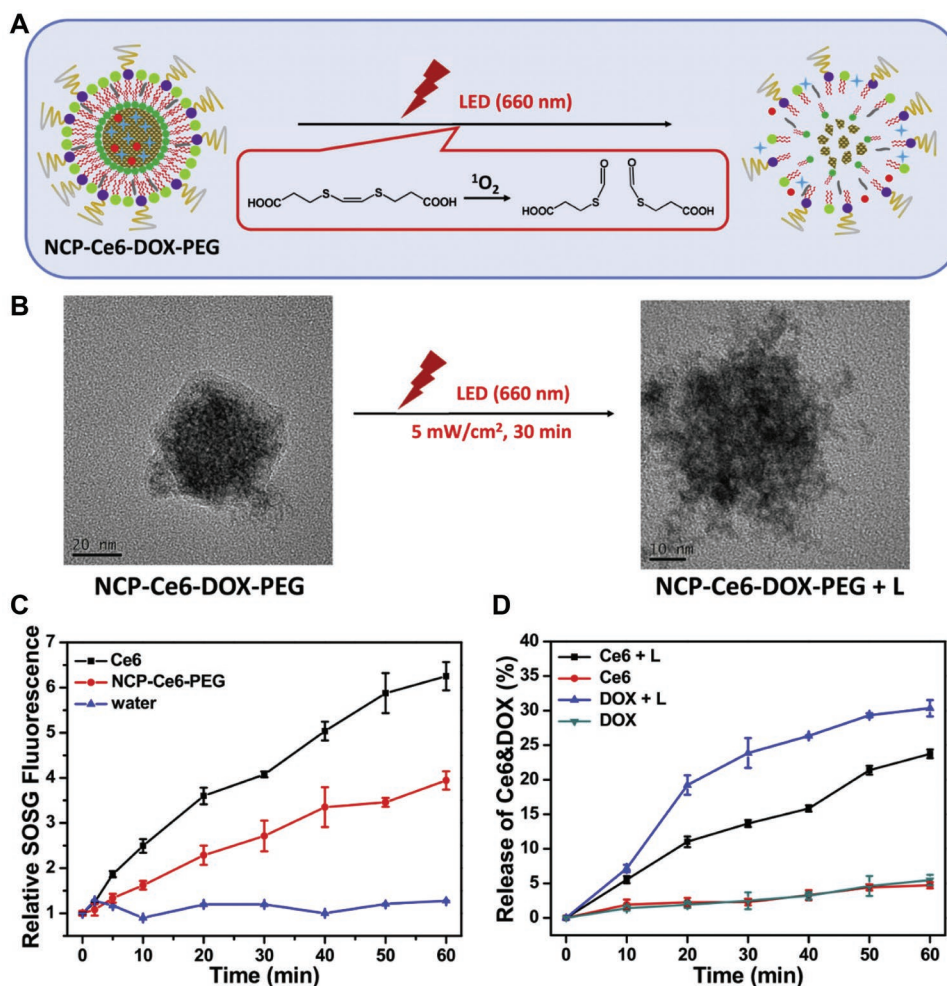


Figure 39. Light-triggered drug release by linker degradation. A nanoscale coordination polymer based on Hf^{4+} and a reactive oxygen species sensitive linker bis-(alkylthio) alkene (BATA) is loaded with the photosensitizer chlorin e6 and doxorubicin. External lipid coating and PEG modification mediate colloidal stability of NXP-Ce6-DOX-PEG. Chlorin e6 generates singlet oxygen which cleaves BATA and mediates nanoparticle degradation. Reproduced with permission.^[401] Copyright 2017, Elsevier.

betamethasone phosphate, chemotherapeutic 5'-fluoro-2'-deoxyuridine 5'-monophosphate) or fluorescent dyes (phenylumbelliferon phosphate, methylfluorescein phosphate, resorufin phosphate, and Dyomics-647 uridine triphosphate. Similar to other coordination polymers based on drug derivatives enormous loading capacities of up to 80% can be achieved.

Photodynamic Therapy: Photodynamic therapy (PDT) represents a minimally invasive therapeutic modality for the treatment of cancer and other diseases.^[407] Mechanistically, it can be described as a chemically sensitized phototoxicity induced by administered photosensitizers (PS) and light irradiation. The PDT process requires the simultaneous presence of three separate factors in the target tissue which are harmless individually: PS, light and oxygen.^[21g] The PS molecules absorb light and raise electrons to an excited state which can trigger photochemical reactions and production of reactive oxygen species (ROS).^[21g,408] Important requirement for efficient PDT is the accumulation of PS in the target tissue. Analog to the delivery of anticancer drugs, the utilization of nanocarriers is rational to control the biodistribution of PS and achieve

preferential accumulation. Reticular framework nanoparticles represent particularly suitable carrier materials due their modular assembly on the one hand, and the molecular characteristics of several PS on the other hand. It was demonstrated that MOF nanoparticles can be assembled from photosensitizing organic linkers, such as porphyrin or chlorin derivatives, with remarkable therapeutic effects in tumor models (Figure 44).^[409]

Table 5 gives an overview over MOF architectures based on photosensitizing linkers.^[21g]

COFs can also be utilized for photodynamic therapy. A nanoscale COF-LZU1, based on imine-linked 1,3,5-triformylbenzene and 1,4-diaminobenzene,^[410] has been grafted with boron-dipyromethene (BODIPY) derivatives as singlet oxygen generating photosensitizers (Figure 45).^[411] The BODIPY-conjugation was realized by Schiff-base condensation of amino-substituted BODIPY derivatives and free formyl groups present on the COF surface due to bonding defects. The intrinsic bonding defects in a COF matrix provide the possibility for a generic functionalization and versatile modification for specific purposes. This "bonding defects functionalization"

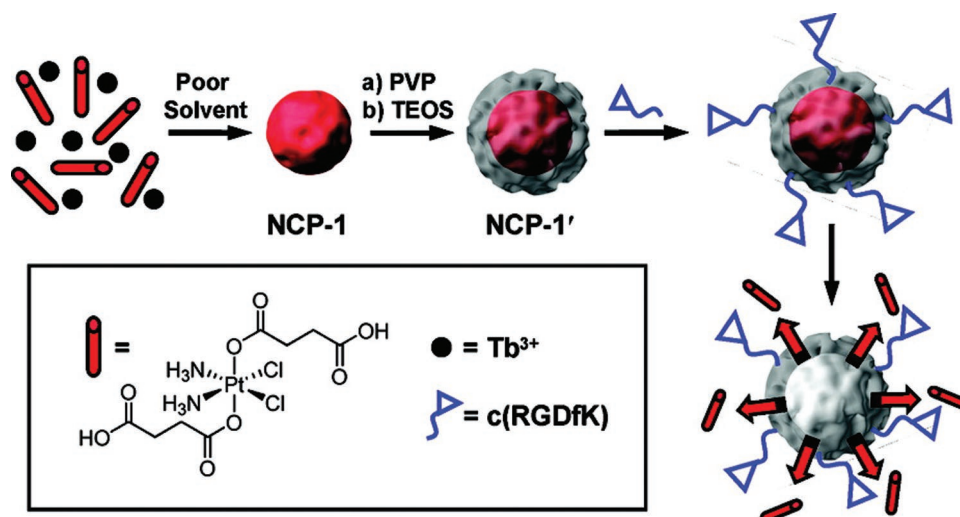


Figure 40. Therapeutic nanoscale coordination polymer built from an antitumoral platinum drug. The metal-binding cisplatin derivative disuccinaptolatin assembles into coordination polymers with Tb^{3+} in poor solvent. External silica polymerization (TEOS) after polyvinylpyrrolidone (PVP) interfacing provides stabilization and controlled drug release. A c(RGDfK) ligand mediates affinity to $\alpha_v\beta_3$ -integrins frequently overexpressed in different types of cancer. Reproduced with permission.^[26a] Copyright 2008, American Chemical Society.

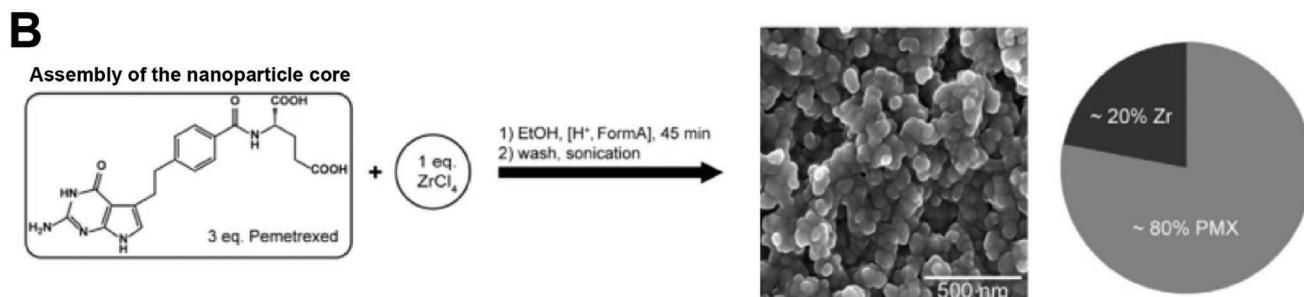
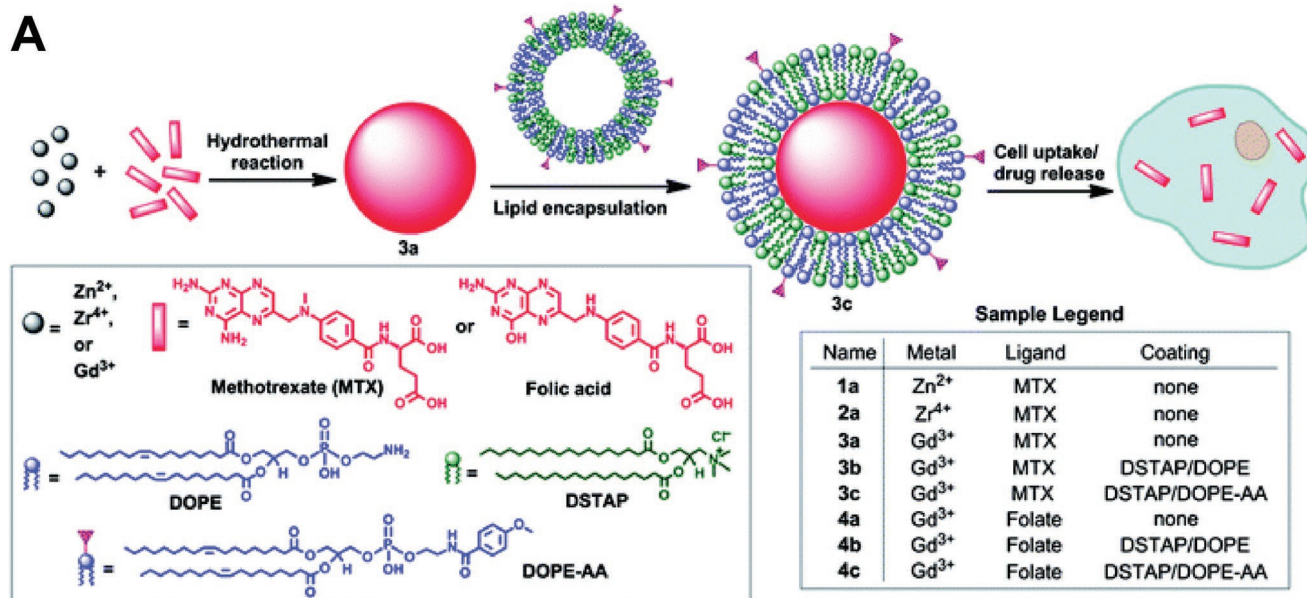


Figure 41. Antifolate containing therapeutic nanoparticles. Top: Nanoscale coordination polymers based on methotrexate and Zn^{2+} , Zr^{4+} , Gd^{3+} , and lipid coatings. Reproduced with permission.^[372] Copyright 2012, The Royal Society of Chemistry. Bottom: Formation of coordination polymers from Zr^{4+} and Pemetrexed. Adapted under the terms of the Creative Commons International CC-BY 4.0 License.^[147b] Copyright 2019, The Authors. Published by Wiley-VCH.

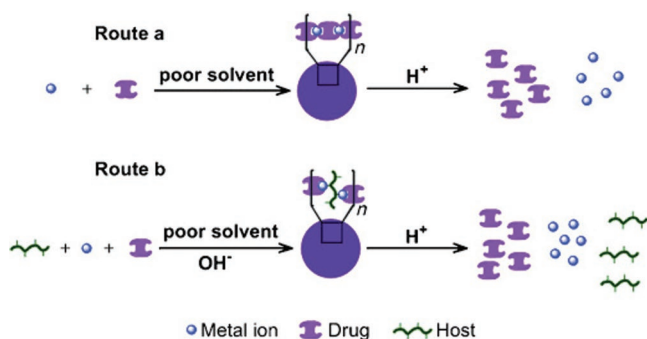


Figure 42. Assembly of a pH-responsive drug-metal coordination nanoparticles. Route a: At neutral pH drug molecules with Lewis base functions polymerize with metal ions by coordinative interaction. At low pH, the nanoparticles degrade and release the drug. Route b: With the addition of “host” molecules (e.g., PEG), coordination nanoparticles can be formed with a “host–metal–drug” architecture. Reproduced with permission.^[405] Copyright 2011, Wiley-VCH.

approach yielded COFs with BODIPY amounts of 0.1360 and 0.1545 mmol g⁻¹, depending on the BODIPY derivative. The nanoscale COFs exhibited a size of approximately 110 nm, low cytotoxicity in the dark, but mediated high phototoxicity to HeLa and MCF-7 cells upon irradiation with green light. Local injection into xenografted MCF-7 tumors followed by

irradiation with green light effectively inhibited tumor growth in nude mice in vivo.

In addition to serving as nanocarriers or grafting scaffolds for the delivery of drugs and photosensitizers, reticular frameworks themselves can be the basis for therapeutic effects. COF-808 and COF-909 are synthesized by solvothermal reaction of tetra-topic aldehyde building blocks and *p*-phenylenediamine (Figure 46).^[412] The separate building units do not exhibit photosensitizing activity and are unable to generate reactive oxygen species. COF-909, constructed from 4,4',4''-(1,4-phenylene)bis([(2,2':6',2''-terpyridine)-5,5''-dicarbaldehyde]) (L-3N), exhibits a band gap of 1.96 eV which can be excited by infrared light at 630 nm due to π -conjugation of the linkers across the framework. Photons with energy exceeding the band gap, lead to generation of electrons which are transferred to O₂ dissolved in water inside the COF pores. ROS, superoxide and hydroxyl radicals, are formed. COF-909 promotes ROS generation at a three times higher rate than the established photosensitizer, tetra(4-carboxyphenyl) porphyrin (TCPP). Nanosized COF-909 was able to mediate efficient tumor cell killing in vitro after irradiation with infrared light at 630 nm and significantly inhibited growth of CT26 tumors in mice after local injection and irradiation.

Photothermal Therapy: Photothermal therapy (PTT) represents an alternative noninvasive treatment of cancer by

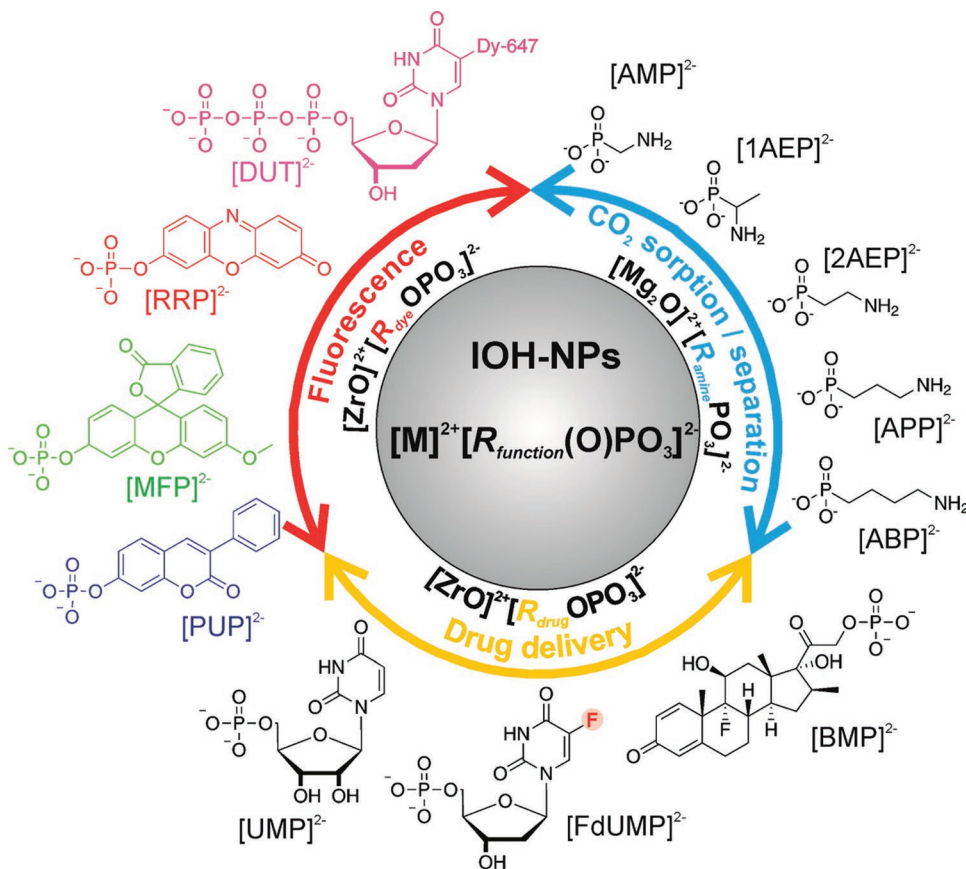


Figure 43. Illustration of metal-organic hybrid nanoparticles for different purposes. Phosphate or phosphonate containing functional molecules (fluorescent dyes, drugs, or CO₂ adsorbents) are complexed with [ZrO]²⁺ or [Mg₂O]²⁺. Reproduced with permission.^[406] Copyright 2015, American Chemical Society.

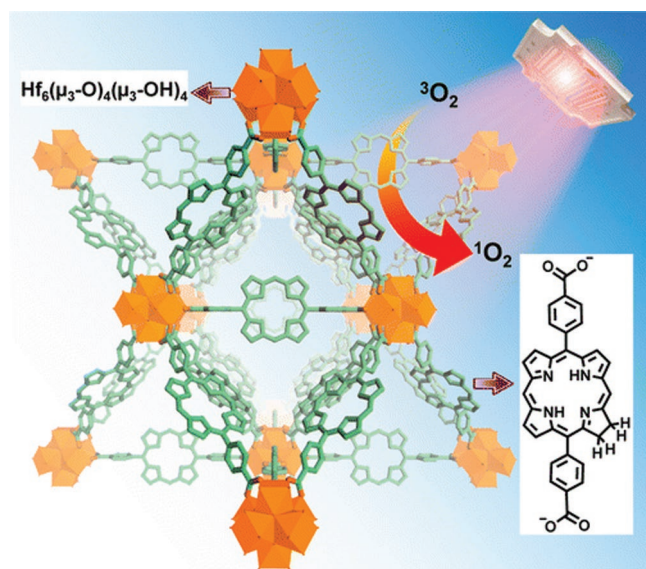


Figure 44. Schematic illustration of singlet oxygen generation upon irradiation of the chlorin-based nanoscale MOF, DBC-UiO. Reproduced with permission.^[409c] Copyright 2015, American Chemical Society.

conversion of light energy into local heat which induces apoptosis and tumor ablation.^[413] Beside merely organic^[413a,414] and inorganic materials,^[415] MOF nanoparticles have demonstrated potential for PTT applications.^[416] Multifunctional MOF and ZIF nanoparticles for a combined chemo- and PTT have been designed based on ZIF-8, UiO-66 and MIL-101.^[416d] The established reticular framework drug carriers were loaded with doxorubicin and subsequently functionalized with an external polydopamine (PDA) shell. The PDA shell serves as a reactive interface for conjugation of folic acid or an aptamer with affinity toward human protein tyrosine kinase-7 (PTK-7) as tumor targeting ligands. In addition, PDA has photothermal conversion efficiency and can be used for additional PTT effects.^[417] **Figure 47** shows the photothermal effect and heat development of ZIF-8 nanoparticles with PDA shell.

Photodynamic and photothermal therapy have also been combined by using zirconium-ferriporphyrin (Zr-FeP) MOF nanoparticles.^[418] Here, the ferriporphyrin linker serves as photosensitizer for the generation of reactive oxygen species (hydroxyl radical and singlet oxygen) under near infrared irradiation. The Zr-FeP MOF nanoparticles also changed the temperature of an aqueous suspension ($50 \mu\text{g mL}^{-1}$) from 20.2 to 45.4 °C within 10 min irradiation at 635 nm (1.9 W cm^{-2}). The multifunctional Zr-FeP MOF nanoshuttles were additionally loaded with Hsp70 siRNA (76.13%) to inhibit the expression of heat shock protein 70 in response to the PTT treatment. Finally, the combination of PDT, PTT and siRNA delivery resulted in significant suppression of tumor growth *in vitro* and *in vivo*.

8.2. Diagnostic Applications

Another important application that makes use of the synergistic combination of the nanoworld and those of reticular materials is diagnostics. The small size of nanoparticles allows

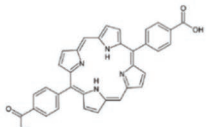
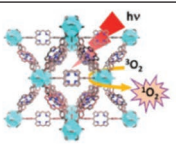
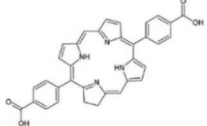
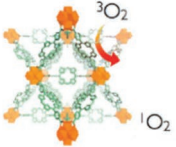
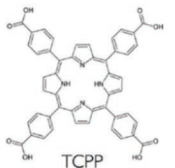
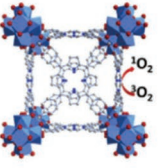
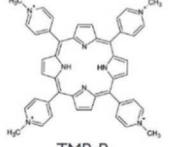
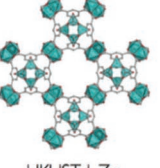
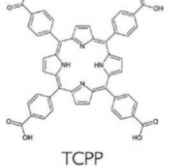
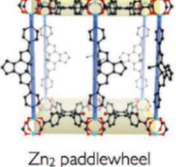

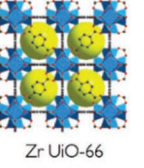
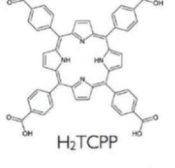
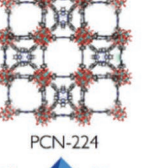
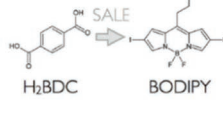
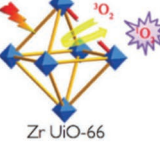
for efficient transport in the blood system and for tissue and cell uptake. Further, the nanoparticles can be equipped with targeting functionality to act as diagnostic marker for specific targets.^[333] The properties of the reticular material in turn facilitate detection of the diagnostic signal. The material can, e.g., be designed to provide MRI (magnetic resonance imaging), X-ray CT (computer tomography), or PET (positron emission tomography) contrast or serve as dye for optical imaging. Furthermore, it can serve as sensor for a variety of disease associated markers, such as nucleic acids, bacteria, metals, pH, and many more. In this case, the material changes its properties upon contact with the marker and these changes are detected with light, MRI, PET, or other means.

For diagnostic purposes, the porous reticular nanoparticle acts as amplifier: since it is composed of many building blocks, it focuses many molecules with the desired properties for detection of the diagnosis signal to one spot. Thereby, the building blocks themselves can act as signal generator or they can host other molecules with the capacity to generate the signal. Hence, instead of the signal of just one molecule, all molecules of the nanoparticle participate in signal generation resulting in a significantly amplified signal. When used as a sensor for certain molecules, the nanoparticle also offers a multitude of binding sites enhancing the number of molecules that are able to bind to one detection unit. Furthermore, the large number of binding sites on the nanoparticle leads to enhanced on-times of binding since a molecule that detached from a binding site most likely binds to a neighboring binding site immediately. Thus, the increased number of binding sites compared to single-molecule sensors also contributes to signal amplification.

8.2.1. Nanoparticles as Contrast Agents

A key diagnostic application of reticular framework nanoparticles is in MRI.^[20a] To this end, mainly Gd-, Mn-, and Fe-based MOF nanoparticles are used. They offer the advantage that the nanoparticle itself is the active component leading to a high functional efficiency. Gd and Mn are both used in clinics as contrast agents.^[20a] The use of Gd- and Mn-based MOF nanoparticles could enhance the safety of these contrast agents. Even though both metals are considered nontoxic, there is concern that the ions may not be fully cleared by the reticulo-endothelial system leading to potential side effects. Integration of the metals into a nanoparticle via stable bonds enhances the clearance efficiency and thus safety of the contrast agent. Furthermore, nanoparticles can improve the MRI signal. This increase in contrast is a complex mechanism and does not linearly relate to the number of ions.^[20a] It is a rather indirect process in which the original signal resulting from water is modulated by the contrast agent in its relaxivity. Several Gd-based MOF nanoparticles have been shown to increase the contrast of Gd.^[296,356,419] This increase is dependent on many parameters, among them to a certain extent the size of the nanoparticle,^[296] as well as the magnetic field strength.^[419] Also Mn-based MOF nanorods were reported to increase contrast compared to the clinically used molecular Mn-based contrast agent.^[294] Most research, however, has been done on Fe-based MOFs as contrast

Table 5. Nanoscale MOFs based on photosensitizing organic linkers. Adapted with permission.^[21g] Copyright 2017, Wiley-VCH.

IBU's metal	Photosensitizer	MOF type	NPs size	PS loading	$^1\text{O}_2$	$^3\text{O}_2$	<i>In vitro/in vivo</i> Study	Ref.
Hf ⁴⁺	 H ₂ DBP	 DBP-UiO	Nanoplate 100 nm length 10 nm thick	77 %	↗		Tumor shrinking & tumor eradication	[409a]
Hf ⁴⁺	 H ₂ DBC	 DBC-UiO	Nanoplate 150 nm length 5.5 nm thick	72 %	↗↗		Rapid tumor shrinking & tumor eradication	[409c]
Hf ⁴⁺	 TCPP	 UiO-66	80-150 nm	54.6 %	↗↗		Reduced tumor growth	[409d]
Zn ²⁺	 TMFP	 HKUST-1-Zn	100 nm	Ship in a bottle 32.8 %	↗		53 % of apoptotic cells	[479]
Zn ²⁺	 TCPP	 Zn ₂ paddlewheel	Not NPs	×	↗ 30% open ↗ 15% close		×	[409b]
Zr ⁴⁺	 TCPP	 Zr UiO-66	70 nm	Ship in a bottle	↘		PDT less effective	[480]
Zr ⁴⁺	 H ₂ TCPP	 PCN-224	90 nm	×	×		1.7 times higher PDT efficacy	[481]
Zr ⁴⁺	 H ₂ BDC BODIPY	 Zr UiO-66	70 nm	31.4 %	↘		PDT less effective	[482]

agents.^[20a] Compared to Gd and Mn, Fe is considered less critical in terms of toxicity. Additionally, Fe-based MOF nanoparticles can be synthesized in ethanol or water as opposed to toxic

solvents that are used for synthesis of other MOF nanoparticles. This reduces the risk of remaining toxic solvent molecules after extraction of the particles. Various Fe-based MOF nanoparticles

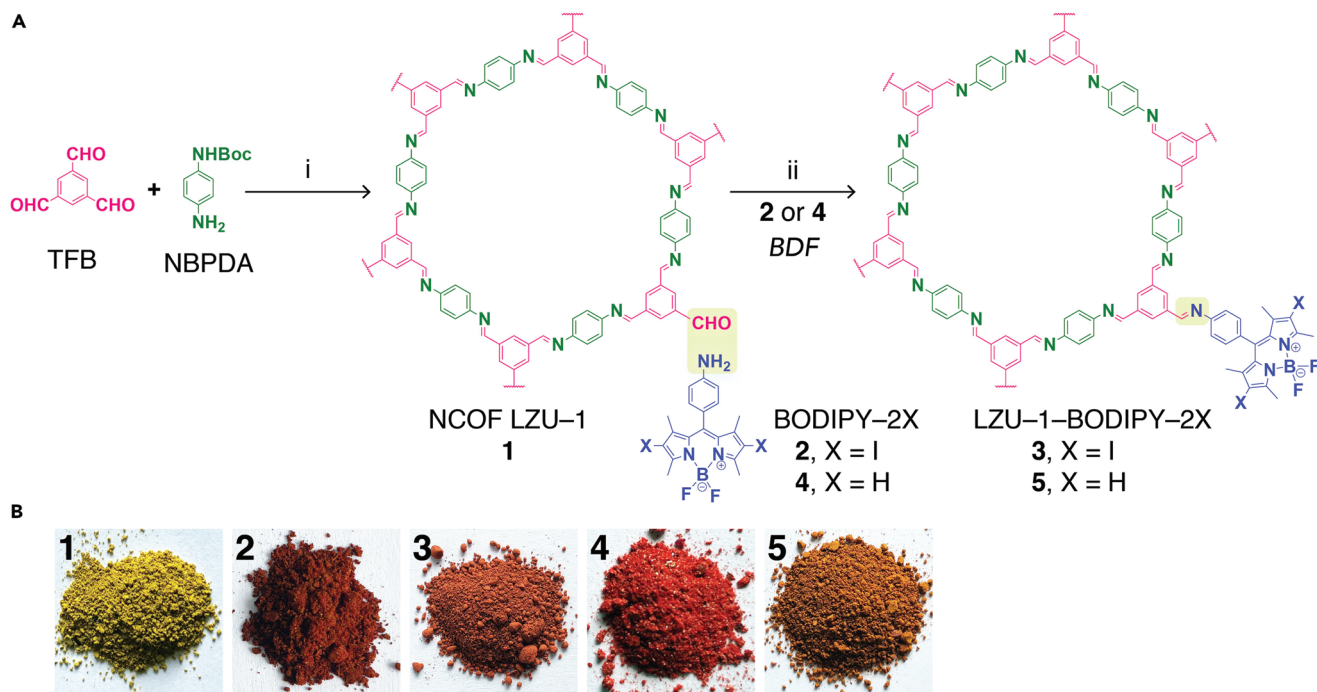


Figure 45. BODIPY-decorated nanoscale COFs for photodynamic therapy. A) The imine-linked COF-LZU1 is generated from 1,3,5-triformylbenzene and 1,4-diaminobenzene in 1:1.5 ratio. Amine-containing derivatives of the photosensitizer BODIPY are grafted to COF-LZU1 via bonding defects functionalization (BDF). B) Photographs of 1, 2, 3, 4, and 5. Reproduced under the terms of the Creative Commons CC-BY 4.0 License.^[411] Copyright 2019, The Authors. Published by Elsevier.

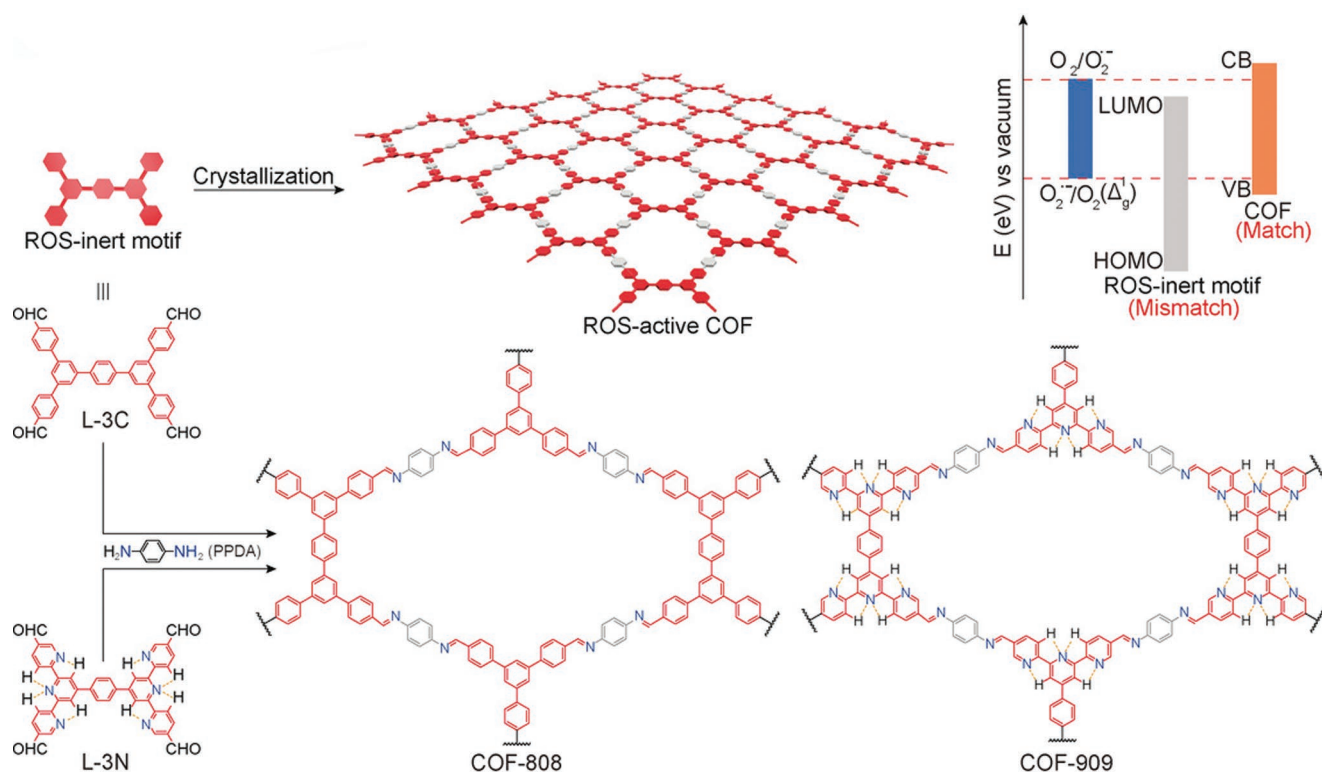


Figure 46. Conversion of ROS-inactive molecules into ROS-active COF-based photosensitizers. The tetra-topic aldehyde linkers L-3C and L-3N are unable in ROS generation, but assemble into highly active photosensitizing COFs with *p*-phenylenediamine. Reproduced with permission.^[412] Copyright 2019, Wiley-VCH.

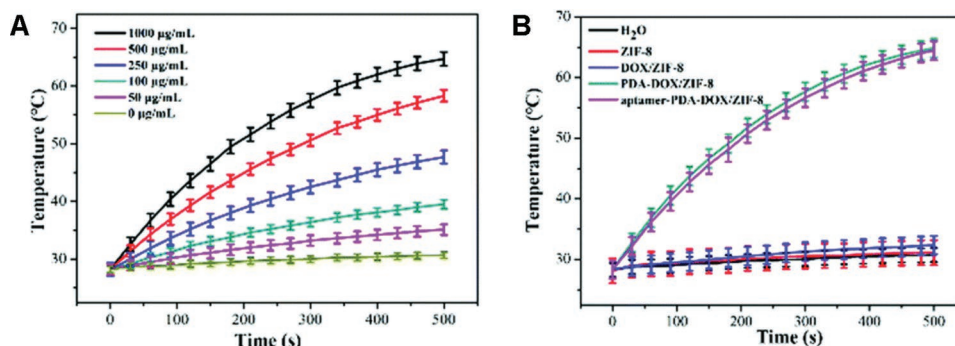


Figure 47. Photothermal effects of PDA coated ZIF-8 nanoparticles. A) Heat generation of sgc-8 aptamer-PDA-DOX/ZIF-8 in aqueous suspensions with different concentrations upon infrared light irradiation at 808 nm. B) Heat generation of ZIF-8, DOX/ZIF-8, PDA-DOX/ZIF-8 and sgc-8-PDA-DOX/ZIF-8 dispersion upon infrared light irradiation at 808 nm. Reproduced with permission.^[416d] Copyright 2019, The Royal Society of Chemistry.

have been investigated for their use as MRI contrast agent.^[20a] Among them, MIL-100(Fe) was studied most thoroughly under diverse conditions all of them revealing promising values of contrast enhancement.^[26b,300,360] In all publications, cytotoxicity of the nanoparticles was assessed in vitro, i.e., in cell culture, and none of them found significant toxicity underlining their potential as contrast agent. Finally, several in vivo studies show the MRI contrast of Fe-based MOF nanoparticles in mice with tumors.^[301,420] Thus, Fe-based MOF nanoparticles may serve as alternatives for traditional contrast agents in the future. Their multifunctionality, e.g., based on external surface functionalization, makes reticular framework nanoparticles specifically interesting as contrast agent. To this end, functionalized MOF-nanoparticles have been designed and tested for their MRI properties and various other functions. Functionalization with targeting ligands such as folate, e.g., enhances their uptake of tumor cells and still provides MRI contrast enabling tumor screening.^[360] Also other imaging agents have been included into MRI-active MOF nanoparticles allowing for multiplex imaging (see **Figure 48**). For instance, attachment of or loading with a fluorescent dye for combined MRI and fluorescence imaging,^[360,420b] deposition of gold nanoparticles for combined MRI and CT,^[420a] or doping with Eu³⁺ or Tb³⁺ for additional luminescence imaging.^[44b] Moreover, MRI active nanoparticles can be loaded with drugs or they can be built from drugs, e.g., as organic linker molecules (see Section 8.1). This creates theranostic particles that facilitate MRI-based diagnosis as well as therapy. First nanoparticles exist that are functionalized with MRI contrast agents and with drugs, such as doxorubicin^[421] and certainly more are to come in the future, since they pave the way to a personalized multifunctional medicine.

8.2.2. X-Ray Computer Tomography and Positron Emission Tomography

Reticular framework nanoparticles have also been used as contrast agents for X-ray CT. Radiocontrast agents are designed to absorb X-ray radiation leading to a reduced signal at the detector. Usually, iodine or barium sulphate is used, but they can cause severe side effects. Gold nanoparticles have been shown to significantly attenuate X-ray radiation. Therefore, they were integrated into Gd-based MOF nanoparticles to yield

a nanocomposite that offers MRI and X-ray CT contrast.^[303] They were also used in multimodal MRI/X-ray core-shell gold nanorod@MIL-88(Fe) nanostars for X-ray CT imaging. The nanostars could successfully detect brain tumors in vivo.^[420a] Furthermore, MOF nanoparticles were synthesized with building blocks that provide radiocontrast and thus a higher multifunctionality than nanocomposites. An example is the synthesis of Zn and Cu based coordination polymers with iodinated organic linkers. In this case, the iodine of the linker provides the contrast.^[298] Next to the organic linker, also the

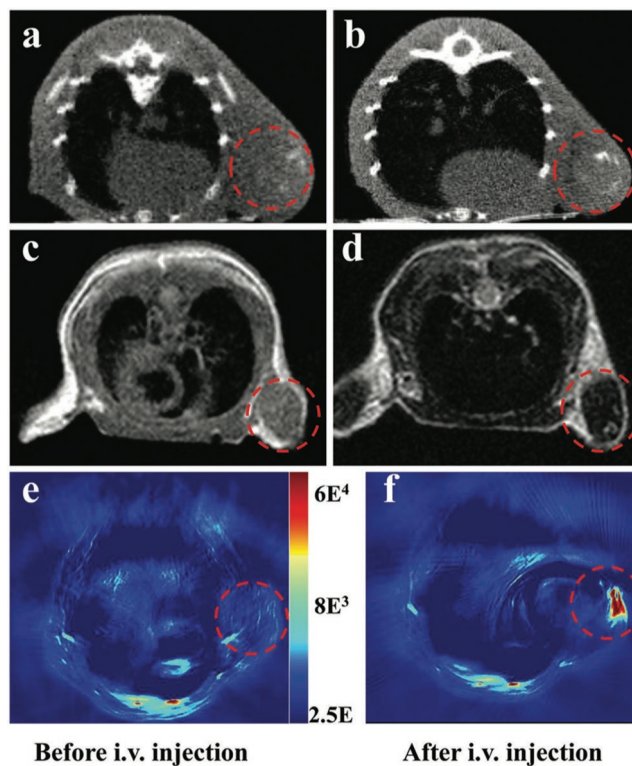


Figure 48. Images of U87 MG subcutaneous tumor-bearing mice with Fe-based MOF nanoparticles (Au@MIL88(Fe)) as contrast agent. A,B) CT images before and after injection of nanoparticles; C,D) MR-images before and after injection of nanoparticles; E,F) photoacoustic images before and after injection of nanoparticles. Reproduced with permission.^[420a] Copyright 2017, Wiley-VCH.

metal ions of MOF nanoparticles were used to achieve X-ray contrast. To this end, UiO structures with Hf and Zr as metals were synthesized.^[422] They were successfully used in vivo for X-ray CT. However, they had to be coated with silica and PEG to enhance the biocompatibility and allow for in vivo experiments. Another successful in vivo study for X-ray CT uses iodine-boron-dipyromethene to generate contrast.^[423] It is introduced into UiO-66 MOF nanoparticles via linker exchange. The resulting UiO-PDT nanoparticles were shown to provide X-ray CT contrast in tumors in vivo without signs of toxicity.

As opposed to X-ray CT contrast agents, which have to attenuate the radiation signal, contrast agents for PET have to be radioactive. Such a contrast agent has also already been realized with MOF nanoparticles. UiO-66 nanoparticles have been synthesized employing ⁸⁹Zr as radioactive metal building block.^[424] After PEGylation and functionalization with a targeting ligand the nanoparticles successfully marked tumors in PET of mice in vivo.

8.2.3. Photoacoustic Imaging and Optical Imaging

Another technique for which reticular frameworks can serve as contrast agent is photoacoustic imaging. In this application, they accumulate for instance at a tumor and when radiated with pulsed light, they convert the radiation into heat creating ultrasound signals. Both, MOF as well as COF nanostructures have been designed for this application. Examples again using active building blocks are bacteriochlorin-based MOF nanosheets^[425] and 2,2'-bipyridine-based COFs^[426] that were converted to a cationic radical framework. Both have been used in vivo and successfully showed tumors in photoacoustic imaging and at the same time they acted as agent for photothermal therapy.

Next to the above described imaging techniques, MOF, ZIF and COF nanoparticles have also been used as dye for fluorescence imaging^[360,365,427] and as source for luminescence^[428] or phosphorescence.^[429] For optical imaging, dyes have been attached to the surface,^[360] loaded into the nanoparticle,^[365] or used as building blocks.^[430] Even though optical imaging is limited in vivo due to the short penetration depth of visible light into tissue, successful in vivo experiments have been performed. An example are curcumin-functionalized COF nanocomposites that were used to detect and treat tumors in mice.^[365]

8.2.4. Nanoparticles as Sensors

An area in diagnostics that makes use of reticular framework nanoparticles is that of sensing, specifically for laboratory diagnostics, e.g., in the detection of DNA/RNA or bacterial infections. Reticular framework nanoparticles have been used for a wide variety of sensing applications in diagnostics ranging from metal ions^[431] to nucleic acid polymers^[432] and all the way to entire organisms such as bacteria.^[433] A selection of them will be presented in the following.

Metal ions are important indicators in diagnosis. For example, neurodegenerative diseases are considered to be associated with elevated levels of Zn²⁺, Cu²⁺, Fe³⁺, and Al³⁺.^[431] Thus, detecting these ions selectively and with confidence will gain increasing

interest with the aging population and the increase in neurodegenerative diseases. Metal sensors exist with luminescence and fluorescence as detection methods.^[431] Different metal-sensing mechanisms have been realized: interactions with the framework by collapse or exchange of metal ions (in the case of MOFs and ZIFs), interaction with ligands, which provide the detection signal, or interaction with the signal itself. Another concept for ion sensing employs the crystalline framework as host for fluorescent reporter molecules, as demonstrated for fluoride ions.^[155c] Here, the detection is based on the decomposition of the particle and release of the fluorescence dye. Various reticular framework-based sensors for a wide variety of ions have been realized at least in bulk material.^[333,431,434] Among them, iron detection (Fe²⁺ and Fe³⁺) is the furthest developed method. While all also bulk COFs have been utilized for Fe detection,^[434,435] MOFs have been used as nanoparticles for Fe detection. Luminescent 2D-nanosheet MOFs (NTU-9-NS) were employed to detect Fe³⁺ ions in aqueous solution.^[435] Here, the ions interfere with the luminescence signal via quenching and the structure of the nanosheets provides a high surface area for the interaction. Fluorescence turn-off has been used for Fe²⁺ sensing with nanoscale MOFs (nMOF-253s).^[436] With this sensor Fe²⁺ could be detected in cancer cells via a significant quenching of the MOF's fluorescence.

Reticular framework nanoparticles have also been used as sensors for nucleic acids.^[432] Three different detection techniques have been employed: fluorescence, electrochemistry, and colorimetry. Most assays are based on fluorescence turn-on mechanisms. The principle is based on competitive binding. A probe strand of DNA or RNA with a fluorescence marker binds to the nanoparticle, which quenches the fluorescent dye. Upon addition of the target strand, both strands hybridize releasing the probe strand from the nanoparticle and thus restoring the fluorescence of the attached marker (see **Figure 49**). This technique has been used with ZIF and MOF nanoparticles.^[432] Examples are ZIF-8,^[437] which has been used to detect HIV-DNA, and MIL-88B, which could discriminate single-point mutations in DNA.^[438] Various extensions of the fluorescence method have been designed to enhance the performance, such as additional amplification by hybridization chain reaction^[439] and to extend it for detection of RNA.^[439,440] Also multiplexing detection has been done based on the fluorescence technique using molecular beacons on an MOF nanoparticle as probe.^[441] A second method that has been used for nucleic acid detection is based on electrochemistry. It employs the catalytic properties of MOF nanoparticles to enhance the electrochemical signal of nucleic acids.^[442] However, due to the limited electrical conductivity of MOFs, this method is so far limited to nanocomposites with MOFs as catalysts and other components that enhance the conductivity.^[432] The third method for nucleic acid detection with reticular frameworks uses colorimetry. Here, a composite of MIL-88(Fe) and Au nanoparticles catalyzes a reaction, which is silenced by addition of the probe strand.^[443] In presence of the target strand the probe strand is released from the nanoparticles and hybridizes with the target strand. This restores the catalytic reaction, which is accompanied by a color shift. This technique could detect HIV-DNA. Also, COF-materials have been designed for the detection of nucleic acids;^[444] however, to the best of our knowledge, these are so far 2D materials, but no nanoparticles.

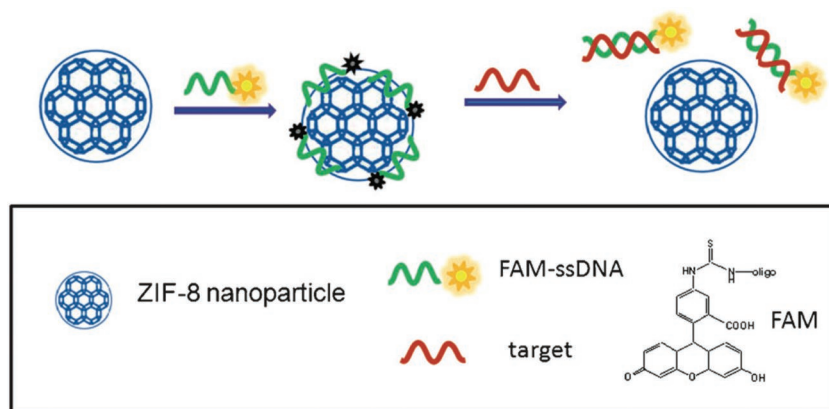


Figure 49. Schematic of fluorescence-based detection of nucleic acids with reticular framework nanoparticles. The probe strand with a fluorescence marker binds to the nanoparticle, which quenches the dye. Presence of the target strand releases the probe strand and restores fluorescence. Reproduced with permission.^[437] Copyright 2012, Wiley-VCH.

Beyond nucleic acid detection, MOFs have even been used to detect bacteria. The detection was based on electrochemistry, thus the electrical conductivity of HKUST-1 was increased by polyaniline yielding a nanocomposite, which was further functionalized by attachment of an aptamer for highly specific bacteria detection.^[433] The electrochemical signal could then be used to detect bacteria and investigate the effect of antibacterial agents.

Due to the importance of tumor diagnostics, many different reticular framework-based sensors for tumor markers have been designed in addition to the above-mentioned contrast agents. One of them uses Ni-hemin metal organic frameworks functionalized with folate as targeting ligand as tumor marker. The mechanism is based on a colorimetric reaction of the peroxidase mimicking MOF and H_2O_2 .^[445] Also, sensors for ATP as metabolic marker have been designed. Among them a COF-sensor,^[444] who still has to be transferred to the nanoscale. Already at the nanoscale is an ATP sensor based on polydopamine-coated UiO-66 MOF nanoparticles.^[446]

These are only some of many possibilities for applications of reticular framework nanoparticles in diagnosis. The already large number of examples raises the promise for successful diagnosis with MOF, ZIF and COF nanoparticles in the laboratory and all the way to the clinics.

8.3. Reticular Nanoparticles as Tools for Bionanotechnology

A closer look inside living matter reveals that basic units of living beings, such as proteins, nucleic acids and macromolecular assemblies, have sizes on the nanometer scale. Interestingly, these basic units present spectacular reactivity and chemical specificity that were naturally optimized through life evaluations. Over the last decade and owing to the size homology between naturally occurring and man-made nanomaterials (e.g., nanoparticles), a close collaboration/interaction between life and material sciences has been developed to tackle limitations encountered in the diagnosis of diseases and their therapies. Reticular materials are highly versatile and modular due to their hybrid character: they can be mixed heterogeneously and additionally functionalized in various ways at all levels, i.e., linkers, guest molecules, surfaces, etc. (see Sections 4–6). The synergistic combination of biological macromolecules, assemblies or even natural cells with artificial reticular nanomaterials, hence allows to exploit the advantageous properties of each system and to create new tunable platforms for various biological applications.

The assembly of MOF nanoparticles with biomolecules was limited at first to molecules that matched the size of the frameworks' pores or that could withstand solvents during synthesis.^[390c] The introduction of the biomimetic mineralization^[447] of MOF frameworks on biomacromolecules could overcome this hurdle at physiological conditions.^[448] MOFs form porous nanoshells around biomolecules in a synergistic manner due to the charged nature of the encapsulated macromolecules (**Figure 50**; left). The precise, molecular mechanism is still under investigation.^[449] The reaction occurs spontaneously in deionized water without the need of heat, organic solvent or other chemical compounds. The target biomolecules act as nucleators for crystallization of porous shells in a one-pot synthesis. The successful procedure has been demonstrated for various frameworks^[448] including ZIF-8, HKUST-1 and MIL-88A. To date, most applications related to

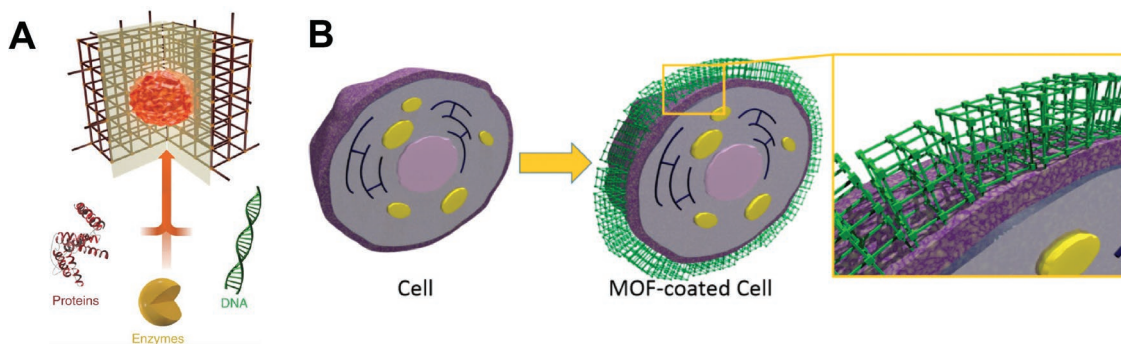


Figure 50. Biomimetic mineralization of biomacromolecules and complexes. A) Schematic of an MOF/biomolecule composite. Biomacromolecules such as proteins and DNA are encapsulated within a crystalline shell. Reproduced with permission.^[448] Copyright 2015, Springer Nature. B) Encapsulation of mammalian cells by MOF nanoparticles. Reproduced with permission.^[449] Copyright 2018, American Chemical Society.

MOF based encapsulation are based on ZIF-8, a framework made of Zn ions and 2-methyl-imidazole. Biomimetic mineralization is applicable to various classes of molecules such as oligonucleotides, proteins and hormones,^[448] e.g., ovalbumin, lipase and insulin. In addition, the encapsulation within porous shells made of ZIF-8 has been demonstrated for even larger complexes such as viruses,^[450] bacteria,^[451] yeast,^[452] and even living cells^[453] (Figure 50; right). The encapsulation strategy of enzymes by reticular nanoparticles has been realized for MOF,^[454] COF,^[455] mesoporous silica,^[456] and HOF.^[457]

Biomacromolecules or complexes are encapsulated by the porous network, with varying crystal size, morphology and crystallinity depending on the seed structure and chosen MOF framework. For horse-radish peroxidase and trypsin in ZIF-8, e.g., nanoflowers and nanostars are observed, while ssDNA encapsulation in ZIF-8 leads to rhombic dodecahedron crystals.^[448] The thickness of shells is on the order of 100–250 nm and can be adjusted by sequential growth steps.^[452] In the case of ZIF-8, the shell formation depends on the external pH and is reversible allowing for the controlled release of biomacromolecules with full biological function.^[448,452] The removal of the outer shell can be also triggered by addition of ethylene diaminetetraacid acid (EDTA) and other metal chelators independent of the pH.

When encapsulated in the porous shell, proteins and enzymes are still active and capable to catalyze their substrate. On first glance, one expects the molecular transport of the ligand through the shell to be limited by the pore size of the shell, i.e., that the chosen framework is part of the preselection. It acts like a molecular sieve that is dedicated to substrates of defined molecular structure such as ions, metabolites and ligands like sugars. Nevertheless, also ligands larger than the diameter of the pore overcome the encapsulating shell. ZIF-8 has a pore aperture size of 3.4 Å. As expected, it protects against cytotoxins, like lyticase, an enzyme with a diameter of roughly 5.3 nm.^[452] Also small molecules such as the antifungal drug filipin (averaged

diameter ≈ 1.4 Å) can be shielded.^[452] At the same time, it acts as selectively permeable shell. ZIF-8 encapsulated yeast cells^[452] are metabolically active—which means they do have access to essential nutrients within the cell medium. This includes glucose (average diameter of nearly 8 Å), that should not diffuse through the shell.^[458] A potential explanation might be defects in the encapsulating layer. In this case, however, the protective role even against small drug molecules cannot be explained. The exact mechanism of diffusion of ligands through encapsulating MOF shells, is a topic of current research to better understand the selective size-exclusion of metabolites.

Similar to nature, where biomineral coatings serve for protection, MOF-based nanoshells clearly provide improved robustness against organic solvent (that would normally lead to degradation) and prevent enzymes from degradation at non-physiological temperatures. Incubating HRP encapsulated in ZIF-8 for 1 h in dimethylparaformamide at 153 °C, e.g.,^[448] does not harm its activity.^[448] MOF shells further act as protecting agents at low temperatures. Zr-based MOF nanoparticles, in particular UiO-66, UiO-67 and MOF-808 were used in cryopreservation by serving as cryoprotectant needed to prevent damage due to ice growth at -80 °C.^[453a] This property could be employed for storing enzymes, vaccines and DNA for therapeutic applications.^[449]

Biomimetic encapsulation of biomacromolecules in particular proteins in MOF frameworks preserves biological function under inhospitable conditions such as high temperatures or in denaturing, proteolytic agents. Although ZIF-8 has become the most widely used framework for biomimetic mineralization, its hydrophobic nature can lead to inactive enzymes, as, e.g., in the case of catalase. Proteins often interact with hydrophobic surfaces with greater affinity, associated with conformational changes of the protein,^[459] which can lead to deactivation. A recent work^[460] has addressed this issue by investigating more hydrophilic frameworks ZIF-90 and MAF-7 for biomimetic mineralization in comparison to ZIF-8 (Figure 51).

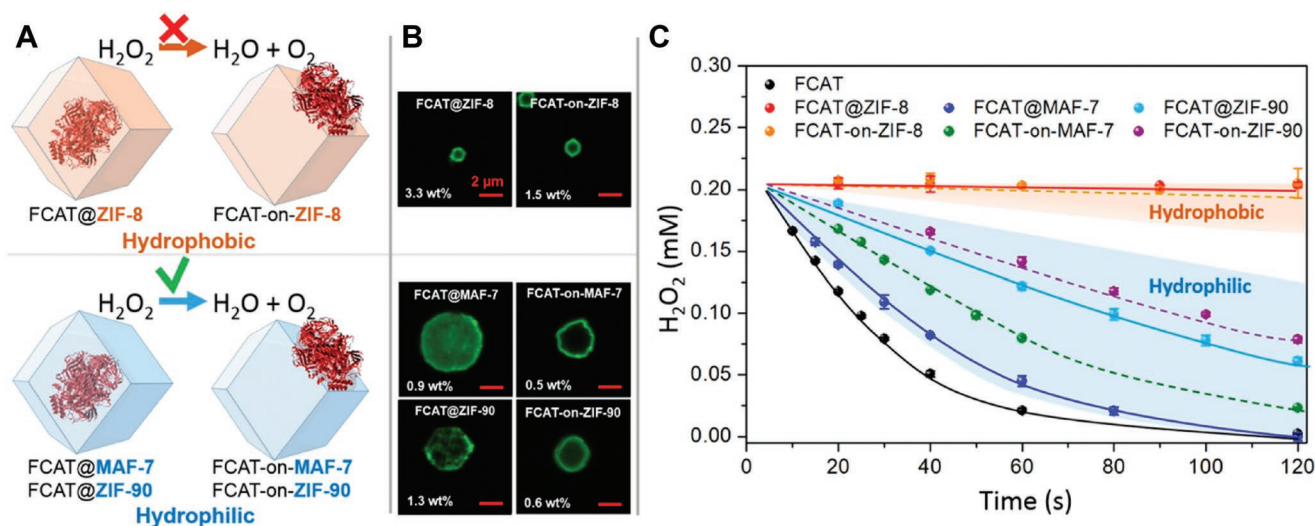


Figure 51. Role of hydrophobicity in biomimetic mineralization of fluorescently labeled catalase (FCAT) by various types of MOF nanoparticles. A) Schematic representation of enzyme/ZIF-8 composites in hydrophobic (orange) and hydrophilic frameworks. B) Confocal images of enzyme/ZIF-8 composites. C) Catalytic activity of the encapsulated catalase. Reproduced with permission.^[459] Copyright 2019, American Chemical Society.

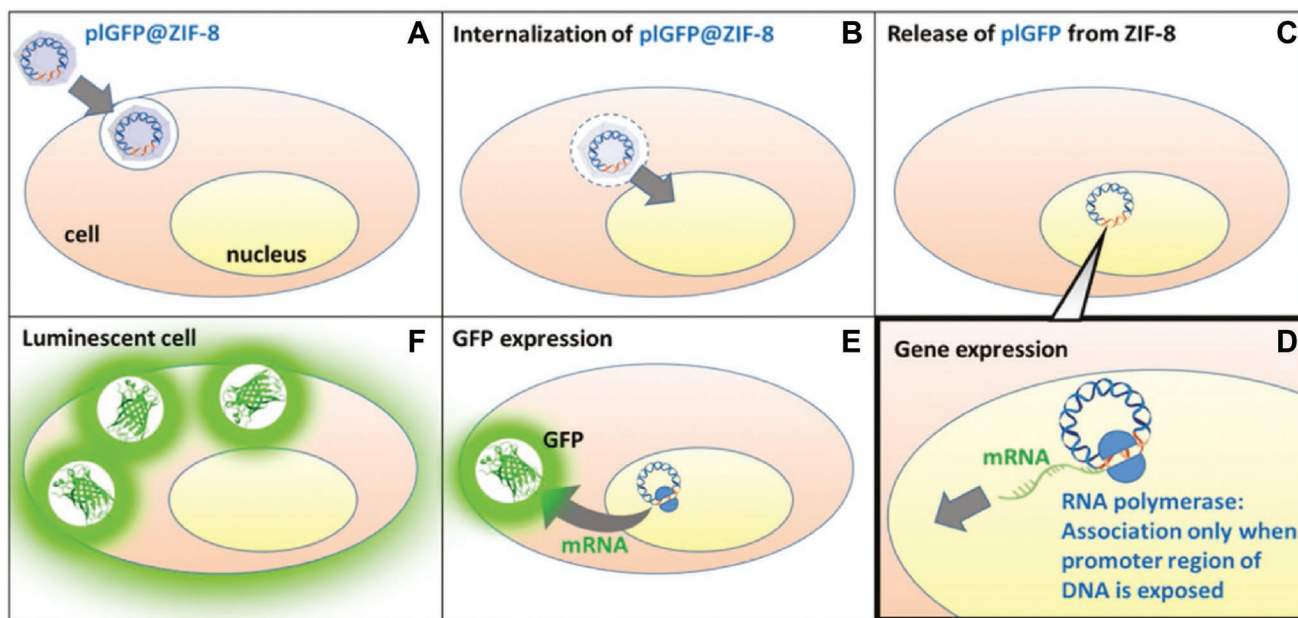


Figure 52. Schematic of gene expression mechanism after cellular uptake of GFP-encoding plasmid encapsulated in ZIF-8. Reproduced with permission.^[463] Copyright 2019, Wiley-VCH.

These Zn-based frameworks are formed by more hydrophilic linkers (3-methyl-1,2,4-troazolate; MAF-7 and 2-imidazole carboxaldehyde; ZIF-90) in comparison to 2-methyl imidazole (ZIF-8). Both frameworks show enhanced and preserved activity of catalase in comparison to ZIF-8. MAF-7 provides better protection overall. The findings are in line with reports on enzyme/polymer interaction, where the optimization of hydrophobic and hydrophilic interactions is a prerequisite for effective stabilization and encapsulation of biomolecules.^[461]

Reticular nanoparticles as unique nanotechnological tool serve as building blocks in protective hierarchical structures^[462] that can deliver encoding biomolecules like RNA and DNA. MOF nanoparticles were recently employed as simultaneous carrier and protection system of large-size intact gene sets. Circular DNA with 6.5 kbp was encapsulated in ZIF-8 nanoparticles,^[463] which served as transfection vector encoding GFP. After cellular uptake by mammalian cells followed by gradual and biocompatible degradation of the ZIF-8 framework (Figure 52), the circular DNA was released and a retarded expression of GFP was observed. MOF based nanoparticle have hence the potential to overcome current limitations of gene therapy, since MOF encapsulation maintains the functional activity of DNA.

Many living organisms fabricate molecular architectures to provide exoskeletal protection and structural support for soft tissue.^[448] Biomimetic mineralization has been introduced to complex bioentities, such as viruses, bacteria, and mammalian cells.^[452,453,464]

In a first work, ZIF-8 was successfully employed to encapsulate living yeast and bacteria, which did not affect the cell viability of both systems.^[452] The introduced ZIF-8 coating acts like a semipermeable exoskeleton that allows small ligands like glucose or amino acids within the cell medium to reach

the cells. The cell can “survive”; however, it does not divide any longer. The ZIF-8 shell leads to an extended lag phase in cell growth due to the external exoskeleton.^[452] Removal of the encapsulation by EDTA can restore cell growth.

A subsequent work generalized the approach to various mammalian cell lines and types of nanoparticles (Figure 53). Following a different synthesis approach based on preformed nanoparticles, instantaneous exoskeleton formation around living cells (including HeLa, A549, and HL-60 cells) is achieved in presence of interparticle linking ligands. The encapsulating shell may consist of arbitrary nanoparticle building blocks (and combinations thereof). Shell formation was demonstrated for nanoparticles made of MOF (including ZIF-8, MIL-100, UiO-66-NH₂, and MET-3-Fe), mesoporous silica (including mSiO₂) and iron oxide (Fe₃O₄). It is achieved via tannic acid-mediated interparticle binding due to strong multivalent metal-phenolic complexation, which leads to homogenous conformal exoskeletons around cells. The structural and chemical composition of the involved nanoparticles remains unaltered.

With respect to viability and metabolism, all encapsulated cells show no alteration except for cell growth and proliferation. The formed exoskeleton poses a (reversible) barrier also to mammalian cell lines that forces the cell to enter a spore-like state. The mechanical behavior was examined by nanoindentation and showed a 2–4 time greater stiffness and elastic modulus.^[453b]

The applied porous exoskeleton does not only protect against toxins and pathogens larger than 5 nm,^[453b] it also endows the encapsulated cells with a plethora of new functionalities: cells are more resistant against osmotic stress, reactive oxygen species, pH and UV. Additionally, abiotic properties for employed nanoparticles can be symbiotically incorporated into the encapsulated cells, such as sensing, magnetic and conductive properties or multifluorescent emission. Multifluorescent

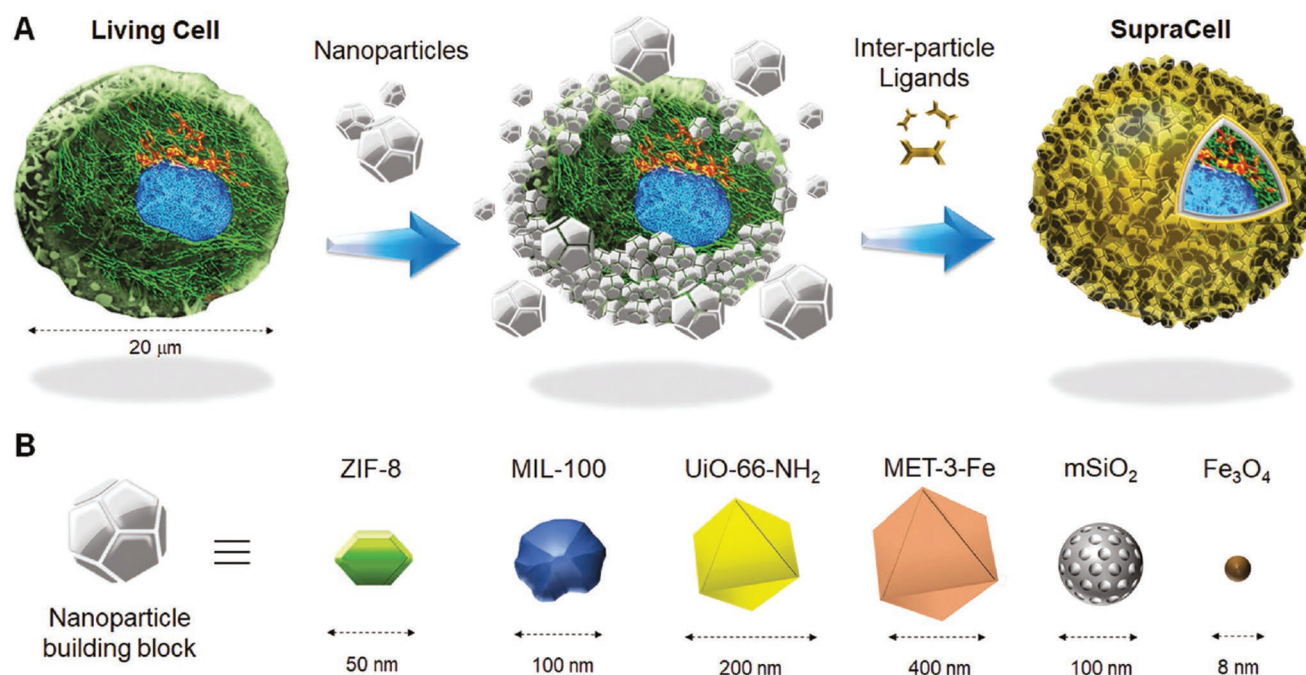


Figure 53. Schematic of SupraCell formation. A) Mammalian cells are encapsulated by preformed nanoparticles that instantaneously build a porous shell around the cellular membrane in presence of interparticle ligands. B) Representation of selected nanoparticle building blocks applicable for cellular exoskeleton formation. Reproduced with permission.^[453b] Copyright 2019, Wiley-VCH.

cells were achieved by encapsulation with differently labeled mesoporous silica nanoparticles.^[453b] NO sensing based on luminescence quenching was realized by UiO-66-NH₂ encapsulation of cells.^[465] The application of iron oxide nanoparticles within the exoskeletons leads to cells that can be externally controlled by a magnetic field during cell migration.^[453b] In fact, a plethora of properties reported for MOF, ZIF, and silica particles could be incorporated and even be combined by using heterogeneous mixtures of nanoparticles with different physicochemical properties during shell formation. Postsynthetic modifications, modification due to host-guest interactions as well as the incorporation of enzymes into the functionalized cell coating could even further extend this approach.

The above-mentioned strategy is also applicable to highly fragile cells. Recently, the approach has been employed to red blood cells (RBCs),^[464] which are responsible for oxygen delivery and drug delivery of natural compounds in vertebrates. RBCs are highly sensitive and instable structures that strongly depend on the environment such as the tonicity and reaction conditions. While the interaction of single nanoparticles with the RBCs often results in membrane rupture and hemolysis, the new encapsulation approach overcomes this limitation. The application of all above-mentioned types of nanoparticles lead to intact, unaltered RBCs,^[464] that are still biologically active in vivo. Additionally, abiotic properties by the employed nanoparticles can be symbiotically added to the RBCs. Indeed, the introduction of an exoskeleton to RBCs stabilizes the cells and enables long-term storage over days without hemolysis. Even after freezing a cell, recovery up to 40% was observed.^[453a,464] The introduced encapsulation modulates cell-cell contact and cell-adhesion. It shields the cell surface of RBCs and prevents agglutination due to different epitopes of blood group antigens,

a property that could easily be extended to leucocytes, which play a pivotal role in immunity and inflammatory processes. The increased stability, storage capability and antiagglutination property strongly supports the survival of RBCs during blood transfusion and transplantations.

In conclusion, the presented coating strategy holds great promises for the design of new functional microarchitectures, in particular under the aspect that the assembly process is reversible and applicable to enzymes, proteins and even cells. Cells within the external exoskeleton remain unaltered, but can still serve as probe for imaging and sensing in vitro and in vivo. More strikingly, the external coating can act as carrier system in personalized medicine. It strongly supports cell-based therapy approaches^[466] for many disorders like Parkinson's diseases or multiple sclerosis that might help to compensate, repair and restore biological function of damaged cells and tissue. This novel approach, clearly enlarges the tool box of hybrid nanomedicine and unlocks their potential for different fields ranging from therapeutics, sensing, and imaging to personalized medicine.

8.4. Heterogeneous Catalysis

A heterogeneous catalyst is a functional material that facilitates chemical reactions by lowering the energy barrier of the reaction pathway without itself being consumed or changed. The transformation of the reactants occurs at the catalytic active sites present at the surface of a catalyst. So, the greater the surface area to volume ratio of the catalyst, the more efficiently the catalyst will function. Decreasing the size of a catalyst to the nanolevel drastically increases the available surface area of the

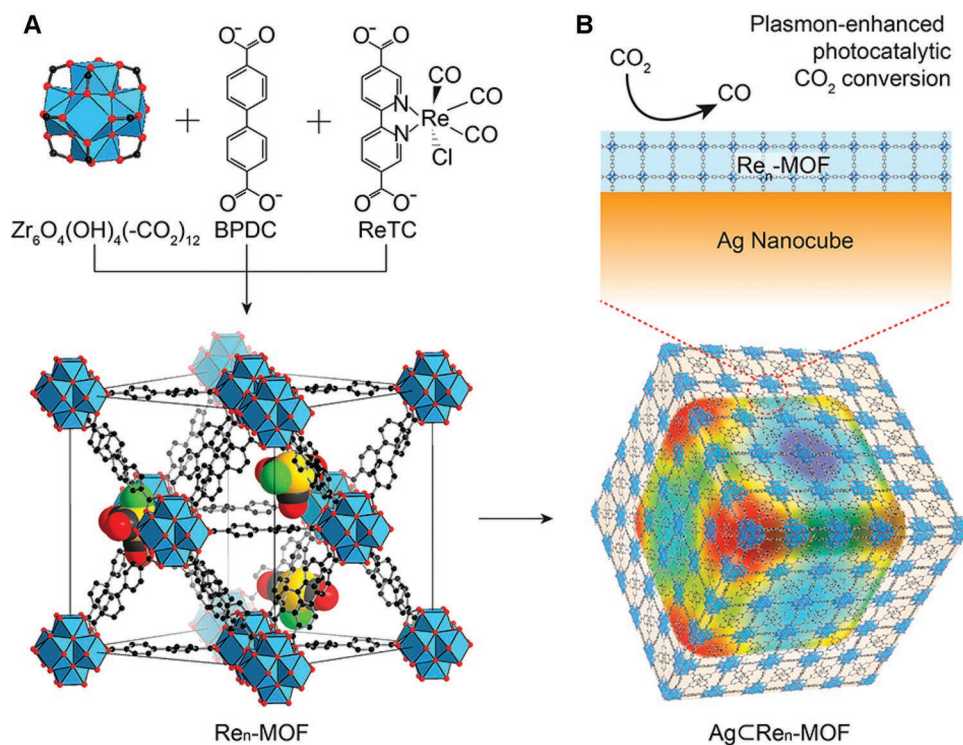


Figure 54. Structure of the used MOF for plasmon-enhanced photocatalytic CO_2 conversion. Reproduced with permission.^[156] Copyright 2017, American Chemical Society.

catalyst, providing a large number of active sites and virtually eliminating inactive sites. Although this catalytic optimization is common in nanoscience in general,^[467] reticular nanoparticles are largely excluded from this practice.

The shape dependence of ZIF-8 rhombic dodecahedra and nanocubes was systematically studied for the Knoevenagel condensation.^[468] The higher catalytic activity of the nanocubes compared to rhombic dodecahedra of similar surface area could be attributed to the intrinsically higher density of coordinatively unsaturated metal sites on {100} facets. In another study, ZIF-8 nanoparticles were used for the Knoevenagel synthesis of α,β -unsaturated cyanoesters and 3-cyanocoumarins with excellent yields ranging from 89% to 95%, and the particles could be reused up to five times.^[469] ZIF-8 nanoparticles could be further used for a couple of hydrolysis reactions.^[470] By replacing water internally and externally and hydroxyl groups on coordinatively unsaturated Zr sites with sulfate groups, superacidity could be created.^[471] The superacidic MOF-808 particles with 200–800 nm diameter were found to be catalytically active in diverse reactions including Friedel–Craft acylation, esterification, and isomerization. Another interesting example is the covalent attachment of Cu atoms onto the coordinatively unsaturated Zr sites (defect sites) in UiO-66 nanoparticles.^[472] In this case the oxidation of CO takes place in the interior of the MOF, but the nanodimension ensures faster diffusion kinetics compared to the bulk material. A similar approach deals with the synthesis of porphyrinic MOF nanoparticles for photodynamic therapy.^[218] Here, the porphyrinic OBU interacts with light to generate reactive oxygen species, which can be used in medicine to eradicate cancer cells.

The incorporation of catalytically active metal nanoparticles (MNPs) into porous reticular nanoparticles or their bulk counterparts, however, is common practice.^[17a,354b,473] This core-shell approach ensures spatial separation of the active centers, preventing the MNPs from aggregating and hampering their catalytic performance. Additionally, a porous reticular matrix provides size selectivity, and with it the possibility to tune the reactant uptake and diffusion rate through the active MNPs.

Reticular materials are easily accessible for functionalization, so the electronic and photophysical properties of the MNP can be easily tuned. An elegant example is the incorporation of photoactive centers into an MOF backbone, which was used for coating of silver nanocubes. The incorporation results in increased plasmon-enhanced photocatalytic CO_2 conversion (Figure 54).^[156] Platinum core nanoparticles in different MOF shells could be tuned to regulate the selectivity of hydrogenation reactions.^[474] The significantly enhanced selectivity toward unsaturated alcohols is attributed to the preferential interaction of the MOF's coordinatively unsaturated metal sites with the carbon–oxygen rather than the carbon–carbon group of the reactants.

The reactant selectivity of reticular catalysts is an important feature and warrants further development. In a systematic study of Pd nanoparticles, Pd-ZIF-8 mesoscopic structures and Pd-ZIF-8 yolk-shell structures, reactant selectivity has already been improved.^[475] The yolk-shell structure of Pd nanoparticles enclosed by the ZIF-8 shell provides 100 nm void space for catalytic reactions. A cascade reaction that combines the catalytically active Pd nanoparticle core and -functionalized IRMOF-3 shell would produce a multifunctional catalyst.^[476]

This was further advanced by using two functional linkers, sulfonic acid and ammonium (bearing weak and strong acidity), for the creation of a Pt-UiO-66 core-shell system.^[477] The ratio of the sulfonic acid and ammonium linkers to the unfunctionalized linker was tuned in order to optimize the catalytic outcome. Last but not least, Pd nanoparticles were introduced into COF pores displaying nice catalytic results under highly acidic or basic conditions.^[478] All of these examples demonstrate that pairing catalytically active metal nanoparticles with reticular materials have the potential to improve the activity, selectivity and stability of the catalytic system.

9. Conclusion

In this review, we provided an overview of the chemical richness of reticular materials. This diversity reaches far beyond that of conventional solid-state materials. Bringing the chemistry of reticular materials to the nanoscale amplifies the range of possibilities even further paving the way for customization of nanoparticles with distinct properties for specific applications. While the potential of reticular framework nanoparticles is huge, they have to overcome certain challenges in order to facilitate their breakthrough in applications. These challenges are shared with other nanoparticle classes and can thus be addressed in synergistic efforts.

One of the main challenges is reproducibility. Since many characteristics of nanoparticles are determined by their size, small changes in size may lead to very different properties. Thus, a high degree of reproducibility is crucial for reliable nanoparticle properties and a key milestone for their application. In order to test this reproducibility, each nanoparticle batch has to be thoroughly characterized. Both for industrial applications as well as comparison of new nanoparticles with literature standard characterization protocols and SOPs are needed in order to guarantee reproducibility and comparability. Such careful characterization also requires suitable characterization techniques. With the daily emergence of new materials, we have millions of new materials with new properties arising from different characteristics meanwhile. These origins of the properties have to be understood to identify and develop new characterization techniques in order to enable a molecular understanding of structure-activity relationships. The development of proper characterization techniques for new materials is essential for applications and progress in the field—a fact that has been widely underrated so far. Reticular frameworks, particularly MOFs, ZIFs and COFs can be characterized in detail via X-ray techniques based on their crystalline structure. However, this provides only part of the picture of their characteristics and needs to be complemented with other techniques depending on the respective properties.

Another key challenge, which needs to be overcome specifically for industrial applications, is an easy synthesis of the materials. The easier the synthesis, the higher are the chances for real-world applications. In this case, easy synthesis implies a synthesis procedure that is commercially scalable and allows for economically sustainable mass production—including synthesis of the nanoparticle and all functionalization steps. Ideally, the entire functionalized nanoparticle can be produced

in a one-step and with a one-pot synthesis. The more reaction steps are involved and the more complicated they are, the less likely it will be for the nanoparticle product to reach industrial applications.

Box 6. The future of reticular framework nanoparticles

Due to the modular assembly of an infinite number of potential building units, the chemical space of reticular framework nanoparticles will continuously expand in the future. We envision the following aspects to have major impact to the research field:

- 1) Design and utilization of ab initio functional components instead of passive scaffold materials will generate new nanomaterials with very high multifunctional efficiency.
- 2) Extensive pool of framework nanoparticles and precise tunability will enable selection of most suitable materials for specific applications.
- 3) Self-assembly driven facile, scalable and cost-effective production of framework nanoparticles will promote the translation of functional nanomaterials to industrial manufacturing and general applications.

Reticular framework nanoparticles will continue to make important contributions to healthcare, agriculture, energy, resource efficiency, environmental programs, climate protection, mobility and civil security. Entirely new fields of application for the remarkable and versatile material class may emerge in the future.

A specific challenge for hybrid materials is their stability. Depending on the different chemistries used for synthesis and functionalization as well as on different environments used for the respective applications stabilities may vary strongly and need to be optimized for the specific application in the best case.

Toxicity is another important issue that needs to be addressed. This is key challenge especially for biological applications, but has to be considered for all other applications too. Due to the huge variety of material properties, both biodistribution as well as toxic effects may vary greatly between different nanomaterials. Thus, they have to be assessed for each single nanoparticle formulation. This can be done in first experiments for the material as synthesized, but has to be performed in full depth with the nanoparticles as used for the application by the respective industry that wants to use the nanoparticles. Hereby “toxicity” again has to be carefully addressed—if the effect can be specified to certain areas and directed to affect primarily the intended regions of the body, it may even turn into a therapeutically useful tool. However, lack of specificity will turn it into an unwanted toxic material, which is not desirable for applications.

The field of nanomaterial research is highly interdisciplinary based on the chemistry of the materials, their wide range of applications and the required characterization as well as the assessment of their impact on human health. Thus, only a joint effort of scientists from different disciplines, such as chemistry, physics, biology, pharmacy, medicine, engineering, and computer science can overcome the above-mentioned challenges to pave the way of reticular framework nanoparticles to reach their promise in all applications.

It seems beyond question that nanoparticles can and will make a huge impact on society. Given the feasibility and potential of reticular nanomaterials, we believe that they can revolutionize the field of nanotechnology (Box 6).

Conflict of Interest

The authors declare no conflict of interest.

Keywords

covalent organic frameworks, metal-organic frameworks, nanoparticles, reticular chemistry, zeolitic imidazolate frameworks

Received: November 1, 2019

Revised: December 13, 2019

Published online: February 24, 2020

- [1] a) H. Goesmann, C. Feldmann, *Angew. Chem., Int. Ed.* **2010**, *49*, 1362; b) R. Jin, C. Zeng, M. Zhou, Y. Chen, *Chem. Rev.* **2016**, *116*, 10346.
- [2] a) G. Chen, I. Roy, C. Yang, P. N. Prasad, *Chem. Rev.* **2016**, *116*, 2826; b) H. Zhang, H.-M. Cheng, P. Ye, *Chem. Soc. Rev.* **2018**, *47*, 6009; c) R. V. Uljin, R. Jerala, *Chem. Soc. Rev.* **2018**, *47*, 3391; d) H. Zhang, M. Chhowalla, Z. Liu, *Chem. Soc. Rev.* **2018**, *47*, 3015; e) X. Liu, C.-H. Yan, J. A. Capobianco, *Chem. Soc. Rev.* **2015**, *44*, 1299; f) L. M. Liz-Marzán, C. J. Murphy, J. Wang, *Chem. Soc. Rev.* **2014**, *43*, 3820; g) F. Caruso, T. Hyeon, V. M. Rotello, *Chem. Soc. Rev.* **2012**, *41*, 2537; h) D. V. Talapin, E. V. Shevchenko, *Chem. Rev.* **2016**, *116*, 10343; i) W. Lin, *Chem. Rev.* **2015**, *115*, 10407; j) F. Xia, H. Wang, D. Xiao, M. Dubey, A. Ramasubramaniam, *Nat. Photonics* **2014**, *8*, 899; k) B. Pelaz, C. Alexiou, R. A. Alvarez-Puebla, F. Alves, A. M. Andrews, S. Ashraf, L. P. Balogh, L. Ballerini, A. Bestetti, C. Brendel, S. Bosi, M. Carril, W. C. W. Chan, C. Chen, X. Chen, X. Chen, Z. Cheng, D. Cui, J. Du, C. Dullin, A. Escudero, N. Feliu, M. Gao, M. George, Y. Gogotsi, A. Grünweller, Z. Gu, N. J. Halas, N. Hampf, R. K. Hartmann, M. C. Hersam, P. Hunziker, J. Jian, X. Jiang, P. Jungebluth, P. Kadhiresan, K. Kataoka, A. Khademhosseini, J. Kopeček, N. A. Kotov, H. F. Krug, D. S. Lee, C.-M. Lehr, K. W. Leong, X.-J. Liang, M. Ling Lim, L. M. Liz-Marzán, X. Ma, P. Macchiarini, H. Meng, H. Möhwald, P. Mulvaney, A. E. Nel, S. Nie, P. Nordlander, T. Okano, J. Oliveira, T. H. Park, R. M. Penner, M. Prato, V. Puentes, V. M. Rotello, A. Samarakoon, R. E. Schaak, Y. Shen, S. Sjöqvist, A. G. Skirtach, M. G. Soliman, M. M. Stevens, H.-W. Sung, B. Z. Tang, R. Tietze, B. N. Udugama, J. S. VanEpps, T. Weil, P. S. Weiss, I. Willner, Y. Wu, L. Yang, Z. Yue, Q. Zhang, Q. Zhang, X.-E. Zhang, Y. Zhao, X. Zhou, W. J. Parak, *ACS Nano* **2017**, *11*, 2313; l) M. W. Tibbitt, J. E. Dahlman, R. Langer, *J. Am. Chem. Soc.* **2016**, *138*, 704; m) O. C. Farokhzad, R. Langer, *ACS Nano* **2009**, *3*, 16.
- [3] a) G. V. Lowry, A. Avellan, L. M. Gilbertson, *Nat. Nanotechnol.* **2019**, *14*, 517; b) M. Kah, N. Tufenkji, J. C. White, *Nat. Nanotechnol.* **2019**, *14*, 532; c) J. P. Giraldo, H. Wu, G. M. Newkirk, S. Kruss, *Nat. Nanotechnol.* **2019**, *14*, 541.
- [4] a) L. Midolo, A. Schliesser, A. Fiore, *Nat. Nanotechnol.* **2018**, *13*, 11; b) Q. Zhang, E. Uchaker, S. L. Candelaria, G. Cao, *Chem. Soc. Rev.* **2013**, *42*, 3127; c) Y. Li, G. A. Somorjai, *Nano Lett.* **2010**, *10*, 2289; d) A. Rani, R. Reddy, U. Sharma, P. Mukherjee, P. Mishra, A. Kuila, L. C. Sim, P. Saravanan, *J. Nanostruct. Chem.* **2018**, *8*, 255; e) M. Manikandan, T. Tanabe, P. Li, S. Ueda, G. V. Ramesh, R. Kodiyath, J. Wang, T. Hara, A. Dakshnamoorthy, S. Ishihara, K. Ariga, J. Ye, N. Umezawa, H. Abe, *ACS Appl. Mater. Interfaces* **2014**, *6*, 3790; f) W. Zhang, X. Jiang, X. Wang, Y. V. Kaneti, Y. Chen, J. Liu, J.-S. Jiang, Y. Yamauchi, M. Hu, *Angew. Chem., Int. Ed.* **2017**, *56*, 8435.
- [5] a) A. Zimpel, N. Al Danaf, B. Steinborn, J. Kuhn, M. Höhn, T. Bauer, P. Hirschle, W. Schrimpf, H. Engelke, E. Wagner, M. Barz, D. C. Lamb, U. Lächelt, S. Wuttke, *ACS Nano* **2019**, *13*, 3884; b) M. Steinfeldt, A. von Gleich, U. Petschow, R. Haum, *Nanotechnologies, Hazards and Resource Efficiency*, Spinger, Berlin **2007**; c) I. Iavicoli, V. Leso, W. Ricciardi, L. L. Hodson, M. D. Hoover, *Environ. Health* **2014**, *13*, 78.
- [6] a) N. Yousefi, X. Lu, M. Elimelech, N. Tufenkji, *Nat. Nanotechnol.* **2019**, *14*, 107; b) P. Westerhoff, A. Atkinson, J. Fortner, M. S. Wong, J. Zimmerman, J. Gardea-Torresdey, J. Ranville, P. Herckes, *Nat. Nanotechnol.* **2018**, *13*, 661; c) W. Gao, J. Wang, *ACS Nano* **2014**, *8*, 3170.
- [7] a) D. Alezi, Y. Belmabkhout, M. Suyetin, P. M. Bhatt, Ł. J. Weselirski, V. Solovyeva, K. Adil, I. Spanopoulos, P. N. Trikalitis, A.-H. Erwas, M. Eddaoudi, *J. Am. Chem. Soc.* **2015**, *137*, 13308; b) H. K. Lee, C. S. L. Koh, Y. H. Lee, C. Liu, I. Y. Phang, X. Han, C.-K. Tsung, X. Y. Ling, *Sci. Adv.* **2018**, *4*, eaar3208; c) C. A. Trickett, A. Helal, B. A. Al-Maythaly, Z. H. Yamani, K. E. Cordova, O. M. Yaghi, *Nat. Rev. Mater.* **2017**, *2*, 17045; d) M. Ding, R. W. Flaig, H.-L. Jiang, O. M. Yaghi, *Chem. Soc. Rev.* **2019**, *48*, 2783; e) M. T. Kapelewski, T. Runčevski, J. D. Tarver, H. Z. H. Jiang, K. E. Hurst, P. A. Parilla, A. Ayala, T. Gennett, S. A. FitzGerald, C. M. Brown, J. R. Long, *Chem. Mater.* **2018**, *30*, 8179; f) U. Eberle, M. Felderhoff, F. Schüth, *Angew. Chem., Int. Ed.* **2009**, *48*, 6608.
- [8] a) H.-J. Jin, J. Weissmüller, *Science* **2011**, *332*, 1179; b) C. Joachim, G. Rapenne, *ACS Nano* **2013**, *7*, 11; c) R. Asmatulu, in *Corrosion Protection and Control Using Nanomaterials* (Eds: V. S. Saji, R. Cook), Woodhead Publishing, Cambridge **2012**, p. 357.
- [9] a) V. K. Bajpai, M. Kamle, S. Shukla, D. K. Mahato, P. Chandra, S. K. Hwang, P. Kumar, Y. S. Huh, Y.-K. Han, *J. Food Drug Anal.* **2018**, *26*, 1201; b) V. D. Krishna, K. Wu, D. Su, M. C. J. Cheeran, J.-P. Wang, A. Perez, *Food Microbiol.* **2018**, *75*, 47; c) N. M. Julkapli, S. Bagheri, in *Nanotechnology in Environmental Science* (Eds: C. M. Hussain, A. K. Mishra), Wiley-VCH Verlag GmbH & Co. KGaA, Weinheim, Germany **2018**, Ch. 14, p. 443, <https://doi.org/10.1002/9783527808854>.
- [10] a) H. Furukawa, K. E. Cordova, M. O'Keeffe, O. M. Yaghi, *Science* **2013**, *341*, 1230444; b) S. Horike, S. Shimomura, S. Kitagawa, *Nat. Chem.* **2009**, *1*, 695; c) H.-C. Zhou, J. R. Long, O. M. Yaghi, *Chem. Rev.* **2012**, *112*, 673; d) H.-C. Zhou, S. Kitagawa, *Chem. Soc. Rev.* **2014**, *43*, 5415; e) G. Maurin, C. Serre, A. Cooper, G. Férey, *Chem. Soc. Rev.* **2017**, *46*, 3104.
- [11] a) B. Chen, Z. Yang, Y. Zhu, Y. Xia, *J. Mater. Chem. A* **2014**, *2*, 16811; b) A. Phan, C. J. Doonan, F. J. Uribe-Romo, C. B. Knobler, M. O'Keeffe, O. M. Yaghi, *Acc. Chem. Res.* **2010**, *43*, 58; c) J.-P. Zhang, Y.-B. Zhang, J.-B. Lin, X.-M. Chen, *Chem. Rev.* **2012**, *112*, 1001; d) D. Rodríguez-San-Miguel, F. Zamora, *Chem. Soc. Rev.* **2019**, *48*, 4375.
- [12] a) C. S. Diercks, O. M. Yaghi, *Science* **2017**, *355*, eaal1585; b) H. Wang, Z. Zeng, P. Xu, L. Li, G. Zeng, R. Xiao, Z. Tang, D. Huang, L. Tang, C. Lai, D. Jiang, Y. Liu, H. Yi, L. Qin, S. Ye, X. Ren, W. Tang, *Chem. Soc. Rev.* **2019**, *48*, 488; c) M. S. Lohse, T. Bein, *Adv. Funct. Mater.* **2018**, *28*, 1705553; d) S. Kandambeth, K. Dey, R. Banerjee, *J. Am. Chem. Soc.* **2019**, *141*, 1807; e) S. J. Lyle, P. J. Waller, O. M. Yaghi, *Trends Chem.* **2019**, *1*, 172; f) X. Feng, X. Ding, D. Jiang, *Chem. Soc. Rev.* **2012**, *41*, 6010; g) R. P. Bisbey, W. R. Dichtel, *ACS Cent. Sci.* **2017**, *3*, 533.
- [13] P. Z. Moghadam, A. Li, S. B. Wiggin, A. Tao, A. G. P. Maloney, P. A. Wood, S. C. Ward, D. Fairen-Jimenez, *Chem. Mater.* **2017**, *29*, 2618.

- [14] a) Y. He, W. Zhou, G. Qian, B. Chen, *Chem. Soc. Rev.* **2014**, *43*, 5657; b) X. Han, S. Yang, M. Schröder, *Nat. Rev. Chem.* **2019**, *3*, 108; c) K. Adil, Y. Belmabkhout, R. S. Pillai, A. Cadiou, P. M. Bhatt, A. H. Assen, G. Maurin, M. Eddaoudi, *Chem. Soc. Rev.* **2017**, *46*, 3402; d) N. S. Bobbitt, M. L. Mendonca, A. J. Howarth, T. Islamoglu, J. T. Hupp, O. K. Farha, R. Q. Snurr, *Chem. Soc. Rev.* **2017**, *46*, 3357; e) B. Li, H.-M. Wen, W. Zhou, B. Chen, *J. Phys. Chem. Lett.* **2014**, *5*, 3468; f) S. Ma, H.-C. Zhou, *Chem. Commun.* **2010**, *46*, 44; g) Y. Lin, C. Kong, Q. Zhang, L. Chen, *Adv. Energy Mater.* **2017**, *7*, 1601296; h) E. Barea, C. Montoro, J. A. R. Navarro, *Chem. Soc. Rev.* **2014**, *43*, 5419.
- [15] a) X. Zhao, Y. Wang, D.-S. Li, X. Bu, P. Feng, *Adv. Mater.* **2018**, *30*, 1705189; b) Z. Kang, L. Fan, D. Sun, *J. Mater. Chem. A* **2017**, *5*, 10073; c) M. S. Denny Jr., J. C. Moreton, L. Benz, S. M. Cohen, *Nat. Rev. Mater.* **2016**, *1*, 16078; d) X. Li, Y. Liu, J. Wang, J. Gascon, J. Li, B. Van der Bruggen, *Chem. Soc. Rev.* **2017**, *46*, 7124; e) B. Van de Voorde, B. Bueken, J. Denayer, D. De Vos, *Chem. Soc. Rev.* **2014**, *43*, 5766.
- [16] a) J. Canivet, A. Fateeva, Y. Guo, B. Coasne, D. Farrusseng, *Chem. Soc. Rev.* **2014**, *43*, 5594; b) M. J. Kalmutzki, C. S. Diercks, O. M. Yaghi, *Adv. Mater.* **2018**, *30*, 1704304; c) F. Fathieh, M. J. Kalmutzki, E. A. Kapustin, P. J. Waller, J. Yang, O. M. Yaghi, *Sci. Adv.* **2018**, *4*, eaat3198; d) H. Kim, S. Yang, S. R. Rao, S. Narayanan, E. A. Kapustin, H. Furukawa, A. S. Umans, O. M. Yaghi, E. N. Wang, *Science* **2017**, *356*, 430.
- [17] a) S. M. J. Rogge, A. Bavykina, J. Hajek, H. Garcia, A. I. Olivos-Suarez, A. Sepúlveda-Escribano, A. Vimont, G. Clet, P. Bazin, F. Kapteijn, M. Daturi, E. V. Ramos-Fernandez, F. X. Llabrés i Xamena, V. Van Speybroeck, J. Gascon, *Chem. Soc. Rev.* **2017**, *46*, 3134; b) C. S. Diercks, Y. Liu, K. E. Cordova, O. M. Yaghi, *Nat. Mater.* **2018**, *17*, 301; c) A. Dhakshinamoorthy, Z. Li, H. Garcia, *Chem. Soc. Rev.* **2018**, *47*, 8134; d) C. J. Doonan, C. J. Sumbly, *CrystEngComm* **2017**, *19*, 4044; e) X. Yu, L. Wang, S. M. Cohen, *CrystEngComm* **2017**, *19*, 4126; f) A. Herbst, C. Janiak, *CrystEngComm* **2017**, *19*, 4092; g) M. B. Majewski, A. J. Howarth, P. Li, M. R. Wasielewski, J. T. Hupp, O. K. Farha, *CrystEngComm* **2017**, *19*, 4082.
- [18] a) A. E. Baumann, D. A. Burns, B. Liu, V. S. Thoi, *Commun. Chem.* **2019**, *2*, 86; b) J. Calbo, M. J. Golomb, A. Walsh, *J. Mater. Chem. A* **2019**, *7*, 16571; c) L. Sun, M. G. Campbell, M. Dincă, *Angew. Chem., Int. Ed.* **2016**, *55*, 3566; d) S.-L. Li, Q. Xu, *Energy Environ. Sci.* **2013**, *6*, 1656; e) W. Zheng, C.-S. Tsang, L. Y. S. Lee, K.-Y. Wong, *Mater. Today Chem.* **2019**, *12*, 34.
- [19] a) L. E. Kreno, K. Leong, O. K. Farha, M. Allendorff, R. P. Van Duyne, J. T. Hupp, *Chem. Rev.* **2012**, *112*, 1105; b) A. Chidambaram, K. C. Stylianou, *Inorg. Chem. Front.* **2018**, *5*, 979; c) W. P. Lustig, S. Mukherjee, N. D. Rudd, A. V. Desai, J. Li, S. K. Ghosh, *Chem. Soc. Rev.* **2017**, *46*, 3242; d) I. Stassen, N. Burtch, A. Talin, P. Falcaro, M. Allendorff, R. Ameloot, *Chem. Soc. Rev.* **2017**, *46*, 3185; e) P. Falcaro, R. Ricco, C. M. Doherty, K. Liang, A. J. Hill, M. J. Styles, *Chem. Soc. Rev.* **2014**, *43*, 5513.
- [20] a) M. Peller, K. Böll, A. Zimpel, S. Wuttke, *Inorg. Chem. Front.* **2018**, *5*, 1760; b) Y. Cui, J. Zhang, H. He, G. Qian, *Chem. Soc. Rev.* **2018**, *47*, 5740; c) H.-S. Wang, *Coord. Chem. Rev.* **2017**, *349*, 139; d) E. Miller Sophie, H. Teplensky Michelle, Z. Moghadam Peyman, D. Fairen-Jimenez, *Interface Focus* **2016**, *6*, 20160027.
- [21] a) W. Chen, C. Wu, *Dalton Trans.* **2018**, *47*, 2114; b) S. Wang, C. M. McGuirk, A. d'Aquino, J. A. Mason, C. A. Mirkin, *Adv. Mater.* **2018**, *30*, 1800202; c) T. Simon-Yarza, A. Mielcarek, P. Couvreur, C. Serre, *Adv. Mater.* **2018**, *30*, 1707365; d) S. Wuttke, M. Lismont, A. Escudero, B. Rungtaweeworanit, W. J. Parak, *Biomaterials* **2017**, *123*, 172; e) P. Horcajada, R. Gref, T. Baati, P. K. Allan, G. Maurin, P. Couvreur, G. Férey, R. E. Morris, C. Serre, *Chem. Rev.* **2012**, *112*, 1232; f) C. He, D. Liu, W. Lin, *Chem. Rev.* **2015**, *115*, 11079; g) M. Lismont, L. Dreesen, S. Wuttke, *Adv. Funct. Mater.* **2017**, *27*, 1606314; h) M. Zhang, Z.-Y. Gu, M. Bosch, Z. Perry, H.-C. Zhou, *Coord. Chem. Rev.* **2015**, *293–294*, 327.
- [22] a) B. J. Smith, L. R. Parent, A. C. Overholts, P. A. Beaucage, R. P. Bisbey, A. D. Chavez, N. Hwang, C. Park, A. M. Evans, N. C. Gianneschi, W. R. Dichtel, *ACS Cent. Sci.* **2017**, *3*, 58; b) R. L. Li, N. C. Flanders, A. M. Evans, W. Ji, I. Castano, L. X. Chen, N. C. Gianneschi, W. R. Dichtel, *Chem. Sci.* **2019**, *10*, 3796; c) S. Mitra, H. S. Sasmal, T. Kundu, S. Kandambeth, K. Illath, D. Díaz Díaz, R. Banerjee, *J. Am. Chem. Soc.* **2017**, *139*, 4513; d) L. Bai, S. Z. F. Phua, W. Q. Lim, A. Jana, Z. Luo, H. P. Tham, L. Zhao, Q. Gao, Y. Zhao, *Chem. Commun.* **2016**, *52*, 4128.
- [23] V. K. LaMer, R. H. Dinegar, *J. Am. Chem. Soc.* **1950**, *72*, 4847.
- [24] B. S. Barros, O. J. de Lima Neto, A. C. de Oliveira Frós, J. Kulesza, *ChemistrySelect* **2018**, *3*, 7459.
- [25] a) J. Huo, M. Brightwell, S. El Hankari, A. Garai, D. Bradshaw, *J. Mater. Chem. A* **2013**, *1*, 15220; b) Y. Pan, Y. Liu, G. Zeng, L. Zhao, Z. Lai, *Chem. Commun.* **2011**, *47*, 2071.
- [26] a) W. J. Rieter, K. M. Pott, K. M. L. Taylor, W. Lin, *J. Am. Chem. Soc.* **2008**, *130*, 11584; b) P. Horcajada, T. Chalati, C. Serre, B. Gillet, C. Sebrie, T. Baati, J. F. Eubank, D. Heurtaux, P. Clayette, C. Kreuz, J.-S. Chang, Y. K. Hwang, V. Marsaud, P.-N. Bories, L. Cynober, S. Gil, G. Férey, P. Couvreur, R. Gref, *Nat. Mater.* **2010**, *9*, 172.
- [27] L. H. Wee, M. R. Lohe, N. Janssens, S. Kaskel, J. A. Martens, *J. Mater. Chem.* **2012**, *22*, 13742.
- [28] X. Han, X.-J. Wang, P.-Z. Li, R. Zou, M. Li, Y. Zhao, *CrystEngComm* **2015**, *17*, 8596.
- [29] a) Z. Xin, J. Bai, Y. Pan, M. J. Zaworotko, *Chem. – Eur. J.* **2010**, *16*, 13049; b) P. Horcajada, H. Chevreau, D. Heurtaux, F. Benyettou, F. Salles, T. Devic, A. Garcia-Marquez, C. Yu, H. Lavrard, C. L. Dutton, E. Magner, G. Maurin, E. Elkaïm, C. Serre, *Chem. Commun.* **2014**, *50*, 6872.
- [30] X. Cheng, A. Zhang, K. Hou, M. Liu, Y. Wang, C. Song, G. Zhang, X. Guo, *Dalton Trans.* **2013**, *42*, 13698.
- [31] a) M. Tsuji, *ChemistrySelect* **2017**, *2*, 805; b) Y.-J. Zhu, F. Chen, *Chem. Rev.* **2014**, *114*, 6462; c) A. V. Nikam, B. L. V. Prasad, A. A. Kulkarni, *CrystEngComm* **2018**, *20*, 5091.
- [32] a) J. Klinowski, F. A. Almeida Paz, P. Silva, J. Rocha, *Dalton Trans.* **2011**, *40*, 321; b) E. Haque, N. A. Khan, C. M. Kim, S. H. Jhung, *Cryst. Growth Des.* **2011**, *11*, 4413; c) A. Laybourn, J. Katrib, R. S. Ferrari-John, C. G. Morris, S. Yang, O. Udoudo, T. L. Easun, C. Dodds, N. R. Champness, S. W. Kingman, M. Schröder, *J. Mater. Chem. A* **2017**, *5*, 7333; d) J.-S. Choi, W.-J. Son, J. Kim, W.-S. Ahn, *Microporous Mesoporous Mater.* **2008**, *116*, 727.
- [33] a) T. Chalati, P. Horcajada, R. Gref, P. Couvreur, C. Serre, *J. Mater. Chem.* **2011**, *21*, 2220; b) S. H. Jhung, J. H. Lee, J. W. Yoon, C. Serre, G. Férey, J. S. Chang, *Adv. Mater.* **2007**, *19*, 121; c) S. Wuttke, S. Braigt, T. Preiß, A. Zimpel, J. Sicklinger, C. Bellomo, J. O. Rädler, A. M. Vollmar, T. Bein, *Chem. Commun.* **2015**, *51*, 15752.
- [34] a) K. Okitsu, M. Ashokkumar, F. Grieser, *J. Phys. Chem. B* **2005**, *109*, 20673; b) K. S. Suslick, T. Hyeon, M. Fang, *Chem. Mater.* **1996**, *8*, 2172.
- [35] E. Haque, N. A. Khan, J. H. Park, S. H. Jhung, *Chem. – Eur. J.* **2010**, *16*, 1046.
- [36] J. Amaro-Gahete, R. Klee, D. Esquivel, J. R. Ruiz, C. Jiménez-Sanchidrián, F. J. Romero-Salguero, *Ultrason. Sonochem.* **2019**, *50*, 59.
- [37] S. Choi, M. Oh, *Angew. Chem., Int. Ed.* **2019**, *58*, 866.
- [38] a) A. Schaate, P. Roy, A. Godt, J. Lippke, F. Waltz, M. Wiebcke, P. Behrens, *Chem. – Eur. J.* **2011**, *17*, 6643; b) T. Tsuruoka, S. Furukawa, Y. Takashima, K. Yoshida, S. Isoda, S. Kitagawa, *Angew. Chem., Int. Ed.* **2009**, *48*, 4739; c) M. Calik, T. Sick, M. Dogru, M. Döblinger, S. Datz, H. Budde, A. Hartschuh, F. Auras, T. Bein, *J. Am. Chem. Soc.* **2016**, *138*, 1234.
- [39] D. Jiang, A. D. Burrows, K. J. Edler, *CrystEngComm* **2011**, *13*, 6916.

- [40] Y. Zhao, Q. Zhang, Y. Li, R. Zhang, G. Lu, *ACS Appl. Mater. Interfaces* **2017**, *9*, 15079.
- [41] W. Morris, S. Wang, D. Cho, E. Auyeung, P. Li, O. K. Farha, C. A. Mirkin, *ACS Appl. Mater. Interfaces* **2017**, *9*, 33413.
- [42] a) C. V. McGuire, R. S. Forgan, *Chem. Commun.* **2015**, *51*, 5199; b) F. Vermoortele, B. Bueken, G. Le Bars, B. Van de Voorde, M. Vandichel, K. Houthoofd, A. Vimont, M. Daturi, M. Waroquier, V. Van Speybroeck, C. Kirschhock, D. E. De Vos, *J. Am. Chem. Soc.* **2013**, *135*, 11465; c) W. Schrimpf, J. Jiang, Z. Ji, P. Hirschle, D. C. Lamb, O. M. Yaghi, S. Wuttke, *Nat. Commun.* **2018**, *9*, 1647; d) L. Liu, Z. Chen, J. Wang, D. Zhang, Y. Zhu, S. Ling, K.-W. Huang, Y. Belmabkhout, K. Adil, Y. Zhang, B. Slater, M. Eddaoudi, Y. Han, *Nat. Chem.* **2019**, *11*, 622; e) S. Dissegna, K. Epp, W. R. Heinz, G. Kieslich, R. A. Fischer, *Adv. Mater.* **2018**, *30*, 1704501; f) C. D. Fast, J. Woods, J. Lentchner, T. A. Makal, *Dalton Trans.* **2019**, *48*, 14696.
- [43] a) Y. Wan, Zhao, *Chem. Rev.* **2007**, *107*, 2821; b) F. Schüth, *Angew. Chem., Int. Ed.* **2003**, *42*, 3604.
- [44] a) W. J. Rieter, K. M. L. Taylor, W. Lin, *J. Am. Chem. Soc.* **2007**, *129*, 9852; b) W. J. Rieter, K. M. L. Taylor, H. An, W. Lin, W. Lin, *J. Am. Chem. Soc.* **2006**, *128*, 9024.
- [45] W. Shang, X. Kang, H. Ning, J. Zhang, X. Zhang, Z. Wu, G. Mo, X. Xing, B. Han, *Langmuir* **2013**, *29*, 13168.
- [46] X. Cai, Z. Xie, M. Pang, J. Lin, *Cryst. Growth Des.* **2019**, *19*, 556.
- [47] X.-X. Huang, L.-G. Qiu, W. Zhang, Y.-P. Yuan, X. Jiang, A.-J. Xie, Y.-H. Shen, J.-F. Zhu, *CrystEngComm* **2012**, *14*, 1613.
- [48] Y. Zhao, J. Zhang, B. Han, J. Song, J. Li, Q. Wang, *Angew. Chem., Int. Ed.* **2011**, *50*, 636.
- [49] X. Sang, J. Zhang, J. Xiang, J. Cui, L. Zheng, J. Zhang, Z. Wu, Z. Li, G. Mo, Y. Xu, J. Song, C. Liu, X. Tan, T. Luo, B. Zhang, B. Han, *Nat. Commun.* **2017**, *8*, 175.
- [50] J.-Z. Wei, X.-L. Wang, X.-J. Sun, Y. Hou, X. Zhang, D.-D. Yang, H. Dong, F.-M. Zhang, *Inorg. Chem.* **2018**, *57*, 3818.
- [51] A. B. D. Nandiyanto, X. He, W.-N. Wang, *CrystEngComm* **2019**, *21*, 2268.
- [52] K. Leng, Y. Sun, X. Li, S. Sun, W. Xu, *Cryst. Growth Des.* **2016**, *16*, 1168.
- [53] K. Užarević, T. C. Wang, S.-Y. Moon, A. M. Fidelli, J. T. Hupp, O. K. Farha, T. Friščić, *Chem. Commun.* **2016**, *52*, 2133.
- [54] X. Li, Z. Zhang, W. Xiao, S. Deng, C. Chen, N. Zhang, *J. Mater. Chem. A* **2019**, *7*, 14504.
- [55] a) J. Ma, S. M.-Y. Lee, C. Yi, C.-W. Li, *Lab Chip* **2017**, *17*, 209; b) Y. Liu, X. Jiang, *Lab Chip* **2017**, *17*, 3960; c) S. A. Khan, A. Günther, M. A. Schmidt, K. F. Jensen, *Langmuir* **2004**, *20*, 8604; d) G. M. Whitesides, *Nature* **2006**, *442*, 368; e) N. Convery, N. Gadegaard, *Micro Nano Eng.* **2019**, *2*, 76.
- [56] S. Tai, W. Zhang, J. Zhang, G. Luo, Y. Jia, M. Deng, Y. Ling, *Microporous Mesoporous Mater.* **2016**, *220*, 148.
- [57] a) M. Rubio-Martinez, M. P. Batten, A. Polyzos, K.-C. Carey, J. I. Mardel, K.-S. Lim, M. R. Hill, *Sci. Rep.* **2014**, *4*, 5443; b) A. Polyzoidis, T. Altenburg, M. Schwarzer, S. Loebbecke, S. Kaskel, *Chem. Eng. J.* **2016**, *283*, 971; c) C. McKinstry, R. J. Cathcart, E. J. Cussen, A. J. Fletcher, S. V. Patwardhan, J. Sefcik, *Chem. Eng. J.* **2016**, *285*, 718; d) L. Paseta, B. Seoane, D. Julve, V. Sebastián, C. Téllez, J. Coronas, *ACS Appl. Mater. Interfaces* **2013**, *5*, 9405; e) K.-J. Kim, Y. J. Li, P. B. Kreider, C.-H. Chang, N. Wannenmacher, P. K. Thallapally, H.-G. Ahn, *Chem. Commun.* **2013**, *49*, 11518; f) A. S. Munn, P. W. Dunne, S. V. Y. Tang, E. H. Lester, *Chem. Commun.* **2015**, *51*, 12811; g) G. H. Albuquerque, R. C. Fitzmorris, M. Ahmadi, N. Wannenmacher, P. K. Thallapally, B. P. McGrail, G. S. Herman, *CrystEngComm* **2015**, *17*, 5502; h) T. Rhauderwiek, S. Waitschat, S. Wuttke, H. Reinsch, T. Bein, N. Stock, *Inorg. Chem.* **2016**, *55*, 5312; i) R. Ameloot, F. Vermoortele, W. Vanhove, M. B. J. Roeffaers, B. F. Sels, D. E. De Vos, *Nat. Chem.* **2011**, *3*, 382; j) M. Rubio-Martinez, T. D. Hadley, M. P. Batten, K. Constanti-Carey, T. Barton, D. Marley, A. Mönch, K.-S. Lim, M. R. Hill, *ChemSusChem* **2016**, *9*, 938; k) M. Taddei, D. A. Steitz, J. A. van Bokhoven, M. Ranocchiar, *Chem. – Eur. J.* **2016**, *22*, 3245; l) D. Rodríguez-San-Miguel, A. Abrishamkar, J. A. R. Navarro, R. Rodríguez-Trujillo, D. B. Amabilino, R. Mas-Ballesté, F. Zamora, J. Puigmartí-Luis, *Chem. Commun.* **2016**, *52*, 9212; m) V. Singh, S. Jang, N. K. Vishwakarma, D.-P. Kim, *NPG Asia Mater.* **2018**, *10*, e456; n) A. Abrishamkar, D. Rodríguez-San-Miguel, J. A. Rodríguez Navarro, R. Rodríguez-Trujillo, D. B. Amabilino, R. Mas-Ballesté, F. Zamora, A. J. deMello, J. Puigmartí-Luis, *J. Vis. Exp.* **2017**, *125*, e56020; o) Y. Zhao, Z. Liao, Z. Xiang, *Chem. Eng. Sci.* **2019**, *195*, 801.
- [58] L. D'Arras, C. Sasso, L. Rozes, C. Sanchez, J. Marrot, S. Marre, C. Aymonier, *New J. Chem.* **2014**, *38*, 1477.
- [59] G.-Y. Jeong, R. Ricco, K. Liang, J. Ludwig, J.-O. Kim, P. Falcaro, D.-P. Kim, *Chem. Mater.* **2015**, *27*, 7903.
- [60] M. Faustini, J. Kim, G.-Y. Jeong, J. Y. Kim, H. R. Moon, W.-S. Ahn, D.-P. Kim, *J. Am. Chem. Soc.* **2013**, *135*, 14619.
- [61] a) M. M. Modena, B. Rühle, T. P. Burg, S. Wuttke, *Adv. Mater.* **2019**, *31*, 1901556; b) P. Hirschle, T. Preiß, F. Auras, A. Pick, J. Völkner, D. Valdepérez, G. Witte, W. J. Parak, J. O. Rädler, S. Wuttke, *CrystEngComm* **2016**, *18*, 4359; c) P. Hirschle, C. Hirschle, K. Böll, M. Döblinger, M. Höhn, J. M. Tuffnell, C. W. Ashling, D. A. Keen, T. D. Bennett, J. O. Rädler, E. Wagner, M. Peller, U. Lächelt, S. Wuttke, unpublished.
- [62] a) P. C. Lin, S. Lin, P. C. Wang, R. Sridhar, *Biotechnol. Adv.* **2014**, *32*, 711; b) A. J. Howarth, A. W. Peters, N. A. Vermeulen, T. C. Wang, J. T. Hupp, O. K. Farha, *Chem. Mater.* **2017**, *29*, 26; c) R. S. Forgan, *Dalton Trans.* **2019**, *48*, 9037; d) D. Ongari, P. G. Boyd, S. Barthel, M. Witman, M. Haranczyk, B. Smit, *Langmuir* **2017**, *33*, 14529; e) B. E. G. Lucier, S. Chen, Y. Huang, *Acc. Chem. Res.* **2018**, *51*, 319.
- [63] A. L. González, C. Noguez, J. Beránek, A. S. Barnard, *J. Phys. Chem. C* **2014**, *118*, 9128.
- [64] S. Zhang, J. Li, G. Lykotraftis, G. Bao, S. Suresh, *Adv. Mater.* **2009**, *21*, 419.
- [65] S. Pal, C. Dalal, N. R. Jana, *ACS Omega* **2017**, *2*, 8948.
- [66] S. Shen, Y. Wu, Y. Liu, D. Wu, *Int. J. Nanomed.* **2017**, *12*, 4085.
- [67] Y. Bai, Y. Dou, L.-H. Xie, W. Rutledge, J.-R. Li, H.-C. Zhou, *Chem. Soc. Rev.* **2016**, *45*, 2327.
- [68] M. Li, D. Li, M. O'Keeffe, O. M. Yaghi, *Chem. Rev.* **2014**, *114*, 1343.
- [69] a) H. Deng, C. J. Doonan, H. Furukawa, R. B. Ferreira, J. Towne, C. B. Knobler, B. Wang, O. M. Yaghi, *Science* **2010**, *327*, 846; b) A. C. H. Sue, R. V. Mannige, H. Deng, D. Cao, C. Wang, F. Gándara, J. F. Stoddart, S. Whitelam, O. M. Yaghi, *Proc. Natl. Acad. Sci. USA* **2015**, *112*, 5591.
- [70] J. H. Cavka, S. Jakobsen, U. Olsbye, N. Guillou, C. Lamberti, S. Bordiga, K. P. Lillerud, *J. Am. Chem. Soc.* **2008**, *130*, 13850.
- [71] Y. V. Kaneti, J. Tang, R. R. Salunkhe, X. Jiang, A. Yu, K. C. W. Wu, Y. Yamauchi, *Adv. Mater.* **2017**, *29*, 1604898.
- [72] a) V. Klang, N. B. Matsko, C. Valenta, F. Hofer, *Micron* **2012**, *43*, 85; b) A. Ponce, S. Mejía-Rosales, M. José-Yacamán, in *Nanoparticles in Biology and Medicine: Methods and Protocols* (Ed: M. Soloviev), Humana Press, Totowa, NJ **2012**, p. 453, https://doi.org/10.1007/978-1-61779-953-2_37; c) J. Y. Liu, *J. Electron Microsc.* **2005**, *54*, 251; d) K. D. Vernon-Parry, *III-Vs Review* **2000**, *13*, 40; e) N. de Jonge, F. M. Ross, *Nat. Nanotechnol.* **2011**, *6*, 695; f) E. Buhr, N. Senftleben, T. Klein, D. Bergmann, D. Grieser, C. G. Frase, H. Bosse, *Meas. Sci. Technol.* **2009**, *20*, 084025.
- [73] a) S. Rades, V.-D. Hodoroba, T. Salge, T. Wirth, M. P. Lobera, R. H. Labrador, K. Natte, T. Behnke, T. Gross, W. E. S. Unger, *RSC Adv.* **2014**, *4*, 49577; b) P. Luo, I. Morrison, A. Dudkiewicz, K. Tiede, E. Boyes, P. O'Toole, S. Park, A. B. Boxall, *J. Microsc.* **2013**, *250*, 32.

- [74] a) M. Malatesta, *Eur. J. Histochem.* **2016**, *60*, 2751; b) M. Asadi Asadabad, M. Jafari Eskandari, *Synth. React. Inorg., Met.-Org., Nano-Met. Chem.* **2015**, *45*, 323; c) D. Su, *Green Energy Environ.* **2017**, *2*, 70; d) J. E. Evans, K. L. Jungjohann, N. D. Browning, I. Arslan, *Nano Lett.* **2011**, *11*, 2809.
- [75] C. Wiktor, M. Meledina, S. Turner, O. I. Lebedev, R. A. Fischer, *J. Mater. Chem. A* **2017**, *5*, 14969.
- [76] B. J. Graham, D. G. C. Hildebrand, A. T. Kuan, J. T. Maniates-Selvin, L. A. Thomas, B. L. Shanny, W.-C. A. Lee, *bioRxiv* **2019**, <https://doi.org/10.1101/657346>.
- [77] R. Fernandez-Leiro, S. H. W. Scheres, *Nature* **2016**, *537*, 339.
- [78] R. T. Schirra, Jr., P. Zhang, *Curr. Protoc. Cytom.* **2014**, *70*, 12.36.1.
- [79] N. J. Severs, *Nat. Protoc.* **2007**, *2*, 547.
- [80] a) Y. F. Dufrêne, T. Ando, R. Garcia, D. Alsteens, D. Martinez-Martin, A. Engel, C. Gerber, D. J. Müller, *Nat. Nanotechnol.* **2017**, *12*, 295; b) A. N. Patel, C. Kranz, *Annu. Rev. Anal. Chem.* **2018**, *11*, 329; c) P. Klapetek, M. Valtr, D. Nečas, O. Salyk, P. Dzik, *Nanoscale Res. Lett.* **2011**, *6*, 514; d) J. Zhong, J. Yan, *RSC Adv.* **2016**, *6*, 1103; e) Y. Ebenstein, E. Nahum, U. Banin, *Nano Lett.* **2002**, *2*, 945; f) I. U. Vakarelski, S. C. Brown, B. M. Moudgil, K. Higashitani, *Adv. Powder Technol.* **2007**, *18*, 605.
- [81] Y. Seo, W. Jhe, *Rep. Prog. Phys.* **2007**, *71*, 016101.
- [82] F. Pederzoli, G. Tosi, M. A. Vandelli, D. Belletti, F. Forni, B. Ruozi, *Wiley Interdiscip. Rev.: Nanomed. Nanobiotechnol.* **2017**, *9*, e1467.
- [83] a) V. Filipe, A. Hawe, W. Jiskoot, *Pharm. Res.* **2010**, *27*, 796; b) J. B. Simonsen, J. B. Larsen, C. Hempel, N. Eng, A. Fossum, T. L. Andresen, *Cytometry A* **2019**, *95*, 917; c) F. Caputo, J. Clogston, L. Calzolari, M. Rösslein, A. Prina-Mello, *J. Controlled Release* **2019**, *299*, 31.
- [84] H. Rauscher, K. Rasmussen, B. Sokull-Klütgen, *Chem. Ing. Tech.* **2017**, *89*, 224.
- [85] International Organization for Standardization, *Particle Size Analysis: Laser Diffraction Methods, [ISO 13320:2009(E)]*, ISO, Geneva, Switzerland **2009**.
- [86] J. Stetefeld, S. A. McKenna, T. R. Patel, *Biophys. Rev.* **2016**, *8*, 409.
- [87] a) R. Xu, *Particuology* **2015**, *18*, 11; b) B. Chu, T. Liu, *J. Nanopart. Res.* **2000**, *2*, 29.
- [88] a) S. K. Brar, M. Verma, *Trends Anal. Chem.* **2011**, *30*, 4; b) P. J. Wyatt, *Anal. Chem.* **2014**, *86*, 7171.
- [89] C. Y. Tay, M. I. Setyawati, J. Xie, W. J. Parak, D. T. Leong, *Adv. Funct. Mater.* **2014**, *24*, 5936.
- [90] a) V. A. Bloomfield, *Annu. Rev. Biophys. Bioeng.* **1981**, *10*, 421; b) P. Zakharov, F. Scheffold, in *Light Scattering Reviews 4: Single Light Scattering and Radiative Transfer* (Ed: A. A. Kokhanovsky), Springer, Berlin **2009**, p. 433.
- [91] a) W. Burchard, *Light Scattering from Polymers*, Springer-Verlag, Berlin **1983**; b) D. K. Carpenter, *J. Chem. Educ.* **1977**, *54*, A430.
- [92] a) S. W. Provencher, *Comput. Phys. Commun.* **1982**, *27*, 229; b) D. E. Koppel, *J. Chem. Phys.* **1972**, *57*, 4814; c) P. A. Hassan, S. K. Kulshreshtha, *J. Colloid Interface Sci.* **2006**, *300*, 744.
- [93] a) L. Shang, G. U. Nienhaus, *Acc. Chem. Res.* **2017**, *50*, 387; b) G. U. Nienhaus, P. Maffre, K. Nienhaus, in *Methods Enzymol.*, Vol. 519, (Ed: S. Y. Tetin) Academic Press, San Diego, CA **2013**, p. 115; c) S. Dominguez-Medina, S. Chen, J. Blankenburg, P. Swanglap, C. F. Landes, S. Link, *Annu. Rev. Phys. Chem.* **2016**, *67*, 489.
- [94] K. Koynov, H. J. Butt, *Curr. Opin. Colloid Interface Sci.* **2012**, *17*, 377.
- [95] a) J. Gross, S. Sayle, A. R. Karow, U. Bakowsky, P. Garidel, *Eur. J. Pharm. Biopharm.* **2016**, *104*, 30; b) M. Wright, *Methods Mol. Biol.* **2012**, *906*, 511.
- [96] R. Dzakupas, D. Axelrod, *Biophys. J.* **2004**, *87*, 1288.
- [97] a) W. Anderson, D. Kozak, V. A. Coleman, Å. K. Jämting, M. Trau, *J. Colloid Interface Sci.* **2013**, *405*, 322; b) P. Hole, K. Sillence, C. Hannell, C. M. Maguire, M. Roeslein, G. Suarez, S. Capracotta, Z. Magdolenova, L. Horev-Azaria, A. Dybowska, L. Cooke, A. Haase, S. Contal, S. Manø, A. Vennemann, J.-J. Sauvain, K. C. Staunton, S. Anguissola, A. Luch, M. Dusinska, R. Korenstein, A. C. Gutleb, M. Wiemann, A. Prina-Mello, M. Riediker, P. Wick, *J. Nanopart. Res.* **2013**, *15*, 2101.
- [98] a) C. Minelli, A. Sikora, R. Garcia-Diez, K. Sparnacci, C. Gollwitzer, M. Krumrey, A. G. Shard, *Anal. Methods* **2018**, *10*, 1725; b) A. G. Shard, K. Sparnacci, A. Sikora, L. Wright, D. Bartczak, H. Goenaga-Infante, C. Minelli, *Anal. Methods* **2018**, *10*, 2647; c) D. Langevin, O. Lozano, A. Salvati, V. Kestens, M. Monopoli, E. Raspaud, S. Mariot, A. Salonen, S. Thomas, M. Driessen, A. Haase, I. Nelissen, N. Smisdorn, P. P. Pompa, G. Maiorano, V. Puntès, D. Puchowicz, M. Stępnik, G. Suárez, M. Riediker, F. Benetti, I. Mičetić, M. Venturini, W. G. Kreyling, M. van der Zande, H. Bouwmeester, S. Milani, J. O. Rädler, S. Mühlhopt, I. Lynch, K. Dawson, *NanoImpact* **2018**, *10*, 97; d) V. Kestens, V. A. Coleman, P.-J. De Temmerman, C. Minelli, H. Woehlecke, G. Roebben, *Langmuir* **2017**, *33*, 8213.
- [99] a) C. E. Marshall, R. Whytlaw-Gray, *Proc. R. Soc. London, Ser. A* **1930**, *126*, 427; b) M. P. Monopoli, D. Walczyk, A. Campbell, G. Elia, I. Lynch, F. Baldelli Bombelli, K. A. Dawson, *J. Am. Chem. Soc.* **2011**, *133*, 2525; c) M. A. Livshits, E. Khomyakova, E. G. Evtushenko, V. N. Lazarev, N. A. Kulemin, S. E. Semina, E. V. Generozov, V. M. Govorun, *Sci. Rep.* **2015**, *5*, 17319; d) P. M. Kelly, C. Åberg, E. Polo, A. O'Connell, J. Cookman, J. Fallon, Ž. Krpetić, K. A. Dawson, *Nat. Nanotechnol.* **2015**, *10*, 472.
- [100] T. Svedberg, *Nature* **1937**, *139*, 1051.
- [101] a) P. Schuck, *Biophys. Rev.* **2013**, *5*, 159; b) D. Mehn, I. M. Rio-Echevarria, D. Gilliland, M. Kaiser, K. Vilsmeier, P. Schuck, W. Wohlleben, *NanoImpact* **2018**, *10*, 87; c) A. Bekdemir, F. Stellacci, *Nat. Commun.* **2016**, *7*, 13121; d) J. A. Jamison, K. M. Krueger, J. T. Mayo, C. T. Yavuz, J. J. Redden, V. L. Colvin, *Nanotechnology* **2009**, *20*, 355702; e) T. LeBrun, P. Schuck, R. Wei, J. S. Yoon, X. Dong, N. Y. Morgan, J. Fagan, H. Zhao, *PLoS One* **2018**, *13*, e0201529.
- [102] J. Walter, R. Löhr, E. Karabudak, W. Reis, J. Mikhael, W. Peukert, W. Wohlleben, H. Cölfen, *ACS Nano* **2014**, *8*, 8871.
- [103] a) S. Süß, C. Metzger, C. Damm, D. Segets, W. Peukert, *Powder Technol.* **2018**, *339*, 264; b) L. Pitkänen, A. M. Striegel, *Trends Anal. Chem.* **2016**, *80*, 311; c) A. Badasyan, A. Mavrič, I. Kralj Cigić, T. Bencik, M. Valant, *Soft Matter* **2018**, *14*, 4735; d) J. D. Robertson, L. Rizzello, M. Avila-Olias, J. Gaitzsch, C. Contini, M. S. Magorí, S. A. Renshaw, G. Battaglia, *Sci. Rep.* **2016**, *6*, 27494; e) S. Podzimek, *Light Scattering, Size Exclusion Chromatography and Asymmetric Flow Field Flow Fractionation: Powerful Tools for the Characterization of Polymers, Proteins and Nanoparticles*, John Wiley & Sons, New York **2011**.
- [104] S. Paul-Dauphin, F. Karaca, T. J. Morgan, M. Millan-Agorio, A. A. Herod, R. Kandiyoti, *Energy Fuels* **2007**, *21*, 3484.
- [105] P. Hong, S. Koza, E. S. P. Bouvier, *J. Liq. Chromatogr. Relat. Technol.* **2012**, *35*, 2923.
- [106] S. Øien-Ødegaard, G. C. Shearer, D. S. Wragg, K. P. Lillerud, *Chem. Soc. Rev.* **2017**, *46*, 4867.
- [107] M. O'Keefe, M. A. Peskov, S. J. Ramsden, O. M. Yaghi, *Acc. Chem. Res.* **2008**, *41*, 1782.
- [108] a) A. A. Bunaciu, E. g. Udriștioiu, H. Y. Aboul-Enein, *Crit. Rev. Anal. Chem.* **2015**, *45*, 289; b) B. Ingham, *Crystallogr. Rev.* **2015**, *21*, 229.
- [109] T. Skarzynski, *Acta Crystallogr., Sect. D: Biol. Crystallogr.* **2013**, *69*, 1283.
- [110] T. Tschentscher, M. Altarelli, R. Brinkmann, T. Delissen, A. S. Schwarz, K. Witte, *Synchrotron Radiat. News* **2006**, *19*, 13.
- [111] A. Spek, *Acta Crystallogr., Sect. C: Struct. Chem.* **2015**, *71*, 9.
- [112] O. V. Dolomanov, L. J. Bourhis, R. J. Gildea, J. A. K. Howard, H. Puschmann, *J. Appl. Crystallogr.* **2009**, *42*, 339.
- [113] C. E. Wilmer, M. Leaf, C. Y. Lee, O. K. Farha, B. G. Hauser, J. T. Hupp, R. Q. Snurr, *Nat. Chem.* **2011**, *4*, 83.

- [114] O. K. Farha, A. M. Shultz, A. A. Sarjeant, S. T. Nguyen, J. T. Hupp, *J. Am. Chem. Soc.* **2011**, *133*, 5652.
- [115] C. Baerlocher, F. Gramm, L. Massuger, L. B. McCusker, Z. B. He, S. Hovmöller, X. D. Zou, *Science* **2007**, *315*, 1113.
- [116] T. Li, A. J. Senesi, B. Lee, *Chem. Rev.* **2016**, *116*, 11128.
- [117] P. Tarazona, U. M. B. Marconi, R. Evans, *Mol. Phys.* **1987**, *60*, 573.
- [118] E. P. Barrett, L. G. Joyner, P. P. Halenda, *J. Am. Chem. Soc.* **1951**, *73*, 373.
- [119] a) K. S. W. Sing, *Colloids Surf.* **1989**, *38*, 113; b) K. A. Cychosz, M. Thommes, *Engineering* **2018**, *4*, 559.
- [120] a) J. A. Mason, M. Veenstra, J. R. Long, *Chem. Sci.* **2014**, *5*, 32; b) B. Streppel, M. Hirscher, *Phys. Chem. Chem. Phys.* **2011**, *13*, 3220.
- [121] M. Thommes, K. Kaneko, A. V. Neimark, J. P. Olivier, F. Rodriguez-Reinoso, J. Rouquerol, K. S. W. Sing, *Pure Appl. Chem.* **2015**, *87*, 1051.
- [122] J. Rouquerol, F. Rouquerol, P. Llewellyn, G. Maurin, K. S. Sing, *Adsorption by Powders and Porous Solids: Principles, Methodology and Applications*, Academic Press, New York **2013**.
- [123] F. Gandara, T. D. Bennett, *IUCrj* **2014**, *1*, 563.
- [124] D. A. Gómez-Gualdrón, P. Z. Moghadam, J. T. Hupp, O. K. Farha, R. Q. Snurr, *J. Am. Chem. Soc.* **2016**, *138*, 215.
- [125] Z. Yu, F. Yang, S. Dai, R. Qiao, *Sci. Rep.* **2018**, *8*, 5191.
- [126] T. L. Doane, C.-H. Chuang, R. J. Hill, C. Burda, *Acc. Chem. Res.* **2012**, *45*, 317.
- [127] N. Bukar, S. S. Zhao, D. M. Charbonneau, J. N. Pelletier, J.-F. Masson, *Chem. Commun.* **2014**, *50*, 4947.
- [128] M. Gumustas, C. T. Sengel-Turk, A. Gumustas, S. A. Ozkan, B. Uslu, in *Multifunctional Systems for Combined Delivery, Biosensing and Diagnostics* (Ed: A. M. Grumezescu), Elsevier, Amsterdam **2017**, Ch. 5, p. 67.
- [129] R. Vogel, A. K. Pal, S. Jambhrunkar, P. Patel, S. S. Thakur, E. Reátegui, H. S. Parekh, P. Saá, A. Stassinopoulos, M. F. Broom, *Sci. Rep.* **2017**, *7*, 17479.
- [130] a) P. M. Carvalho, M. R. Felício, N. C. Santos, S. Gonçalves, M. M. Domingues, *Front. Chem.* **2018**, *6*, 237; b) A. Sikora, A. G. Shard, C. Minelli, *Langmuir* **2016**, *32*, 2216.
- [131] S. Bhattacharjee, *J. Controlled Release* **2016**, *235*, 337.
- [132] a) E. Weatherall, G. R. Willmott, *Analyst* **2015**, *140*, 3318; b) E. L. C. J. Blundell, R. Vogel, M. Platt, *Langmuir* **2016**, *32*, 1082.
- [133] D. Kozak, W. Anderson, R. Vogel, S. Chen, F. Antaw, M. Trau, *ACS Nano* **2012**, *6*, 6990.
- [134] N. Arjmandi, W. Van Roy, L. Lagae, G. Borghs, *Anal. Chem.* **2012**, *84*, 8490.
- [135] a) J. M. Costa-Fernández, M. Menéndez-Miranda, D. Bouzas-Ramos, J. R. Encinar, A. Sanz-Medel, *Trends Anal. Chem.* **2016**, *84*, 139; b) W. Ma, S. Xu, W. Ai, C. Lin, Y. Bai, H. Liu, *Chem. Commun.* **2019**, *55*, 6898; c) Y.-H. Shih, C.-H. Chien, B. Singco, C.-L. Hsu, C.-H. Lin, H.-Y. Huang, *Chem. Commun.* **2013**, *49*, 4929; d) C. Chang, J. Zhang, Z. Li, L. Li, L. Xu, X. Li, B. Feng, Y. Bai, H. Liu, in *Handbook of Nanoparticles* (Ed: M. Aliofkhazraei), Springer International Publishing, Cham, Switzerland **2016**, p. 1313, https://doi.org/10.1007/978-3-319-15338-4_30; e) S. Naasz, S. Weigel, O. Borovinskaya, A. Serva, C. Cascio, A. K. Undas, F. C. Simeone, H. J. P. Marvin, R. J. B. Peters, *J. Anal. At. Spectrom.* **2018**, *33*, 835.
- [136] a) T. C. Wang, N. A. Vermeulen, I. S. Kim, A. B. F. Martinson, J. F. Stoddart, J. T. Hupp, O. K. Farha, *Nat. Protoc.* **2015**, *11*, 149; b) H. Fei, J. Shin, Y. S. Meng, M. Adelhardt, J. Sutter, K. Meyer, S. M. Cohen, *J. Am. Chem. Soc.* **2014**, *136*, 4965; c) P. Schanda, M. Ernst, *Prog. Nucl. Magn. Reson. Spectrosc.* **2016**, *96*, 1; d) P. Duan, J. C. Moreton, S. R. Tavares, R. Semino, G. Maurin, S. M. Cohen, K. Schmidt-Rohr, *J. Am. Chem. Soc.* **2019**, *141*, 7589; e) J. J. van der Klink, H. B. Brom, *Prog. Nucl. Magn. Reson. Spectrosc.* **2000**, *36*, 89.
- [137] a) N. Stock, *Microporous Mesoporous Mater.* **2010**, *129*, 287; b) M. L. Kelly, W. Morris, A. T. Gallagher, J. S. Anderson, K. A. Brown, C. A. Mirkin, T. D. Harris, *Chem. Commun.* **2016**, *52*, 7854; c) S. Bauer, C. Serre, T. Devic, P. Horcajada, J. Marrot, G. Férey, N. Stock, *Inorg. Chem.* **2008**, *47*, 7568; d) P. M. Forster, N. Stock, A. K. Cheetham, *Angew. Chem., Int. Ed.* **2005**, *44*, 7608; e) E. Biemmi, S. Christian, N. Stock, T. Bein, *Microporous Mesoporous Mater.* **2009**, *117*, 111.
- [138] X. Tian, K. R. Lind, B. Yuan, S. Shaw, O. Siemianowski, L. Cademartiri, *Adv. Mater.* **2017**, *29*, 1604681.
- [139] R. Freund, U. Lächelt, T. Gruber, B. Rühle, S. Wuttke, *ACS Nano* **2018**, *12*, 2094.
- [140] a) W. Lu, Z. Wei, Z.-Y. Gu, T.-F. Liu, J. Park, J. Park, J. Tian, M. Zhang, Q. Zhang, T. Gentle Iii, M. Bosch, H.-C. Zhou, *Chem. Soc. Rev.* **2014**, *43*, 5561; b) S.-Y. Ding, W. Wang, *Chem. Soc. Rev.* **2013**, *42*, 548; c) P. Martinez-Bulit, A. J. Stirk, S. J. Loeb, *Trends Chem.* **2019**, *1*, 588.
- [141] a) H. Li, M. Eddaoudi, M. O'Keeffe, O. M. Yaghi, *Nature* **1999**, *402*, 276; b) M. Eddaoudi, J. Kim, N. Rosi, D. Vodak, J. Wachter, M. Keffe, O. M. Yaghi, *Science* **2002**, *295*, 469.
- [142] a) Y.-N. Gong, D.-C. Zhong, T.-B. Lu, *CrystEngComm* **2016**, *18*, 2596; b) R. J. Marshall, C. T. Lennon, A. Tao, H. M. Senn, C. Wilson, D. Fairen-Jimenez, R. S. Forgan, *J. Mater. Chem. A* **2018**, *6*, 1181; c) H.-L. Jiang, T. A. Makal, H.-C. Zhou, *Coord. Chem. Rev.* **2013**, *257*, 2232; d) F. Zarekarizi, M. Joharian, A. Morsali, *J. Mater. Chem. A* **2018**, *6*, 19288.
- [143] H. Deng, S. Grunder, K. E. Cordova, C. Valente, H. Furukawa, M. Hmadeh, F. Gándara, A. C. Whalley, Z. Liu, S. Asahina, H. Kazumori, M. O'Keeffe, O. Terasaki, J. F. Stoddart, O. M. Yaghi, *Science* **2012**, *336*, 1018.
- [144] a) C.-D. Wu, A. Hu, L. Zhang, W. Lin, *J. Am. Chem. Soc.* **2005**, *127*, 8940; b) C.-D. Wu, W. Lin, *Angew. Chem., Int. Ed.* **2007**, *46*, 1075; c) L. Ma, C.-D. Wu, M. M. Wanderley, W. Lin, *Angew. Chem., Int. Ed.* **2010**, *49*, 8244.
- [145] a) W. Schrimpf, G. Ossato, P. Hirschle, S. Wuttke, D. C. Lamb, *Small* **2016**, *12*, 3651; b) S. A. Diamantis, A. Margariti, A. D. Pournara, G. S. Papaefstathiou, M. J. Manos, T. Lazarides, *Inorg. Chem. Front.* **2018**, *5*, 1493.
- [146] B. Rühle, E. Virmani, H. Engelke, F. M. Hinterholzinger, T. von Zons, B. Brosent, T. Bein, A. Godt, S. Wuttke, *Chem. – Eur. J.* **2019**, *25*, 6349.
- [147] a) I. Imaz, M. Rubio-Martínez, J. An, I. Solé-Font, N. L. Rosi, D. MasPOCH, *Chem. Commun.* **2011**, *47*, 7287; b) B. Steinborn, P. Hirschle, M. Höhn, T. Bauer, M. Barz, S. Wuttke, E. Wagner, U. Lächelt, *Adv. Ther.* **2019**, *0*, 1900120.
- [148] a) D. D. Medina, T. Sick, T. Bein, *Adv. Energy Mater.* **2017**, *7*, 1700387; b) Q. Xu, S. Tao, Q. Jiang, D. Jiang, *J. Am. Chem. Soc.* **2018**, *140*, 7429; c) C. H. Hendon, A. J. Rieth, M. D. Korzyński, M. Dincă, *ACS Cent. Sci.* **2017**, *3*, 554; d) D. Sheberla, J. C. Bachman, J. S. Elias, C.-J. Sun, Y. Shao-Horn, M. Dincă, *Nat. Mater.* **2016**, *16*, 220.
- [149] a) A. Gonzalez-Nelson, F.-X. Coudert, A. M. van der Veen, *Nanomaterials* **2019**, *9*, 330; b) A. Comotti, S. Bracco, T. Ben, S. Qiu, P. Sozzani, *Angew. Chem.* **2014**, *126*, 1061; c) A. Comotti, S. Bracco, P. Sozzani, *Acc. Chem. Res.* **2016**, *49*, 1701.
- [150] H. Deng, M. A. Olson, J. F. Stoddart, O. M. Yaghi, *Nat. Chem.* **2010**, *2*, 439.
- [151] E. Virmani, O. Beyer, U. Lüning, U. Ruschewitz, S. Wuttke, *Mater. Chem. Front.* **2017**, *1*, 1965.
- [152] T. M. Osborn Popp, O. M. Yaghi, *Acc. Chem. Res.* **2017**, *50*, 532.
- [153] a) S. M. Cohen, *Chem. Rev.* **2012**, *112*, 970; b) J. D. Evans, C. J. Sumby, C. J. Doonan, *Chem. Soc. Rev.* **2014**, *43*, 5933.

- [154] a) K. Oisaki, Q. Li, H. Furukawa, A. U. Czaja, O. M. Yaghi, *J. Am. Chem. Soc.* **2010**, *132*, 9262; b) V. Pascanu, G. González Miera, A. K. Inge, B. Martin-Matute, *J. Am. Chem. Soc.* **2019**, *141*, 7223.
- [155] a) C. Dietl, H. Hintz, B. Rühle, J. Schmedt auf der Günne, H. Langhals, S. Wuttke, *Chem. – Eur. J.* **2015**, *21*, 10714; b) S. Wuttke, C. Dietl, F. M. Hinterholzinger, H. Hintz, H. Langhals, T. Bein, *Chem. Commun.* **2014**, *50*, 3599; c) F. M. Hinterholzinger, B. Rühle, S. Wuttke, K. Karaghiosoff, T. Bein, *Sci. Rep.* **2013**, *3*, 2562.
- [156] K. M. Choi, D. Kim, B. Rungtaweevoranit, C. A. Trickett, J. T. D. Barmantek, A. S. Alshammari, P. Yang, O. M. Yaghi, *J. Am. Chem. Soc.* **2017**, *139*, 356.
- [157] A. M. Fracaroli, P. Siman, D. A. Nagib, M. Suzuki, H. Furukawa, F. D. Toste, O. M. Yaghi, *J. Am. Chem. Soc.* **2016**, *138*, 8352.
- [158] a) M. Lalonde, W. Bury, O. Karagiari, Z. Brown, J. T. Hupp, O. K. Farha, *J. Mater. Chem. A* **2013**, *1*, 5453; b) S. Sen, S. Neogi, K. Rissanen, P. K. Bharadwaj, *Chem. Commun.* **2015**, *51*, 3173; c) S. Bommakanti, S. K. Das, *CrystEngComm* **2019**, *21*, 2438; d) K. S. Asha, R. Bhattacharjee, S. Mandal, *Angew. Chem., Int. Ed.* **2016**, *55*, 11528; e) M. Kim, J. F. Cahill, H. Fei, K. A. Prather, S. M. Cohen, *J. Am. Chem. Soc.* **2012**, *134*, 18082.
- [159] a) B. J. Burnett, P. M. Barron, C. Hu, W. Choe, *J. Am. Chem. Soc.* **2011**, *133*, 9984; b) S. Kim, K. W. Dawson, B. S. Gelfand, J. M. Taylor, G. K. H. Shimizu, *J. Am. Chem. Soc.* **2013**, *135*, 963; c) O. Karagiari, W. Bury, E. Tylanakis, A. A. Sarjeant, J. T. Hupp, O. K. Farha, *Chem. Mater.* **2013**, *25*, 3499; d) N. A. Vermeulen, O. Karagiari, A. A. Sarjeant, C. L. Stern, J. T. Hupp, O. K. Farha, J. F. Stoddart, *J. Am. Chem. Soc.* **2013**, *135*, 14916.
- [160] a) O. Karagiari, W. Bury, J. E. Mondloch, J. T. Hupp, O. K. Farha, *Angew. Chem., Int. Ed.* **2014**, *53*, 4530; b) P. Deria, J. E. Mondloch, O. Karagiari, W. Bury, J. T. Hupp, O. K. Farha, *Chem. Soc. Rev.* **2014**, *43*, 5896.
- [161] a) M. B. Lalonde, J. E. Mondloch, P. Deria, A. A. Sarjeant, S. S. Al-Juaid, O. I. Osman, O. K. Farha, J. T. Hupp, *Inorg. Chem.* **2015**, *54*, 7142; b) K. C. Jayachandrababu, D. S. Sholl, S. Nair, *J. Am. Chem. Soc.* **2017**, *139*, 5906.
- [162] J. L. Segura, S. Royuela, M. Mar Ramos, *Chem. Soc. Rev.* **2019**, *48*, 3903.
- [163] a) C. Qiao, L. Sun, S. Zhang, P. Liu, L. Chang, C. Zhou, Q. Wei, S. Chen, S. Gao, *J. Mater. Chem. C* **2017**, *5*, 1064; b) S.-C. Xiang, Z. Zhang, C.-G. Zhao, K. Hong, X. Zhao, D.-R. Ding, M.-H. Xie, C.-D. Wu, M. C. Das, R. Gill, K. M. Thomas, B. Chen, *Nat. Commun.* **2011**, *2*, 204.
- [164] A. P. Katsoulidis, D. Antypov, G. F. S. Whitehead, E. J. Carrington, D. J. Adams, N. G. Berry, G. R. Darling, M. S. Dyer, M. J. Rosseinsky, *Nature* **2019**, *565*, 213.
- [165] a) A. B. Kanj, J. Bürck, S. Grosjean, S. Bräse, L. Heinke, *Chem. Commun.* **2019**, *55*, 8776; b) S. Lee, E. A. Kapustin, O. M. Yaghi, *Science* **2016**, *353*, 808.
- [166] Q. Li, W. Zhang, O. Š. Miljanić, C.-H. Sue, Y.-L. Zhao, L. Liu, C. B. Knobler, J. F. Stoddart, O. M. Yaghi, *Science* **2009**, *325*, 855.
- [167] M. D. Allendorf, R. Medishetty, R. A. Fischer, *MRS Bull.* **2016**, *41*, 865.
- [168] a) Y. Luo, M. Ahmad, A. Schug, M. Tsotsalas, *Adv. Mater.* **2019**, *31*, 1901744; b) J. D. Evans, G. Fraux, R. Gaillac, D. Kohen, F. Trouselet, J.-M. Vanson, F.-X. Coudert, *Chem. Mater.* **2017**, *29*, 199; c) S. O. Odoh, C. J. Cramer, D. G. Truhlar, L. Gagliardi, *Chem. Rev.* **2015**, *115*, 6051; d) V. Van Speybroeck, K. Hemelsoet, L. Joos, M. Waroquier, R. G. Bell, C. R. A. Catlow, *Chem. Soc. Rev.* **2015**, *44*, 7044; e) F.-X. Coudert, A. H. Fuchs, *Coord. Chem. Rev.* **2016**, *307*, 211.
- [169] G. Manos, L. J. Dunne, *Nanomaterials* **2018**, *8*, 818.
- [170] a) J. J. Potoff, J. I. Siepmann, *AIChE J.* **2001**, *47*, 1676; b) S. Amirjalayer, R. Schmid, *J. Phys. Chem. C* **2008**, *112*, 14980; c) M. Tafipolsky, R. Schmid, *J. Phys. Chem. B* **2009**, *113*, 1341; d) M. Tafipolsky, S. Amirjalayer, R. Schmid, *J. Phys. Chem. C* **2010**, *114*, 14402; e) S. Bureekaew, S. Amirjalayer, M. Tafipolsky, C. Spickermann, T. K. Roy, R. Schmid, *Phys. Status Solidi B* **2013**, *250*, 1128; f) P. G. Boyd, S. M. Moosavi, M. Witman, B. Smit, *J. Phys. Chem. Lett.* **2017**, *8*, 357; g) J. Heinen, D. Dubbeldam, *Wiley Interdiscip. Rev.: Comput. Mol. Sci.* **2018**, *8*, e1363.
- [171] Q. Yang, C. Zhong, J.-F. Chen, *J. Phys. Chem. C* **2008**, *112*, 1562.
- [172] a) Y. B. Band, Y. Avishai, in *Quantum Mechanics with Applications to Nanotechnology and Information Science* (Eds: Y. B. Band, Y. Avishai), Academic Press, Amsterdam **2013**, p. 871; b) P. Hohenberg, W. Kohn, *Phys. Rev.* **1964**, *136*, B864.
- [173] R. Ferrando, J. Jellinek, R. L. Johnston, *Chem. Rev.* **2008**, *108*, 845.
- [174] a) L. G. Verga, J. Aarons, M. Sarwar, D. Thompsett, A. E. Russell, C. K. Skylaris, *Faraday Discuss.* **2018**, *208*, 497; b) V. Bernales, M. A. Ortuño, D. G. Truhlar, C. J. Cramer, L. Gagliardi, *ACS Cent. Sci.* **2018**, *4*, 5; c) D. Nazarian, J. S. Camp, Y. G. Chung, R. Q. Snurr, D. S. Sholl, *Chem. Mater.* **2017**, *29*, 2521.
- [175] a) C. L. Whitford, C. J. Stephenson, D. A. Gómez-Gualdrón, J. T. Hupp, O. K. Farha, R. Q. Snurr, P. C. Stair, *J. Phys. Chem. C* **2017**, *121*, 25079; b) M. Chin, C. Cisneros, S. M. Araiza, K. M. Vargas, K. M. Ishihara, F. Tian, *RSC Adv.* **2018**, *8*, 26987; c) A. Knebel, B. Geppert, K. Volkmann, D. I. Kolokolov, A. G. Stepanov, J. Twiefel, P. Heitjans, D. Volkmer, J. Caro, *Science* **2017**, *358*, 347; d) N. Park, K. Choi, J. Hwang, D. W. Kim, D. O. Kim, J. Ihm, *Proc. Natl. Acad. Sci. USA* **2012**, *109*, 19893.
- [176] a) R.-L. Wang, D.-P. Li, L.-J. Wang, X. Zhang, Z.-Y. Zhou, J.-L. Mu, Z.-M. Su, *Dalton Trans.* **2019**, *48*, 1051; b) H. Hashemzadeh, H. Raissi, *J. Phys. D: Appl. Phys.* **2018**, *51*, 345401.
- [177] W. Kohn, L. J. Sham, *Phys. Rev.* **1965**, *140*, A1133.
- [178] P. Horcajada, C. Serre, G. Maurin, N. A. Ramsahye, F. Balas, M. Vallet-Regí, M. Sebban, F. Taulelle, G. Férey, *J. Am. Chem. Soc.* **2008**, *130*, 6774.
- [179] M. Dixit, T. A. Maark, S. Pal, *Int. J. Hydrogen Energy* **2011**, *36*, 10816.
- [180] Q. Cui, G. Qin, W. Wang, G. K. R. A. Du, Q. Sun, *J. Mater. Chem. A* **2019**, *7*, 14510.
- [181] S. Barthel, E. V. Alexandrov, D. M. Proserpio, B. Smit, *Cryst. Growth Des.* **2018**, *18*, 1738.
- [182] J. C. Tan, B. Civalleri, A. Erba, E. Albanese, *CrystEngComm* **2015**, *17*, 375.
- [183] a) S. Neukermans, N. Veldeman, E. Janssens, P. Lievens, Z. Chen, P. v. R. Schleyer, *Eur. Phys. J. D* **2007**, *45*, 301; b) M. J. López, J. Jellinek, *J. Chem. Phys.* **1999**, *110*, 8899; c) F. Cleri, V. Rosato, *Phys. Rev. B* **1993**, *48*, 22; d) A. P. Sutton, J. Chen, *Philos. Mag. Lett.* **1990**, *61*, 139.
- [184] a) A. D. Becke, *Phys. Rev. A* **1988**, *38*, 3098; b) C. Lee, W. Yang, R. G. Parr, *Phys. Rev. B* **1988**, *37*, 785; c) W. Kohn, A. D. Becke, R. G. Parr, *J. Chem. Phys.* **1996**, *100*, 12974.
- [185] J. P. Perdew, A. Ruzsinszky, G. I. Csonka, O. A. Vydrov, G. E. Scuseria, L. A. Constantin, X. Zhou, K. Burke, *Phys. Rev. Lett.* **2008**, *100*, 136406.
- [186] P. Tian, *Annu. Rep. Prog. Chem., Sect. C: Phys. Chem.* **2008**, *104*, 142.
- [187] D. Esqué-de los Ojos, E. Pellicer, J. Sort, *Materials* **2016**, *9*.
- [188] M. A. Addicoat, N. Vankova, I. F. Akter, T. Heine, *J. Chem. Theory Comput.* **2014**, *10*, 880.
- [189] G. Garberoglio, A. I. Skoulidas, J. K. Johnson, *J. Phys. Chem. B* **2005**, *109*, 13094.
- [190] L. Vanduyfhuys, S. Vandenbrande, T. Verstraelen, R. Schmid, M. Waroquier, V. Van Speybroeck, *J. Comput. Chem.* **2015**, *36*, 1015.
- [191] S. Kmiecik, D. Gront, M. Kolinski, L. Wieteska, A. E. Dawid, A. Kolinski, *Chem. Rev.* **2016**, *116*, 7898.

- [192] S. J. Marrink, H. J. Risselada, S. Yefimov, D. P. Tieleman, A. H. de Vries, *J. Phys. Chem. B* **2007**, *111*, 7812.
- [193] K. T. Thomson, K. E. Gubbins, *Langmuir* **2000**, *16*, 5761.
- [194] L.-M. Yang, E. Ganz, S. Svelle, M. Tilset, *J. Mater. Chem. C* **2014**, *2*, 7111.
- [195] M. Wahiduzzaman, S. Wang, B. J. Sikora, C. Serre, G. Maurin, *Chem. Commun.* **2018**, *54*, 10812.
- [196] C. Mellot-Draznieks, J. Dutour, G. Férey, *Angew. Chem., Int. Ed.* **2004**, *43*, 6290.
- [197] G. Férey, C. Mellot-Draznieks, C. Serre, F. Millange, J. Dutour, S. Surblé, I. Margiolaki, *Science* **2005**, *309*, 2040.
- [198] I. A. Baburin, S. Leoni, G. Seifert, *J. Phys. Chem. B* **2008**, *112*, 9437.
- [199] S. Bureekaew, R. Schmid, *CrystEngComm* **2013**, *15*, 1551.
- [200] a) S. M. Moosavi, A. Chidambaram, L. Talirz, M. Haranczyk, K. C. Stylianou, B. Smit, *Nat. Commun.* **2019**, *10*, 539; b) N. S. Bobbitt, R. Q. Snurr, *Mol. Simul.* **2019**, *45*, 1069.
- [201] a) C. Mellot-Draznieks, *J. Mater. Chem.* **2007**, *17*, 4348; b) O. K. Farha, A. Özgür Yazaydin, I. Eryazici, C. D. Malliakas, B. G. Hauser, M. G. Kanatzidis, S. T. Nguyen, R. Q. Snurr, J. T. Hupp, *Nat. Chem.* **2010**, *2*, 944.
- [202] Y. J. Colón, R. Q. Snurr, *Chem. Soc. Rev.* **2014**, *43*, 5735.
- [203] a) A. N. V. Azar, S. Velioglu, S. Keskin, *ACS Sustainable Chem. Eng.* **2019**, *7*, 9525; b) D. Banerjee, C. M. Simon, S. K. Elsaidi, M. Haranczyk, P. K. Thallapally, *Chem* **2018**, *4*, 466; c) W. Yang, H. Liang, F. Peng, Z. Liu, J. Liu, Z. Qiao, *Nanomaterials* **2019**, *9*, 467.
- [204] a) M. Tong, Y. Lan, Q. Yang, C. Zhong, *Green Energy Environ.* **2018**, *3*, 107; b) Z. Qiao, Q. Xu, J. Jiang, *J. Mater. Chem. A* **2018**, *6*, 18898.
- [205] a) Y. J. Colón, D. Fairen-Jimenez, C. E. Wilmer, R. Q. Snurr, *J. Phys. Chem. C* **2014**, *118*, 5383; b) A. W. Thornton, C. M. Simon, J. Kim, O. Kwon, K. S. Deeg, K. Konstas, S. J. Pas, M. R. Hill, D. A. Winkler, M. Haranczyk, B. Smit, *Chem. Mater.* **2017**, *29*, 2844.
- [206] R. L. Martin, C. M. Simon, B. Smit, M. Haranczyk, *J. Am. Chem. Soc.* **2014**, *136*, 5006.
- [207] A. Jain, S. P. Ong, G. Hautier, W. Chen, W. D. Richards, S. Dacek, S. Cholia, D. Gunter, D. Skinner, G. Ceder, K. A. Persson, *APL Mater.* **2013**, *1*, 011002.
- [208] L. Yu, A. Zunger, *Phys. Rev. Lett.* **2012**, *108*, 068701.
- [209] R. Armiento, B. Kozinsky, M. Fornari, G. Ceder, *Phys. Rev. B* **2011**, *84*, 014103.
- [210] A. S. Rosen, J. M. Notestein, R. Q. Snurr, *J. Comput. Chem.* **2019**, *40*, 1305.
- [211] K. Yang, W. Setyawan, S. Wang, M. Buongiorno Nardelli, S. Curtarolo, *Nat. Mater.* **2012**, *11*, 614.
- [212] C. Sun, Q. Dong, J. Yang, Z. Dai, J. Lin, P. Chen, W. Huang, X. Dong, *Nano Res.* **2016**, *9*, 2234.
- [213] G. A. Duncan, M. A. Bevan, *Nanoscale* **2015**, *7*, 15332.
- [214] a) S. M. J. Rogge, R. Goeminne, R. Demuyck, J. J. Gutiérrez-Sevillano, S. Vandenberghe, L. Vanduyfhuys, M. Waroquier, T. Verstraelen, V. Van Speybroeck, *Adv. Theory Simul.* **2019**, *2*, 1800177; b) S. A. Sapchenko, D. N. Dybtsev, D. G. Samsonenko, R. V. Belosludov, V. R. Belosludov, Y. Kawazoe, M. Schröder, V. P. Fedin, *Chem. Commun.* **2015**, *51*, 13918; c) S. Cheng, Y. Wu, J. Jin, J. Liu, D. Wu, G. Yang, Y.-Y. Wang, *Dalton Trans.* **2019**, *48*, 7612; d) T. G. Glover, B. Mu, *Gas Adsorption in Metal-Organic Frameworks: Fundamentals and Applications*, CRC Press, Boca Raton, FL **2018**; e) J.-R. Li, J. Sculley, H.-C. Zhou, *Chem. Rev.* **2012**, *112*, 869; f) T. Wittmann, C. B. L. Tschense, L. Zappe, C. Koschnick, R. Siegel, R. Stäglich, B. V. Lotsch, J. Senker, *J. Mater. Chem. A* **2019**, *7*, 10379; g) M.-C. Schlegel, D. Töbrens, R. Svetogorov, M. Krüger, N. Stock, H. Reinsch, D. Wallacher, R. Stewart, M. Russina, *Phys. Chem. Chem. Phys.* **2016**, *18*, 29258; h) C. L. Hobday, C. H. Woodall, M. J. Lennox, M. Frost, K. Kamenev, T. Düren, C. A. Morrison, S. A. Moggach, *Nat. Commun.* **2018**, *9*, 1429; i) Q. Yang, C. Zhong, *J. Phys. Chem. B* **2005**, *109*, 11862; j) T. Chokbunpiam, S. Fritzsche, C. Chmelik, J. Caro, W. Janke, S. Hannongbua, *J. Phys. Chem. C* **2016**, *120*, 23458; k) H. Zeng, Y. Liu, H. Liu, *Mol. Simul.* **2018**, *44*, 1244.
- [215] A. I. Skoulidas, D. S. Sholl, *J. Phys. Chem. B* **2005**, *109*, 15760.
- [216] H. Frost, T. Düren, R. Q. Snurr, *J. Phys. Chem. B* **2006**, *110*, 9565.
- [217] T. Düren, Y.-S. Bae, R. Q. Snurr, *Chem. Soc. Rev.* **2009**, *38*, 1237.
- [218] H. Daglar, S. Keskin, *J. Phys. Chem. C* **2018**, *122*, 17347.
- [219] S. Amirjalayer, R. Schmid, *J. Phys. Chem. C* **2016**, *120*, 27319.
- [220] S. Amirjalayer, M. Tafipolsky, R. Schmid, *Angew. Chem., Int. Ed.* **2007**, *46*, 463.
- [221] P. Guo, D. Liu, K. Subramanyam, B. Wang, J. Yang, J. Huang, D. T. Augustine, M. A. Moses, *Nat. Commun.* **2018**, *9*, 130.
- [222] a) A. Samanta, T. Furuta, J. Li, *J. Chem. Phys.* **2006**, *125*, 084714; b) M. Fuentes-Cabrera, D. M. Nicholson, B. G. Sumpter, M. Widom, *J. Chem. Phys.* **2005**, *123*, 124713; c) A. Kuc, A. Enyashin, G. Seifert, *J. Phys. Chem. B* **2007**, *111*, 8179.
- [223] J.-C. Tan, B. Civalleri, C.-C. Lin, L. Valenzano, R. Galvelis, P.-F. Chen, T. D. Bennett, C. Mellot-Draznieks, C. M. Zicovich-Wilson, A. K. Cheetham, *Phys. Rev. Lett.* **2012**, *108*, 095502.
- [224] J. C. Tan, A. K. Cheetham, *Chem. Soc. Rev.* **2011**, *40*, 1059.
- [225] J. A. Greathouse, M. D. Allendorf, *J. Am. Chem. Soc.* **2006**, *128*, 10678.
- [226] F. Salles, A. Ghoufi, G. Maurin, R. G. Bell, C. Mellot-Draznieks, G. Férey, *Angew. Chem., Int. Ed.* **2008**, *47*, 8487.
- [227] P. Horcajada, F. Salles, S. Wuttke, T. Devic, D. Heurtaux, G. Maurin, A. Vimont, M. Daturi, O. David, E. Magnier, N. Stock, Y. Filinchuk, D. Popov, C. Riekkel, G. Férey, C. Serre, *J. Am. Chem. Soc.* **2011**, *133*, 17839.
- [228] C. Gaudin, D. Cunha, E. Ivanoff, P. Horcajada, G. Chevé, A. Yasri, O. Loget, C. Serre, G. Maurin, *Microporous Mesoporous Mater.* **2012**, *157*, 124.
- [229] a) L. J. Dunne, G. Manos, *Philos. Trans. R. Soc., A* **2018**, *376*, 20170151; b) J. Zang, S. Nair, D. S. Sholl, *J. Chem. Phys.* **2011**, *134*, 184103; c) D. Bousquet, F.-X. Coudert, A. G. J. Fossati, A. V. Neimark, A. H. Fuchs, A. Boutin, *J. Chem. Phys.* **2013**, *138*, 174706.
- [230] L. J. Dunne, G. Manos, *Dalton Trans.* **2016**, *45*, 4213.
- [231] M. C. Bernini, D. Fairen-Jimenez, M. Pasinetti, A. J. Ramirez-Pastor, R. Q. Snurr, *J. Mater. Chem. B* **2014**, *2*, 766.
- [232] R. Boulé, C. Roiland, T. Bataille, L. Le Pollés, N. Audebrand, A. Ghoufi, *J. Phys. Chem. Lett.* **2019**, *10*, 1698.
- [233] C. Adamo, D. Jacquemin, *Chem. Soc. Rev.* **2013**, *42*, 845.
- [234] L.-M. Yang, R. Pushpa, *J. Mater. Chem. C* **2014**, *2*, 2404.
- [235] M. Mattesini, J. M. Soler, F. Ynduráin, *Phys. Rev. B* **2006**, *73*, 094111.
- [236] D. Yan, G. O. Lloyd, A. Delori, W. Jones, X. Duan, *ChemPlusChem* **2012**, *77*, 1112.
- [237] a) A. Vimont, F. Thibault-Starzyk, M. Daturi, *Chem. Soc. Rev.* **2010**, *39*, 4928; b) A. Vimont, J.-M. Goupil, J.-C. Lavalley, M. Daturi, S. Surblé, C. Serre, F. Millange, G. Férey, N. Audebrand, *J. Am. Chem. Soc.* **2006**, *128*, 3218; c) J. W. Yoon, Y.-K. Seo, Y. K. Hwang, J.-S. Chang, H. Leclerc, S. Wuttke, P. Bazin, A. Vimont, M. Daturi, E. Bloch, P. L. Llewellyn, C. Serre, P. Horcajada, J.-M. Grenèche, A. E. Rodrigues, G. Férey, *Angew. Chem., Int. Ed.* **2010**, *49*, 5949; d) S. Wuttke, P. Bazin, A. Vimont, C. Serre, Y.-K. Seo, Y. K. Hwang, J.-S. Chang, G. Férey, M. Daturi, *Chem. – Eur. J.* **2012**, *18*, 11959.
- [238] T. Wang, L. Gao, J. Hou, S. J. A. Herou, J. T. Griffiths, W. Li, J. Dong, S. Gao, M.-M. Titirici, R. V. Kumar, A. K. Cheetham, X. Bao, Q. Fu, S. K. Smoukov, *Nat. Commun.* **2019**, *10*, 1340.
- [239] I. Strauss, A. Mundstock, M. Treger, K. Lange, S. Hwang, C. Chmelik, P. Rusch, N. C. Bigall, T. Pichler, H. Shiozawa, J. Caro, *ACS Appl. Mater. Interfaces* **2019**, *11*, 14175.

- [240] *Infrared and Raman Spectroscopy: Methods and Applications*, VCH Verlagsgesellschaft mbH, Weinheim, Germany **2007**.
- [241] K. Tan, Y. J. Chabal, in *Metal-Organic Frameworks* (Eds: F. Zafar, E. Sharmim), IntechOpen, London **2016**, p. 19, <https://doi.org/10.5772/64906>.
- [242] H. C. Hoffmann, M. Debowski, P. Müller, S. Paasch, I. Senkovska, S. Kaskel, E. Brunner, *Materials* **2012**, *5*, 2537.
- [243] A. Marchetti, J. Chen, Z. Pang, S. Li, D. Ling, F. Deng, X. Kong, *Adv. Mater.* **2017**, *29*, 1605895.
- [244] J. Fraissard, T. Ito, M. Springuel-Huet, *J. Chim. Phys. Phys.-Chim. Biol.* **1988**, *85*, 747.
- [245] D. Esken, X. Zhang, O. I. Lebedev, F. Schröder, R. A. Fischer, *J. Mater. Chem.* **2009**, *19*, 1314.
- [246] C. Serre, C. Mellot-Draznieks, S. Surble, N. Audebrand, Y. Filinchuk, G. Férey, *Science* **2007**, *315*, 1828.
- [247] M. M. Modena, P. Hirschele, S. Wuttke, T. P. Burg, *Small* **2018**, *14*, 1800826.
- [248] T. P. Burg, M. Godin, S. M. Knudsen, W. Shen, G. Carlson, J. S. Foster, K. Babcock, S. R. Manalis, *Nature* **2007**, *446*, 1066.
- [249] M. M. Modena, T. P. Burg, *J. Appl. Phys.* **2015**, *118*, 224901.
- [250] S. Olcum, N. Cermak, S. C. Wasserman, K. S. Christine, H. Atsumi, K. R. Payer, W. Shen, J. Lee, A. M. Belcher, S. N. Bhatia, S. R. Manalis, *Proc. Natl. Acad. Sci. USA* **2014**, *111*, 1310.
- [251] M. M. Modena, Y. Wang, D. Riedel, T. P. Burg, *Lab Chip* **2014**, *14*, 342.
- [252] S. E. Ashbrook, D. M. Dawson, V. R. Seymour, *Phys. Chem. Chem. Phys.* **2014**, *16*, 8223.
- [253] S. Rojas, A. Arenas-Vivo, P. Horcajada, *Coord. Chem. Rev.* **2019**, *388*, 202.
- [254] a) P. Horcajada, C. Serre, M. Vallet-Regí, M. Sebban, F. Taulelle, G. Férey, *Angew. Chem., Int. Ed.* **2006**, *45*, 5974; b) M. Al Haydar, H. R. Abid, B. Sunderland, S. Wang, *Drug Des., Dev. Ther.* **2017**, *11*, 2685.
- [255] a) K. Zhu, C. A. O'Keefe, V. N. Vukotic, R. W. Schurko, S. J. Loeb, *Nat. Chem.* **2015**, *7*, 514; b) P. L. Anelli, N. Spencer, J. F. Stoddart, *J. Am. Chem. Soc.* **1991**, *113*, 5131; c) W. Danowski, T. van Leeuwen, S. Abdolazadeh, D. Roke, W. R. Browne, S. J. Wezenberg, B. L. Feringa, *Nat. Nanotechnol.* **2019**, *14*, 488.
- [256] V. N. Vukotic, K. J. Harris, K. Zhu, R. W. Schurko, S. J. Loeb, *Nat. Chem.* **2012**, *4*, 456.
- [257] J. Plas, O. Ivasenko, N. Martsinovich, M. Lackinger, S. De Feyter, *Chem. Commun.* **2016**, *52*, 68.
- [258] D. Cui, J. M. MacLeod, M. Ebrahimi, F. Rosei, *CrystEngComm* **2017**, *19*, 4927.
- [259] Y. Chen, Z.-L. Shi, L. Wei, B. Zhou, J. Tan, H.-L. Zhou, Y.-B. Zhang, *J. Am. Chem. Soc.* **2019**, *141*, 3298.
- [260] N. Nijem, H. Wu, P. Canepa, A. Marti, K. J. Balkus, T. Thonhauser, J. Li, Y. J. Chabal, *J. Am. Chem. Soc.* **2012**, *134*, 15201.
- [261] J. Li, B. Liu, X. Zhang, D. Cao, G. Chen, *J. Phys. Chem. C* **2017**, *121*, 25347.
- [262] H. Zheng, Y. Zhang, L. Liu, W. Wan, P. Guo, A. M. Nyström, X. Zou, *J. Am. Chem. Soc.* **2016**, *138*, 962.
- [263] M. Wu, H. Ye, F. Zhao, B. Zeng, *Sci. Rep.* **2017**, *7*, 39778.
- [264] W. Zhang, Y. Wang, Y. Leng, P. Zhang, J. Zhang, P. Jiang, *Catal. Sci. Technol.* **2016**, *6*, 5848.
- [265] a) J. Luo, J.-W. Wang, J.-H. Zhang, S. Lai, D.-C. Zhong, *CrystEngComm* **2018**, *20*, 5884; b) R.-B. Lin, Y. He, P. Li, H. Wang, W. Zhou, B. Chen, *Chem. Soc. Rev.* **2019**, *48*, 1362; c) I. Hisaki, Y. Suzuki, E. Gomez, Q. Ji, N. Tohrai, T. Nakamura, A. Douhal, *J. Am. Chem. Soc.* **2019**, *141*, 2111; d) Y. He, S. Xiang, B. Chen, *J. Am. Chem. Soc.* **2011**, *133*, 14570; e) W. Yang, A. Greenaway, X. Lin, R. Matsuda, A. J. Blake, C. Wilson, W. Lewis, P. Hubberstey, S. Kitagawa, N. R. Champness, M. Schröder, *J. Am. Chem. Soc.* **2010**, *132*, 14457; f) F. Hu, C. Liu, M. Wu, J. Pang, F. Jiang, D. Yuan, M. Hong, *Angew. Chem., Int. Ed.* **2017**, *56*, 2101; g) A. Karmakar, R. Illathvalappil, B. Anothumakkool, A. Sen, P. Samanta, A. V. Desai, S. Kurungot, S. K. Ghosh, *Angew. Chem., Int. Ed.* **2016**, *55*, 10667; h) H. Wang, H. Wu, J. Kan, G. Chang, Z. Yao, B. Li, W. Zhou, S. Xiang, J. Cong-Gui Zhao, B. Chen, *J. Mater. Chem. A* **2017**, *5*, 8292; i) Y.-F. Han, Y.-X. Yuan, H.-B. Wang, *Molecules* **2017**, *22*.
- [266] Q. Huang, W. Li, Z. Mao, L. Qu, Y. Li, H. Zhang, T. Yu, Z. Yang, J. Zhao, Y. Zhang, M. P. Aldred, Z. Chi, *Nat. Commun.* **2019**, *10*, 3074.
- [267] Z. Bao, D. Xie, G. Chang, H. Wu, L. Li, W. Zhou, H. Wang, Z. Zhang, H. Xing, Q. Yang, M. J. Zaworotko, Q. Ren, B. Chen, *J. Am. Chem. Soc.* **2018**, *140*, 4596.
- [268] Q. Yin, P. Zhao, R.-J. Sa, G.-C. Chen, J. Lü, T.-F. Liu, R. Cao, *Angew. Chem., Int. Ed.* **2018**, *57*, 7691.
- [269] a) B. Van de Voorde, M. Boulhout, F. Vermoortele, P. Horcajada, D. Cunha, J. S. Lee, J.-S. Chang, E. Gibson, M. Daturi, J.-C. Lavalley, A. Vimont, I. Beurroies, D. E. De Vos, *J. Am. Chem. Soc.* **2013**, *135*, 9849; b) M. Maes, M. Trekels, M. Boulhout, S. Schouteden, F. Vermoortele, L. Alaerts, D. Heurtaux, Y.-K. Seo, Y. K. Hwang, J.-S. Chang, I. Beurroies, R. Denoyel, K. Temst, A. Vantomme, P. Horcajada, C. Serre, D. E. De Vos, *Angew. Chem.* **2011**, *123*, 4296.
- [270] Z. Wang, Z. Sun, L. Kong, G. Li, *J. Energy Chem.* **2013**, *22*, 869.
- [271] K. A. Cychosz, A. G. Wong-Foy, A. J. Matzger, *J. Am. Chem. Soc.* **2008**, *130*, 6938.
- [272] Z. Hu, Y. Wang, B. B. Shah, D. Zhao, *Adv. Sustainable Syst.* **2019**, *3*, 1800080.
- [273] J. Teyssandier, S. D. Feyter, K. S. Mali, *Chem. Commun.* **2016**, *52*, 11465.
- [274] B. K. Chang, N. C. Bristowe, P. D. Bristowe, A. K. Cheetham, *Phys. Chem. Chem. Phys.* **2012**, *14*, 7059.
- [275] a) S. Zuluaga, P. Canepa, K. Tan, Y. J. Chabal, T. Thonhauser, *J. Phys.: Condens. Matter* **2014**, *26*, 133002; b) P. Z. Moghadam, S. M. J. Rogge, A. Li, C.-M. Chow, J. Wieme, N. Moharrami, M. Aragonés-Anglada, G. Conduit, D. A. Gomez-Gualdrón, V. Van Speybroeck, D. Fairen-Jimenez, *Matter* **2019**, *1*, 219.
- [276] W. Zhang, Y. Ma, I. A. Santos-López, J. M. Lownsbury, H. Yu, W.-G. Liu, D. G. Truhlar, C. T. Campbell, O. E. Vilches, *J. Am. Chem. Soc.* **2018**, *140*, 328.
- [277] Y. Chen, V. Lykourinou, C. Vetrovile, T. Hoang, L.-J. Ming, R. W. Larsen, S. Ma, *J. Am. Chem. Soc.* **2012**, *134*, 13188.
- [278] a) Z. R. Herm, E. D. Bloch, J. R. Long, *Chem. Mater.* **2014**, *26*, 323; b) L. Pan, D. H. Olson, L. R. Ciemnomolonski, R. Heddy, J. Li, *Angew. Chem., Int. Ed.* **2006**, *45*, 616.
- [279] Y. Takashima, V. M. Martínez, S. Furukawa, M. Kondo, S. Shimomura, H. Uehara, M. Nakahama, K. Sugimoto, S. Kitagawa, *Nat. Commun.* **2011**, *2*, 168.
- [280] a) S. K. Bhardwaj, N. Bhardwaj, R. Kaur, J. Mehta, A. L. Sharma, K.-H. Kim, A. Deep, *J. Mater. Chem. A* **2018**, *6*, 14992; b) M. Ko, L. Mendecki, K. A. Mirica, *Chem. Commun.* **2018**, *54*, 7873.
- [281] Z. Li, Z. Zhang, Y. Ye, K. Cai, F. Du, H. Zeng, J. Tao, Q. Lin, Y. Zheng, S. Xiang, *J. Mater. Chem. A* **2017**, *5*, 7816.
- [282] D.-W. Lim, M. Sadakiyo, H. Kitagawa, *Chem. Sci.* **2019**, *10*, 16.
- [283] C. Schneider, D. Ukaj, R. Koerver, A. A. Talin, G. Kieslich, S. P. Pujari, H. Zuilhof, J. Janek, M. D. Allendorf, R. A. Fischer, *Chem. Sci.* **2018**, *9*, 7405.
- [284] A. A. Talin, A. Centrone, A. C. Ford, M. E. Foster, V. Stavila, P. Haney, R. A. Kinney, V. Szalai, F. El Gabaly, H. P. Yoon, F. Léonard, M. D. Allendorf, *Science* **2014**, *343*, 66.
- [285] X. Nie, A. Kulkarni, D. S. Sholl, *J. Phys. Chem. Lett.* **2015**, *6*, 1586.
- [286] C. Young, R. R. Salunkhe, J. Tang, C.-C. Hu, M. Shahabuddin, E. Yanmaz, M. S. A. Hossain, J. H. Kim, Y. Yamauchi, *Phys. Chem. Chem. Phys.* **2016**, *18*, 29308.
- [287] A. Kamyshny, S. Magdassi, *Chem. Soc. Rev.* **2019**, *48*, 1712.

- [288] a) L. Chen, B. Huang, X. Qiu, X. Wang, R. Luque, Y. Li, *Chem. Sci.* **2016**, *7*, 228; b) Z. Zhao, J. Ding, R. Zhu, H. Pang, *J. Mater. Chem. A* **2019**, *7*, 15519.
- [289] H.-Q. Xu, K. Wang, M. Ding, D. Feng, H.-L. Jiang, H.-C. Zhou, *J. Am. Chem. Soc.* **2016**, *138*, 5316.
- [290] a) Y. Inokuma, S. Yoshioka, J. Ariyoshi, T. Arai, Y. Hitora, K. Takada, S. Matsunaga, K. Rissanen, M. Fujita, *Nature* **2013**, *495*, 461; b) Y. Inokuma, S. Yoshioka, J. Ariyoshi, T. Arai, M. Fujita, *Nat. Protoc.* **2014**, *9*, 246.
- [291] H. Cai, Y.-L. Huang, D. Li, *Coord. Chem. Rev.* **2019**, *378*, 207.
- [292] J. Zhou, G. Tian, L. Zeng, X. Song, X.-w. Bian, *Adv. Healthcare Mater.* **2018**, *7*, 1800022.
- [293] M. A. Chowdhury, *ChemBioEng Rev.* **2017**, *4*, 225.
- [294] K. M. L. Taylor, W. J. Rieter, W. Lin, *J. Am. Chem. Soc.* **2008**, *130*, 14358.
- [295] P. Horcajada, T. Chalati, C. Serre, B. Gillet, C. Sebrie, T. Baati, J. F. Eubank, D. Heurtaux, P. Clayette, C. Kreuz, J. S. Chang, Y. K. Hwang, V. Marsaud, P. N. Bories, L. Cynober, S. Gil, G. Ferey, P. Couvreur, R. Gref, *Nat. Mater.* **2010**, *9*, 172.
- [296] W. Hatakeyama, T. J. Sanchez, M. D. Rowe, N. J. Serkova, M. W. Liberatore, S. G. Boyes, *ACS Appl. Mater. Interfaces* **2011**, *3*, 1502.
- [297] K. M. L. Taylor, A. Jin, W. Lin, *Angew. Chem., Int. Ed.* **2008**, *47*, 7722.
- [298] K. E. deKrafft, Z. Xie, G. Cao, S. Tran, L. Ma, O. Z. Zhou, W. Lin, *Angew. Chem., Int. Ed.* **2009**, *48*, 9901.
- [299] B. G. Saar, L. R. Contreras-Rojas, X. S. Xie, R. H. Guy, *Mol. Pharmaceutics* **2011**, *8*, 969.
- [300] S. Sene, M. T. Marcos-Almaraz, N. Menguy, J. Scola, J. Volatron, R. Rouland, J.-M. Grenèche, S. Miraux, C. Menet, N. Guillou, F. Gazeau, C. Serre, P. Horcajada, N. Steunou, *Chem* **2017**, *3*, 303.
- [301] Y. Li, J. Tang, L. He, Y. Liu, Y. Liu, C. Chen, Z. Tang, *Adv. Mater.* **2015**, *27*, 4075.
- [302] J. Garcia, T. Tang, A. Y. Louie, *Nanomedicine* **2015**, *10*, 1343.
- [303] C. Tian, L. Zhu, F. Lin, S. G. Boyes, *ACS Appl. Mater. Interfaces* **2015**, *7*, 17765.
- [304] X. Chen, M. Zhang, S. Li, L. Li, L. Zhang, T. Wang, M. Yu, Z. Mou, C. Wang, *J. Mater. Chem. B* **2017**, *5*, 1772.
- [305] H. Mieno, R. Kabe, N. Notsuka, M. D. Allendorf, C. Adachi, *Adv. Opt. Mater.* **2016**, *4*, 1015.
- [306] G. Lin, H. Ding, D. Yuan, B. Wang, C. Wang, *J. Am. Chem. Soc.* **2016**, *138*, 3302.
- [307] V. Glembockyte, M. Frenette, C. Mottillo, A. M. Durantini, J. Gostick, V. Štrukil, T. Friščić, G. Cosa, *J. Am. Chem. Soc.* **2018**, *140*, 16882.
- [308] J. Zhuang, C.-H. Kuo, L.-Y. Chou, D.-Y. Liu, E. Weerapana, C.-K. Tsung, *ACS Nano* **2014**, *8*, 2812.
- [309] T. Preiß, A. Zimpel, S. Wuttke, O. J. Rädler, *Materials* **2017**, *10*, 216.
- [310] H.-L. Jiang, D. Feng, T.-F. Liu, J.-R. Li, H.-C. Zhou, *J. Am. Chem. Soc.* **2012**, *134*, 14690.
- [311] C. Yang, K. Chen, M. Chen, X. Hu, S.-Y. Huan, L. Chen, G. Song, X.-B. Zhang, *Anal. Chem.* **2019**, *91*, 2727.
- [312] a) A. Kirchon, L. Feng, H. F. Drake, E. A. Joseph, H.-C. Zhou, *Chem. Soc. Rev.* **2018**, *47*, 8611; b) Y. Liu, Y. Zhao, X. Chen, *Theranostics* **2019**, *9*, 3122; c) C.-s. Wu, Z.-h. Xiong, C. Li, J.-m. Zhang, *RSC Adv.* **2015**, *5*, 82127; d) P.-F. Wei, M.-Z. Qi, Z.-P. Wang, S.-Y. Ding, W. Yu, Q. Liu, L.-K. Wang, H.-Z. Wang, W.-K. An, W. Wang, *J. Am. Chem. Soc.* **2018**, *140*, 4623; e) L. Li, F. Lu, R. Xue, B. Ma, Q. Li, N. Wu, H. Liu, W. Yao, H. Guo, W. Yang, *ACS Appl. Mater. Interfaces* **2019**, *11*, 26355; f) X. Li, C. Zhang, S. Cai, X. Lei, V. Altoe, F. Hong, J. J. Urban, J. Ciston, E. M. Chan, Y. Liu, *Nat. Commun.* **2018**, *9*, 2998.
- [313] D. Liu, K. Lu, C. Poon, W. Lin, *Inorg. Chem.* **2014**, *53*, 1916.
- [314] D. Peralta, G. Chaplais, A. Simon-Masseron, K. Barthelet, C. Chizallet, A.-A. Quoineaud, G. D. Pirngruber, *J. Am. Chem. Soc.* **2012**, *134*, 8115.
- [315] S. S. Y. Chui, S. M. F. Lo, J. P. H. Charmant, A. G. Orpen, I. D. Williams, *Science* **1999**, *283*, 1148.
- [316] Q. Min Wang, D. Shen, M. Bülow, M. Ling Lau, S. Deng, F. R. Fitch, N. O. Lemcoff, J. Semanscin, *Microporous Mesoporous Mater.* **2002**, *55*, 217.
- [317] T. M. Nicholson, S. K. Bhatia, *J. Phys. Chem. B* **2006**, *110*, 24834.
- [318] X. Hou, Y. Hu, A. Grinthal, M. Khan, J. Aizenberg, *Nature* **2015**, *519*, 70.
- [319] S. Sorribas, P. Gorgojo, C. Téllez, J. Coronas, A. G. Livingston, *J. Am. Chem. Soc.* **2013**, *135*, 15201.
- [320] World Economic Forum, These are the top 10 emerging technologies of 2017, <https://www.weforum.org/agenda/2017/06/these-are-the-top-10-emerging-technologies-of-2017/>, (accessed: January 2020).
- [321] N. Hanikel, M. S. Prévot, F. Fathieh, E. A. Kapustin, H. Lyu, H. Wang, N. J. Diercks, T. G. Glover, O. M. Yaghi, *ACS Cent. Sci.* **2019**, *5*, 1699.
- [322] W. Chen, C. S. Wu, *Dalton Trans.* **2018**, *47*, 2114.
- [323] a) J. Garthwaite, *Eur. J. Neurosci.* **2008**, *27*, 2783; b) J. T. Coyle, P. Puttfarcken, *Science* **1993**, *262*, 689; c) J. Garthwaite, *Trends Neurosci.* **1991**, *14*, 60.
- [324] C. Bogdan, *Nat. Immunol.* **2001**, *2*, 907.
- [325] a) H. Alimoradi, A. Barzegar-Fallah, I. A. Sammut, K. Greish, G. I. Giles, *Free Radical Biol. Med.* **2019**, *130*, 297; b) F. Murad, *Mol. Neurodegener.* **2012**, *7*, L1.
- [326] a) P. S. Wheatley, A. R. Butler, M. S. Crane, S. Fox, B. Xiao, A. G. Rossi, I. L. Megson, R. E. Morris, *J. Am. Chem. Soc.* **2006**, *128*, 502; b) L. K. Keefer, *Nat. Mater.* **2003**, *2*, 357.
- [327] a) X. Ma, Y. Cheng, H. Jian, Y. Feng, Y. Chang, R. Zheng, X. Wu, L. Wang, X. Li, H. Zhang, *Adv. Healthcare Mater.* **2019**, *8*, 1900256; b) M. B. Witte, A. Barbul, *Am. J. Surg.* **2002**, *183*, 406.
- [328] a) T. Akaike, H. Maeda, *Immunology* **2000**, *101*, 300; b) G. F. Rimmelzwaan, M. M. Baars, P. de Lijster, R. A. Fouchier, A. D. Osterhaus, *J. Virol.* **1999**, *73*, 8880.
- [329] a) S. Schwager, M. Detmar, *Front. Immunol.* **2019**, *10*; b) J. N. Sharma, A. Al-Omran, S. S. Parvathy, *Inflammopharmacology* **2007**, *15*, 252.
- [330] a) X. Wang, Z. Gray, J. Willette-Brown, F. Zhu, G. Shi, Q. Jiang, N.-Y. Song, L. Dong, Y. Hu, *Cell Death Discovery* **2018**, *4*, 46; b) L. Ying, L. J. Hofseth, *Cancer Res.* **2007**, *67*, 1407.
- [331] M. A. Cinelli, H. T. Do, G. P. Miley, R. B. Silverman, *Med. Res. Rev.* **2020**, *40*, 158.
- [332] a) S. Bahrani, S. A. Hashemi, S. M. Mousavi, R. Azhdari, *Drug Metab. Rev.* **2019**, *51*, 356; b) T. Yang, A. N. Zelikin, R. Chandrawati, *Adv. Sci.* **2018**, *5*, 1701043; c) J. F. Eubank, P. S. Wheatley, G. Lebars, A. C. McKinlay, H. Leclerc, P. Horcajada, M. Daturi, A. Vimont, R. E. Morris, C. Serre, *APL Mater.* **2014**, *2*, 124112; d) A. C. McKinlay, J. F. Eubank, S. Wuttke, B. Xiao, P. S. Wheatley, P. Bazin, J. C. Lavalley, M. Daturi, A. Vimont, G. De Weireld, P. Horcajada, C. Serre, R. E. Morris, *Chem. Mater.* **2013**, *25*, 1592; e) N. J. Hinks, A. C. McKinlay, B. Xiao, P. S. Wheatley, R. E. Morris, *Microporous Mesoporous Mater.* **2010**, *129*, 330; f) A. C. McKinlay, B. Xiao, D. S. Wragg, P. S. Wheatley, I. L. Megson, R. E. Morris, *J. Am. Chem. Soc.* **2008**, *130*, 10440; g) B. Xiao, P. S. Wheatley, X. Zhao, A. J. Fletcher, S. Fox, A. G. Rossi, I. L. Megson, S. Bordiga, L. Regli, K. M. Thomas, R. E. Morris, *J. Am. Chem. Soc.* **2007**, *129*, 1203.
- [333] G. Chedid, A. Yassin, *Nanomaterials* **2018**, *8*, 916.
- [334] a) S. Diring, D. O. Wang, C. Kim, M. Kondo, Y. Chen, S. Kitagawa, K.-i. Kamei, S. Furukawa, *Nat. Commun.* **2013**, *4*, 2684; b) M. Mowbray, X. Tan, P. S. Wheatley, R. E. Morris, R. B. Weller, *J. Invest. Dermatol.* **2008**, *128*, 352.

- [335] a) H. Nurhasni, J. Cao, M. Choi, I. Kim, B. L. Lee, Y. Jung, J.-W. Yoo, *Int. J. Nanomed.* **2015**, *10*, 3065; b) B. Wu, B. Gerlitz, B. W. Grinnell, M. E. Meyerhoff, *Biomaterials* **2007**, *28*, 4047; c) F. DeRosa, M. R. Kibbe, S. F. Najjar, M. L. Citro, L. K. Keefer, J. A. Hrabie, *J. Am. Chem. Soc.* **2007**, *129*, 3786.
- [336] P. Horcajada, R. Gref, T. Baati, P. K. Allan, G. Maurin, P. Couvreur, G. Férey, R. E. Morris, C. Serre, *Chem. Rev.* **2012**, *112*, 1232.
- [337] a) N. Naghavi, A. de Mel, O. S. Alavijeh, B. G. Cousins, A. M. Seifalian, *Small* **2013**, *9*, 22; b) M. R. Miller, I. L. Megson, *Br. J. Pharmacol.* **2007**, *151*, 305.
- [338] J. A. Hrabie, L. K. Keefer, *Chem. Rev.* **2002**, *102*, 1135.
- [339] L. K. Keefer, *Curr. Top. Med. Chem.* **2005**, *5*, 625.
- [340] J. G. Nguyen, K. K. Tanabe, S. M. Cohen, *CrystEngComm* **2010**, *12*, 2335.
- [341] a) M. Klink, M. Kielbik, I. S. Kielbik, P. Przygodzka, Z. Sulowska, *Redox Biol.* **2015**, *5*, 420; b) N. L. Fry, P. K. Mascharak, *Acc. Chem. Res.* **2011**, *44*, 289; c) S. Sortino, *Chem. Soc. Rev.* **2010**, *39*, 2903; d) C. Napoli, L. J. Ignarro, *Annu. Rev. Pharmacol. Toxicol.* **2003**, *43*, 97.
- [342] a) B. Xiao, P. S. Wheatley, R. E. Morris, in *Stud. Surf. Sci. Catal. Vol. 170*, (Eds: R. Xu, Z. Gao, J. Chen, W. Yan) Elsevier, Amsterdam **2007**, p. 902; b) L. Englander, A. Friedman, *J. Clin. Aesthet. Dermatol.* **2010**, *3*, 45.
- [343] a) M. Neidrauer, U. K. Ercan, A. Bhattacharyya, J. Samuels, J. Sedlak, R. Trikha, K. A. Barbee, M. S. Weingarten, S. G. Joshi, *J. Med. Microbiol.* **2014**, *63*, 203; b) S. Fox, T. S. Wilkinson, P. S. Wheatley, B. Xiao, R. E. Morris, A. Sutherland, A. J. Simpson, P. G. Barlow, A. R. Butler, I. L. Megson, A. G. Rossi, *Acta Biomater.* **2010**, *6*, 1515.
- [344] E. B. Caruso, S. Petralia, S. Conoci, S. Giuffrida, S. Sortino, *J. Am. Chem. Soc.* **2007**, *129*, 480.
- [345] a) H. Alimoradi, A. Barzegar-Fallah, I. A. Sammut, K. Greish, G. I. Giles, *Data Brief* **2018**, *21*, 1771; b) B. J. Heilman, J. St. John, S. R. J. Oliver, P. K. Mascharak, *J. Am. Chem. Soc.* **2012**, *134*, 11573.
- [346] L. Li, P. K. Moore, *Biochem. Soc. Trans.* **2007**, *35*, 1138.
- [347] a) E. Sánchez-González, P. G. M. Mileo, M. Sagastuy-Breña, J. R. Álvarez, J. E. Reynolds, A. Villarreal, A. Gutiérrez-Alejandre, J. Ramírez, J. Balmaseda, E. González-Zamora, G. Maurin, S. M. Humphrey, I. A. Ibarra, *J. Mater. Chem. A* **2018**, *6*, 16900; b) A. Evans, R. Luebke, C. Petit, *J. Mater. Chem. A* **2018**, *6*, 10570; c) P. Wang, F. Zhou, C. Zhang, S.-Y. Yin, L. Teng, L. Chen, X.-X. Hu, H.-W. Liu, X. Yin, X.-B. Zhang, *Chem. Sci.* **2018**, *9*, 8402; d) S. Diring, A. Carné-Sánchez, J. Zhang, S. Ikemura, C. Kim, H. Inaba, S. Kitagawa, S. Furukawa, *Chem. Sci.* **2017**, *8*, 2381; e) Y. Hao, S. Chen, Y. Zhou, Y. Zhang, M. Xu, *Nanomaterials* **2019**, *9*, 974.
- [348] L. Hamon, H. Leclerc, A. Ghoufi, L. Oliviero, A. Travert, J.-C. Lavalley, T. Devic, C. Serre, G. Férey, G. De Weireld, A. Vimont, G. Maurin, *J. Phys. Chem. C* **2011**, *115*, 2047.
- [349] J. N. Joshi, G. Zhu, J. J. Lee, E. A. Carter, C. W. Jones, R. P. Lively, K. S. Walton, *Langmuir* **2018**, *34*, 8443.
- [350] S. Chavan, F. Bonino, L. Valenzano, B. Civalleri, C. Lamberti, N. Acerbi, J. H. Cavka, M. Leistner, S. Bordiga, *J. Phys. Chem. C* **2013**, *117*, 15615.
- [351] a) M. S. Shah, M. Tsapatsis, J. I. Siepmann, *Chem. Rev.* **2017**, *117*, 9755; b) K. Vikrant, V. Kumar, Y. S. Ok, K.-H. Kim, A. Deep, *Trends Anal. Chem.* **2018**, *105*, 263; c) Y. Ma, X. Li, A. Li, P. Yang, C. Zhang, B. Tang, *Angew. Chem., Int. Ed.* **2017**, *56*, 13752; d) Y. Zheng, B. Yu, L. K. De La Cruz, M. Roy Choudhury, A. Anifowose, B. Wang, *Med. Res. Rev.* **2018**, *38*, 57; e) A. Karmakar, P. Samanta, A. V. Desai, S. K. Ghosh, *Acc. Chem. Res.* **2017**, *50*, 2457.
- [352] R. A. Sperling, W. J. Parak, *Philos. Trans. R. Soc., A* **2010**, *368*, 1333.
- [353] a) R. Mout, D. F. Moyano, S. Rana, V. M. Rotello, *Chem. Soc. Rev.* **2012**, *41*, 2539; b) R. Thiruppathi, S. Mishra, M. Ganapathy, P. Padmanabhan, B. Gulyás, *Adv. Sci.* **2017**, *4*, 1600279; c) B. Pelaz, P. del Pino, P. Maffre, R. Hartmann, M. Gallego, S. Rivera-Fernández, J. M. de la Fuente, G. U. Nienhaus, W. J. Parak, *ACS Nano* **2015**, *9*, 6996.
- [354] a) Q.-L. Zhu, Q. Xu, *Chem. Soc. Rev.* **2014**, *43*, 5468; b) S. Li, F. Huo, *Nanoscale* **2015**, *7*, 7482; c) Y. Zhang, X. Feng, S. Yuan, J. Zhou, B. Wang, *Inorg. Chem. Front.* **2016**, *3*, 896; d) T. Kitao, Y. Zhang, S. Kitagawa, B. Wang, T. Uemura, *Chem. Soc. Rev.* **2017**, *46*, 3108; e) A. Azhar, Y. Li, Z. Cai, M. B. Zakaria, M. K. Masud, M. S. A. Hossain, J. Kim, W. Zhang, J. Na, Y. Yamauchi, M. Hu, *Bull. Chem. Soc. Jpn.* **2019**, *92*, 875.
- [355] a) V. Agostoni, P. Horcajada, M. Noiray, M. Malanga, A. Aykaç, L. Jicsinszky, A. Vargas-Berenguel, N. Semiramo, S. Daoud-Mahammed, V. Nicolas, C. Martineau, F. Taulelle, J. Vigneron, A. Etcheberry, C. Serre, R. Gref, *Sci. Rep.* **2015**, *5*, 7925; b) E. Bellido, T. Hidalgo, M. V. Lozano, M. Guillevic, R. Simón-Vázquez, M. J. Santander-Ortega, Á. González-Fernández, C. Serre, M. J. Alonso, P. Horcajada, *Adv. Healthcare Mater.* **2015**, *4*, 1246; c) T. Hidalgo, M. Giménez-Marqués, E. Bellido, J. Avila, M. C. Asensio, F. Salles, M. V. Lozano, M. Guillevic, R. Simón-Vázquez, A. González-Fernández, C. Serre, M. J. Alonso, P. Horcajada, *Sci. Rep.* **2017**, *7*, 43099.
- [356] a) M. D. Rowe, C.-C. Chang, D. H. Thamm, S. L. Kraft, J. F. Harmon, A. P. Vogt, B. S. Sumerlin, S. G. Boyes, *Langmuir* **2009**, *25*, 9487; b) M. D. Rowe, D. H. Thamm, S. L. Kraft, S. G. Boyes, *Biomacromolecules* **2009**, *10*, 983.
- [357] R. Röder, T. Preiß, P. Hirschle, B. Steinborn, A. Zimpel, M. Höhn, J. O. Rädler, T. Bein, E. Wagner, S. Wuttke, U. Lächelt, *J. Am. Chem. Soc.* **2017**, *139*, 2359.
- [358] K. M. L. Taylor-Pashow, J. Della Rocca, Z. Xie, S. Tran, W. Lin, *J. Am. Chem. Soc.* **2009**, *131*, 14261.
- [359] H. Hintz, S. Wuttke, *Chem. Commun.* **2014**, *50*, 11472.
- [360] A. Zimpel, T. Preiß, R. Röder, H. Engelke, M. Ingrisich, M. Peller, J. O. Rädler, E. Wagner, T. Bein, U. Lächelt, S. Wuttke, *Chem. Mater.* **2016**, *28*, 3318.
- [361] M. Giménez-Marqués, E. Bellido, T. Berthelot, T. Simón-Yarza, T. Hidalgo, R. Simón-Vázquez, Á. González-Fernández, J. Avila, M. C. Asensio, R. Gref, P. Couvreur, C. Serre, P. Horcajada, *Small* **2018**, *14*, 1801900.
- [362] F. Shu, D. Lv, X.-L. Song, B. Huang, C. Wang, Y. Yu, S.-C. Zhao, *RSC Adv.* **2018**, *8*, 6581.
- [363] H. Lee, S. M. Dellatore, W. M. Miller, P. B. Messersmith, *Science* **2007**, *318*, 426.
- [364] S. He, H. Wang, C. Zhang, S. Zhang, Y. Yu, Y. Lee, T. Li, *Chem. Sci.* **2019**, *10*, 1816.
- [365] G. Zhang, X. Li, Q. Liao, Y. Liu, K. Xi, W. Huang, X. Jia, *Nat. Commun.* **2018**, *9*, 2785.
- [366] a) B. Illes, P. Hirschle, S. Barnert, V. Cauda, S. Wuttke, H. Engelke, *Chem. Mater.* **2017**, *29*, 8042; b) K. M. Au, A. Satterlee, Y. Min, X. Tian, Y. S. Kim, J. M. Caster, L. Zhang, T. Zhang, L. Huang, A. Z. Wang, *Biomaterials* **2016**, *82*, 178.
- [367] S. Wang, W. Morris, Y. Liu, C. M. McGuirk, Y. Zhou, J. T. Hupp, O. K. Farha, C. A. Mirkin, *Angew. Chem.* **2015**, *127*, 14951.
- [368] W. Zhu, G. Xiang, J. Shang, J. Guo, B. Motevalli, P. Durfee, J. O. Agola, E. N. Coker, C. J. Brinker, *Adv. Funct. Mater.* **2018**, *28*, 1705274.
- [369] a) V. Cauda, H. Engelke, A. Sauer, D. Arcizet, C. Bräuchle, J. Rädler, T. Bein, *Nano Lett.* **2010**, *10*, 2484; b) J. Liu, X. Jiang, C. Ashley, C. J. Brinker, *J. Am. Chem. Soc.* **2009**, *131*, 7567.
- [370] A. O. Hohner, M. P. C. David, J. O. Rädler, *Biointerphases* **2010**, *5*, 1.
- [371] N. Nasihat Sheno, S. Farhadi, A. Maleki, M. Hamidi, *New J. Chem.* **2019**, *43*, 1956.
- [372] R. C. Huxford, K. E. deKrafft, W. S. Boyle, D. Liu, W. Lin, *Chem. Sci.* **2012**, *3*, 198.

- [373] B. Illes, S. Wuttke, H. Engelke, *Nanomaterials* **2017**, 7, 351.
- [374] J. Yang, X. Chen, Y. Li, Q. Zhuang, P. Liu, J. Gu, *Chem. Mater.* **2017**, 29, 4580.
- [375] R. Kawano, N. Horike, Y. Hijikata, M. Kondo, A. Carné-Sánchez, P. Larpent, S. Ikemura, T. Osaki, K. Kamiya, S. Kitagawa, S. Takeuchi, S. Furukawa, *Chem* **2017**, 2, 393.
- [376] a) B. Fadeel, L. Farcas, B. Hardy, S. Vázquez-Campos, D. Hristozov, A. Marcomini, I. Lynch, E. Valsami-Jones, H. Alenius, K. Savolainen, *Nat. Nanotechnol.* **2018**, 13, 537; b) M. Faria, M. Björnalm, K. J. Thurecht, S. J. Kent, R. G. Parton, M. Kavallaris, A. P. R. Johnston, J. J. Gooding, S. R. Corrie, B. J. Boyd, P. Thordarson, A. K. Whittaker, M. M. Stevens, C. A. Prestidge, C. J. H. Porter, W. J. Parak, T. P. Davis, E. J. Crampin, F. Caruso, *Nat. Nanotechnol.* **2018**, 13, 777.
- [377] a) B. Pelaz, G. Charron, C. Pfeiffer, Y. Zhao, J. M. de la Fuente, X.-J. Liang, W. J. Parak, P. del Pino, *Small* **2013**, 9, 1573; b) C. Corbo, R. Molinaro, A. Parodi, N. E. Toledano Furman, F. Salvatore, E. Tasciotti, *Nanomedicine* **2015**, 11, 81.
- [378] C. Buzea, I. I. Pacheco, K. Robbie, *Biointerphases* **2007**, 2, MR17.
- [379] N. Lewinski, V. Colvin, R. Drezek, *Small* **2008**, 4, 26.
- [380] a) R. Grall, T. Hidalgo, J. Delic, A. Garcia-Marquez, S. Chevillard, P. Horcajada, *J. Mater. Chem. B* **2015**, 3, 8279; b) S. Wuttke, A. Zimpel, T. Bein, S. Braig, K. Stoiber, A. Vollmar, D. Müller, K. Haastert-Talini, J. Schaeske, M. Stiesch, G. Zahn, A. Mohmeyer, P. Behrens, O. Eickelberg, D. A. Bölükbas, S. Meiners, *Adv. Healthcare Mater.* **2017**, 6, 1600818; c) F. Joris, D. Valdepérez, B. Pelaz, S. J. Soenen, B. B. Manshian, W. J. Parak, S. C. De Smedt, K. Raemdonck, *J. Nanobiotechnol.* **2016**, 14, 69.
- [381] C. Tamames-Tabar, D. Cunha, E. Imbuluzqueta, F. Ragon, C. Serre, M. J. Blanco-Prieto, P. Horcajada, *J. Mater. Chem. B* **2014**, 2, 262.
- [382] À. Ruyra, A. Yazdi, J. Espín, A. Carné-Sánchez, N. Roher, J. Lorenzo, I. Imaz, D. MasPOCH, *Chem. – Eur. J.* **2015**, 21, 2508.
- [383] S. George, T. Xia, R. Rallo, Y. Zhao, Z. Ji, S. Lin, X. Wang, H. Zhang, B. France, D. Schoenfeld, R. Damoiseaux, R. Liu, S. Lin, K. A. Bradley, Y. Cohen, A. E. Nel, *ACS Nano* **2011**, 5, 1805.
- [384] T. Baati, L. Njim, F. Neffati, A. Kerkeni, M. Bouttemi, R. Gref, M. F. Najjar, A. Zakhama, P. Couvreur, C. Serre, P. Horcajada, *Chem. Sci.* **2013**, 4, 1597.
- [385] T. Baati, P. Horcajada, R. Gref, P. Couvreur, C. Serre, *J. Chromatogr. B* **2011**, 879, 2311.
- [386] a) H. S. Leong, K. S. Butler, C. J. Brinker, M. Azzawi, S. Conlan, C. Dufés, A. Owen, S. Rannard, C. Scott, C. Chen, M. A. Dobrovolskaia, S. V. Kozlov, A. Prina-Mello, R. Schmid, P. Wick, F. Caputo, P. Boisseau, R. M. Crist, S. E. McNeil, B. Fadeel, L. Tran, S. F. Hansen, N. B. Hartmann, L. P. W. Clausen, L. M. Skjolding, A. Baun, M. Ågerstrand, Z. Gu, D. A. Lamprou, C. Hoskins, L. Huang, W. Song, H. Cao, X. Liu, K. D. Jandt, W. Jiang, B. Y. S. Kim, K. E. Wheeler, A. J. Chetwynd, I. Lynch, S. M. Moghimi, A. Nel, T. Xia, P. S. Weiss, B. Sarmento, J. das Neves, H. A. Santos, L. Santos, S. Mitragotri, S. Little, D. Peer, M. M. Amiji, M. J. Alonso, A. Petri-Fink, S. Balog, A. Lee, B. Drasler, B. Rothen-Rutishauser, S. Wilhelm, H. Acar, R. G. Harrison, C. Mao, P. Mukherjee, R. Ramesh, L. R. McNally, S. Busatto, J. Wolfram, P. Bergese, M. Ferrari, R. H. Fang, L. Zhang, J. Zheng, C. Peng, B. Du, M. Yu, D. M. Charron, G. Zheng, C. Pastore, *Nat. Nanotechnol.* **2019**, 14, 629; b) T. Lammers, G. Storm, *Nat. Nanotechnol.* **2019**, 14, 626; c) R. van der Meel, E. Sulheim, Y. Shi, F. Kiessling, W. J. M. Mulder, T. Lammers, *Nat. Nanotechnol.* **2019**, 14, 1007.
- [387] X. Unamuno, E. Imbuluzqueta, F. Salles, P. Horcajada, M. J. Blanco-Prieto, *Eur. J. Pharm. Biopharm.* **2018**, 132, 11.
- [388] M. R. di Nunzio, V. Agostoni, B. Cohen, R. Gref, A. Douhal, *J. Med. Chem.* **2014**, 57, 411.
- [389] a) C. He, K. Lu, D. Liu, W. Lin, J. *Am. Chem. Soc.* **2014**, 136, 5181; b) W. Morris, W. E. Briley, E. Auyeung, M. D. Cabezas, C. A. Mirkin, *J. Am. Chem. Soc.* **2014**, 136, 7261.
- [390] a) S. K. Alsaiani, S. Patil, M. Alyami, K. O. Alamoudi, F. A. Aleisa, J. S. Merzaban, M. Li, N. M. Khashab, *J. Am. Chem. Soc.* **2018**, 140, 143; b) P. Kumar, V. Bansal, A. K. Paul, L. M. Bharadwaj, A. Deep, K.-H. Kim, *Appl. Nanosci.* **2016**, 6, 951; c) F. Lyu, Y. Zhang, R. N. Zare, J. Ge, Z. Liu, *Nano Lett.* **2014**, 14, 5761.
- [391] a) Y. Matsumura, H. Maeda, *Cancer Res.* **1986**, 46, 6387; b) J. Fang, H. Nakamura, H. Maeda, *Adv. Drug Delivery Rev.* **2011**, 63, 136.
- [392] a) T. Lammers, F. Kiessling, W. E. Hennink, G. Storm, *J. Controlled Release* **2012**, 161, 175; b) Y. Nakamura, A. Mochida, P. L. Choyke, H. Kobayashi, *Bioconjugate Chem.* **2016**, 27, 2225.
- [393] T. Simon-Yarza, T. Baati, F. Neffati, L. Njim, P. Couvreur, C. Serre, R. Gref, M. F. Najjar, A. Zakhama, P. Horcajada, *Int. J. Pharm.* **2016**, 511, 1042.
- [394] T. Simon-Yarza, M. Giménez-Marqués, R. Mrimi, A. Mielcarek, R. Gref, P. Horcajada, C. Serre, P. Couvreur, *Angew. Chem., Int. Ed.* **2017**, 56, 15565.
- [395] X. Wang, D. Miao, X. Liang, J. Liang, C. Zhang, J. Yang, D. Kong, C. Wang, H. Sun, *Biomater. Sci.* **2017**, 5, 658.
- [396] W. Cai, J. Wang, C. Chu, W. Chen, C. Wu, G. Liu, *Adv. Sci.* **2019**, 6, 1801526.
- [397] C.-Y. Sun, C. Qin, X.-L. Wang, G.-S. Yang, K.-Z. Shao, Y.-Q. Lan, Z.-M. Su, P. Huang, C.-G. Wang, E.-B. Wang, *Dalton Trans.* **2012**, 41, 6906.
- [398] A. Bansal, M. C. Simon, *J. Cell Biol.* **2018**, 217, 2291.
- [399] a) J. Zhao, Y. Yang, X. Han, C. Liang, J. Liu, X. Song, Z. Ge, Z. Liu, *ACS Appl. Mater. Interfaces* **2017**, 9, 23555; b) B. Lei, M. Wang, Z. Jiang, W. Qi, R. Su, Z. He, *ACS Appl. Mater. Interfaces* **2018**, 10, 16698.
- [400] C. C. Epley, K. L. Roth, S. Lin, S. R. Ahrenholtz, T. Z. Grove, A. J. Morris, *Dalton Trans.* **2017**, 46, 4917.
- [401] J. Liu, G. Yang, W. Zhu, Z. Dong, Y. Yang, Y. Chao, Z. Liu, *Biomaterials* **2017**, 146, 40.
- [402] S. Jha, P. K. Sharma, R. Malviya, *Achiev. Life Sci.* **2016**, 10, 161.
- [403] a) K. Jiang, L. Zhang, Q. Hu, Q. Zhang, W. Lin, Y. Cui, Y. Yang, G. Qian, *Chem. – Eur. J.* **2017**, 23, 10215; b) W. Lin, Q. Hu, J. Yu, K. Jiang, Y. Yang, S. Xiang, Y. Cui, Y. Yang, Z. Wang, G. Qian, *ChemPlusChem* **2016**, 81, 804; c) W. Lin, Y. Cui, Y. Yang, Q. Hu, G. Qian, *Dalton Trans.* **2018**, 47, 15882.
- [404] D. Liu, C. Poon, K. Lu, C. He, W. Lin, *Nat. Commun.* **2014**, 5, 4182.
- [405] L. Xing, H. Zheng, S. Che, *Chem. – Eur. J.* **2011**, 17, 7271.
- [406] J. G. Heck, J. Napp, S. Simonato, J. Möllmer, M. Lange, H. M. Reichardt, R. Staudt, F. Alves, C. Feldmann, *J. Am. Chem. Soc.* **2015**, 137, 7329.
- [407] Á. Juarranz, P. Jaén, F. Sanz-Rodríguez, J. Cuevas, S. González, *Clin. Transl. Oncol.* **2008**, 10, 148.
- [408] a) B. W. Henderson, T. J. Dougherty, *Photochem. Photobiol.* **1992**, 55, 145; b) T. J. Dougherty, C. J. Gomer, B. W. Henderson, G. Jori, D. Kessel, M. Korbelik, J. Moan, Q. Peng, *J. Natl. Cancer Inst.* **1998**, 90, 889.
- [409] a) K. Lu, C. He, W. Lin, *J. Am. Chem. Soc.* **2014**, 136, 16712; b) J. Park, D. Feng, S. Yuan, H.-C. Zhou, *Angew. Chem., Int. Ed.* **2015**, 54, 430; c) K. Lu, C. He, W. Lin, *J. Am. Chem. Soc.* **2015**, 137, 7600; d) J. Liu, Y. Yang, W. Zhu, X. Yi, Z. Dong, X. Xu, M. Chen, K. Yang, G. Lu, L. Jiang, Z. Liu, *Biomaterials* **2016**, 97, 1.
- [410] S.-Y. Ding, J. Gao, Q. Wang, Y. Zhang, W.-G. Song, C.-Y. Su, W. Wang, *J. Am. Chem. Soc.* **2011**, 133, 19816.
- [411] Q. Guan, D.-D. Fu, Y.-A. Li, X.-M. Kong, Z.-Y. Wei, W.-Y. Li, S.-J. Zhang, Y.-B. Dong, *iScience* **2019**, 14, 180.
- [412] L. Zhang, S. Wang, Y. Zhou, C. Wang, X.-Z. Zhang, H. Deng, *Angew. Chem., Int. Ed.* **2019**, 58, 14213.

- [413] a) H. S. Jung, P. Verwilt, A. Sharma, J. Shin, J. L. Sessler, J. S. Kim, *Chem. Soc. Rev.* **2018**, *47*, 2280; b) Y. Liu, P. Bhattarai, Z. Dai, X. Chen, *Chem. Soc. Rev.* **2019**, *48*, 2053; c) L. Zhao, Y. Liu, R. Chang, R. Xing, X. Yan, *Adv. Funct. Mater.* **2019**, *29*, 1806877.
- [414] Y. Zhang, N. Song, Y. Li, Z. Yang, L. Chen, T. Sun, Z. Xie, *J. Mater. Chem. B* **2019**, *7*, 4717.
- [415] Z. D. Hood, K. P. Kubelick, K. D. Gilroy, D. Vanderlaan, X. Yang, M. Yang, M. Chi, S. Y. Emelianov, Y. Xia, *Nanoscale* **2019**, *11*, 3013.
- [416] a) W. Zhu, Y. Liu, Z. Yang, L. Zhang, L. Xiao, P. Liu, J. Wang, C. Yi, Z. Xu, J. Ren, *J. Mater. Chem. B* **2018**, *6*, 265; b) X. Zheng, L. Wang, M. Liu, P. Lei, F. Liu, Z. Xie, *Chem. Mater.* **2018**, *30*, 6867; c) Y. Li, N. Xu, J. Zhou, W. Zhu, L. Li, M. Dong, H. Yu, L. Wang, W. Liu, Z. Xie, *Biomater. Sci.* **2018**, *6*, 2918; d) J. Feng, Z. Xu, P. Dong, W. Yu, F. Liu, Q. Jiang, F. Wang, X. Liu, *J. Mater. Chem. B* **2019**, *7*, 994.
- [417] a) Y. Liu, K. Ai, J. Liu, M. Deng, Y. He, L. Lu, *Adv. Mater.* **2013**, *25*, 1353; b) X. Ding, J. Liu, D. Liu, J. Li, F. Wang, L. Li, Y. Wang, S. Song, H. Zhang, *Nano Res.* **2017**, *10*, 3434.
- [418] K. Zhang, X. Meng, Y. Cao, Z. Yang, H. Dong, Y. Zhang, H. Lu, Z. Shi, X. Zhang, *Adv. Funct. Mater.* **2018**, *28*, 1804634.
- [419] A. Carné-Sánchez, C. S. Bonnet, I. Imaz, J. Lorenzo, É. Tóth, D. MasPOCH, *J. Am. Chem. Soc.* **2013**, *135*, 17711.
- [420] a) W. Shang, C. Zeng, Y. Du, H. Hui, X. Liang, C. Chi, K. Wang, Z. Wang, J. Tian, *Adv. Mater.* **2017**, *29*, 1604381; b) X. Gao, M. Zhai, W. Guan, J. Liu, Z. Liu, A. Damirin, *ACS Appl. Mater. Interfaces* **2017**, *9*, 3455; c) Y. Zhang, C. Liu, F. Wang, Z. Liu, J. Ren, X. Qu, *Chem. Commun.* **2017**, *53*, 1840.
- [421] a) M. He, J. Zhou, J. Chen, F. Zheng, D. Wang, R. Shi, Z. Guo, H. Wang, Q. Chen, *J. Mater. Chem. B* **2015**, *3*, 9033; b) R. Bian, T. Wang, L. Zhang, L. Li, C. Wang, *Biomater. Sci.* **2015**, *3*, 1270.
- [422] K. E. deKrafft, W. S. Boyle, L. M. Burk, O. Z. Zhou, W. Lin, *J. Mater. Chem.* **2012**, *22*, 18139.
- [423] T. Zhang, L. Wang, C. Ma, W. Wang, J. Ding, S. Liu, X. Zhang, Z. Xie, *J. Mater. Chem. B* **2017**, *5*, 2330.
- [424] D. Chen, D. Yang, C. A. Dougherty, W. Lu, H. Wu, X. He, T. Cai, M. E. Van Dort, B. D. Ross, H. Hong, *ACS Nano* **2017**, *11*, 4315.
- [425] K. Zhang, Z. Yu, X. Meng, W. Zhao, Z. Shi, Z. Yang, H. Dong, X. Zhang, *Adv. Sci.* **2019**, *6*, 1900530.
- [426] Z. Mi, P. Yang, R. Wang, J. Unruangsri, W. Yang, C. Wang, J. Guo, *J. Am. Chem. Soc.* **2019**, *141*, 14433.
- [427] C. G. Jones, V. Stavila, M. A. Conroy, P. Feng, B. V. Slaughter, C. E. Ashley, M. D. Allendorf, *ACS Appl. Mater. Interfaces* **2016**, *8*, 7623.
- [428] S. E. Miller, M. H. Teplensky, P. Z. Moghadam, D. Fairen-Jimenez, *Interface Focus* **2016**, *6*, 20160027.
- [429] D. Liu, R. C. Huxford, W. Lin, *Angew. Chem., Int. Ed.* **2011**, *50*, 3696.
- [430] C.-X. Chen, Q.-F. Qiu, M. Pan, C.-C. Cao, N.-X. Zhu, H.-P. Wang, J.-J. Jiang, Z.-W. Wei, C.-Y. Su, *Chem. Commun.* **2018**, *54*, 13666.
- [431] Z. Liao, J. Zhang, E. Yu, Y. Cui, *Polyhedron* **2018**, *151*, 554.
- [432] D. I. Osman, S. M. El-Sheikh, S. M. Sheta, O. I. Ali, A. M. Salem, W. G. Shousha, S. F. El-Khamisy, S. M. Shawky, *Biosens. Bioelectron.* **2019**, *141*, 111451.
- [433] S. Shahrokhian, S. Ranjbar, *Analyst* **2018**, *143*, 3191.
- [434] S. Liu, Z. Xiang, Z. Hu, X. Zheng, D. Cao, *J. Mater. Chem.* **2011**, *21*, 6649.
- [435] H. Xu, J. Gao, X. Qian, J. Wang, H. He, Y. Cui, Y. Yang, Z. Wang, G. Qian, *J. Mater. Chem. A* **2016**, *4*, 10900.
- [436] Y. Lu, B. Yan, J.-L. Liu, *Chem. Commun.* **2014**, *50*, 9969.
- [437] S. Liu, L. Wang, J. Tian, Y. Luo, G. Chang, A. M. Asiri, A. O. Al-Youbi, X. Sun, *ChemPlusChem* **2012**, *77*, 23.
- [438] J. Tian, Q. Liu, J. Shi, J. Hu, A. M. Asiri, X. Sun, Y. He, *Biosens. Bioelectron.* **2015**, *71*, 1.
- [439] W.-J. Song, *Talanta* **2017**, *170*, 74.
- [440] Y. Wu, J. Han, P. Xue, R. Xu, Y. Kang, *Nanoscale* **2015**, *7*, 1753.
- [441] a) T. Ye, Y. Liu, M. Luo, X. Xiang, X. Ji, G. Zhou, Z. He, *Analyst* **2014**, *139*, 1721; b) M. Zhao, Y. Wang, Q. Ma, Y. Huang, X. Zhang, J. Ping, Z. Zhang, Q. Lu, Y. Yu, H. Xu, Y. Zhao, H. Zhang, *Adv. Mater.* **2015**, *27*, 7372.
- [442] P. Ling, J. Lei, L. Zhang, H. Ju, *Anal. Chem.* **2015**, *87*, 3957.
- [443] Y. L. Liu, W. L. Fu, C. M. Li, C. Z. Huang, Y. F. Li, *Anal. Chim. Acta* **2015**, *861*, 55.
- [444] W. Li, C.-X. Yang, X.-P. Yan, *Chem. Commun.* **2017**, *53*, 11469.
- [445] N. Alizadeh, A. Salimi, R. Hallaj, F. Fathi, F. Soleimani, *J. Nanobiotechnol.* **2018**, *16*, 93.
- [446] P. Xu, G. Liao, *Materials* **2018**, *11*, 1616.
- [447] a) S. Wang, Z. Guo, *Colloids Surf., B* **2014**, *113*, 483; b) R. Ricco, C. Pfeiffer, K. Sumida, C. J. Sumbly, P. Falcaro, S. Furukawa, N. R. Champness, C. J. Doonan, *CrystEngComm* **2016**, *18*, 6532.
- [448] K. Liang, R. Ricco, C. M. Doherty, M. J. Styles, S. Bell, N. Kirby, S. Mudie, D. Haylock, A. J. Hill, C. J. Doonan, P. Falcaro, *Nat. Commun.* **2015**, *6*, 7240.
- [449] R. Ricco, W. Liang, S. Li, J. J. Gassensmith, F. Caruso, C. Doonan, P. Falcaro, *ACS Nano* **2018**, *12*, 13.
- [450] S. Li, M. Dharmarwardana, R. P. Welch, Y. Ren, C. M. Thompson, R. A. Smaldone, J. J. Gassensmith, *Angew. Chem., Int. Ed.* **2016**, *55*, 10691.
- [451] N. Nassif, O. Bouvet, M. Noelle Rager, C. Roux, T. Coradin, J. Livage, *Nat. Mater.* **2002**, *1*, 42.
- [452] K. Liang, J. J. Richardson, J. Cui, F. Caruso, C. J. Doonan, P. Falcaro, *Adv. Mater.* **2016**, *28*, 7910.
- [453] a) W. Zhu, J. Guo, J. O. Agola, J. G. Croissant, Z. Wang, J. Shang, E. Coker, B. Motevalli, A. Zimpel, S. Wuttke, C. J. Brinker, *J. Am. Chem. Soc.* **2019**, *141*, 7789; b) W. Zhu, J. Guo, S. Amini, Y. Ju, J. O. Agola, A. Zimpel, J. Shang, A. Nouredine, F. Caruso, S. Wuttke, J. G. Croissant, C. J. Brinker, *Adv. Mater.* **2019**, *31*, 1900545.
- [454] R. J. Drout, L. Robison, O. K. Farha, *Coord. Chem. Rev.* **2019**, *381*, 151.
- [455] Q. Sun, C.-W. Fu, B. Aguila, J. Perman, S. Wang, H.-Y. Huang, F.-S. Xiao, S. Ma, *J. Am. Chem. Soc.* **2018**, *140*, 984.
- [456] S. Hudson, J. Cooney, E. Magner, *Angew. Chem., Int. Ed.* **2008**, *47*, 8582.
- [457] W. Liang, F. Carraro, M. B. Solomon, S. G. Bell, H. Amenitsch, C. J. Sumbly, N. G. White, P. Falcaro, C. J. Doonan, *J. Am. Chem. Soc.* **2019**, *141*, 14298.
- [458] O. M. Sabek, S. Ferrati, D. W. Fraga, J. Sih, E. V. Zabre, D. H. Fine, M. Ferrari, A. O. Gaber, A. Grattoni, *Lab Chip* **2013**, *13*, 3675.
- [459] G. Faccio, *Sensors* **2018**, *18*, 1204.
- [460] W. Liang, H. Xu, F. Carraro, N. K. Maddigan, Q. Li, S. G. Bell, D. M. Huang, A. Tazria, M. B. Solomon, H. Amenitsch, L. Vaccari, C. J. Sumbly, P. Falcaro, C. J. Doonan, *J. Am. Chem. Soc.* **2019**, *141*, 2348.
- [461] B. Panganiban, B. Qiao, T. Jiang, C. DelRe, M. M. Obadia, T. D. Nguyen, A. A. A. Smith, A. Hall, I. Sit, M. G. Crosby, P. B. Dennis, E. Drockenmuller, M. Olvera de la Cruz, T. Xu, *Science* **2018**, *359*, 1239.
- [462] a) C. Avci, I. Imaz, A. Carné-Sánchez, J. A. Pariente, N. Tasios, J. Pérez-Carvajal, M. I. Alonso, A. Blanco, M. Dijkstra, C. López, D. MasPOCH, *Nat. Chem.* **2017**, *10*, 78; b) J. Guo, B. L. Tardy, A. J. Christofferson, Y. Dai, J. J. Richardson, W. Zhu, M. Hu, Y. Ju, J. Cui, R. R. Dagastine, I. Yarovsky, F. Caruso, *Nat. Nanotechnol.* **2016**, *11*, 1105.
- [463] A. Poddar, J. J. Conesa, K. Liang, S. Dhakal, P. Reineck, G. Bryant, E. Pereiro, R. Ricco, H. Amenitsch, C. Doonan, X. Mulet, C. M. Doherty, P. Falcaro, R. Shukla, *Small* **2019**, *15*, 1902268.
- [464] J. Guo, W. Zhu, R. Serda, J. O. Agola, A. Nouredine, E. Ploetz, S. Wuttke, C. J. Brinker, unpublished.
- [465] A. V. Desai, P. Samanta, B. Manna, S. K. Ghosh, *Chem. Commun.* **2015**, *51*, 6111.

- [466] E. Buzhor, L. Leshansky, J. Blumenthal, H. Barash, D. Warshawsky, Y. Mazor, R. Shtrichman, *Regener. Med.* **2014**, *9*, 649.
- [467] a) A. T. Bell, *Science* **2003**, *299*, 1688; b) R. Schlögl, *Angew. Chem., Int. Ed.* **2015**, *54*, 3465; c) G. A. Somorjai, J. Y. Park, *Angew. Chem., Int. Ed.* **2008**, *47*, 9212.
- [468] L. Chen, B. Duan, Q. Luo, Z. Gu, J. Liu, C. Duan, *Catal. Sci. Technol.* **2016**, *6*, 1616.
- [469] O. Kolmykov, N. Chebbat, J.-M. Commenge, G. Medjahdi, R. Schneider, *Tetrahedron Lett.* **2016**, *57*, 5885.
- [470] J. Chen, L. Huang, Q. Wang, W. Wu, H. Zhang, Y. Fang, S. Dong, *Nanoscale* **2019**, *11*, 5960.
- [471] a) J. Jiang, F. Gándara, Y.-B. Zhang, K. Na, O. M. Yaghi, W. G. Klemperer, *J. Am. Chem. Soc.* **2014**, *136*, 12844; b) J. Jiang, O. M. Yaghi, *Chem. Rev.* **2015**, *115*, 6966.
- [472] A. M. Abdel-Mageed, B. Rungtaweeworanit, M. Parlinska-Wojtan, X. Pei, O. M. Yaghi, R. J. Behm, *J. Am. Chem. Soc.* **2019**, *141*, 5201.
- [473] a) H. Furukawa, U. Müller, O. M. Yaghi, *Angew. Chem., Int. Ed.* **2015**, *54*, 3417; b) Q. Yang, Q. Xu, H.-L. Jiang, *Chem. Soc. Rev.* **2017**, *46*, 4774; c) P. Falcaro, R. Ricco, A. Yazdi, I. Imaz, S. Furukawa, D. Maspoch, R. Ameloot, J. D. Evans, C. J. Doonan, *Coord. Chem. Rev.* **2016**, *307*, 237; d) N. Van Velthoven, S. Waitschat, S. M. Chavan, P. Liu, S. Smolders, J. Vercammen, B. Bueken, S. Bals, K. P. Lillerud, N. Stock, D. E. De Vos, *Chem. Sci.* **2019**, *10*, 3616; e) A. Zanon, F. Verpoort, *Coord. Chem. Rev.* **2017**, *353*, 201; f) P. Hu, J. V. Morabito, C.-K. Tsung, *ACS Catal.* **2014**, *4*, 4409; g) M. L. Foo, R. Matsuda, S. Kitagawa, *Chem. Mater.* **2014**, *26*, 310; h) M. Meilikhov, K. Yussenko, D. Esken, S. Turner, G. Van Tendeloo, R. A. Fischer, *Eur. J. Inorg. Chem.* **2010**, *2010*, 3701; i) N. A. Khan, Z. Hasan, S. H. Jhung, *Coord. Chem. Rev.* **2018**, *376*, 20.
- [474] M. Zhao, K. Yuan, Y. Wang, G. Li, J. Guo, L. Gu, W. Hu, H. Zhao, Z. Tang, *Nature* **2016**, *539*, 76.
- [475] C.-H. Kuo, Y. Tang, L.-Y. Chou, B. T. Sneed, C. N. Brodsky, Z. Zhao, C.-K. Tsung, *J. Am. Chem. Soc.* **2012**, *134*, 14345.
- [476] M. Zhao, K. Deng, L. He, Y. Liu, G. Li, H. Zhao, Z. Tang, *J. Am. Chem. Soc.* **2014**, *136*, 1738.
- [477] K. M. Choi, K. Na, G. A. Somorjai, O. M. Yaghi, *J. Am. Chem. Soc.* **2015**, *137*, 7810.
- [478] P. Pachfule, M. K. Panda, S. Kandambeth, S. M. Shivaprasad, D. D. Díaz, R. Banerjee, *J. Mater. Chem. A* **2014**, *2*, 7944.
- [479] L. Zhang, J. Lei, F. Ma, P. Ling, J. Liu, H. Ju, *Chem. Commun.* **2015**, *51*, 10831.
- [480] J. Park, Q. Jiang, D. Feng, H.-C. Zhou, *Angew. Chem., Int. Ed.* **2016**, *55*, 7188.
- [481] J. Park, Q. Jiang, D. Feng, L. Mao, H.-C. Zhou, *J. Am. Chem. Soc.* **2016**, *138*, 3518.
- [482] W. Wang, L. Wang, Z. Li, Z. Xie, *Chem. Commun.* **2016**, *52*, 5402.